2003

Force and low speed control in mechatronic systems with friction

John William Lee Simpson
University of Wollongong

FORCE AND LOW SPEED CONTROL IN MECHATRONIC SYSTEMS WITH FRICTION

A thesis submitted in fulfilment of the requirements for the award of the degree

DOCTOR OF PHILOSPHY

From

UNIVERSITY OF WOLLONGONG

By

JOHN WILLIAM LEE SIMPSON, BE, ME(UNSW)

2003

SCHOOL OF ELECTRICAL, COMPUTER AND TELECOMMUNICATIONS ENGINEERING

ACKNOWLEDGEMENTS

The thesis was carried out as part of a Cooperative Research Centre for Intelligent Manufacturing Systems and Technologies funded project within the School of Electrical Computer and Telecommunication Engineering at the University of Wollongong. I like to thank both these organisation for their support which made this thesis possible.

I would like to give a special thanks my supervisor Professor Chris Cook and my co supervisor Dr Zheng Li for their assistance and guidance throughout my candidature.

I would also like to thank fellow researchers Mr Jeff Moscrop, Mr Simon Webb, Ms Marta Fernandes and Mr Stephen Van Duin as colleagues working together in the same area in which ideas could be discussed clearly openly and freely. I would also like to thank Mr Brian Webb for manufacturing the mechanical components of the experiment equipment used in this thesis.

THESIS CERTIFICATION

I, John William Lee Simpson declare that this thesis submitted in fullfillment of the requirements for the award of Doctor of Philosophy in the School of Electrical, Computer and Telecommunications Engineering, University of Wollongong, is wholly my own work unless otherwise referenced or acknowledged. The document has not been submitted for qualification at any other academic institution.

John W.L Simpson

TABLE OF CONTENTS

ABSTRACT

A mechatronic system is one in which mechanical, electrical and intelligent computer control are integrated. Two mechatronic systems were used in this thesis. One was a four axis industrial robot and the other a grinding machine. Friction exist in almost all mechanisms with moving parts and depending on the arrangement of the mechanical components may have a significant influence on the mechatronic system's overall performance. Both the mechatronic systems used in this thesis have large friction components. An understanding of friction and subsequent application of this understanding has been used in force estimation and control schemes and to develop control schemes that lead to improved low speed position tracking.

At low velocities friction has highly non-linear characteristics. In many instances the friction at rest (the static friction) is higher than the friction when the mechanism is moving at low velocities. This in many mechanical systems leads to a phenomena referred to as "stick slip". Stick slip is a periodic cycle of alternating motion and rest which limits the velocity and position accuracy of many machines. An impulsive control scheme for low velocity position tracking which reduces the stick slip limit cycle was developed in this thesis.

A force control scheme in which the applied force is estimated from servo motor information was also developed. The torque applied by the motor is made up of the torque accelerating the mechanical components, the torque required to overcome friction and the torque required to overcome an external force. For many mechanisms the largest force that the motor has to overcome is the friction component. Therefore accurate friction models of the mechanical system were used to extract the required

information about the external force from the motor torque signals. The friction models used here include viscous, coulomb and position dependent friction components.

The force estimation and control techniques developed were applied to the grinding process. A series of experiments were conducted in which grinding forces were calculated from servo motor information and a control scheme to control grinding forces without using force sensors was implemented.

PUBLISHED PAPERS ARISING FROM THIS THESIS

1. J.W.L Simpson, C.D Cook, Z. Li. "A controller for SCARA robots with friction". *Proceedings of the Fifth International Conference on Control, Automation, Robotics and Vision.* Singapore December 1998.
2. J.W.L Simpson, C.D Cook, Z. Li . "Position tracking in two dimensional workspace for SCARA robots with friction". *Proceedings of the Australian Conference on Robotics and Automation.* Brisbane, March 1999.
3. J.W.L Simpson, C.D Cook, Z. Li " A friction controller using fuzzy logic for Parameter Adjustment, for use in systems with friction." *Proceedings of the 1999 IEEE Hong Kong Symposium on Robotics and Control.* Hong Kong July 2-3. 1999.
4. J.W.L Simpson, C.D Cook, Z.Li "Multi-Sensor Grinding Machine for Investigating Grinding Performance." *Proceedings of the 9th International Power Electronics and Motion Control Symposium.* Kosice Slovak Republic 5-7 September 2000
5. J.W.L Simpson , C.D Cook, Z.Li "An improved PID controller for machines with friction" *Proceedings of the 1st IFAC Conference on Mechatronic Systems*, Darmstadt Germany 18-20 September 2000.
6. Li Xue, Fazel Naghdy , John Simpson "Heuristic monitoring and control of surface finishing in the grinding process". *Proceedings of ICME2000*, Sydney, August 2000.
7. Cook C, Naghdy F, Li Z, Moscrop J, Simpson J "Industrial automation research at the university of Wollongong" *International Manufacturing Leaders Forum*, pp113-118, 8-10 Feb 2002, Adelaide, Australia

1 INTRODUCTION

1.1 Background

Two mechatronic systems were used in this thesis. One was an industrial robot and the other was a grinding machine. Both these systems had mechanical arrangements in which friction was significant. These mechatronic systems were used to develop low speed position tracking control schemes and force estimation and control schemes.

One of the motivations for developing force estimation and control schemes was to measure and record grinding forces. Today "Grinding is a major manufacturing process that accounts for about 20-25% of the total expenditure on machining operations in industrial countries"[1]. Improvements in the grinding process therefore provide significant benefits for manufacturing. The measurement of grinding force gives valuable information about the grinding process. Grinding forces are proportional to metal removal rates and can also be used to indicate work piece burn and degree of wheel dullness.

Grinding forces can be measured using force sensors. However these are expensive and typically require a special mounting arrangement for the work piece. Measuring grinding forces without using force sensors would be of considerable advantage. One approach is to use the torque which is applied by the servomotors to drive the work piece into the grinding wheel. The torque applied by the motor is made up of the torque accelerating the mechanical components, the torque required to overcome friction and the torque required to overcome the grinding force. Thus the grinding force can be found if the frictional and acceleration components are known.

One significant problem with this approach is caused by the high gearing typically used in most machine tools and many robots. The high gearing is an essential part of the machine, which gives it the necessary precision and rigidity required in most applications. The gearing however significantly reduces the external force as seen by the motor. Typically the largest force that the motor has to overcome is the friction component and the grinding force can be less than 10% of this value as seen at the motor. Therefore accurate friction models of the mechanical system are needed to be able to extract the grinding force information from the motor torque signals. The friction models used here considered viscous, Coulomb and position dependent friction components. The techniques used to estimate grinding forces were also applied to the robotic system.

As part of the study of friction the low speed characteristics of friction were considered. At low velocities friction has highly non-linear characteristics. In many instances the friction at rest (the static friction) is higher than the friction when the mechanism is moving at low velocities. This in many mechanical systems leads to a phenomena referred to as "stick slip". Stick slip is a periodic cycle of alternating motion and rest, which determines the lower performance bounds of many machines. A control algorithm developed by Li et al [2], which reduces the stick slip limit cycling, was used in this thesis. The controller was implemented on a conventional industrial robot and a grinding machine. The controller applies a series of torque pulses with magnitudes above the static friction value. This gave an improvement in position tracking compared with a conventional PID controller.

In this chapter a literature review of work relevant to this thesis is given. Other authors have considered in detail the mechanism of grinding and their work is discussed in Section 1.2. In particular the interrelationship between grinding forces and the grinding process are discussed. In Section 1.3 previous work detailing the benefits of using force controlled grinding is given. There have been many grinding force control schemes developed and these are also described in Section 1.3. In Section 1.4 robotic grinding schemes and sensorless force control schemes are reviewed.

In Section 1.5 previous work on friction models is discussed. The discussion briefly describes friction mechanisms, conventional friction models and position dependent friction. In Section 1.6 low speed frictional control schemes are discussed. Other authors have documented stick slip phenomena, described the performance of conventional PID and PD controllers and detailed model based friction compensation and dither control schemes. In Section 1.7 other research work in the area of impulsive control schemes is discussed.

1.2 Grinding Mechanisms

Grinding is the name given to the machining process which utilizes hard abrasives as the cutting medium. The grinding process is not new, from "the Neolithic period (15000 to 5000BC) onward man has used the abrasive properties of a number of naturally occurring substances, such as sandstone, emery and jewels to cut and form other very hard materials"[1]. In the 1500s Leonardo da Vinci produced a series of drawings for a machine to sharpen and polish needles. This was one of the earliest steps in mechanising the grinding process. It was not until the 1830's that a "grinding machine that we could properly call a machine tool appeared"[1]. By the 1890's grinding machines were making precision hardened steel parts, applications of which included

the bicycle manufacturing industry, which was significantly more important in the 1890's than at present. This ability to efficiently machine hardened steel components was an essential precursor to the automobile industry of the next century and later on the aeronautical industry.

Other authors have considered in detail the mechanisms of grinding and discussed the relationships between grinding forces and the grinding process. Only a brief discussion of grinding mechanisms is given here concentrating on the interrelationships between grinding forces, metal removal rates, specific grinding energies and power. Though this thesis is not in the area of the mechanics of grinding a review of the grinding process does aid one of the main objectives of this thesis, the estimation and control of grinding forces.

Forces are developed between the work piece and the wheel as part of the grinding process. The tangential and normal forces F_n and F_t respectively are shown in figure 1.1, for a surface grinding arrangement.

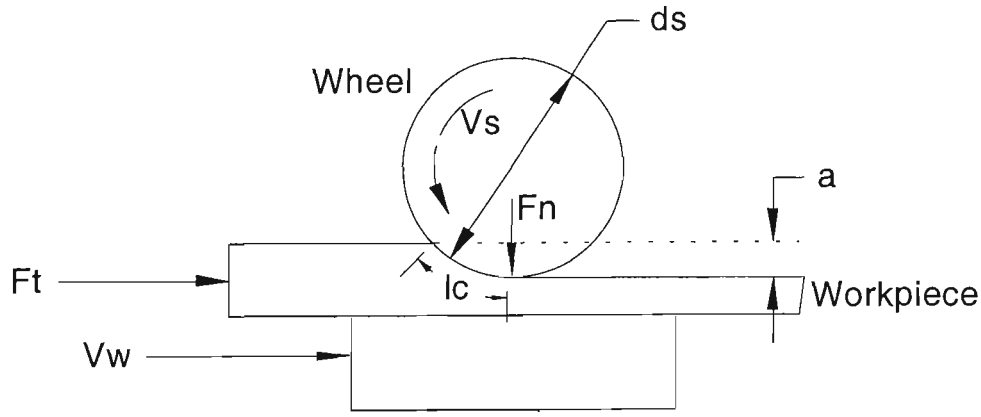

Figure 1.1 Force components of plunge grinding [3]

The grinding power P is given by:

$$P = F_t(v_s - v_w) \qquad \text{Eq 1.1}$$

where v_w=work piece velocity, v_s=grinding wheel velocity.

Normally the grinding wheel or spindle wheel velocity is considerably greater than the work piece velocity and Eq 1.1 can be reduced to:

$$P = F_t v_s \qquad \text{Eq 1.2}$$

A measure used extensively in the discussion of the grinding process is the specific grinding energy u:

$$u = \frac{P}{Q_w} \qquad \text{where} \qquad Q_w = v_w ab \qquad \text{Eq 1.3}$$

where a=cut depth b=wheel width. Combining Eq 1.3, 1.2 an expression relating the feedrate to the tangential grinding force and used in Chapter 6 is given by:

$$F_t = \frac{u v_w ab}{v_s} \qquad \text{Eq 1.4}$$

Tonshoff in his survey of grinding models [4] gives a more detailed model of a similar form where:

$$F_t = c_{wp} c_{wp} \left(\frac{v_w}{v_s} \right)^{e1} a^{e2} b^{e2} \qquad \text{Eq 1.5}$$

where c_{wp} is the work piece constant and c_{wg} is the grinding wheel constant.e_1,e_2,e_3 are constants. Eq 1.5 reduces to Eq 1.4 by letting $e_1 = e_2 = e_3 = 1$ and $u = c_{wp} c_{wg}$

Although not specifically used in this thesis a discussion of the grinding process in terms of chip formation shows the interconnection of grinding forces, the grinding process and work piece finish. This illustrates one of the main motivations of wanting to monitor grinding forces as a realistic measure of the grinding process and expected work piece quality. The grinding process occurs by chip formation similarly to other machining processes such as milling and turning but on a much finer scale. The grinding wheel can be seen as a series of randomly distributed cutting points of undefined geometry. Malkin [3] in his discussion of the grinding process says that the

specific grinding energy is made up of chip formation, sliding and ploughing components. The specific grinding energy u is given by:

$$u = u_{ch} + u_{sl} + u_{pl} \qquad \text{Eq 1.6}$$

where u_{ch} ,u_{sl} ,u_{sl} are the chip formation, ploughing and sliding components respectively. The chip formation energy u_{ch} is the only part which is expended in material removal and is the minimum grinding energy required. Typically the minimum grinding energy approaches the melting energy of the material being ground. "This does not imply that melting occurs, owing to the decreasing shear resistance of the material as the melting energy is approached"[3]. The metal chips are sheared off due to the force applied by the abrasive grits (cutting tool) just before it melts.

The ploughing component is part of the grinding energy, which deforms the metal but does not remove any material. This is usually associated with the slide flow of metal from the cutting path into ridges. In [3] the chip formation and ploughing component are combined and referred to as the specific cutting energy u_c:

$$u_c = u_{ch} + u_{pl} \qquad \text{Eq 1.7}$$

The grinding process then will consist of cutting and sliding components. The sliding component is due to dulled or flattened abrasive grits sliding along the work piece and not removing any material. These dulled or fattened abrasive grits are often referred to as wear flat areas. "A direct relationship has been obtained between grinding forces and the wheel dullness expressed in terms of the percentage of the wheel surface consisting of wear flats"[3]. This is shown in figure 1.2 where A is the wear-flat area as a percentage of the wheel surface.

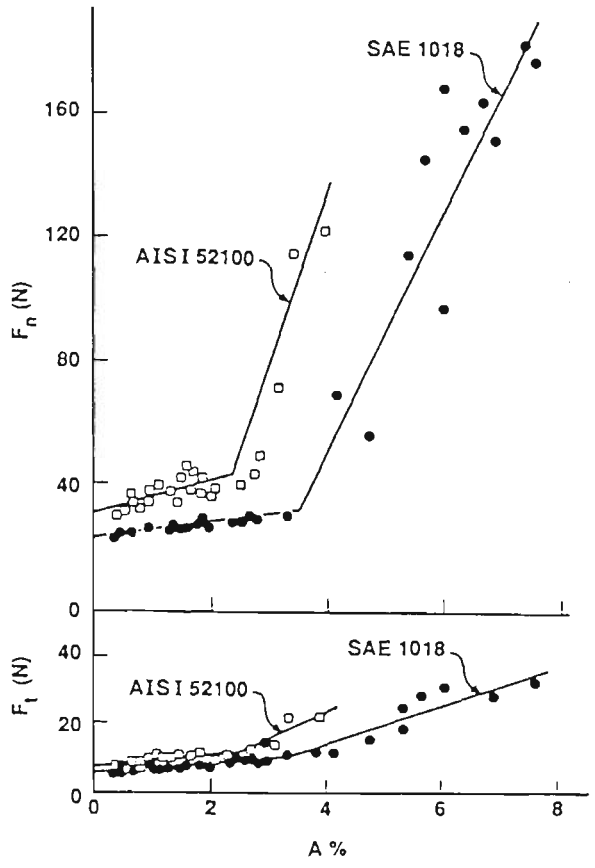

Figure 1.2 Tangential and normal force components for surface plunge grinding of two steels [3]

In figure 1.2 when the wheel dullness is theoretically zero A=0 (y intercept) and the only force present is the cutting forces F_c. The increase in force as the wheel dullness increases is then due to the sliding component. This implies that the tangential force F_t and the normal force F_n can be expressed as follows:

$$F_t = F_{t,c} + F_{t,sl} \qquad F_n = F_{n,c} + F_{n,sl} \qquad \text{Eq 1.8}$$

where $F_{t,c}$, $F_{n,c}$ are the tangential and normal cutting forces and $F_{t,sl}$, $F_{n,sl}$ are the tangential and normal sliding components. The proportional relationship between wheel flats and sliding force implies " a constant average stress p and friction coefficient μ between the wear flat and the work piece"[3]. Eq 1.8 can be rewritten as:

$$F_t = F_{t,c} + \mu \bar{p} A_a \qquad F_n = F_{n,c} + \bar{p} A_a \qquad \text{Eq 1.9}$$

A_a is the actual contact between the wear flats and the work piece and is given by:

$$A_a = b l_c a \qquad \text{Eq 1.10}$$

By rearranging Eq 1.9 an expression between the normal and tangential force can be expressed as:

$$F_n = \frac{1}{\mu} F_t + \frac{\mu F_{n,c} - F_{t,c}}{\mu} \qquad \text{Eq 1.11}$$

"For a given grinding condition, $F_{t,c}$ and $F_{n,c}$ are constant"[3] and Eq 1.11 could be written in the form:

$$F_n = \frac{1}{\mu} F_t + c\,. \qquad \text{Eq 1.12}$$

where c is a constant. An equation of the form of Eq 1.12 is used in many grinding control schemes [5,6,7,8]. A plot of normal force versus tangential force is shown in figure 1.3

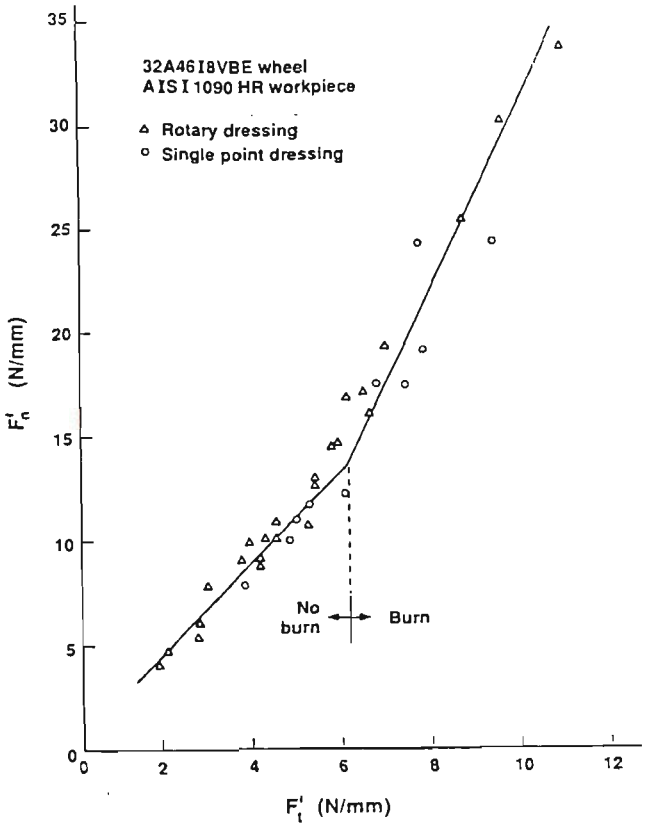

Figure 1.3 Normal versus tangential grinding force [3]

From Eq 1.12 the slope of the line in figure 1.3 is $1/\mu$. As can be seen from figure 1.3 the coefficient μ changes when the work piece starts to burn. The change in the friction coefficient μ relating normal force to tangential grinding has been used in adaptive

grinding control schemes force to stop thermal damage [9]. If μ fell below 0.4 then it was assumed that thermally damaged components were being produced. In [9] it is suggested that there was a relationship between material being removed and work piece burn. The author estimated the average void volume between abrasive grits on the wheel surface. It was observed as the volume of metal being removed approached the void volume " instead of the heat being carried away from the work piece in grinding chips, it is being conducted back into the work piece from chip - work piece contact and causing the work piece to burn"[9].

The measurement of grinding forces can be used to indicate if work piece burn is occurring. Grinding forces could then be controlled to stop work piece damage. Grinding forces are related to metal removal rates. Changing the feedrate or depth of cut and consequently changing the metal removal rate is a strategy that could be used in a control scheme to control grinding forces.

1.3 Grinding Force Control

In many grinding control schemes the feedrate is controlled. In multi axis grinding the velocity of each axis is controlled to produce the desired profile of the work piece. In flat surface grinding the feedrate and depth of cut are controlled and normally held constant. An alternative is to use controlled force grinding. In controlled force grinding typically the feedrate is varied to maintain a constant grinding force. Controlled force grinding is not new. Hahn [10] in 1964 described constant force grinding to be used in internal grinding systems. Hahn [11] gives a detailed discussion of the benefits of controlled force grinding. For example the normal force "governs the surface finish, the deflection in the machine, and the onset of thermal damage"[11].

In conventional grinding where the feedrate is controlled the normal force increases with the metal removal rate. The variation in the normal force can also lead to changes in the deflection of the mechanical parts. This can lead to errors in the contour tracking of the part. This is most apparent at the start (sparkin) and end of grinding (sparkout) where the variation in removal rates and therefore grinding force is greatest and hence the variation in deflection of the machine is a maximum.

As wheel sharpness decreases the normal force increases resulting in increased deflection and sometimes thermal damage. "The increased normal force exerted on the increasing real area of contact at the work wheel interface, produces higher temperatures which at some point exceeds the threshold value, and thermal damage results"[11]. Controlled force grinding has the ability to monitor the wheel sharpness and by not permitting it to drop below a certain value so that thermal damage problems may be eliminated.

Constant force grinding was first implemented via mechanical arrangements. Electrically implemented force control schemes have normally used force transducers.

1.3.1 Mechanical Schemes.

Hahn [10] used a mechanical arrangement for constant force grinding. In figure 1.4a a conventional internal grinding scheme is shown and a scheme proposed for controlled force grinding is shown in figure 1.4b. Internal grinding was one of the first applications of controlled force grinding due to its mechanical arrangement being less rigid and more susceptible to machining error because of deflection of the mechanical system. In the conventional arrangement this deflection increases with the grinding force. This will lead to taper and size error in the finished piece. In figure 1.4b a constant force control

scheme is achieved by mounting the wheel head in an antifriction slide *m*. It is pivoted at *P*, a constant force *F* is applied and since the force is constant the deflection is constant. The stop *B* can be adjusted so no taper occurs.

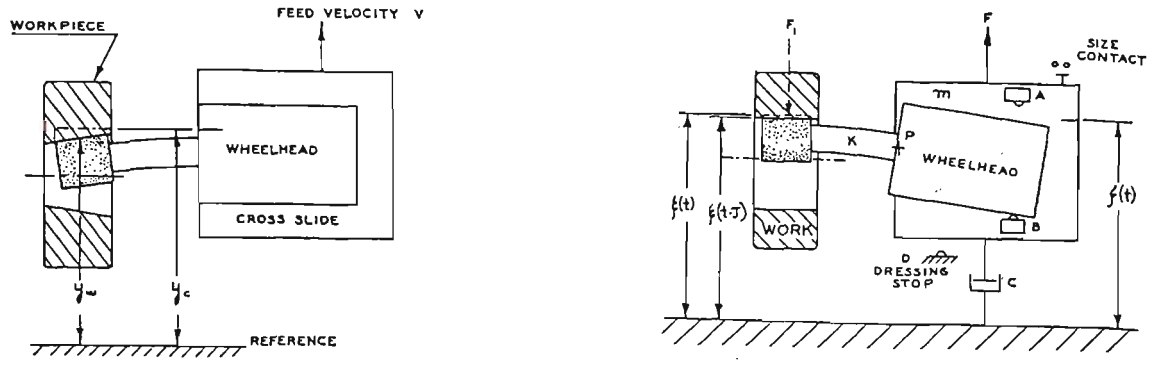

(a) (b)

Figure 1.4 Mechanical constant force grinding schemes [11]

1.3.2 Electrical Schemes

The electrically controlled force grinding schemes in [3,9,12,13,14,15,16,17] require force sensors to provide feedback signals to be used in a control scheme. Jenkins et al [12,13] describe one such scheme. In this control system a two axis-grinding machine is used where the X-axis controls the work piece motion and the Z-axis controls the motion of the grinding wheel (this is very similar to the arrangement used on the grinding machine in this thesis). The force control signal is derived from force transducers. The X-axis is used to control the feed velocity and the normal force is varied by the Z-axis tool position. A least squares estimate was used to analyze the system's response to step inputs. This was used to determine the transfer function between the input command velocity and force and their associated output. Also the relationship between force and velocity functions was determined. The authors also give detailed design requirements. In the force control loop due to the danger of surface damage with too large a normal force the authors set the maximum force overshoot as 1%. Variation in feed velocity was observed to alter the appearance of the work piece and "5% overshoot did not adversely affect the surface finish"[12] and so the velocity

overshoot was limited to 5%. It was also commented that higher velocities resulted in a rougher surface finish. Uniform surface finished is achieved by having uniform velocity.

Two separate control loops were designed. One was for the velocity control and one for force control. Standard PID controllers were used and found to be adequate. Part of the design was to decouple the force and velocity loops and this was achieved by increasing the forward loop gain.

In later work the same authors [13] used an adaptive force controller. A real time grinding model with an adaptive pole zero cancellation technique was used. This was found to give superior performance to their previous control scheme using a fixed gain controller. The system was capable of being used for fine finishing where the lower forces require a control system with a much higher fidelity.

Brinksmeier and Popp [14] used an adaptive control system using normal force measurements from a piezo electric force transducer. The "control system reduced the grinding time and ensured a good work piece quality"[14]. The author has assumed a linear relationship between metal removal rate and normal grinding force. The actual proportionality constant is identified online during the grinding process.

Schemes such as the ones mentioned above show the benefits and the effectiveness of control grinding forces. However all these schemes rely on force sensors added to the grinding machine to measure force.

1.4 Robotic Force Control Schemes

There have been a number of grinding control schemes implemented on robot systems. Their physical arrangement is different from a conventional machine tool in that quite often the grinding wheel is being moved by the robot and the machined part is stationary. Application of robot grinding systems include deburring weld beads and removing excess stock from diecast or press worked pieces. These control schemes have almost all used external force transducers to measure the applied force. In common with machine tool applications the dangers of excess metal removal rates and the associated higher grinding force and possible work piece damage (these are discussed more fully in Section 1.2) also apply to robotic applications.

Robotic grinding systems for weld deburring have included vision systems to find the weld and estimate the amount of material to be removed [5]. Whitney et al [5] used Kalman filtering of the optical data to determine the weld bead profile. The weld profile is essential to the power planner algorithm, which is used to estimate the number of passes and trajectory of the grinding wheel. Gorinevsky et al [8] describes a robot grinding system used for deburring metal parts. Prior to grinding the robot moves the tools along the planned trajectory and using a force sensor determines the actual outline of the work piece. This can be compared with the desired shape and the amount of metal to be removed can be calculated.

There has been a considerable amount of work in the area of force control in robotic systems in addition to grinding applications. In robotic systems motor currents have been used to control forces at the end effector. In the robotics field this area of work is

often referred to as implicit force control. Implicit force control in robotic systems in essence is very similar to the work this thesis addresses in machine tools.

Gorinevisky et al [8] in their discussion of implicit force control schemes suggest that it can only be used with direct drive manipulator arms or if the friction in the gear trains is small. There are examples of implicit control using direct drives in Wada et al [18]. Rocco et al [19] have implemented a force control scheme using a direct drive system. In both Wada et al [18] and Rocco et al [19] models of the robotic manipulator have included inertia and viscous friction components. Ohishi [20] also using a direct drive mechanism used inertia, viscous and Coulomb friction in his force observer. Wang and Jan [21] have applied implicit force control schemes to the grinding task. They used a pneumatic grinder held in the wrist joint of an articulated robot. The wrist joint uses a DC direct drive motor whose angle and current are used to estimate the grinding contact force (normal force).

Gorinevisky [8] in their discussion have commented that in "most industrial manipulator systems joint friction by far exceeds the torques generated in contact tasks". Other authors Elosegui et al [22], Taghirad et al [23], [24], Luh et al [25] have used joint torque sensors to eliminate the effects of friction. The joint torque sensors are installed on the robot linkage side of the gear train and are used as a feedback signal in a torque control loop. Elogegui [22] details the use of joint torque sensors, used to reduce the effects of the non-ideal transmission due to the presence of stiction, Coulomb friction and cogging. Joint torque sensors have been found effective in force control loops as have the use of force sensors at the end effector. Similarly they have the same disadvantages of having to use additional sensors.

Sensorless force control schemes have been used in systems in which friction is neglible (e.g direct drive systems). The problem of implicit force control in systems in which friction is significant has not been solved for robotic systems or for machine tool applications.

1.5 Friction Models.

Friction models have been used in this thesis in both the work on estimating grinding forces from servo motor information and in impulsive control schemes. A discussion of conventional friction models, which describe friction as a function of velocity and position dependent friction, is given in this section.

The mechanical systems used in this thesis, as with many mechanical systems, are lubricated with oil or grease. The discussion of friction models for such systems is given here and draws from the work by Armstrong Helouvry et al [26]. "Grease and oil have more in common than not. Grease is essentially a soap matrix that carries oil, which is released under stress into load bearing junctions"[26]. The most common lubrication mechanism (and used by several mechanisms used in this thesis) is hydrodynamic lubrication "where the lubricant is drawn into the interface by the motion of the parts"[26]. The four major friction regimes described in [26] are static friction, boundary layer lubrication, partial fluid lubrication and full fluid lubrication. These four regions are shown in figure 1.5 and are described as follows:

Regime I – Static friction. This regime typically has been considered to be the region in which the velocity is zero and no motion occurs until the applied force or torque exceeds the static friction value. This is not exactly true due to presliding displacement. This displacement is "approximately a linear function of the applied force up to a

critical force, at which breakaway occurs"[26]. If the force is removed before the critical force is applied the mechanism will be restored to its original position.

Regime II- Boundary Lubrication. This is a region of very slow velocity, which is not adequate to build a film between the surfaces hence fluid lubrication is not obtained, and there is solid to solid contact.

Regime III – Partial Fluid Lubrication. In this region lubrication is drawn in to the contact zone. This region is manifestly unstable. As partial fluid lubrication increases solid to solid contact decreases reducing the friction and hence increasing the acceleration. This is the region of negative viscous friction. This is sometimes referred to as the Stribeck effect or Stribeck friction.

Regime IV - Full fluid lubrication. There is no longer surface contact and the lubricating film completely supports the load. This is the region of viscous friction, which increases linearly with velocity.

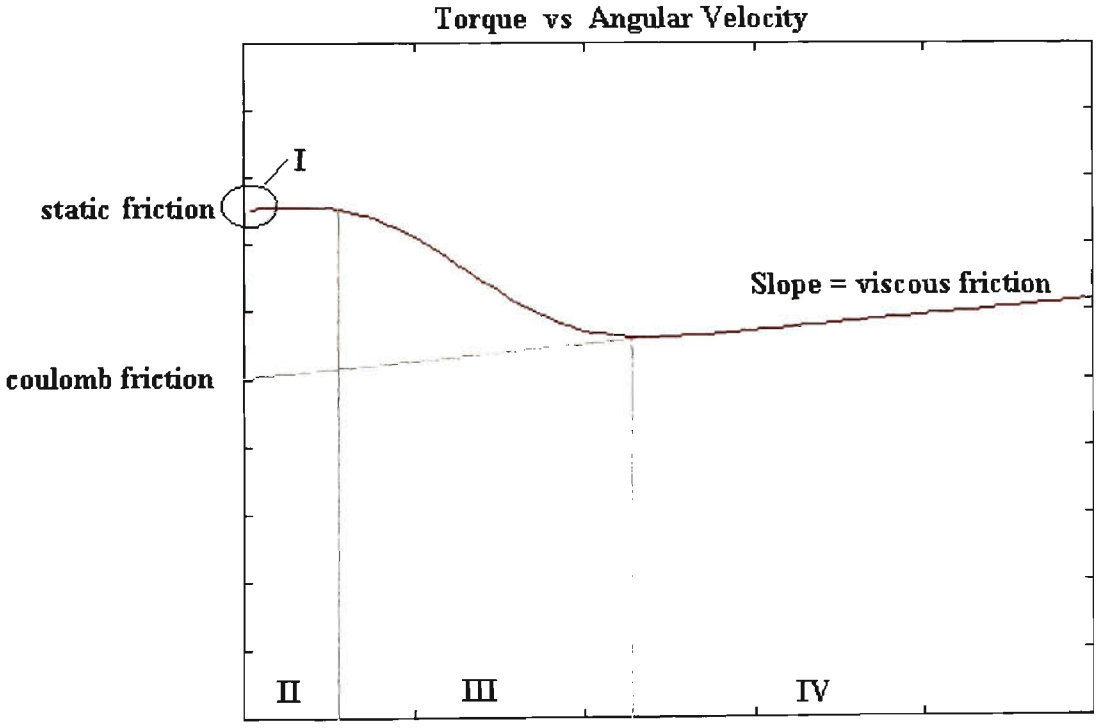

Figure 1.5 Friction Regimes

1.5.1 Conventional Friction Models

Conventional friction models describe friction characteristics solely as a function of velocity. Astrom [27] gives a good summary of conventional friction models. Four different friction models are shown in figure 1.6.

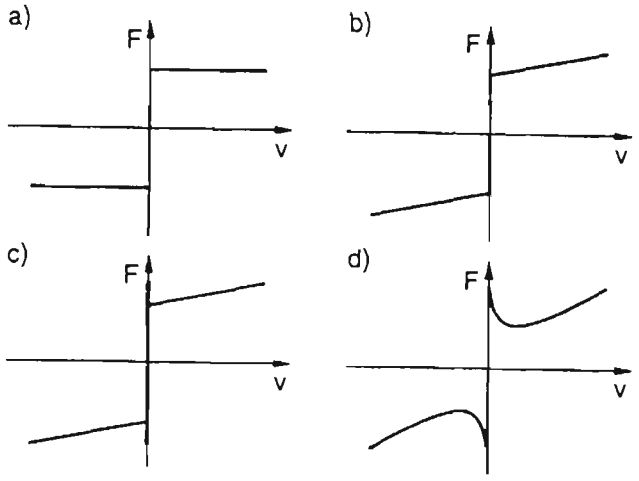

Figure 1.6 Conventional Friction Models [27]

The simplest model only includes Coulomb friction as is shown in figure 1.6a and can be described by $F = f_c \operatorname{sgn}(v)$ where F is the frictional force and f_c is the Coulomb friction coefficient. This model can be improved by adding a viscous friction component f_v, which is proportional to velocity. This is shown in figure 1.6b and can be described by $F = f_c \operatorname{sgn}(v) + f_v v$. This model does not adequately describe the behaviour when the velocity is zero because the sgn function is not defined when the velocity is zero. A model, which includes static friction, f_{stic} is shown in figure 1.6c and for an applied force F_e can be described by:

$$F = \begin{cases} F_e & \text{if} \quad v = 0 \text{ and } |F_e| < |F_{stic}| \\ f_{stic} \operatorname{sgn}(F_e) & \text{if} \quad v = 0 \text{ and } |F_e| \geq |F_{stic}| \\ f_c \operatorname{sgn}(v) + f_v v & \text{if} \quad v \neq 0 \end{cases} \qquad \text{Eq 1.13}$$

As discussed in Section 1.5 the friction does not drop instantaneously from the static friction value to the Coulomb friction value. A model which allows for this is given in [27] and [26] and is described by:

$$F = \mathrm{sgn}(v)\left\{ f_c + (f_s - f_c)e^{-\left|v/v_s\right|^{\partial}} \right\} + f_v v \qquad \text{Eq 1.14}$$

where ∂ and v_s are empirically determined parameters. This model is shown in figure 1.6d.

The viscous and Coulomb friction models described are used in the force estimation work discussed in Chapters 5 and 6 and the models used to describe the friction behaviour in the low speeds region (Eq 1.13, 1.14) are used in the impulsive control schemes discussed in Chapter 4.

1.5.2 Position Dependent Friction

Position dependent friction characteristics are used in this research in the estimation of grinding forces undertaken in Chapter 5 and were also used to produce a static friction lookup table used by the impulsive controller developed in Chapter 3.

Many friction models have been developed for systems with a simple geometry. i.e. two sliding flat surfaces. In more complex "mechanisms with numerous sliding and rolling parts, the simple models cannot fully describe the complexity of the friction phenomena in such mechanisms"[28]. Popovic and Goldenberg [28] and Armstrong [29] suggest describing friction as functions of velocity and position. Both these authors [28] and [29] give results showing that friction has a position dependent component and this relationship has a high degree of repeatability. This was found to be the case for both static and sliding friction.

A series of "breakaway" experiments to measure static friction is described in [28] and [29]. The breakaway experiment consisted of ramping the torque value until motion

occurred and then recording the torque value (i.e. the static friction value). Then the mechanism is allowed to come to rest. This procedure was repeated for the mechanism's entire travel. The static friction data was recorded with position and a Fourier transform of the static friction values was taken to give spectral components in the position domain rather than the time domain. Popovic and Goldenberg [28] conducted their experiments on a PUMA 560 robot and they could attribute the largest spectral components to gears meshing and the sliding of brushes on the commutator.

To calculate the sliding friction values the mechanism can be run at a constant velocity and the motor torque recorded [28]. Webb et al [30] applies a known torque signal and observes the variation in velocity. Using a least squares method the viscous friction, Coulomb friction and inertia of the system are identified. The unmodelled torque component then was attributed to the position dependent friction. The work in [30] was on a precision X-Y test bed similar in construction to that of precision machine tools and the authors were able to attribute spectral components to bearings, belt/pulley cycles, motor poling, stator teeth and pulley teeth.

1.6 Low Speed Friction Control Schemes

As part of the work in this thesis an impulsive control scheme is developed that improves low speed position tracking of systems with friction. There have been other impulsive control schemes as well as model based compensation schemes, dither schemes and conventional PD and PID controllers used on systems with friction at low velocities.

At low velocities friction characteristics as discussed in Section 1.5.1 can be highly non linear and because of this the motion of mechanisms can be intermittent. In such cases

the mechanism's movement has a periodic cycle of alternating motion and rest, which is referred to as "stick slip". "Stick slip determines a performance bound of a machine i.e. the lowest sustainable speed and shortest governable motion"[29]. Stick slip motion has been tested using the spring arrangement shown in figure 1.7.

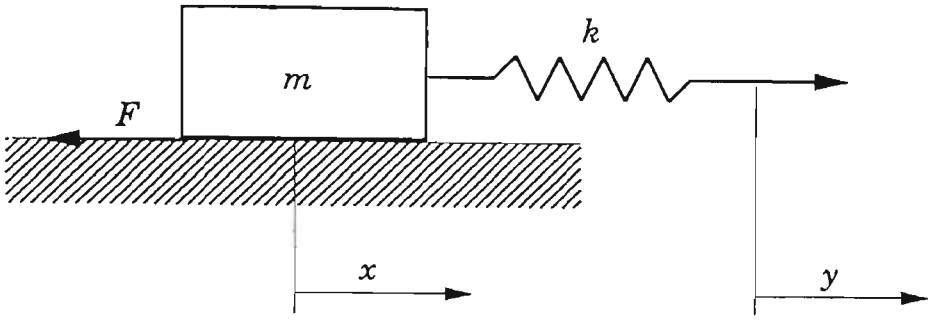

Figure 1.7 Spring Arrangement for Stick Slip Motion [31]

As show in this figure a force is applied such that the free end of the spring moves with a constant velocity. Initially the mass does not move until the spring force exceeds the static friction. Once the mass starts to slide the friction force then drops to the Coulomb friction value. The mass accelerates which decreases the spring length and hence decreases the spring's force and the mass then decelerates and finally stops. The process then repeats itself. The stick slip motion is shown in figure 1.8

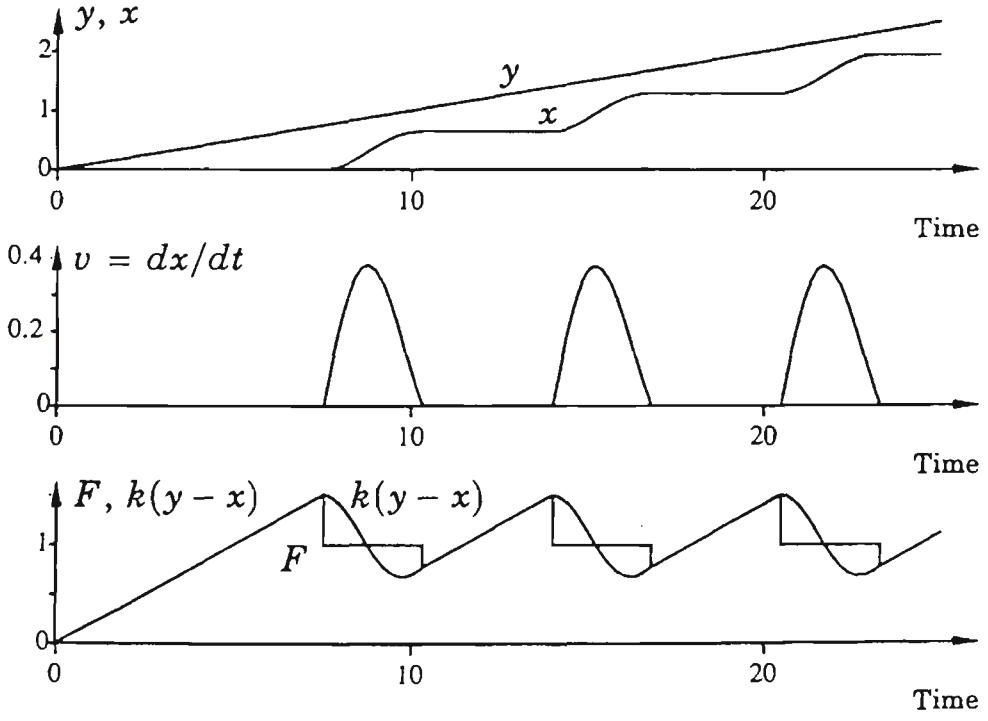

Figure 1.8 Stick Slip Motion [31]

1.6.1 PID and PD Controllers

Proportional Integral and Derivative (PID) controllers and Proportional and Derivative Control (PD) controllers are widely used in industry and are used to control machines with friction. Often PID controllers are used as a basis for comparison with other control schemes to measure the controller's improvement, as is done in this thesis.

The integral part of a PID controller term is used to reduce steady state errors. In position control systems the integral action has been found to cause limit cycling when tracking at low velocities [26]. In other work Armstrong [32] demonstrated that stick slip limit cycles would occur for any PID controller in any mechanism with static friction larger than the Coulomb friction. " To overcome limit cycling one standard technique is to employ a dead band to the integrator block"[26]. The system in this region behaves as a PD controller.

A PD controller in position control schemes does not have stick slip limit cycling; however there will be a steady state position error. The position tracking or velocity control in a PD controller does exhibit stick slip motion at low velocities [26]. In their analysis of stick slip in systems under PD control Armstrong [26] and Rabinowicz [33] have both shown that the stick slip cycle can be decreased by increasing the velocity or by increasing the stiffness of the system. For a PD controller increasing the stiffness is equivalent to increasing the proportional gain. However there are limits to which the proportional gain can be increased before the system becomes unstable.

Another disadvantage of integral control is at velocity reversals. The windup from motion in one direction has to be "unwound" before motion in the other direction occurs. To prevent this the integral action is typically reset at velocity reversals [26].

1.6.2 Model Based Friction Compensation

Canudas de Wit [34] gives a description of the model based friction compensation problem. In the discussion given the author suggests letting the actual frictional torque be $T_f(t)$ and the estimated torque $T_e(t)$. For a system consisting of an electric motor and a load so that the total inertia of the system is J where the control input $u(t)$ is the motor current and the motor constant is k_c, the motor system can be written as:

$$k_c u(t) = J\frac{dw}{dt} + T_f(t) \qquad \text{Eq 1.15}$$

The friction component can be compensated if the control input is $u(t)$:

$$u(t) = u_0(t) + \frac{T_e(t)}{k_e} \qquad \text{Eq 1.16}$$

where k_e is the estimate of the motor constant hence:

$$J\frac{dw}{dt} = k_c u_0(t) + \left\{\frac{k_c}{k_e}T_e(t) - T_f(t)\right\} \qquad \text{Eq 1.17}$$

If the estimates are good i.e. $k_c = k_e$ and $T_e(t) = T_f(t)$ the term within the brackets disappears and the control is then of a simple system with inertia J. A block diagram of typical friction compensation is shown in figure 1.9. The success of this approach clearly depends on the accuracy of the estimates $T_e(t)$ and k_e

Friction compensation schemes are as numerous as friction models. Many of these are based on a conventional friction model in which friction is described as a function of velocity. Examples of this include friction compensation schemes which only include

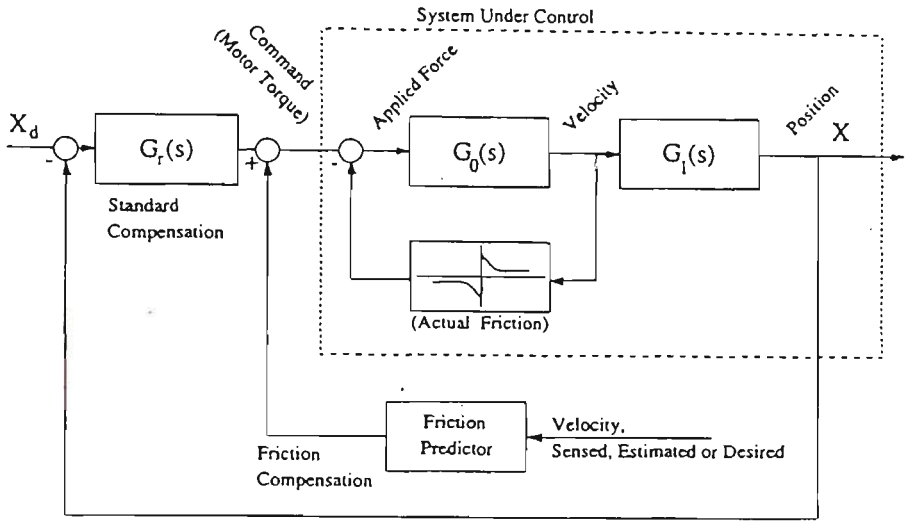

Figure 1.9 Friction Compensation Block Diagram [26]

Coulomb friction such as those described in [26], [25]. In [35] the friction model uses an estimation of Stribeck friction. Armstrong [29] uses a conventional friction model with Coulomb, viscous friction and an additional position dependent friction term. Other models used in friction compensation schemes include the Dahl models [36] and the bristle model, a more generalised form of the Dahl model [31], [37].

For model based compensation schemes to work the model must accurately describe the friction characteristics. "One of the major difficulties in performing friction compensation is the difficulty in modelling friction at very low velocities"[26]. The impulsive controller used in this thesis does not require an accurate friction model at low velocities. This avoids any requirement to model friction at low velocities particularly in the unstable Stribeck region.

1.6.3 Dither

The injection of high frequency AC signals or dither signals has been used in systems with friction. Both normal and tangential dither systems have been used. Dither signals can be added by an external mechanical vibrator. Tangential dither signals can be applied from the control system via the command reference. E.g. the velocity reference. Mossaheb [38] describes using dither signals in non linear systems resulting in

quenching the system's limit cycles and in systems with friction these limit cycles are characterised by the stick slip behaviour described in Section 1.5.

Dither can also be added to the output of the control loop and Canudas de Wit [35] describes how dither signals $A_0 \sin \omega_0 t$ can be added to the torque signal to give a new control torque T_0 such that:

$$T_0 = T + A_0 \sin \omega_0 t \qquad \text{Eq 1.18}$$

where ω_0 should be chosen greater than the system bandwidth and A_0 should exceed the static friction.

In some ways dither is similar to the impulsive controller used in this thesis in that an additional pulse is applied to the control output (output of the PID controller) so as to make the signal larger than the static friction and break the stick slip limit cycling. The similarities end there since the impulsive controller's position error signal is used to calculate the pulse duration to minimise the position error. The pulse duration is adjusted as part of the position control loop.

1.7 Impulsive Controllers

Impulsive controllers suggested by Yang and Tomizuka [39] and Popovic [40] are both used for accurate positioning. Both suggest using conventional control schemes to get close to the reference point and then use their control schemes for the final accurate positioning.

In common with the impulsive controller used in this thesis the impulsive controller developed by Tomizuka [39] applies a pulse that is above the static friction to ensure

motion occurs at each pulse. Also the pulse width is adjusted with the position error. In [39] the pulse width controller is used once the mechanism reaches a point close to the reference point. After the mechanism comes to rest a single pulse is applied. The width of this pulse is a function of the position error, the mechanism moves and the error reduces. The pulse height f_p is chosen to be larger than the static friction value. The pulse width t_p is calculated from $d = bt_p^2 \operatorname{sgn}(f_p)$, where d is the required displacement, b is an arbitrary initial estimate. After each pulse is applied an adaptive algorithm using the previous displacement and pulse width is used to adjust the value of b. This whole process is repeated until the error is reduced to zero.

Popovic et al [40,41,42] describe a fuzzy logic pulse controller. An extensive study was made of the mechanism response to narrow open loop torque pulses and the results are shown in figure 1.10

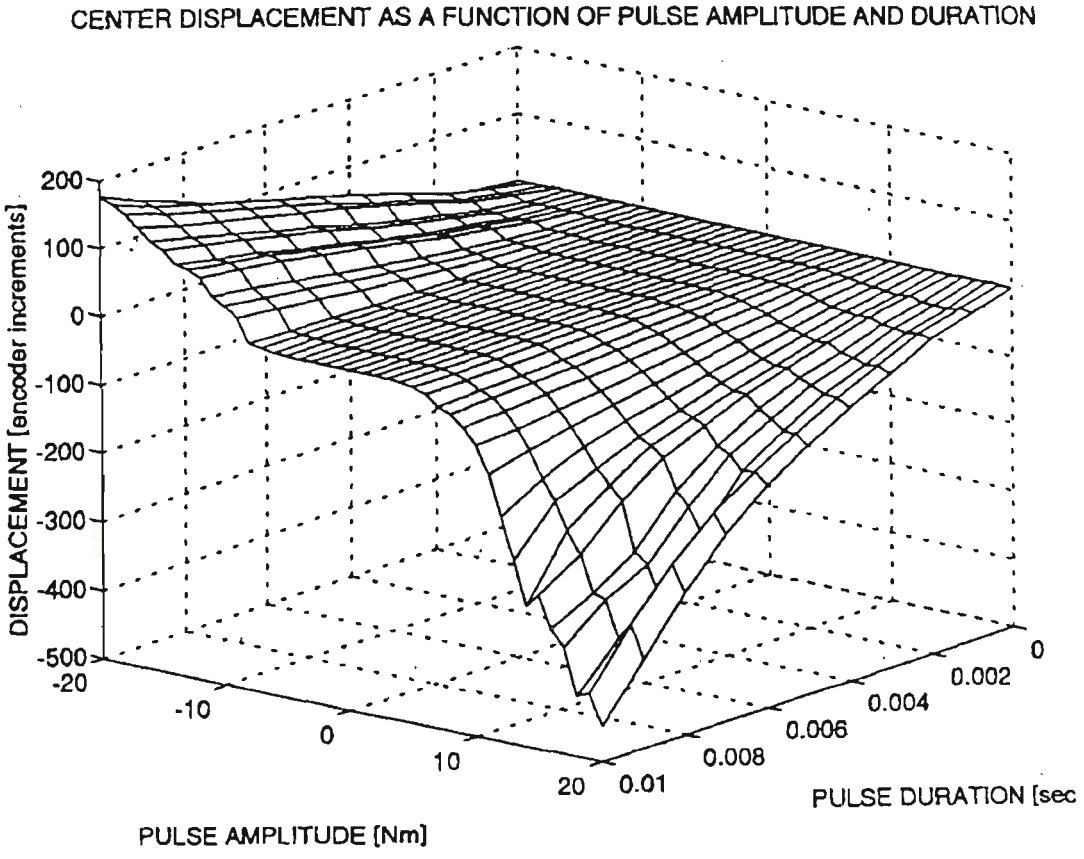

Figure 1.10 Experimental Determined Displacement [40]

The desired pulse shape is chosen using a fuzzy logic controller. The membership functions $u_j(\Delta\theta)$ are shown in figure 1.11

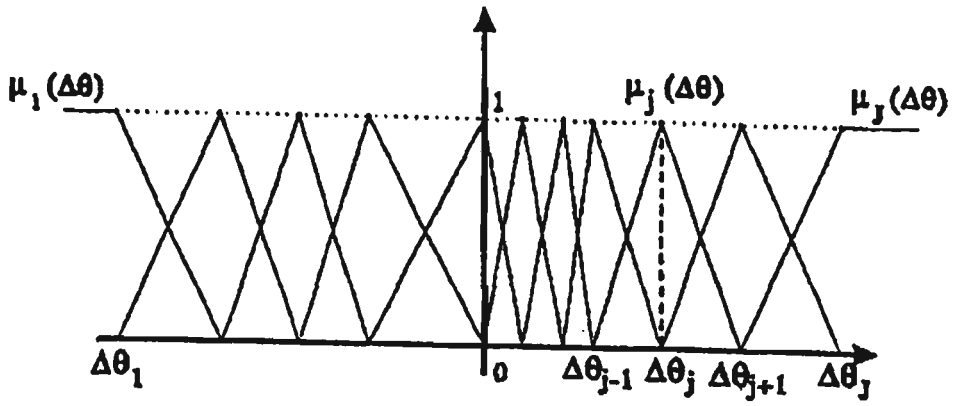

Figure 1.11 Fuzzification procedure [40]

The membership functions are chosen so that any displacement $\Delta\theta$ will be covered by at least two functions. The defuzzification process will lead to a stepped torque output as shown in figure 1.12

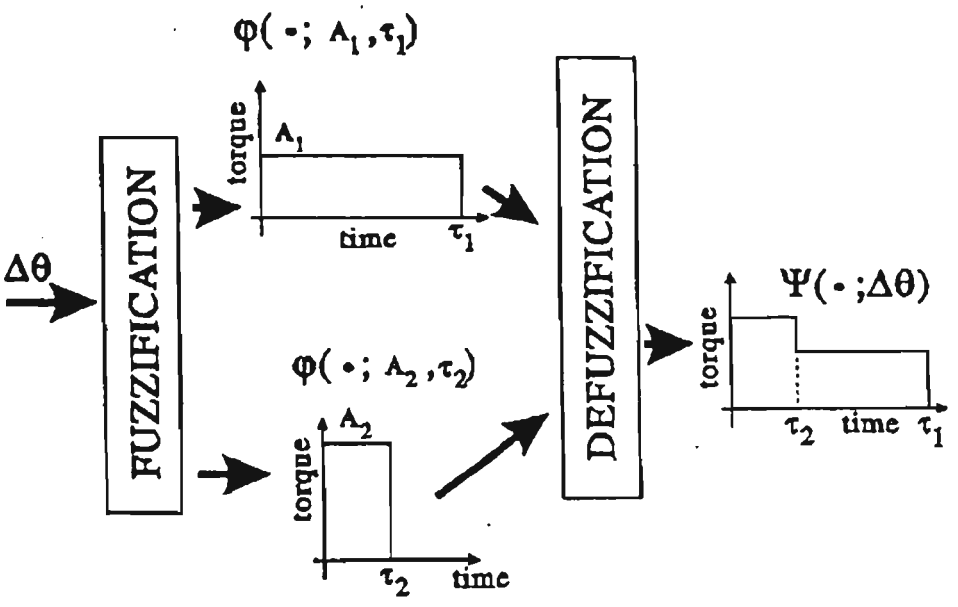

Figure 1.12 Defuzzification Procedure [40]

Armstrong Helouvry [29] uses an impulsive controller for force control. The force compensation operates at low velocity with small displacement. The impulse controller sends a series of torque pulses to achieve the desired contact force. "The torque sequences are tuned empirically during a calibration process and then are loaded with the corresponding force step into a lookup table"[29]. The impulsive controller is used

with command feed forward and a position dependent friction compensation. So the applied torque is given by [29]:

$$\textit{Applied Torque} = \textit{Impulse Torque} + \textit{Desired Torque Feed Forward} + \textit{Position Dependent Friction Compensation}$$

The position dependent friction values are stored in a lookup table. The lookup table consists of position dependent static friction values, determined by a series of "breakaway experiments". These experiments are described in Section 1.5.2.

The impulse controllers described in this section are effective at accurate point to point positioning in systems with friction. They have not been used in the position tracking problem which the impulse controller developed in this thesis addresses.

1.8 Thesis Objectives

From the literature review above it has been shown that there are considerable advantages in measuring and controlling grinding forces. A number of controlled force grinding schemes have already been implemented on grinding machines and have shown improvements in production rates and work piece quality. These control schemes have all used force sensors. There would be considerable advantage in being able to implement grinding force control schemes without the use of force sensors. These include the saving in the cost of the sensors and the removal of additional compliance introduced by the sensor which reduces the stiffness of the machine. Sensors also typically require some special mounting arrangement for the work piece.

From the discussion of robotic force control schemes above there have been several sensorless force control scheme (implicit force control) developed. These have been implemented on direct drive mechanisms which significantly reduces the friction of the

system because there is no mechanical drive (gear box or screw for example). Other robotic researchers not using direct drives have pointed to the difficulties of sensorless force control in the presence of friction. The frictional force normally far exceeds the force trying to be controlled. This is also the case in the mechatronic systems used in this thesis.

In these mechatronic system and in many other applications friction is one of the largest forces the servo system has to overcome. A detailed friction model of the system may aid in the force estimation process. Conventional friction models as well as position dependent friction models were used here in the force estimation process.

One of the main objectives of this thesis is to use detailed friction models of the two mechatronic systems considered in this thesis to estimate external forces using only servo motor information. A related objective is to use the force estimation techniques developed to measure and control grinding forces.

The other major area of work addressed by this thesis is in the area of low speed position tracking. As mentioned in the literature review the non-linear effects of friction at low velocities make the control problem a non trivial task. Standard PID controllers do not perform well and typically induce stick slip limit cycling. Model based compensation schemes have been applied to the problem successfully but have the difficulty that an accurate friction model is required. This model may be hard to generate particularly in the inherently unstable Stribeck region.

Another approach used in this thesis and by other authors is to use an impulsive controller. Such controllers apply short duration pulses with magnitudes greater than the

static friction to break the stick slip limit cycle. The two other impulsive control schemes described in the literature review are particularly suited to the point to point positioning problem. In both of these schemes the mechanism must come to rest after the application of each pulse before the next pulse is applied. This is perfectly suitable for the point to point positioning problem where it is possible to "creep up" to the desired location but is not suitable for the position tracking problem were a specified profile has to be followed and typically the system would always be moving. However the impulsive controller used in this thesis is particularly suited to the position tracking problem because the control scheme does not need the mechanism to come to rest after the application of each pulse. Hence the other major objective of this thesis is to implement and further develop an impulsive control scheme to improve the low speed position tracking of mechanism with friction

1.9 Thesis Outline

The preceding part of this chapter has given an introduction to this thesis, a discussion of the literature relevant to the area of research and the objectives of the thesis.

The second chapter describes the equipment used in this thesis. Two experimental rigs were used in the experimental work. The first is a four axis industrial robot made by Hirata Ltd referred to in the rest of this thesis as the "Hirata Robot". The second system was a manual surface grinding machine that had three axes retrofitted with servo systems and referred to in the rest of the thesis as the "grinding machine". Mass, Inertia viscous and Coulomb friction parameters for both the Hirata robot and the grinding machine are calculated. These values are used subsequently in the force estimation scheme developed in Chapter 5 and 6 and in the friction control schemes developed in Chapter 3.

The third chapter develops an impulsive control scheme for low velocity position tracking in systems with friction. Its performance is compared to a conventional PID controller. The developments including allowances for velocity reversals, modelling the static friction and using a static friction controller to select the pulse height. A fuzzy logic controller was used to adjust the pulse height. The majority of the development work was carried out on the Hirata Robot and for completeness the impulsive controller was also applied to the grinding machine.

Chapter 4 develops the concepts and techniques required to model and process position dependent torque and force variations. The force estimation work described in Chapters 5 and 6 are based on the concepts developed in Chapter 4. The interrelationship between velocity, frequencies in the time domain and position frequencies in the position domain are defined. The use of "position binning" techniques to turn a discrete time domain signal into a discrete position domain signal are described. The position frequency spectrum of the X-axis of the grinding machine is characterized.

Chapter 5 shows how servo motor position and torque information is used to calculate external forces. The position and torque values are collected and the signal processing is carried out later (i.e. offline). An accurate model of the system is made to include mass, viscous friction, Coulomb friction and position dependent torque variations. The signal processing required to extract the force estimation signal from the servo motor data is described. This includes the filtering in the time domain and the position domain. A detailed discussion of noise sources affecting the signal processing of the force estimation signal is given. A series of grinding measurements was conducted where the

grinding forces calculated from servo motor information are compared to those measured using the spindle motor power. The force estimation techniques were also applied to the Hirata robot to estimate external forces.

Chapter 6 describes the implementation of real time force estimation. Many of the processing techniques used are similar to those used in Chapter 5. The techniques for implementing the same signal processing techniques in real time are discussed. The real time force signal is used in a grinding force control scheme. The feedrate is used to control the grinding force. A series of experiments were conducted with different force set points and the control schemes' ability to control the grinding force is shown.

Chapter 7 presents the thesis outcomes and conclusions and suggestions for further work.

2 EXPERIMENTAL EQUIPMENT

2.1 Introduction

The force estimation and low speed position tracking control schemes developed in this thesis were implemented on real mechatronic systems. The two mechatronic systems used were a grinding machine and a Hirata robot. The position tracking control schemes and force estimation techniques were applied to both systems. The Hirata Robot and the grinding machine experimental systems are described in this chapter.

A dedicated Digital Signal Processor (DSP) controls both the Hirata robot and the grinding machine. The positioning information, limit switch and other trip signals are all monitored by the DSP. The control loops are implemented in the DSP and output commands to the drive system are given by the DSP. The DSP gives a flexible and easy to program system that allows a variety of control and signal processing strategies to be implemented. The DSP system is described in detail in Appendix B.1. The Hirata robot uses DC servomotors and the grinding machine uses AC servomotors. Both are in current control mode, which in effect means the output voltage from the DSP gives a torque command to the servomotor.

In Section 2.2 the Hirata robot system is discussed. The mechanical layout of the robot is described and the modification made to the robot's controller and the robot's servo drives are also described. The Hirata robot's servo control loops use DC servo drives that control the armature current. This control loop is analysed and as part of this the electrical and mechanical system's response is calculated. A least squares method is used to calculate the mechanical system's inertia, viscous and Coulomb friction. A set of units referred to as the control units are developed and their relationship with torques

and mechanical system's parameters referred to both the servomotor and robot's arm are defined.

In Section 2.3 the grinding machine system is discussed. The physical arrangement of the grinding machine is described and the modifications made to the grinding machine are detailed. The force sensor, spindle motor power measuring circuits, and AC servo control system are described and shown that it can be analysed in a similar manner to the DC servo system described for the Hirata robot. The grinding machine's electrical and mechanical time constants, mass viscous and Coulomb friction components are calculated using the same least square method as used for the Hirata robot.

The inertia, mass, Coulomb and viscous components for the Hirata robot and the grinding machine are used in the force estimation schemes described in Chapter 5 and six and the friction control schemes developed in Chapter 3.

2.2 Hirata Robot

The Hirata ARi350 SCARA (Selective Compliance Assembly Robot Arm) robot has four axes. The main rotational axes are the A and B axes. The A axis rotates the robot's arm about the fixed base of the robot. The A axis is often referred to as the shoulder joint. The second revolute joint, the B axis, can be thought of as the elbow joint. The B axis rotates about an axis 350mm away from the centre of the A axis. The A and B axes control the motion in the horizontal plane and the Z-axis moves the end effector with a linear motion in the vertical direction. The W axis or the wrist is a revolute joint and rotates the end effector about the Z-axis. The W and Z-axes are centred 300mm from the centre of the B axis. The drawing showing the dimensions of the Hirata robot is given in Appendix B.2 and a photograph of the Hirata robot is shown in figure 2.1.

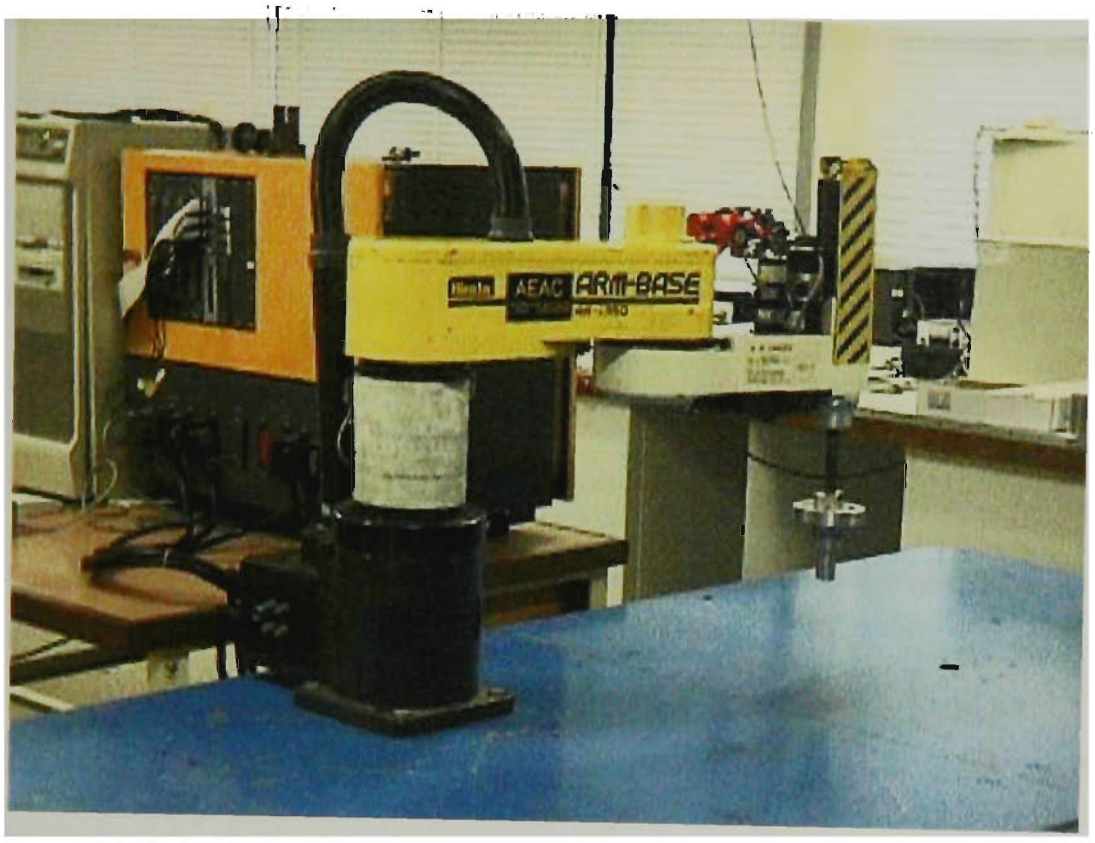

Figure 2.1 Hirata Robot

The A and B axes each have a harmonic gearbox between the motor and the robot arm. The A and B axes gear ratios are respectively 100/1 and 80/1.

The original robot controller was replaced by the DSP system (described in appendix B.1). The A and B axes drives were replaced with Baldor drives. The Z and W axes use the original Yaskawa drives. Additional drive and motor data is given in Appendix B.2.2. On all axes the original motor, mechanical system (gearboxes, screw, belts, etc) limit switches and shaft encoders are used. The shaft encoder resolution and position calibration data are given in Appendix B.2.1. The drives are within the control cubicle (yellow box) and the DSP is within the personnel computer shown in figure 2.1.

2.2.1 Control Scheme

The control scheme for a DC servo system with the drive in armature current control mode is discussed in this section. For a DC motor with armature inductance L_a and

armature resistance R_a the armature voltage expressed in Laplace transform notation $V_a(s)$ is given by:

$$V_a(s) = I_a(s)(R_a + L_a s) + K_m \omega_m(s) \qquad \text{Eq 2.1}$$

The induced emf $e(t)$ expressed in Laplace notation is given by: $E(s) = K_m \omega_m(s)$ where $\omega_m(s)$ is the motor armature's instantaneous angular velocity and K_m is the motor constant. The drives are connected across the DC motor's armature circuit so the drive's output voltage is the DC armature motor voltage V_a. In current control mode the drive's output voltage is adjusted so the output current (i.e. armature current) $I_a(s)$ follows the reference current $I_{ref}(s)$ as closely as possible. If the drive's current controller is given by $G_d(s)$ then the armature voltage is given by:

$$V_a(s) = G_d(s)(I_{ref}(s) - I_a(s)) \qquad \text{Eq 2.2}$$

As discussed in Appendix B.2.2 the reference current I_{ref} is given by:

$$I_{ref}(s) = K_{VI} V_{DSP}(s). \qquad \text{Eq 2.3}$$

The torque T_m developed by the motor is given by:

$$T_m(s) = K_m I_a(s) \qquad \text{Eq 2.4}$$

The torque developed by the motor is equivalent to the torque required to overcome friction, accelerate the system and overcome any external torque disturbance T_d. This is described by Eq 2.5:

$$T_m(s) = \omega_m(s)(Js + f_v) + T_d(s) \qquad \text{Eq 2.5}$$

where J is the inertia and f_v is the viscous friction. This friction model only includes that part of the viscous friction which is directly related to the speed so that the other

friction parameters, eg Coulomb friction, can be included in the disturbance torque T_d.

Using Eqs 2.1, 2.2, 2.4, 2.5 give the block diagram shown in figure 2.2:

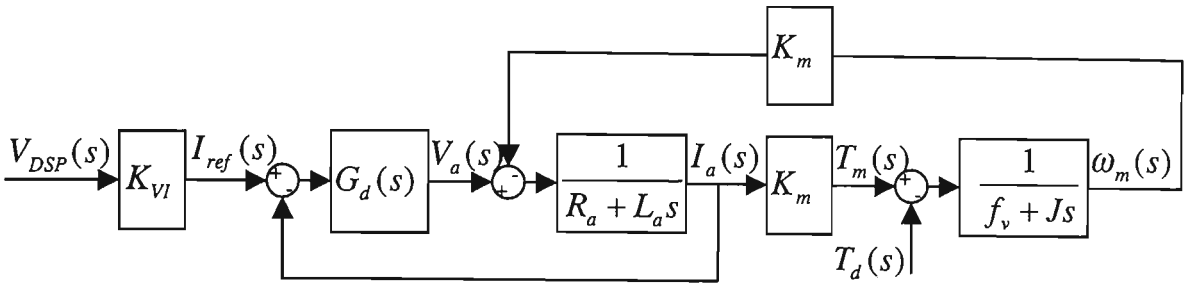

Figure 2.2 DC Motor Control System Block Diagram

2.2.2 Electrical Circuit Response

The electrical system's response was measured by locking the DC motor's rotor. The torque $T_d = T_m$ and the angular velocity $\omega_m = 0$. The block diagram shown in figure 2.2 can be reduced to that shown in figure 2.3:

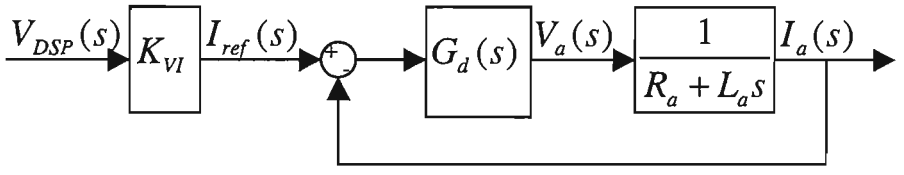

Figure 2.3 Electrical Circuit Block Diagram.

The drive manual [43] specifies the drive's frequency response as 2.5kHz and the maximum output voltage as 100V and so the drive's frequency response is considerably higher than the armature circuit response (as calculated below). Hence the drive's current controller $G_d(s)$ can be modelled as a constant gain K_d and a saturation element in which the output voltage is clipped at $V_d = 100V$. The expanded drive model is shown in figure 2.4.

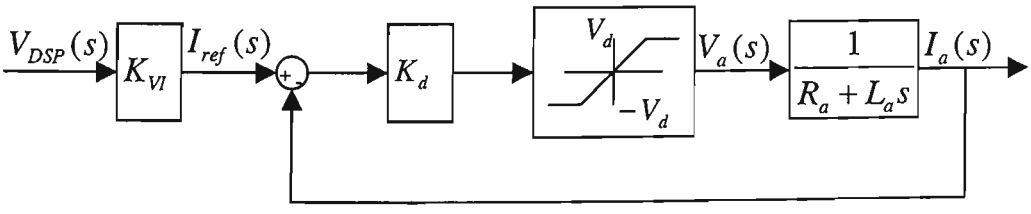

Figure 2.4 Electrical Circuit Block Diagram with expanded Drive Model

In the linear part of the drive's range the armature current $I_a(s)$ and its associated time constant τ is given by:

$$I_a(s) = \frac{1}{1 + \frac{R_a}{K_d} + \frac{L_a}{K_d}s} I_{ref}(s) \qquad \text{where} \qquad \tau = \frac{L_a}{R_a + K_d} \qquad \text{Eq 2.6}$$

If K_d is small then $\tau \approx \frac{L_a}{R_a}$ and if K_d is large $\tau \approx \frac{L_a}{K_d}$:

The drive is in the saturation region when $K_d\left(I_{ref}(s) - I_a(s)\right) > V_d$ and the armature current and associated time constant is given by:

$$I_a(s) = \frac{V_d}{R_a\left(1 + \frac{L_a}{R_a}s\right)} \qquad \text{where} \qquad \tau = \frac{L_a}{R_a} \qquad \text{Eq 2.7}$$

If the drive's current control gain K_d is small or operating in the drive's saturation region the current control loop's time constant is $\tau = \frac{L_a}{R_a}$. For high gain K_d and with the drive supplying a constant current the system operates in the linear region and has a considerably faster time constant $\tau = \frac{L_a}{K_d}$. In the discussion of the mechanical system that follows it is important for the response of the electrical system to be considerably faster (which it is). A conservative approach would be to consider the current control loop's time constant to be the same as the armature circuits time constant (the slower of the two possible) i.e. $\tau = \frac{L_a}{R_a}$. The electrical system's response is also considered in Section 3.2.2 where there are large step changes in the current so the current loop would be in the saturation region so the appropriate time constant is also $\tau = \frac{L_a}{R_a}$. Using this

time constant the block diagram of figure 2.3 can be replaced with the simplified block diagram shown in figure 2.5:

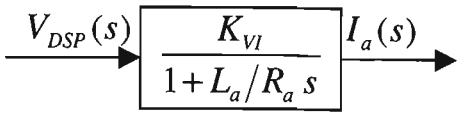

Figure 2.5 Reduced Electrical Block diagram

The response of the electrical circuit was measured by applying a step input and observing the response of the current $I_a(s)$. The top graph of figure 2.6.shows the step response for an output current of 1 Amp. The bottom graph of figure 2.6 also shows the armature current but with the time scale expanded in the rise time region of the current response.

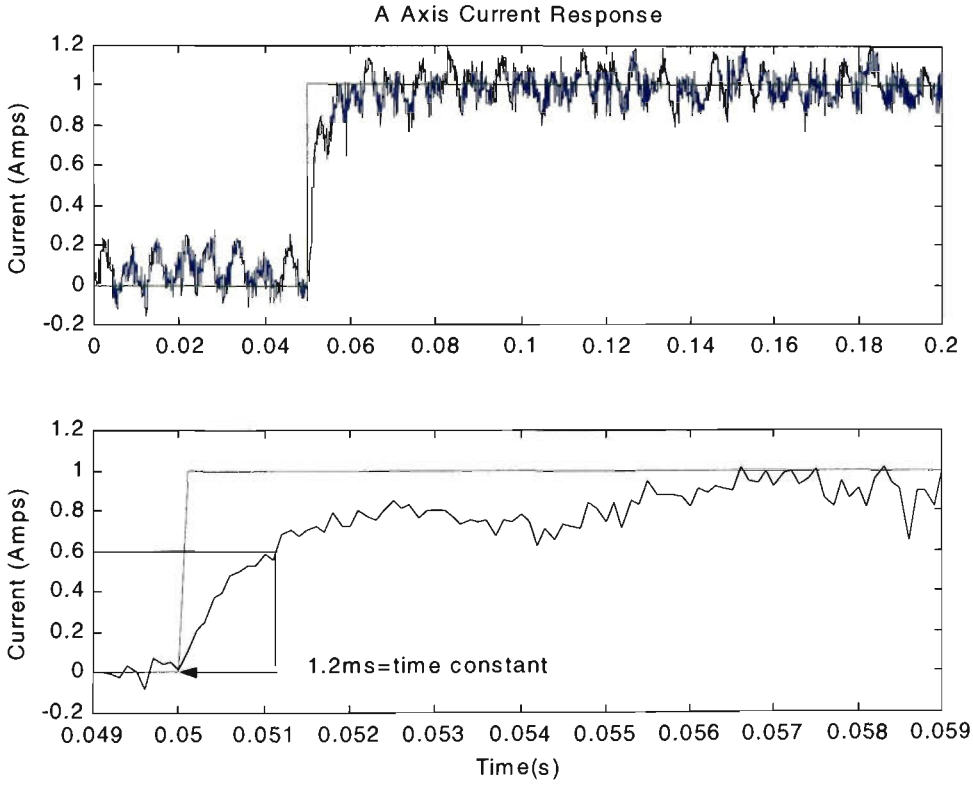

Figure 2.6 A Axis DC motor current Response

If the response is assumed to be that of a first order system the time constant τ is the time it takes for the current to reach 0.63 of its final value. The time constant and the break frequency $1/2\pi\tau$ values for the A and B axes are listed in table 2.1

Table 2.1 A and B axis Electrical and Mechanical Time Constants

	A Axis Electrical	B Axis Electrical	A Axis Mechanical	B Axis Mechanical
Time Constant (mS)	1.2ms	1.5ms	0.4s	0.5
Break Frequency (Hz)	130	105	0.4	0.3

In [53] the DC motor parameters were measured. For the A axis the armature resistance was given as $R_a = 1.2\Omega$ and the inductance as $L_a = 1.4mH$. This gives a time constant $\tau = \frac{L_a}{R_a} = 1.2ms$ which is consistent with the measured time constant given in table 2.1.

The mechanical time constants calculated in Section 2.2.3 are listed in table 2.1. These were more than 300 times slower than the electrical time constant so the angular velocity ω_m and the induced emf $K_m\omega$ will be changing at least 300 times slower than the current control circuit. The electrical circuit can then be replaced by its gain K_{VI}. Combining the electrical circuits gain with the motor constant K_m the constant K_{VT} can be defined such that:

$$K_{VT} = K_m K_{VI} \qquad \text{Eq 2.8}$$

the block diagram of figure 2.2 can be replaced with that shown in figure 2.7:

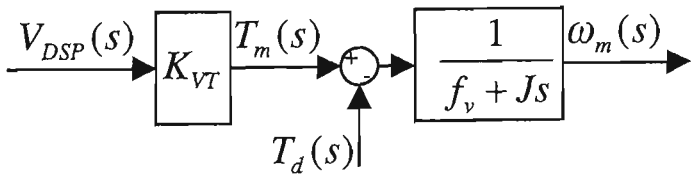

Figure 2.7 Reduced Block Diagram

2.2.3 Mechanical System Parameters

As discussed in Section 2.2.2 the drive's input V_{DSP} will give an armature current and associated motor torque such that:

$$T_m = K_{VT} V_{DSP} \qquad \text{Eq 2.9}$$

The motor torque is assumed to consist of the torque accelerating the system and overcoming friction. A conventional friction model is used and as discussed in

Section.1.5.1 the friction is described as a function of velocity. A relatively simple model only including viscous and Coulomb friction is used. A series of experiments were conducted to determine the inertia, viscous and Coulomb friction. In these experiments a step torque is applied to the system. The mechanism starts from rest and moves rapidly through the low speed non-linear friction region and operates mostly in the linear friction region. As the mechanism spends little time in the non-linear friction region the static friction and Stribeck parameters used to describe this region are not included in the friction model used here.

Using Eq 2.9 and a friction model with viscous friction f_v, Coulomb friction f_c and inertia J the mechanical system can be described by the equation:

$$K_{VT}V_{DSP} = J\frac{d\omega_m}{dt} + f_v\omega_m + f_c\,\mathrm{sgn}(\omega_m) \qquad \text{Eq 2.10}$$

where ω_m is the motor angular velocity. The robot's arm velocity ω is related to the motor's angular velocity by $\omega_m = n\omega$ where n is the gear ratio. Using the robot's arm velocity and rearranging Eq 2.10 becomes:

$$V_{DSP} = \frac{Jn}{K_{VT}}\frac{d\omega}{dt} + \frac{f_v n}{K_{VT}}\omega + \frac{f_c}{K_{VT}}\mathrm{sgn}(\omega) \qquad \text{Eq 2.11}$$

Letting $J' = \frac{Jn}{K_{VT}}$ $\quad f_v' = \frac{f_v n}{K_{VT}}$ $\quad f_c' = \frac{f_c}{K_{VT}}$ and $T = V_{DSP}$ Eq 2.11 then becomes:

$$T = J'\frac{d\omega}{dt} + f_v'\omega + f_c'\,\mathrm{sgn}(\omega) \qquad \text{Eq 2.12}$$

The relationship between the values J', f_v', f_c' and the physical values for inertia, viscous and Coulomb friction referred to the motor or the Robot arms are given in table 2.2.

Table 2.2 Control System Units Conversion Factors

	Torque T (Nm)	**Angular velocity ω (rad/s)**	**Coulomb friction f_c (N.m)**	**Viscous friction f_v (Nms/rad)**	**Inertia J (kgm^2)**
Motor	K_{VT}	n	K_{VT}	$\frac{K_{VT}}{n}$	$\frac{K_{VT}}{n}$
Robot Arm	nK_{VT}	1	nK_{VT}	nK_{VT}	nK_{VT}

The parameters J', f_v', f_c' have the advantage that they are referenced to the most convenient and easiest to observe set of units, the angular velocity of the robot's arm and the input voltage V_{DSP}. The control system software developed on the DSP has used these units. The parameters J', f_v', f_c' will be referred to as the control system's inertia, viscous friction and Coulomb friction.

A set of experiments was conducted to estimate the values of the inertia, viscous and Coulomb friction. Considering the standard torque equation:

$$T = J\dot{\omega} + f_v\omega + f_c\,\mathrm{sgn}(\omega) \qquad \text{Eq 2.13}$$

Using vector notation let θ be the vector of parameters to be determined i.e. J, f_v, f_c. Let ϕ be a vector of functions of the input variable ω, and ϕ^T the transpose vector. Φ is a matrix with each row being the vector ϕ^T recorded at each sampling point from $0.....k$. T is a vector of the output variable torque also recorded at each sampling point.

$$\theta = \begin{bmatrix} J \\ f_v \\ f_c \end{bmatrix} \quad \phi = \begin{bmatrix} \dot{\omega} \\ \omega \\ \mathrm{sgn}(\omega) \end{bmatrix} \quad \Phi = \begin{bmatrix} \phi^T(0) \\ \vdots \\ \phi^T(k) \end{bmatrix} \quad \mathrm{T} = \begin{bmatrix} T(0) \\ \vdots \\ T(k) \end{bmatrix} \qquad \text{Eq 2.14}$$

Let $\hat{\theta}$ be the estimate of θ and $\hat{\mathrm{T}}$ be the estimated torque vector such that $\hat{\mathrm{T}} = \hat{\theta}\Phi$. Let the estimation error be ε. This is given by $\varepsilon = \mathrm{T} - \hat{\mathrm{T}}$. The least squares problem is to

find the parameter estimation vector $\hat{\theta}$ such that $|\varepsilon|^2$ is minimal. The standard solution [44] to this problem is

$$\hat{\theta} = \left[\Phi^T \Phi\right]^{-1} \Phi^T \mathrm{T} \qquad \text{Eq 2.15}$$

A series of torque steps was applied to both the A and B axis (separately) of the robot by applying a number of different input voltages V_{DSP} to the servo drive. The angular velocity of each axis was recorded. The A axis angular velocity measurements are shown in figure 2.8. This data is used in Eq 2.14, 2.15 to calculate the control system parameters J', f_c' and f_v'. Using these parameters a model of the system was made using the MATLAB control toolbox. The same valued torque inputs were applied to the system model and the models response is also shown in figure 2.8.

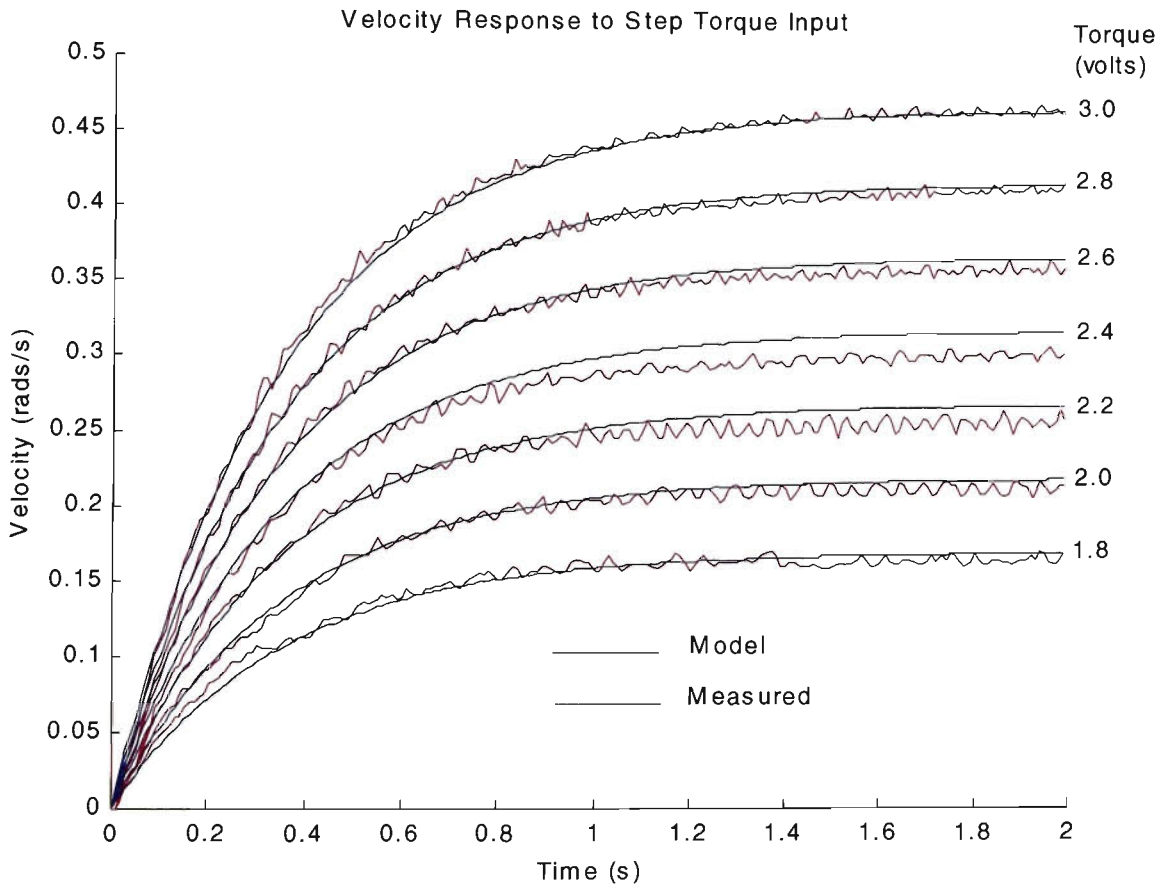

Figure 2.8 Velocity Response to Step Torque Input

The control system values of inertia, viscous and Coulomb friction for both the A and B axes are given in table 2.3. The inertia Coulomb and viscous friction values referred to the motor and to the robot's arm are also given in table 2.3.

Table 2.3 Inertia, Viscous and Coulomb Friction Values

	A Axis			B Axis		
	Inertia J	**Coulomb Friction** f_c	**Viscous Friction** f_v	**Inertia** J	**Coulomb Friction** f_c	**Viscous Friction** f_v
Control Units	1.5 Vs^2/rad	1.1 V	4.0 Vs/rad	0.43 Vs^2/rad	1.4 Volts	0.77 Volts
Motor	$6.6x10^{-4}$ Kgm^2	0.048 Nm	$1.8x10^{-3}$ Nms/rad	$2.0x10^{-4}$ Kgm^2	0.053 Nm	$3.7x10^{-4}$ Nms/rad
Robot Arm	6.6 Kgm^2	4.8 Nm	17.8 Nms/rad	1.3 Kgm^2	4.3 Nm	2.3 Nms/rad

2.3 Grinding Machine

The grinding machine is one of the two mechatronic systems used in this thesis. It was used to provide experimental data for the force estimation and control work developed in Chapters 4,5 and 6. A manual surface-grinding machine was extensively modified with AC Servo drives and motors retro-fitted to automate three axes of the grinding machine. Force sensors and spindle motor power sensors were also installed.

The existing grinding wheel (spindle) motor and its associated control circuits were used. The grinding machine also had an air extraction and coolant circulation system. Figure 2.9 shows a photograph of the grinding machine and its associated drive system and computer.

The three axes of the grinding machine are denoted as the X, Y, and Z axes. The Z-axis moves the grinding wheel in a vertical direction and is used to lower the grinding wheel into the work piece. The X-axis moves a table with the work piece mounted on it in a

Figure 2.9 Grinding Machine

horizontal motion under the grinding wheel. The Y-axis also moves the table in the horizontal plane but at 90 degrees to the motion in the X-axis. The machine is normally used for plunge grinding where the work piece and grinding wheel motion are in the same plane. In plunge grinding the Y-axis velocity is zero and only the X-axis moves. The X-axis velocity is often referred to as the feedrate. The Y-axis is used to move the work piece at the end of each grinding pass. The Y-axis motion is often referred to as the cross feed or traverse rate.

The Y-axis is also used to dress the grinding wheel. A diamond dresser is placed under the grinding wheel and the Z-axis is lowered into it. The diamond dresser is then moved in the Y-axis so the whole width of the wheel is dressed. The process is repeated until enough of the grinding wheel is removed to make it true.

The X-axis mechanism of the original machine was replaced with a linear ball screw. A precision ball screw with double nut separated by a spacer between the two and with preload to eliminate backlash was used. The X-axis servomotor was mounted directly

onto the ball screw's shaft. The existing Z and Y-axis screw arrangements were kept. The original handles for manual control were removed and replaced by servomotors mounted directly on the shaft.

The servomotors on each axis are identical permanent magnet synchronous motors. The position data is obtained from shaft resolvers on the motor shaft. The resolver's resolution, motor and drives constants are given in Appendix B.3. The servo system is controlled by the DSP system described in Appendix B.1.

Several sensors were installed on the grinding machine to allow monitoring of the grinding process. The energy for the grinding process is virtually all supplied by the spindle motor and so a power monitoring circuit was installed in the spindle motor circuit. A three axis piezoelectric force sensor was installed between the work piece and the mounting table. This allows the measuring of tangential and normal grinding forces. The force sensor and spindle motor measurement are discussed in more detail in Appendix B.4 and B.5. Figure 2.10 shows a schematic of the grinding machine's sensors arrangement

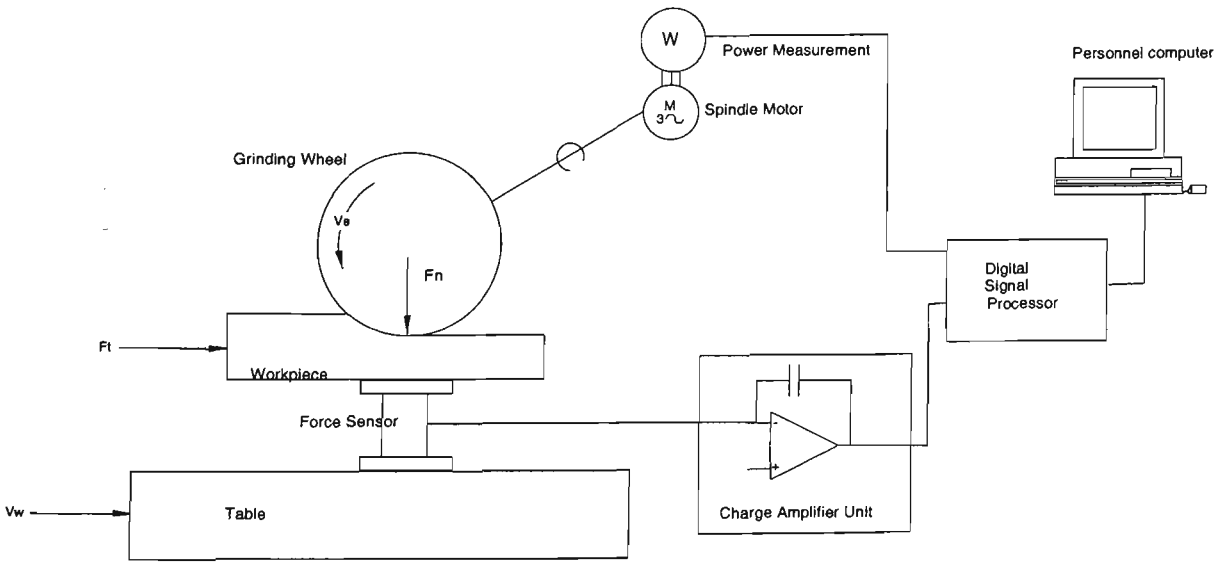

Figure 2.10 Grinding Machine Sensors

2.3.1 Control Scheme

A brief discussion of the modelling of permanent magnet synchronous motors and their vector control is given in this section. The discussion follows the approach given in [45] and [46]. The permanent magnets are built into the machine's rotor. The stator winding is a distributed three phase winding arranged to produce an effective sinusoidal magnetomotive force (mmf). For three phase currents i_a, i_b & i_c a phasor current $\tilde{i}$ can be defined such that:

$$\tilde{i} = i_a + i_b e^{j2\pi/3} + i_c e^{j4\pi/3} \qquad \text{Eq 2.16}$$

The value of the stator phasor current gives the value of the stator mmf and its phase gives the position around the machine where the maximum mmf occurs. Let β be the angle between the mmf produced by the stator phasor current and the mmf produced by the rotor winding (permanent magnets). The stator current phasor referred to the rotor is $\tilde{i}e^{-j\beta}$.

Typically in machines the "direct" or d axis is parallel to the rotor frame of reference and the "quadrature axis" q axis is perpendicular to the rotor's frame of reference. The d axis and q axis currents are given by:

$$\tilde{i}e^{-j\beta} = i_d + ji_q \qquad \text{Eq 2.17}$$

The torque produced by the motor depends on the angle between the two mmf fields. The d axis current will produce no net torque and normally in current control schemes its set point is zero. The torque produced will be due to the q axis current:

$$T = \tilde{K}_m i_q \qquad \text{Eq 2.18}$$

where $\tilde{K}_m$ is the motor constant. The expression for the stator phasor voltage is:

$$\tilde{V} = L\frac{d\tilde{i}}{dt} + j\omega_m \phi e^{j\beta} + R\tilde{i} \qquad \text{Eq 2.19}$$

where R and L are the stator's inductance and resistance respectively. The second term is the emf induced in the stator winding by the rotor currents. Eq 2.18 and Eq 2.19 are analogous to Eq 2.1 and Eq 2.4 describing the dc motor's armature voltage and torque. Using a similar approach to that described in Section 2.2.1 a similar block diagram to that shown in figure 2.2 can be drawn for the ac servo system. Hence the grinding machine control system can be analysed in the same manner as for the dc motor control system. The method in the remainder of this section follows the approach described in Sections 2.2.1,2.2.2 and 2.2.3.

The stator windings' resistance and inductance are given in table B.6. The stator winding time constant $\tau = L/R$ and break frequency are given in table 2.4. The experimentally determined mechanical system's response calculated below is also listed.

Table 2.4 Grinding Machine System Response

	Time Constant (ms)	**Break Frequency (Hz)**
Electrical system	4.2	38
Mechanical system X axis	140	1.1

As for the dc servo system it can be seen that the electrical system is considerably faster than the mechanical system and so the grinding machine block diagram can be simplified to that shown in figure 2.7.

A voltage output from the DSP V_{DSP} will produce a motor torque T_m as described by Eq 2.9. The motor drives a ballscrew that translates rotational motion to linear motion. A ballscrew with pitch l will convert a torque T_m to a force F_m such that:

$$F_m = \frac{2\pi}{l} T_m \qquad \text{Eq 2.20}$$

A force F_m applied to a system with mass m, viscous friction f_v and Coulomb friction f_c can be described by:

$$F_m = m\frac{dv}{dt} + f_v v + f_c \qquad \text{Eq 2.21}$$

Using Eq 2.9 and Eq 2.20, Eq 2.21 becomes:

$$K_{VT}V_{DSP}\frac{2\pi}{l} = m\frac{dv}{dt} + f_v v + f_c \qquad \text{Eq 2 22}$$

Rearranging it follows that:

$$V_{DSP} = \frac{ml}{2\pi K_{VT}}\frac{dv}{dt} + \frac{f_v l}{2\pi K_{VT}}v + \frac{f_c l}{2\pi K_{VT}} \qquad \text{Eq 2.23}$$

Letting $m' = \frac{ml}{2\pi K_{VT}}$, $f_v' = \frac{f_v l}{2\pi K_{VT}}$, $f_c' = \frac{f_c l}{2\pi K_{VT}}$ and $F = V_{DSP}$ Eq 2.23 then becomes:

$$F' = m'\frac{dv}{dt} + f_v' v + f_c' \qquad \text{Eq 2.24}$$

The parameters m', f_v', f_c' can be multiplied by a constant to convert to the mass, viscous friction and Coulomb friction as referred to the linear system. These values are given in table 2.5.

Table 2.5 Control system to linear system conversion factors

Force F**(N)**	**Velocity** v**(m/s)**	**Coulomb friction** f_c **(N)**	**Viscous Friction** f_v **(N)**	**Mass m(Kg)**
$\frac{2\pi K_{VT}}{l}$	1	$\frac{2\pi K_{VT}}{l}$	$\frac{2\pi K_{VT}}{l}$	$\frac{2\pi K_{VT}}{l}$

The values m', f_v', f_c' can be multiplied by constants to give the inertia, viscous friction and Coulomb friction referred to the motor. These constants are given in table 2.6.

Table 2.6 Control System to motor system conversion factors.

Torque T**(N.m)**	**Angular Velocity** ω **(rad/s)**	**Coulomb Friction** f_c **(N.m)**	**Viscous friction** f_v **(Nm/rad)**	**Inertia** J**(Kgm^2)**
K_{VT}	$\frac{2\pi}{l}$	K_{VT}	$K_{VT}\frac{l}{2\pi}$	$K_{VT}\frac{l}{2\pi}$

Using a similar terminology to that adopted in Section 2.2.3 the parameters m', f_v', f_c' will be referred to as the control system's mass, viscous friction and Coulomb friction. These parameters are calculated using the least squares method as described in Section 2.2.3. These values and the actual values referred to the linear system and the motor are given in table 2.7.

Table 2.7 Mass, Inertia, Viscous and Coulomb Friction Values

Axis		Control Units	Linear system	Motor System
X	**Mass**	0.7 Vs^2/m	967Kg	N/A
	Inertia	N/A		$2.0x10^{-4}$
	Coulomb friction	0.28V	387N	0.1
	Viscous Friction	5.1Vs/m	$7.0x10^3$Ns/m	$1.5x10^{-3}$
	Time Constant	0.14	0.14	0.14

The experimental data used to calculate the control unit parameters m', f_v', f_c' is shown in figure 2.11. A model of the system was also made using these parameters and the model response is also shown in figure 2.11.

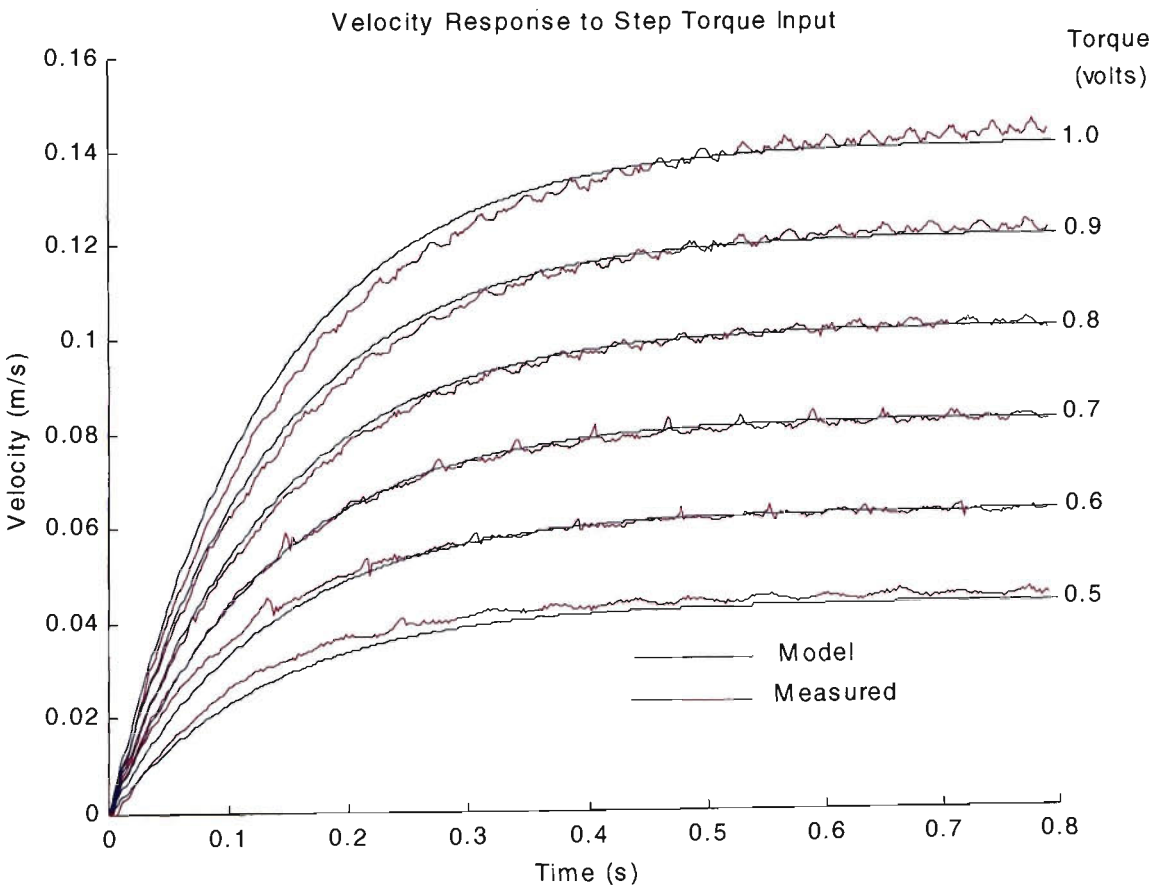

Figure 2.11 Grinding Machine Velocity Response to Step Torque Input

2.4 Conclusions

The experimental equipment used in this thesis has been described in this section. The control system and the system response of both the Hirata robot and the grinding machine have been analysed. The electrical system's response in the case of the Hirata robot was 300 times faster than the mechanical systems response and in the grinding machines case it was 30 times faster. In both systems the electrical system's response is considerable faster than the mechanical system so the electrical system's response can simply be treated as a constant gain. This allows the output voltage from the DSP (input voltage to the servo drive) to be considered as a motor torque value (multiplied by an appropriate scaling factor).

The mechanical system parameters, mass viscous and Coulomb friction were estimated from experimental results using a least squares method. These values were used to produce a system model. There was close agreement between the modelled and measured response of the actual system to step inputs in torque values. This was the case for both the Hirata robot and the grinding machine.

3 LOW SPEED POSITION TRACKING

3.1 Introduction

Friction exists in all mechanical systems and as discussed in Section 1.5 is highly non linear at low velocities. This non linearity presents a major challenge for control system engineers implementing precise motion control at low velocities. An impulsive control scheme for low velocity position tracking in systems with friction is developed in this chapter. This controller will be referred to as the friction controller for the rest of this chapter. The majority of the work on the friction controller was developed on the Hirata robot and consequently the majority of the results given in this chapter are for the Hirata robot. For completeness and to show the friction controller's performance improvements are not limited to one mechanism the friction controller is also applied to the grinding machine.

The friction controller developed in this section is based on the controller developed by Li et al [2]. The controller compensates for stick slip phenomena by driving the machine with a series of torque pulses with magnitude above the static friction and with long enough duration to ensure motion occurs. The controller reverts to a PID controller at higher velocities. The controller is simple to tune and needs a minimum knowledge of the system's friction characteristics. The controller had been previously tested in simulation by Li et al [2]. However as part of the research presented here the controller was applied to real mechatronic systems and improvements made. These improvements include compensation for velocity reversals, the use of a static friction lookup table to select pulse heights and a fuzzy logic controller to adjust pulse heights.

In Section 3.2 the controller developed by Li was applied to a real mechatronic system, the Hirata robot. The structure of the friction controller consisting of a digital PID controller with zero order hold combined with an additional pulse width modulated and hold part is described. There are a number of system parameters include sampling rates, servo drive response and pulse heights that need to be considered when implementing the friction controller. These parameters and their relevant values are discussed. The performance of a conventional PID controller and its typical stick slip behaviour at low velocities is shown. The performance improvement of the friction controller is also shown.

Section 3.3 discusses the friction controller with velocity reversal compensation. As discussed in Section 1.6.1 PID controllers have problems at velocity reversals due to the "wind up" of the integral part of the PID controller. In the controller used the integral term of the PID part of the friction controller is reset at velocity reversals. Coordinated motion of the A and B axis of the Hirata robot is used to compare the performance of the friction controller with velocity reversal compensation with that of a conventional PID controller.

In Section 3.4 detailed static friction characteristics of the Hirata Robot's A axis are recorded. An improved version of the controller developed in this section uses the static friction values to select the pulse height. This controller reduces the magnitude of the applied pulse so that less stress is placed on the mechanical system components.

In Section 3.5 a fuzzy logic controller that is used with the friction controller is developed. The fuzzy logic controller continuously adjusts the pulse height "on-line"

automatically. This allows the friction controller to operate without the user having to know any of the system's friction parameters. This is achieved by observing the velocity at each sampling point to see if the mechanism sticks and then adjusting the pulse height for the next sampling period.

In Section 3.6 the friction controller is applied to the X-axis of the grinding machine. The performance improvement when moving with a constant position tracking rate is shown.

3.2 Friction Controller

A block diagram of the friction controller is shown in figure 3.1:

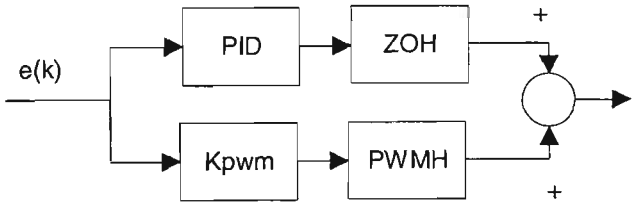

Figure 3.1 Friction Controller Block Diagram

The friction controller consists of two parts. The first part is a digital PID controller with a zero order hold. The second part of the controller is a proportional controller K_{pwm} with a pulse width modulated sampled-data hold (PWMH).

3.2.1 PID Controller and Stick Slip

The PID part of the friction controller is designed and tuned in conventional manner as the first part of the friction controller's design. The performance of the friction controller is compared to that of a conventional PID controller through this chapter. The PID controller's transfer function c(s) is given by:

$$c(s) = \frac{u(s)}{e(s)} = K_P + \frac{K_I}{s} + K_D s \qquad \text{Eq 3.1}$$

where u(s) is the controller's output and e(s) is the controller's input or the error signal. K_P, K_I, K_D are the proportional, integral and derivative terms respectively. Following the approach given in [47] and using standard Z transforms for integration $\frac{1}{s} = \frac{\tau_s}{2}\left[\frac{z+1}{z-1}\right]$ and for differentiation $s = \frac{z-1}{\tau_s z}$ where τ_s is the sampling period. The PID controller in the Z domain can be expressed in the form:

$$c(z) = \frac{u(z)}{e(z)} = \frac{a_0 + a_1 z^{-1} + a_2 z^{-2}}{1 - z^{-1}} \qquad \text{Eq 3.2}$$

The control loop on the Hirata robot used a sampling period τ_s = 20ms i.e. a sampling frequency of 50Hz. This is a relatively slow sampling rate and the DSP system is capable of much higher rates and other control systems controlling similar equipment have used much higher sampling rates. However as discussed in Section 3.2.2 the sampling rate is set by the drive's frequency response and requirements of implementing the PWMH part of the friction controller. It should also be noted that this sampling rate is at least 100 times faster than the mechanical break frequencies (given in Section 2.2.2) of the A and B axes of the Hirata robot.

The PID controller can be described by the linear difference equation:

$$u(k) = u(k-1) + a_0 e(k) + a_1 e(k-1) + a_2 e(k-2) \qquad \text{Eq 3.3}$$

where u(k) and e(k) are the system's outputs and inputs respectively at the kth iteration. At time $k\tau_s$ the constants a_0, a_1 and a_2 are given by:

$$a_0 = K_P + \frac{K_I t_s}{2} + \frac{K_D}{\tau_s} \qquad a_1 = -K_P + \frac{K_I t_s}{2} + \frac{2K_D}{\tau_s} \qquad a_2 = \frac{K_D}{\tau_s} \qquad \text{Eq 3.4}$$

The PID controller was tuned using the Zeigler-Nichols tuning method [48]. The PID controller was tuned at higher velocities above the range of velocities at which "stick

slip" is observed. At very low velocities friction can cause stick slip motion in the mechanism. This phenomena has been well documented and work by other authors is discussed in Section 1.6. When the A Axis was run at very low velocities using the PID controller typical stick slip behaviour was observed and is shown in figure 3.2.

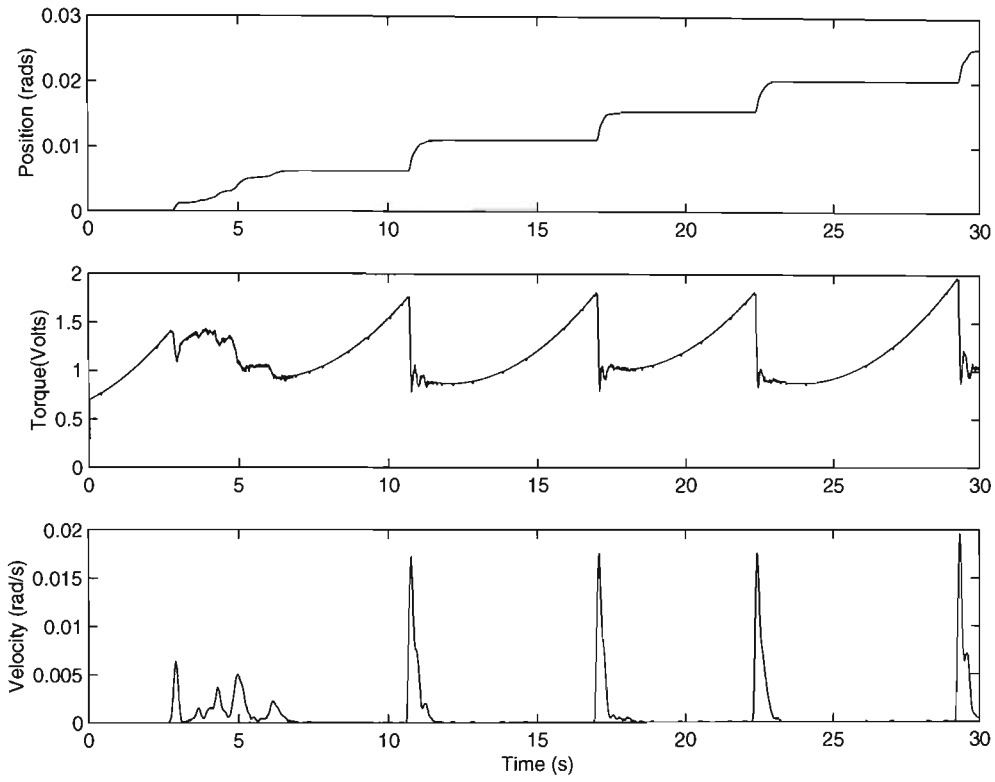

Figure 3.2 Stick Slip Motion with PID control (1 Volt =0.044Nm).

A constant velocity or constant position tracking rate of 8×10^{-4} rad/s was used. This corresponds to one decoder count per sampling period. The desired position profile is a straight line of slope 8×10^{-4} rad/s. Instead a stepped profile was produced. This can be seen in the top graph of figure 3.2. The motion is characterized by regions where the velocity is zero while the torque signal "winds up" to be greater than the static friction. Once the static friction value is reached there is a rapid increase in velocity. The position error reduces and there is a sharp reduction in the torque and the mechanism comes to rest. The cycle then starts again as the torque signal starts to "wind up" again.

3.2.2 Controller Algorithm and Performance.

The second part of the friction controller is the Pulse Width Modulated and Hold (PWMH) part. The PWMH part of the friction controller improves the position tracking performance at low velocity where the non linear effects of friction can lead to stick slip limit cycling. The output $u_{pwm}(t)$ of the PWMH part of the friction as given by Li et al [2] is:

$$u_{pwm}(t) = T_p \operatorname{sgn}(e(k)) \quad \text{for} \quad k\tau_s \le t < k\tau_s + \Delta$$
$$u_{pwm}(t) = 0 \quad \text{for} \quad k\tau_s + \Delta \le t < kt + \tau_s \qquad \text{Eq 3.5}$$

where τ_s is the sampling period and the kth sample is at time $k\tau_s$. Δ is the pulse width and is given by:

$$\Delta = \frac{K_{pwm} e(k) \tau_s}{|T_p|} \quad \text{if} \quad \frac{K_{pwm} e(k) \tau_s}{|T_p|} < \tau_s$$
$$\Delta = \tau_s \quad \text{otherwise} \qquad \text{Eq 3.6}$$

where e(k) is the input to the controller and T_p is the pulse height The output of the PWM part of the controller is a pulse with amplitude T_p and width Δ. This is added to the output of the PID controller. A typical output of the controller is shown in figure 3.3.

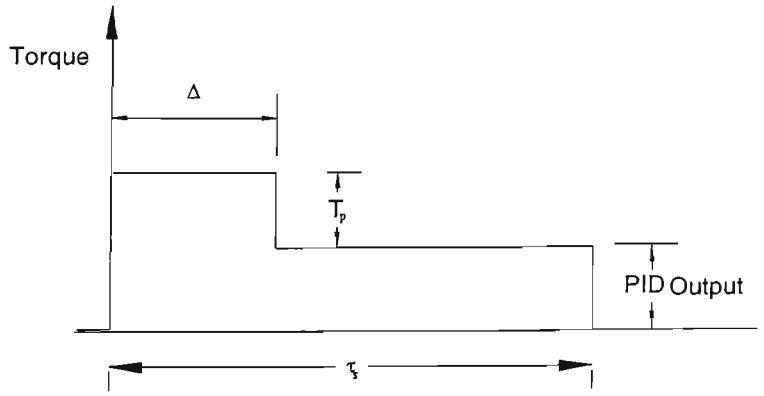

Figure 3.3 Friction Controller Output

If $u_{PID}(t)$ is the output of the PID part of the controller the output of the controller $u(t)$ is then:

$$u(t) = u_{PID}(t) + u_{pwm}(t) \qquad \text{Eq 3.7}$$

The principle of this controller is that a torque pulse will be generated within each sampling period whose width Δ is determined from the controller's input (error signal). The pulse has the same sign as the tracking error and is intended to drive the system out of stiction into the zero tracking error position.

The pulse shape shown in figure 3.3 is an idealised output pulse of the controller. The pulse width Δ cannot be infinitely variable because there are practical limits on sampling times. In the experiments here the sampling period τ_s is divided into 10 subintervals and the actual pulse width can only be integer multiples of this subinterval. The shape of the pulse is also affected by the system's electrical circuit response. As discussed in Section 2.2 the torque applied is proportional to the motor current and the rate at which the current (and hence the torque) changes is dependent on the electrical time constant of the servo motor. As an example the simulated response showing the expected pulse shape for the A axis of the Hirata Robot is shown in figure 3.4.

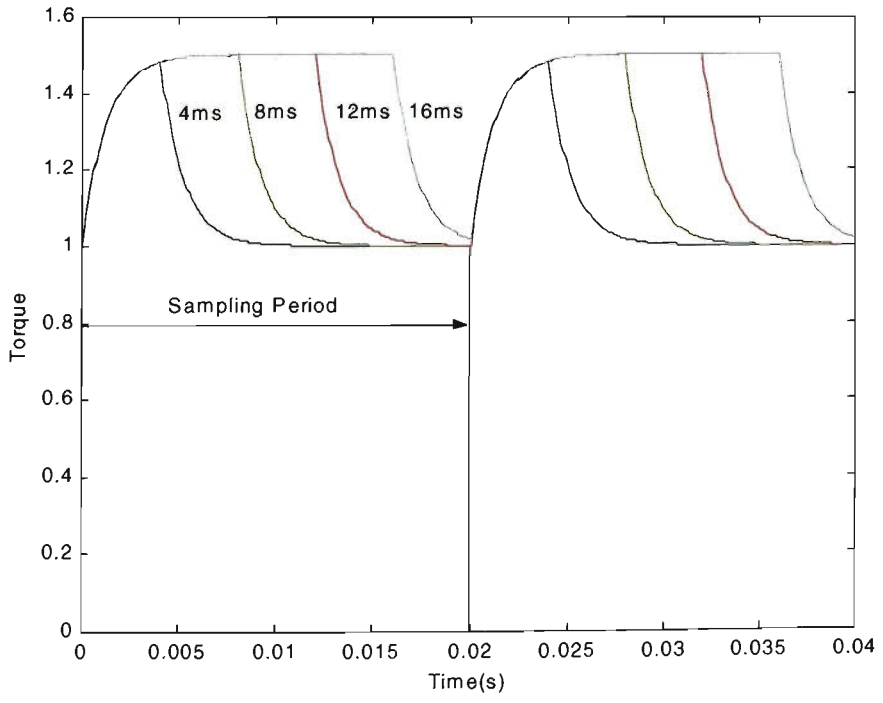

Figure 3.4 Expected Pulse Shapes

The Hirata robot's A axis electrical time constant is given in Section 2.2.2. Two consecutive sampling periods of 20ms duration (i.e. a sampling frequency of 50 Hz) and pulse widths of 4,8,12, and16 ms are shown. The pulse shapes drawn are for a typical situation in which the pulse height is 50 % of the PID output. For this case the PID output has been arbitrarily chosen as 1 so the peak pulse height will be a 1.5. As can be seen from figure 3.4 the expected pulse shapes are not the idealised pulse shape drawn in figure 3.3. As the system's sampling rate increases and approaches the electrical circuit's response the pulse shape will move further away from the idealised pulse. It is suggested that the sampling period be at least 10 times the electrical circuit's time constant. If the sampling period is then broken up into 10 subintervals the minimum pulse width will be greater than the electrical circuits time constant. For the A axis of the Hirata robot the minium pulse width is 2ms and the electrical time constant given in Table 2.1 is 1.2ms.

If the stiction f_{stic} and Coulomb friction f_c were constant then the magnitude of the pulse T_p could be chosen just to be above the difference in the static and Coulomb friction i.e:

$$T_p > f_{stic} - f_c \qquad \text{Eq 3.8}$$

Starting from rest and assuming the output of the PID part of the control is zero, motion will not occur until the integral action of the PID winds the torque value up to the Coulomb friction value. The friction controller output will then be $T_p + f_c$ and from Eq 3.8 the friction controller's output will be greater than the static friction and motion will occur. If the error is zero the pulse width will be zero and the friction controller's output will be the Coulomb friction value and the motion will stop. If the error is positive the

pulse width will not be zero and the output of the controller will again be $T_p + f_c$ and motion occurs. This breaks the limit cycle that would occur in a conventional PID controller where the output would have to wind up and down between the Coulomb and static friction values.

If friction varies significantly over the travel length, then a larger value of T_p is more suitable. The pulse height plus the Coulomb friction should exceed the static friction value for the whole of the mechanism's travel. In improving tracking performance it is better to err on the side of having a larger pulse which will break the stick slip cycle. A pulse height of T_p =0.9 volts (0.04Nm referred to the servo motor as given by table 2.2) was found to be adequate for the entire travel of the A axis. As will be discussed in Section 3.4 this value may be slightly higher than optimal. In Section 3.4 a static friction lookup table is used to give more optimal selection of pulse heights across the mechanism's travel. As also discussed in Section 3.4 the experiments to find the static friction require a considerable amount of time. Although it is beneficial to know the Coulomb friction value and static friction values to select the pulse height it is not absolutely essential. An estimate of the pulse height can be given from the stick slip behaviour shown in the second plot in figure 3.2. An estimate of the pulse height can be gained by observing how much the torque value winds up. The difference between the minimum and maximum torque values over the course of one stick slip limit cycle can be used as an initial estimate. There may need to be some adjustment using trial and error to this initial estimate to give the best performance.

The PWM gain K_{pwm} was chosen so that the minimum acceptable position error generates a pulse width Δ greater than the minimum. For the A axis of the Hirata robot

the minimum error of 1 decoder count per sampling period corresponds to a pulse width of 2ms. The value K_{pwm} can then be calculated using Eq 3.6.

The improved position tracking performance of this friction controller for a velocity of $8x10^{-4}$rad/s is shown in figure 3.5. This can be compared to the performance of the PID controller at the same velocity shown in figure 3.2.

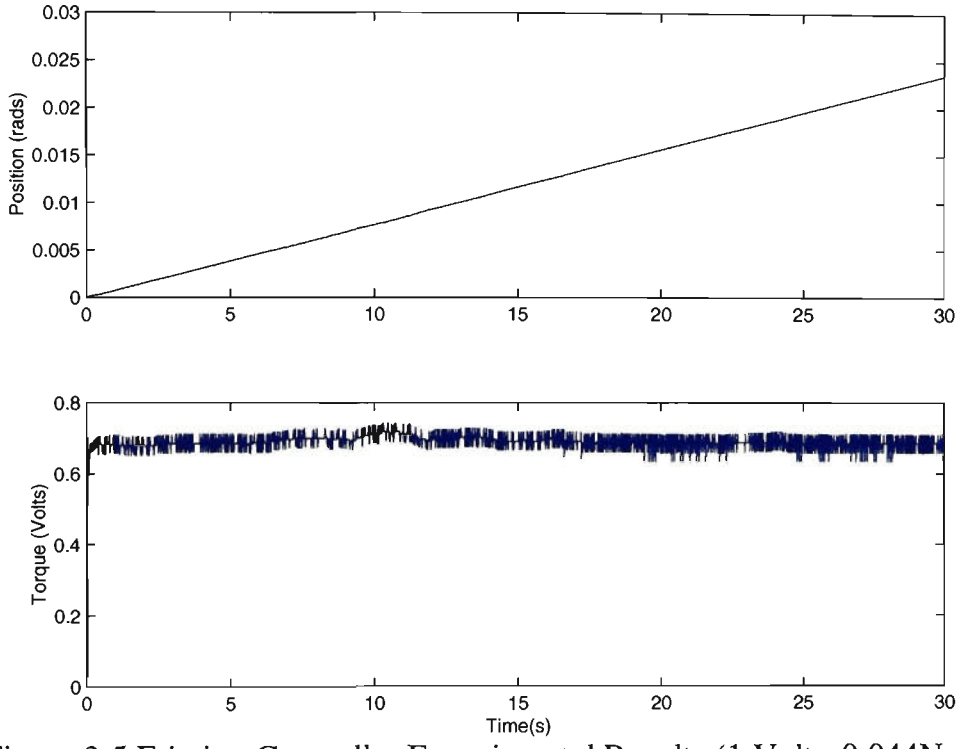

Figure 3.5 Friction Controller Experimental Results (1 Volt =0.044Nm)

The torque signal shown in figure 3.5 is the output of the PID stage of the friction controller. The actual signal applied to the motor is this signal plus the PWM signal. This torque signal is considerably more stable than that shown for the conventional PID controller applied to the same axis of the Hirata robot and shown in figure 3.2. It is clear that this controller has removed the stick slip limit cycling.

3.3 Friction Controller with Velocity Reversal Compensation

The discontinuity of the friction characteristic at zero velocity has been known to cause problems at velocity reversals as mentioned in Section 1.6.1. In PID controllers the

standard solution is to reset the integral term of the PID controller at velocity reversals. A similar approach is used with the friction controller and is discussed in this section. The performance of a conventional PID controller is compared to the performance of the friction controller with velocity reversal compensation. The performance of the friction controller with and without velocity reversals compensation is also compared.

In Section 1.5.1 a model for friction is given and using rotational system variables, angular velocity ω and torque, the frictional torque T_f can be expressed as:

$$T_f = \text{sgn}(\omega)\left\{ f_c + (f_{stic} - f_c)e^{-\left|\omega/\omega_s\right|^{\partial}} \right\} + f_v\omega \qquad \text{Eq 3.9}$$

The static friction value jumps between f_{stic} and $-f_{stic}$ at the origin. If the mechanism is initially moving in the positive direction it will not stop until the torque value drops below the Coulomb friction value f_c. It will then not move in the opposite direction until the torque value exceeds $-f_{stic}$. Using a standard PID controller there is a dead time while the controller "winds down from f_c to $-f_{stic}$. Experimental results from the B axis of the Hirata robot using a standard PID controller are shown in figure 3.6.

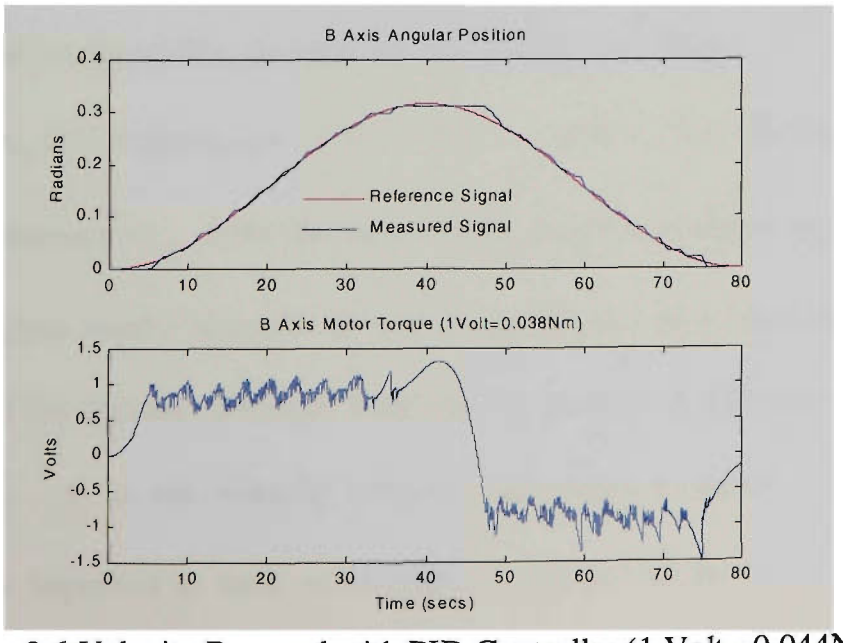

Figure 3.6 Velocity Reversal with PID Controller (1 Volt =0.044Nm)

Similar results were obtained with the A axis. The position reference signal is that used to draw the circles shown in figures 3.10 and 3.11. The effect of velocity reversal is evident from the flat top of the measured position signal.

Figure 3.7 shows the performance of the friction controller while tracking the same position reference signal with no compensation for velocity reversals. There is still a flat top on the measured position signal, although the tracking along the remainder of the path is much better than for the PID controller.

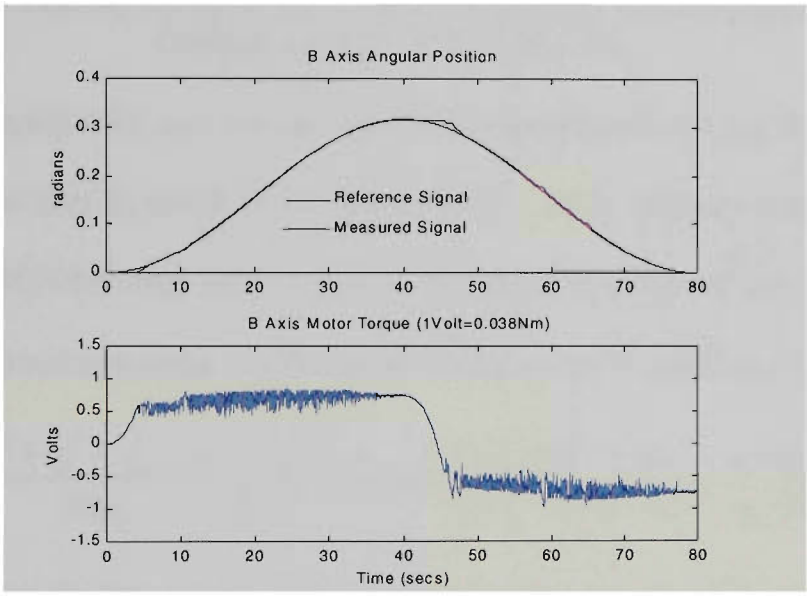

Figure 3.7 Velocity Reversals with Friction Controller (1 Volt =0.044Nm)

Using the expression for the PID controller Eq 3.3 developed in Section 3.2.1 the velocity reversal compensation modifies the u(k-1) term such that;

If $\text{sgn}(\omega_{ref}(k)) \neq \text{sgn}(\omega_{ref}(k-1))$ then $u(k-1) = f_c \,\text{sgn}(\omega_{ref})$ Eq 3.10

The velocity reference ω_{ref} is the derivative of the position reference signal. Figure 3.8 gives experimental results from the B axis of the Hirata robot showing the tracking performance of the friction controller with velocity reversal compensation. The torque signal steps to $-f_c$ at the velocity reversal. As shown in figure 3.8 the tracking performance is improved as there is no longer a flat spot at the top of the measured position signal.

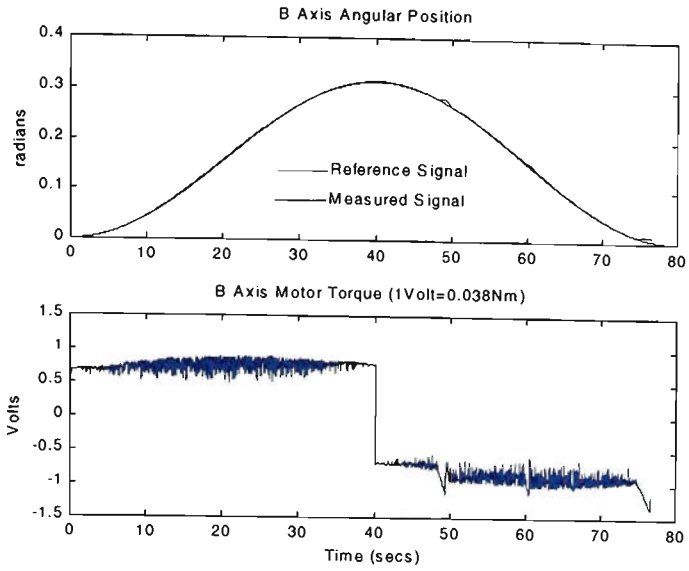

Figure 3.8 Velocity Reversal with Friction Controller and Velocity Reversal Compensation (1 Volt =0.044Nm)

The friction compensation and velocity reversal control schemes were implemented on the main rotation axes A and B of the Hirata robot. Using standard inverse kinematic equations for a SCARA robot [49], positions in the horizontal plane with coordinates x-y can be transformed to a series of joint angles θ_a,θ_b for the A and B axes respectively:

$$\theta_b = \pm\arccos\left(\frac{x^2 + y^2 - r_a^2 - r_b^2}{2r_a r_b}\right) \quad \theta_a = \arctan 2\left(\frac{xr_b \sin\theta_b + y(r_a + r_b\cos\theta_b)}{x(r_a + r_b\cos\theta_b) - yr_b\sin\theta_b}\right) \quad \text{Eq 3.11}$$

Where r_b and r_a are the link lengths links associated with axes A and B respectively. The $\pm$ values for θ_b are the left and right handed solutions. The values θ_a,θ_b are the position reference values for the A and B axes control systems.

A 100mm-diameter circle was drawn by the robot to compare the different control schemes. The circles are drawn with an angular velocity of 78mrad/s. The tool tip speed is 3.9mm/s. This is a slow tracking speed used to emphasize the improvement at low speed. The circles start at position x=50 y=0 and are drawn in an anti clockwise direction. The A and B axes position reference inputs θ_a,θ_b to track a 100mm diameter

circle are shown in figure 3.9. The measured values of angles θ_a,θ_b are converted to x ,y coordinates using the kinematic equations for a SCARA robot:

$$x = r_a \cos\theta_a + r_b \cos(\theta_b + \theta_a) \qquad y = r_a \sin\theta_a + r_b \sin(\theta_b + \theta_a) \qquad \text{Eq 3.12}$$

The position tracking experimental results for the PID controller are shown in figures 3.10 and the results for the friction controller with velocity reversal compensation are shown in figure 3.11.

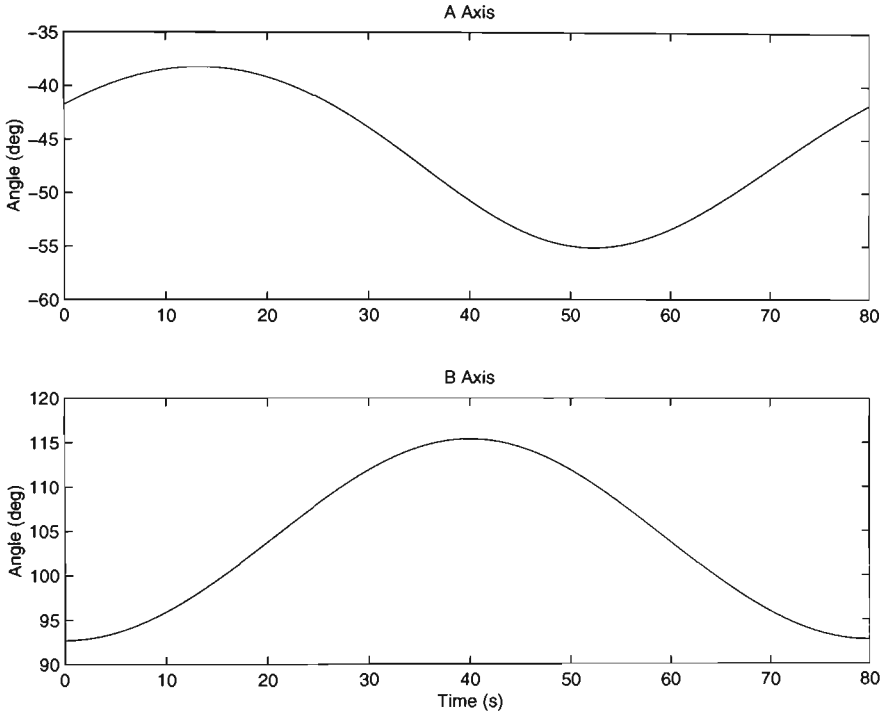

Figure 3.9 Control signals for A and B axes

As can be seen from the control inputs in figure 3.9 the velocity reversals for the B axis occur at t=0s and t=40 and the A axis reversals occur at t=10s and t=50s. The total tracking time is 80s and since the angular velocity is constant t=40s corresponds to a point half way round the circle. The B axis velocity reversals are more pronounced and in figure 3.10 can be seen for the PID controller at position (50,0) t=0 and position (-50,0) t=40s as a flat Section of the circle. The A axis reversals are at position (30,40) t=10s and at position (-30,-40) t=50s. The "stair case" effect around the circle is the stick-slip limit cycling.

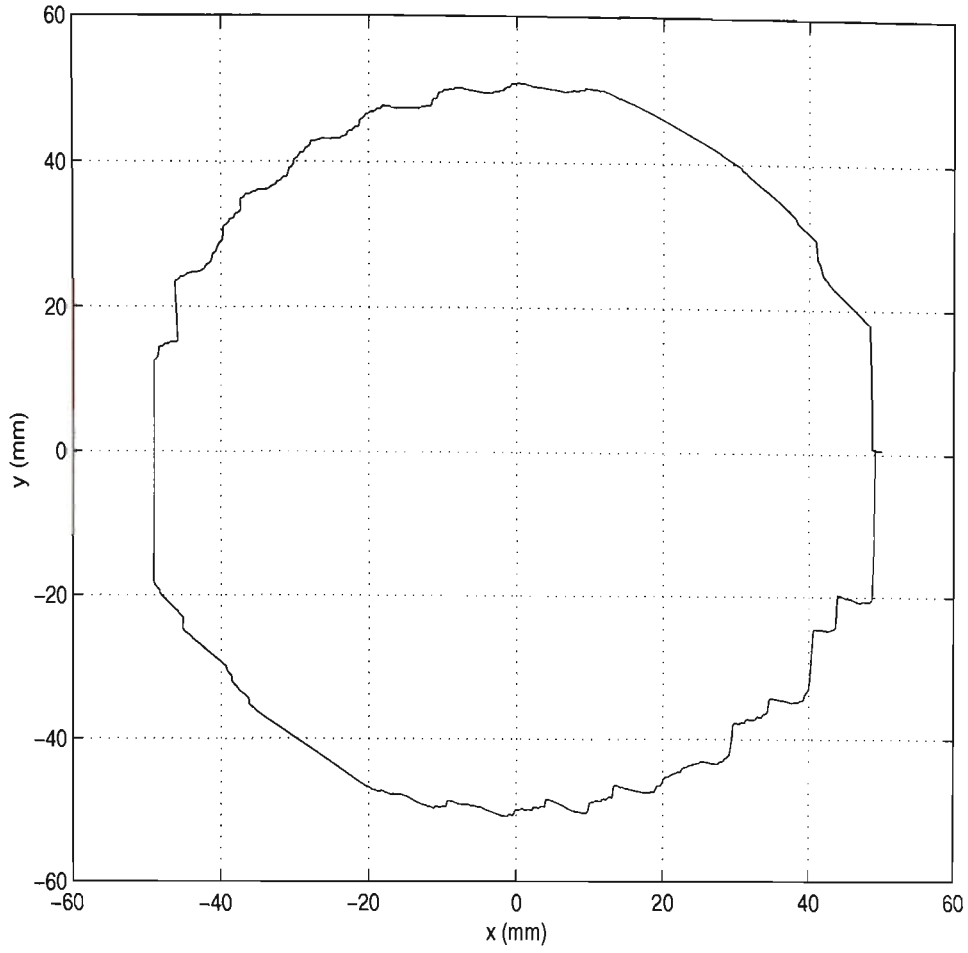

Figure 3.10 Circle with PID controller

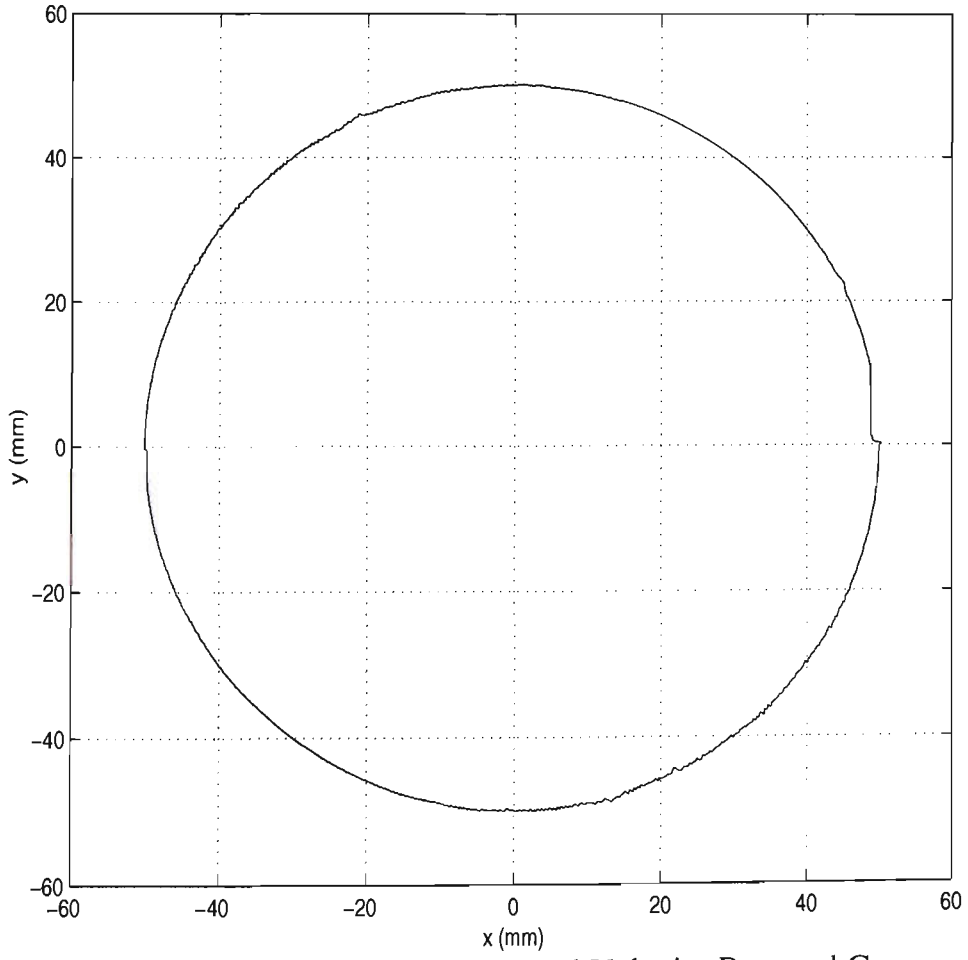

Figure 3.11 Circle with Friction Controller and Velocity Reversal Compensation

As shown by comparing figures 3.10 and 3.11 the friction controller with velocity reversal compensation has significantly reduced the four flat spots associated with the velocity reversals and reduced the distortion due to stick slip behaviour. The desired tracking path is a circle with a 100mm radius. The deviation from this desired circle for the two control schemes is shown in figure 3.12.

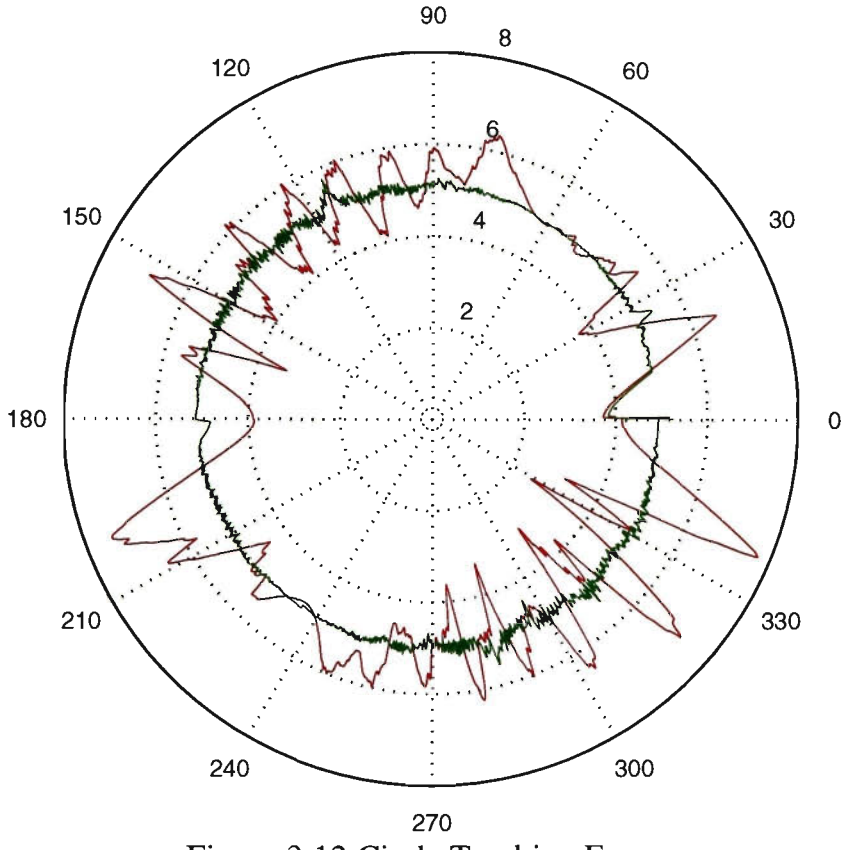

Figure 3.12 Circle Tracking Errors

This is a polar plot where the error for the PID and friction controllers have been expanded. The maximum deviation from the circle using the PID controller is ± 2.5mm. The maximum error using the friction controller with velocity reversals is less than 1.2mm. This occurs at t=0s and is associated with the robot arm moving from its home position to the start of the circle. If this was discounted the maximum error would be less than ± 0.5mm. The combined effect of the friction controller and velocity reversal compensation demonstrates a significant improvement over a conventional PID controller in position tracking performance at low velocities.

3.4 Friction Controller with Static Friction Lookup Table

An improvement can be made to the friction controller by using a static friction lookup table. The idea is to keep the overall control torque just above the static friction by taking position dependent static friction into account and adjusting the pulse height according to the magnitude of the PID controller. The position tracking performance of the controller is not reduced but it does reduce the peak torque and hence reduces the stress placed on the mechanical system.

The experimental procedure to generate the static friction lookup up table takes a considerable amount of time. In the case of the A axis of the Hirata robot it took over 20 hours of the Robots operational time. The friction controller using the static friction lookup table control scheme was only implemented on the A axis of the Hirata robot.

3.4.1 Static Friction Lookup Table

The static friction lookup table relates static friction with position. As discussed in Section 1.5.2 other authors [28] and [29] conducted a series of "breakaway" experiments to determine the static friction lookup table. A similar approach was used on the Hirata robot to determine the static friction parameters of the A axis of the Robot. Using an open loop control system the torque signal was increased until the robot moved and the maximum torque (i.e. static friction value) was recorded as a function of position. The torque was reduced to zero and the procedure was repeated until the robot had moved the entire length of its travel. This whole experiment was repeated a number of times so each position along the robot path had a significant number of data points. The position axis was broken up into a series of "bins" whose width was a constant fraction of the robots travel. The bin width used was 20 decoder counts or 3.1×10^{-4}rad (see table B.1 for conversion factor.) The torque values falling within each position bin

were grouped together and the average value calculated. Figure 3.13 shows a graph of static friction versus position after the torque values had been grouped into these position bins.

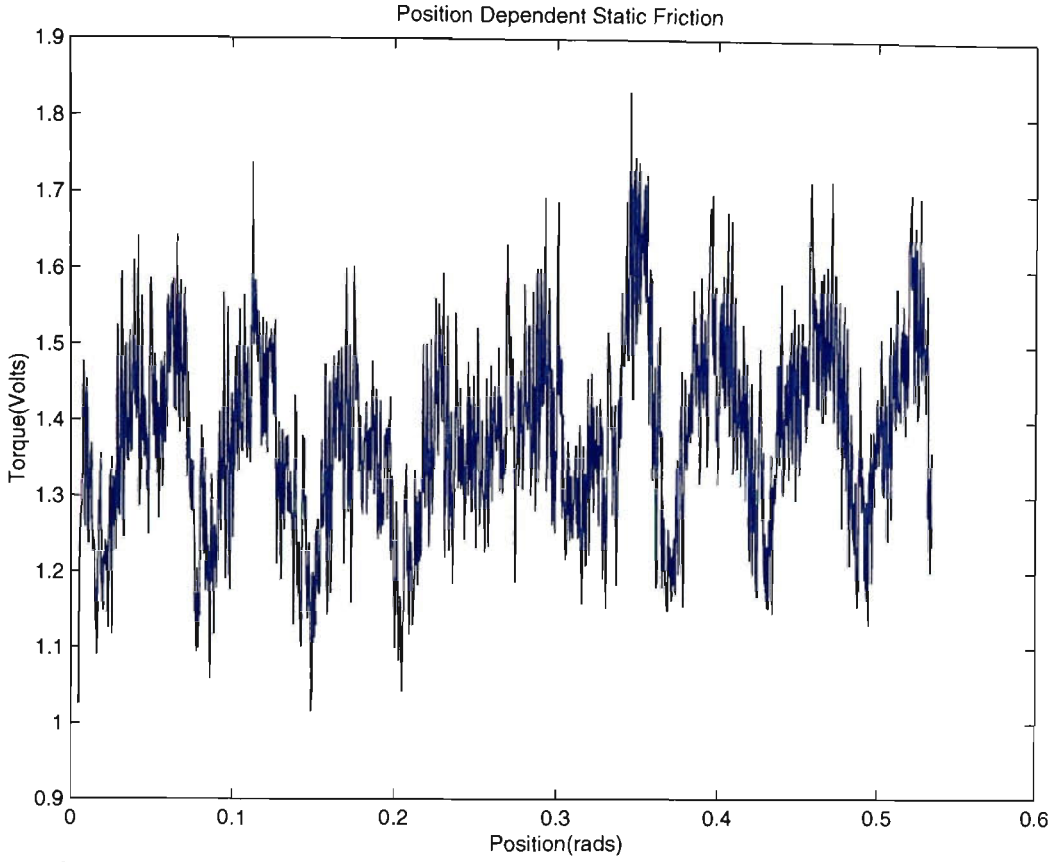

Figure 3.13 Position Dependent Static Friction (1 Volt =0.044Nm).

The static friction values are listed in table 3.1. As discussed in Section 2.2.3 friction values can be referred to the motor, robot's arm or the control system units.

Table 3.1 A Axis Static Friction Values

	Mean	**Standard Deviation**	**Minimum**	**Maximum**
Control Units (Volts)	1.4	0.13	1.0	1.8
Motor (Nm)	0.062	0.0057	0.0441	0.0794
Robot (Nm)	6.2	0.57	4.41	7.94

3.4.2 Control Algorithm and controller performance

As shown in figure 3.13 the static friction values can be plotted against position. The static friction values are stored in a lookup table so that the static friction can be expressed as a function of position. If at the kth sampling interval the position is x the static friction is denoted as $f_{stic}(x)$.

The peak torque u_{pk} is applied from the start of the sampling period to time Δ after the start of the sampling period and has a value given by:

$$u_{pk}(k) = T_p(k) + u_{PID}(k) \qquad \text{Eq 3.13}$$

For motion to occur the peak torque should exceed the static friction value i.e:

$$\left|u_{pk}(k)\right| > f_{stic}(x) \qquad \text{Eq 3.14}$$

Letting the peak torque exceed the static friction by a margin of 10% and using equations Eq 3.13 and 3.14 the pulse height can be given by:

$$T_p(k) = 1.1 f_{stic}(k) - \left|u_{pid}(k)\right| \qquad \text{Eq 3.15}$$

The pulse height is then substituted in Eq 3.5 and the friction controller's pulse width is calculated as before. The performance of the friction controller using the static friction lookup table is shown in figure 3.14.

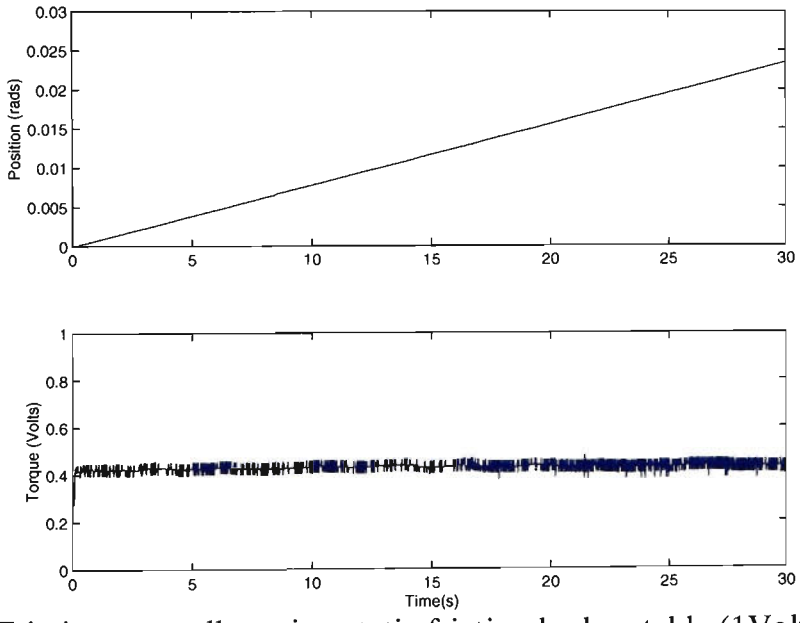

Figure 3.14 Friction controller using static friction lookup table (1Volt =0.044Nm)

The tracking performance is no worse than that achieved by the friction controller using constant pulse heights T_p =0.9 volts (=0.044Nm at the servo motor) as shown in figure 3.5. A comparison of the peak torque values for the friction controller using a constant pulse height with a friction controller using a static friction lookup table is shown in figure 3.15.

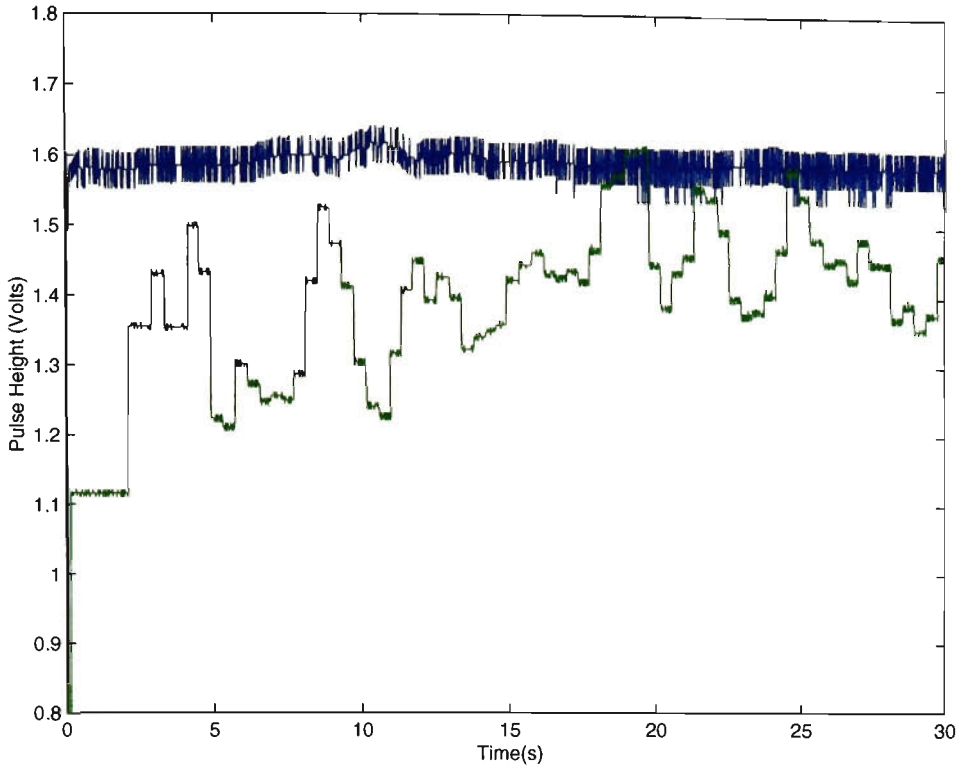

Figure 3.15 Comparison of Peak Torque Values (1Volt =0.044Nm)

The lower graph shown in figure 3.15 is the peak torque value $u_{pk}(k)$ for the friction controller using the static friction lookup table. As discussed the peak torque value is simply the static friction value determined from the lookup table. The curve above this is the peak torque value when using the friction controller with a constant pulse height of 0.9 volts. The peak torque value is calculated from Eq 3.13. The curve is simply the torque value shown in figure 3.5 with 0.9volts added to it. As can be seen from figure 3.15 the peak torque value for the friction controller using the static friction lookup table is never greater than when the friction controller is using a constant pulse height of 0.9(volts) and for much of the time it is considerably less.

3.5 Friction Controller with Fuzzy Logic Pulse Height Adjustment

It is shown in this section using a fuzzy logic controller in conjunction with the friction controller it is possible to reduce stick slip cycling without needing to know any of the friction characteristics of the system. The friction controller with fuzzy logic pulse

height adjustment adds a pulse of height T_p and width Δ to the output of the PID section (as does the basic friction controller discussed in Section 3.2.2). The pulse width is calculated from the error signal (in exactly the same manner as the basic friction controller) and the fuzzy controller developed in this section adjusts the pulse height. The fuzzy logic controller adjusts the pulse height automatically. The user does not have to select the pulse height and therefore needs no knowledge of the system's friction characteristics.

The fuzzy logic controller was designed using the MATLAB fuzzy logic toolbox. A MATLAB m–file was written that converted the fuzzy logic structure to a C program that could be used by the DSP. The fuzzy logic controller was implemented in real time on the DSP. The logic operators *AND* and *OR* were implemented as *min* and *max* functions respectively. A Sugeno type inference system [50] was used. The defuzzification method was weighted average.

3.5.1 Membership Function

The one output variable was *Pulse Height* and it has five output states; d*ecrease, decrease slightly, leave, increase slightly and increase.* There are three input membership functions, *Velocity, PID* and *Friction controller.*

In figure 3.2 it can be observed that the velocity is zero (or sticking) for a large part of the time. The velocity is a most relevant variable to determine if stick slip is occurring and is used as one of the inputs to the fuzzy logic controller. If the velocity reference is not zero and the velocity goes to zero then the system is "sticking". Otherwise the mechanism is moving. The membership function for velocity is shown in figure 3.16.

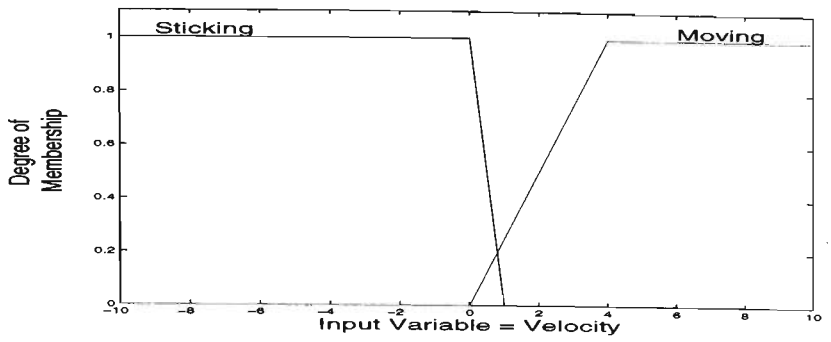

Figure 3.16 Velocity Membership Function

As discussed in Section 3.3. the pulse height should be such that the, applied torque is above the static friction. If stick slip is occurring then it is assumed that the pulse height is less than required. Therefore if the system sticks then the pulse height should be increased. Therefore Rule1 for the Fuzzy logic controller is

RULE 1: IF *Velocity* is *Sticking* THEN *increase* the *Pulse Height*

As discussed in Section 3.3 the friction controller's output is the sum of the PID and PWMH parts of the controller. The output of the PWMH part of the control is a pulse of duration Δ and magnitude f_p as discussed in Section 3.2.2. The sign of the pulse is the same as the error signal. If the error is negative the pulse is subtracted from the PID output. If the pulse height is greater than the PID output, the output of the friction controller could be negative. The rapid application of torque pulses of different signs lead to noisier mechanical operation and increased vibration of the robot's arm. This was an undesirable operating regime and to limit this the pulse height is reduced. This is done if the mechanism is moving. The second fuzzy logic rule is;

RULE 2; IF *Friction Controller is Negative* AND *Velocity* is *Moving*
THEN *decrease Pulse_height.*

The membership function for the friction controller is shown in figure 3.17

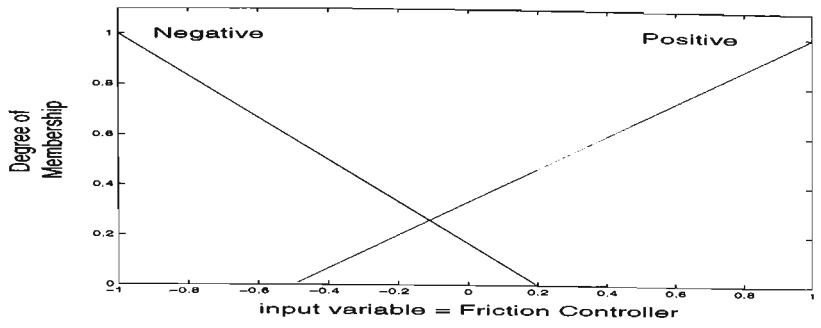

Fig 3.17 Friction Controller Output Membership Function

If when the mechanism is moving at a constant velocity the PID output increases the most likely reason for this would be an increase in friction characteristics. If the sliding friction has increased then it would not be unreasonable to expect the static friction to also have increased. Therefore it would be wise to increase the pulse height if the PID output increases and decrease the Pulse height if the PID output decreases. The PID membership function is shown in figure 3.18

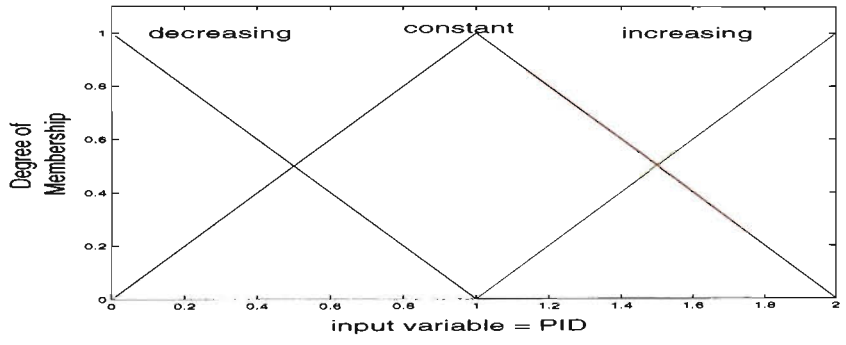

Figure 3.18 PID controller output membership function

Since the position dependent variation in friction is usually less than the difference between static and Coulomb friction it is only necessary to slightly modify the pulse height. The fuzzy logic controllers Rules 5,6,7 are therefore suggested as follows;

RULE 5; IF *Velocity* is *Moving* AND Friction *Controller* is *Positive* AND *PID* is *increasing* THEN *slightly Increase Pulse_height.*

RULE 6: IF *Velocity* is *Moving* AND *Friction Controller* is *Positive* AND *PID* is *decreasing* THEN *slightly decrease Pulse_height.*

RULE 7:IF *Velocity* is *Moving* AND *Friction Controller* is *Positive* AND *PID* is *constant* THEN *same Pulse_height.*

3.5.2 Pulse Height Adjustment

The results of running the fuzzy logic controller with the friction controller are shown in figure 3.19. The position reference signal was increasing at 8×10^{-4} rad/s. In the test arrangement the pulse height was initially chosen to be zero. This was to make the controller's task more difficult. In an actual system it may be more efficient to save the pulse height which was used previously and adjust from there.

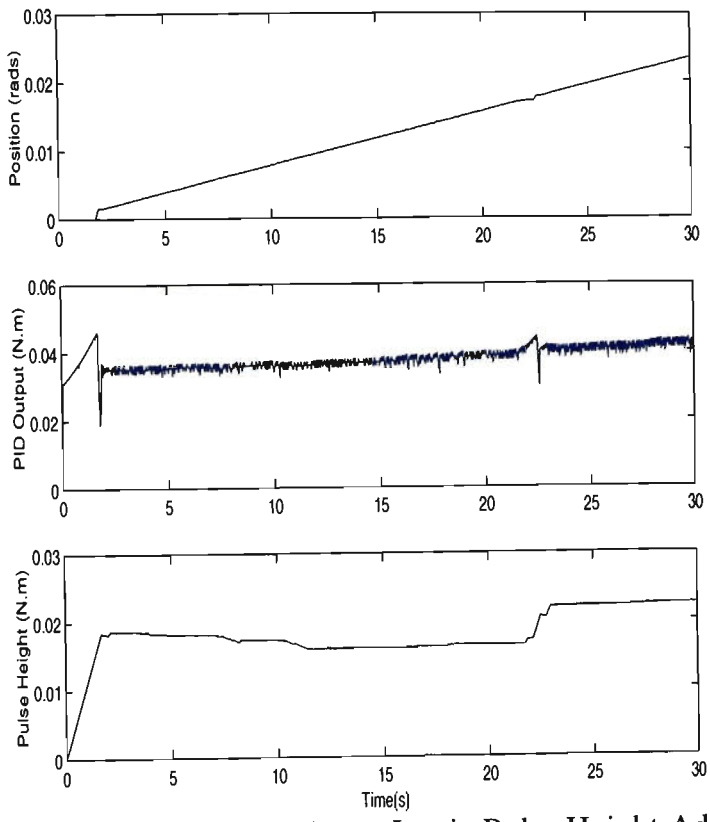

Figure 3.19 Friction Controller with Fuzzy Logic Pulse Height Adjustment Results

If the pulse height is zero the system behaves as a PID controller. In figure 3.19 there is a flat spot in the position plot at the origin. Initially the system sticks as for the PID controller. In this time the pulse height increases rapidly. Once motion is achieved the pulse remains for a period approximately constant. There are slight adjustments due to the PID output changing marginally. At about time =22s in figure 3.19 the system sticks again. This can be seen by the glitch in the position graph and the PID output starts to wind up. The pulse height also increases. The effect on the position accuracy is considerably less for this stick slip event than the effect at the origin.

The friction controller with fuzzy logic pulse height adjustment has the same improvement in position tracking performance as the basic friction controller and the friction controller using the static friction lookup table. However the friction controller with fuzzy logic pulse height adjustment has the advantage that the friction characteristics of the mechanism do not have to be known. This removes the need to determine these parameters experimentally. Also if the friction characteristics change then this control scheme can adapt to those changes

3.6 Friction Controller and Grinding Machine

The results given so far in this chapter have been for the Hirata Robot. The A and B axes of the Hirata robot have harmonic gear boxes (as discussed in Section 2.2) and there is no reason that the application of the friction controller should be limited to this mechanical arrangement. To show that the friction controller is applicable to other mechanical systems the friction controller was also applied to the X axis of the grinding machine. The mechanism of the X axis of the grinding machine is a linear ball screw arrangement (as described in Section 2.3).

The basic friction controller described in Section 3.2 was implemented on the X axis of the grinding machine. A sampling frequency of 100Hz was used. The reference signal was a constant position tracking rate of $30\mu m/s$; this corresponds to 1 decoder count per sampling period. The minimum velocity that could be achieved without stick slip occurring using a PID controller was 2mm/s. The PID controller was tuned at this velocity. The reference signal ($30\mu m/s$) chosen was considerably less than 2mm/s and so the system was operating well within the region where stick slip occurs for a PID controller.

The performance of a conventional PID controller applied to the grinding machine is shown in figure 3.20.

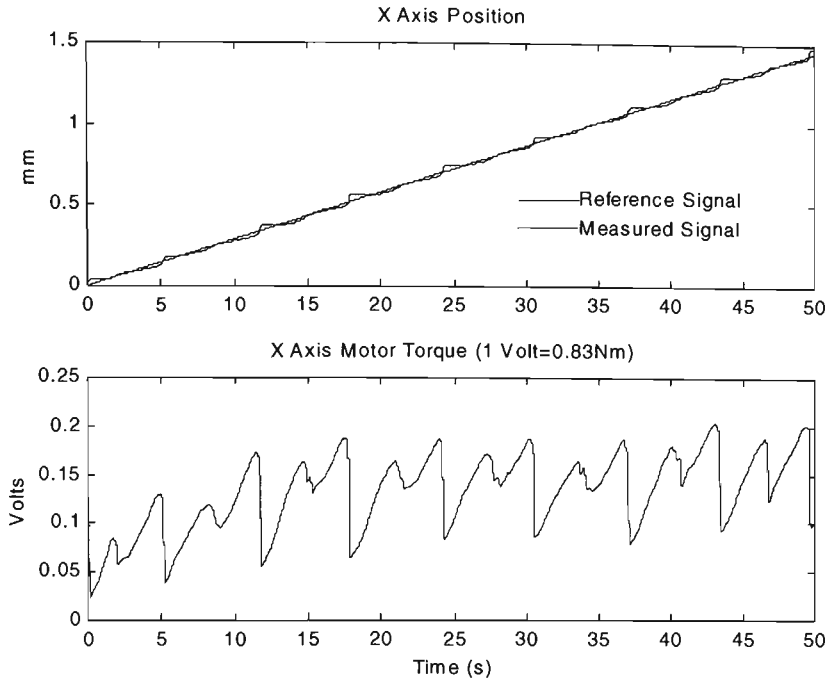

Figure 3.20 PID Controller Position Tracking Performance (1 Volt=1.1Nm)

The graphs of position and torque exhibit the classic stick slip behaviour discussed in Section 1.6 and also seen with the Hirata robot in figure 3.2.

The friction controller's performance is shown in figure 3.21. The torque signal shown is the output of the PID stage of the friction controller. The actual signal applied to the motor is this signal plus the PWM signal. This torque signal is considerably more stable than that shown for the conventional PID controller. The stick slip limit cycling has been removed.

The tracking error for the PID controller and the friction controller are shown in figure 3.22. As can be seen from the bottom graph of figure 3.22 apart from the initial error at the start the position error is less than $2\mu m$ as compared with $40\mu m$ for the PID controller.

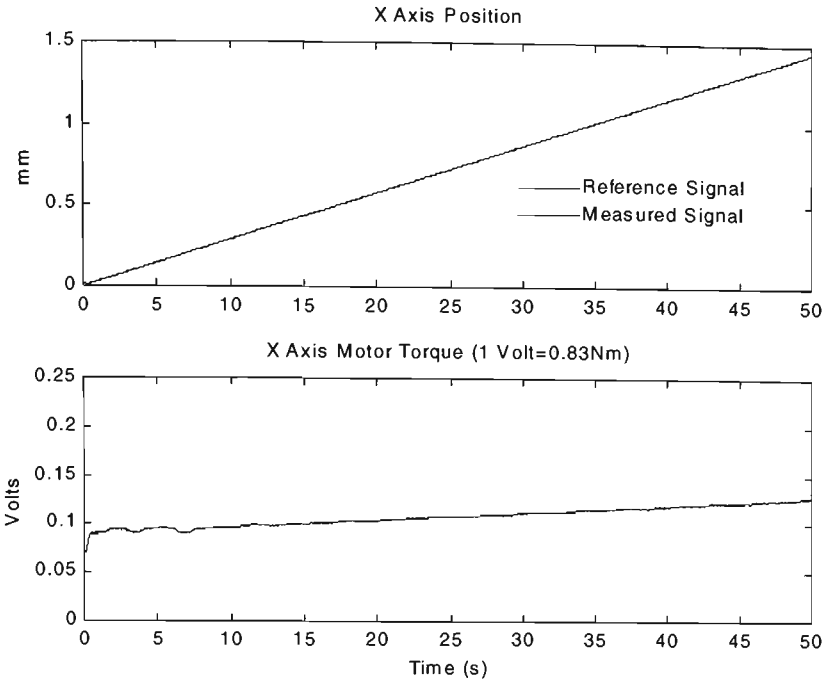

Figure 3.21 Friction Controller Position Tracking Performance (1 Volt =1.1Nm)

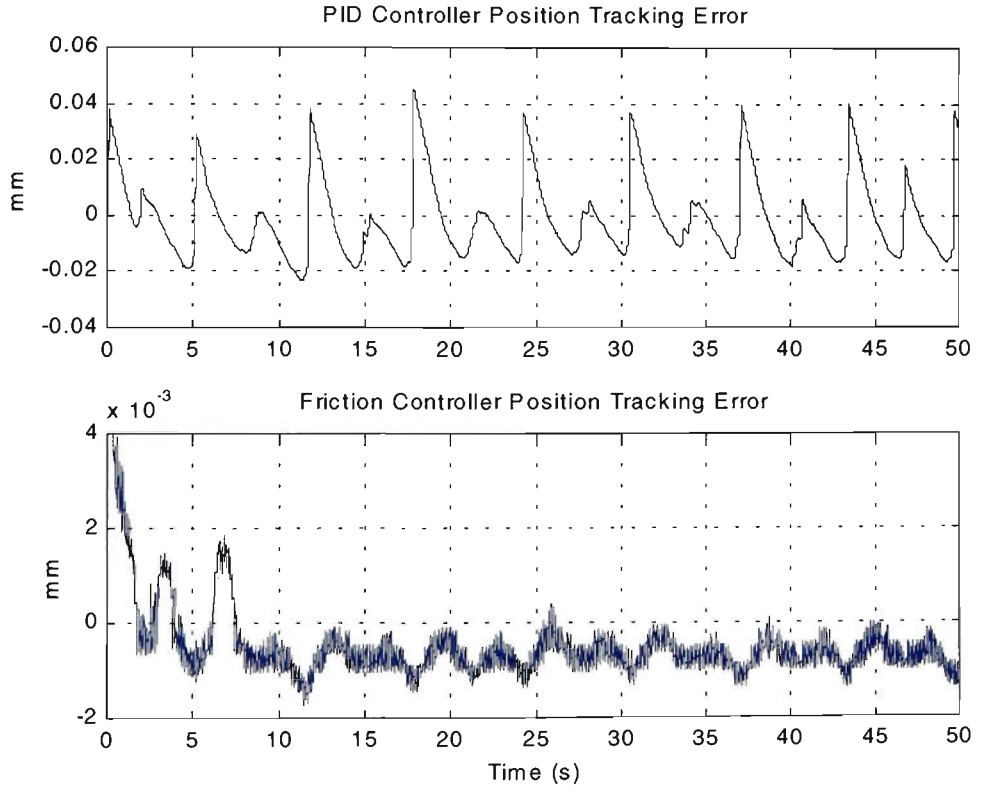

Figure 3.22 Position Tracking Errors (1Volt=1.1Nm).

3.7 Conclusions

Three new friction controllers based on the work by Li et al [2] have been developed and implemented on two different mechanisms. The new controllers showed substantial improvements in position tracking accuracy at low speeds as compared with the

"benchmark" PID controller. It was shown that in systems using PID control when classic stick slip characteristics were observed at low velocities the new friction controllers were successful in removing "stick slip" phenomena

The first stage of adjusting the friction controller is to tune the PID part of the controller. The next stage is to select the correct pulse height. This is easy to achieve since the pulse height only has to be greater than the "worst case" difference of the static and Coulomb friction. Three distinct methods were developed to choose the pulse height. All three methods produce similar improvement in position tracking performance.

In the first method the pulse height is selected manually. An initial estimate of the difference in the static and Coulomb friction can be gained from the stick slip torque characteristics. From this initial estimate the pulse height is adjusted by trial and error. The minimum pulse height which removes the stick slip limit cycling is used. This is a very quick and convenient way of producing a working controller whose performance is shown in Section 3.2

The second method for choosing pulse heights presented here is to use a static friction lookup table. This finds the minimum possible pulse height which always exceeds the static friction value. This has the benefit of reducing the pulse height applied to the mechanism and reduces the stress on the mechanical components. However it requires time consuming experimentation which can be automated, to collect the data for the static friction lookup table. The static friction lookup table and controller performance are given in Section 3.4

The third method was to use a fuzzy logic controller to adjust the pulse height. The velocity is observed to see if the mechanism is sticking and the pulse height is adjusted accordingly. This method has the significant advantage that the pulse height is chosen without user intervention. The user does not need to know any friction characteristic or look at stick slip characteristics to select the pulse height. This method was implemented successfully and the results shown in Section 3.5

It was also shown that the friction controller with velocity reversals compensation substantially improved position error at velocity reversals while maintaining the low speed position tracking performance. The "flat spots" at velocity reversals were substantially reduced. This was demonstrated in experiments using coordinated motion of the A and B axis of the Hirata robot. In plotting circles of 100mm diameter at low velocities the position error was reduced from 2.5mm for a conventional controller to 0.5mm for the friction controller with velocity reversals. This is shown in Section 3.3.

The basic friction controller was also applied to a different mechanism utilizing a linear ballscrew on the grinding machine. It was shown when applied to the X axis of the grinding machine and using low position tracking rates, the friction controller reduced the position error to less than $2\mu m$. This compared with the PID controller position tracking error of $40\mu m$ under the same operating criteria. The position tracking performance of the grinding machine is shown in Section 3.6.

4. POSITION DOMAIN SIGNAL PROCESSING

4.1 Introduction

This chapter presents the concepts and techniques required to model and process position domain signals. These concepts and techniques are used extensively in the force estimation work described in Chapters 5 and 6. The force estimation work requires an accurate system model and part of this includes considering the force components that are position dependent. These components are more easily described and analysed in the position domain. This chapter describes how a discrete time signal can be transformed into a discrete position signal and develops the idea that the discrete position signal can be processed with many of the signal processing techniques used with discrete time signals eg Fast Fourier Transforms (FFTs) and digital filtering.

In this discussion the torque or force required to move a mechanical system is assumed to be made up of the torques/forces required to accelerate the system's mass, overcome the friction and torque/force components that are position dependent. In the rest of the discussion the position dependent torque component will be referred to as Position Dependent Torque Variations (PDTV). In the linear reference frame where a force is applied to the system the position dependent components will be referred to as Position Dependent Force Variations (PDFV).

In Section 4.2 a number of terms are introduced to described PDFV; these include position period and position frequency. In the position domain these are analogous to period and frequency in the time domain.

In Section 4.3 a description of how PDFV are seen in the time domain is developed. A solution for a system moving with a constant velocity is given. The Fourier transforms in both the position and time domain are used to derive this solution. As a further example a system with a constant applied force is also considered. A computer simulation is used to give a numerical solution to the differential equations that describe the system.

In Section 4.4 the process of turning a discrete time signal into a discrete position signal is described. This process is referred to as "position binning" and involves breaking the position axis into a number of intervals or "bins". In order to create a discrete position signal at least one data point must fall within each position "bin". A method to calculate the desirable number of data points per bin is discussed. The position sampling and Nyquist position frequency are also discussed.

The observability of PDFV is discussed in Section 4.5. This is dependent on the magnitude and position frequency of the PDFV, the resolution of the position measurement and the system's frequency response. In Section 4.6 the the position frequency spectrum of the x-axis of the grinding machine is discussed and an explanation of each of the observed PDFV is given.

4.2 Force Torque and Position Frequency Definitions

As discussed in Section 2.3 all the axes of the grinding machine have a mechanical arrangement, which translate the rotational movement of the servomotor into linear motion. For a screw with pitch l the relationship between the motor torque T_{motor} and force F_{motor} and that between angular velocity ω and velocity v are as follows [51]:

$$T_{motor} = \frac{l}{2\pi} F_{motor} \quad \text{or} \quad F_{motor} = \frac{2\pi}{l} T_{motor}$$

$$\omega = \frac{2\pi}{l} v \quad \text{or} \quad v = \frac{l}{2\pi} \omega \qquad \text{Eq 4.1}$$

To describe PDFV a number of terms will be introduced. For a periodic function of position x, its period X will be referred to as position period. Introducing the position frequency Φ' and angular position frequency Ω the relationship between Φ', Ω and X and their analogy in the time domain is given in table 4.1

Table 4.1 Position Dependent Friction Variables

Position Domain			Time Domain		
Description	**Symbol**	**Equation**	**Description**	**Symbol**	**Equation**
Position Period	X		Period	τ	
Position Frequency	Φ'	$\Phi' = 1/X$	Frequency	f	$f = 1/\tau$
Angular Position Frequency	Ω	$\Omega = 2\pi\Phi'$	Angular Frequency	ω	$\omega = 2\pi f$

The position frequency Φ' given in table 4.1 has units of m^{-1}. Another possible unit is Cycles Per Revolution (CPR). A periodic function of position that has *n* cycles per revolution of the shaft or rotor of the motor has a position frequency of *n* CPR. If the position frequency in cycles per revolution (CPR) is Φ then:

$$\Phi' = \frac{\Phi}{l} \quad \text{and} \quad \Omega = \frac{2\pi}{l} \Phi \qquad \text{Eq 4.2}$$

For example a PDFV with a position frequency of 10 (CPR) repeats 10 times per revolution with a screw pitch of 5mm this results in a position period of 0.5mm. A position frequency of 0.5 (CPR) repeats every 2 revolutions and has a position period of 10mm.

4.3 Position Dependent Force Variations in the Time Domain

The PDFV are by definition functions of position. However under certain circumstances they can also be analysed in the time domain. Two cases are analysed, the first is for a

constant velocity and the second is for a constant applied motor torque. In both cases the analysis uses the differential equation describing the mechanical system:

$$F_{motor} = m\frac{d^2x}{dt^2} + f_v\frac{dx}{dt} + f_c + F_{pos}(x) \qquad \text{Eq 4.3}$$

where m is the mass, x is the position, f_c is the Coulomb friction and f_v is the viscous friction. F_{motor} is the equivalent force generated by the motor torque T_{motor} as given by Eq 4.1. $F_{pos}(x)$ is the PDFV and is periodic in x and can be described by the Fourier series as follows:

$$F_{pos} = \frac{a_0}{2} + \sum_{n=1}^{n=\infty} a_n \sin(n\Omega_0 x) + b_n \cos(n\Omega_0 x) = \sum_{n=-\infty}^{n=\infty} c_n e^{jn\Omega_0 x} \qquad \text{Eq 4.4}$$

where Ω_0 is the fundamental angular position frequency. It follows from Eq 4.3 that:

$$F_{motor} = m\frac{d^2x}{dt^2} + f_v\frac{dx}{dt} + f_c + \sum_{n=-\infty}^{n=\infty} c_n e^{jn\Omega_0 x} \qquad \text{Eq 4.5}$$

4.3.1 Constant Velocity Analysis

The simplest case to consider is a system moving with a constant velocity. From basic mechanics the relationship between position x and time t for a system moving with constant velocity V is simply $x = Vt$. This Section seeks to determine if a similar simple relationship exists between position frequency observed in the position domain and frequency observed in the time domain.

Consider a function g(x) and let its Fourier transform be $G(j\Omega)$. These two are related by the Fourier and inverse Fourier transforms:

$$G(j\Omega) = \int_{-\infty}^{\infty} e^{-j\Omega x} g(x)dx$$

$$g(x) = \int_{-\infty}^{\infty} e^{-j\Omega x} G(j\Omega)d\Omega \qquad \text{Eq 4.6}$$

where Ω is angular position frequency and x is position. Let g(x) be a periodic function of x described by a Fourier series:

$$g(x) = \sum_{n=-\infty}^{n=\infty} c_n e^{jn\Omega_0 x} \qquad \text{Eq 4.7}$$

Substituting Eq 4.7 in Eq 4.6:

$$G(j\Omega) = \int_{-\infty}^{\infty} e^{-j\Omega x} \sum_{n=-\infty}^{n=\infty} c_n e^{jn\Omega_0 x} dx = \sum_{n=-\infty}^{n=\infty} c_n \int_{-\infty}^{\infty} e^{-j\Omega x} e^{-jn\Omega_0 x} dx \qquad \text{Eq 4.8}$$

Using standard Fourier transform pairs the position frequency function $G(j\Omega)$ can be expressed as:

$$G(j\Omega) = 2\pi \sum_{n=-\infty}^{n=\infty} c_n \delta(\Omega - n\Omega_0) \qquad \text{Eq 4.9}$$

Where δ is the unit impulse. As expected the Fourier transform of a Fourier series will produce a position frequency spectrum, which is a series of spectral lines at each position frequency $n\Omega_0$.

For velocity $v(t)$ the position $x(t)$ is given by $x(t) = \int v(t)dt$ and if $v(t)$ is a constant V then $x = \int v(t)dt = Vt$. Eq 4.7 expressed as function of time t is:

$$g(Vt) = h(t) = \sum_{n=-\infty}^{n=\infty} c_n e^{jn\Omega Vt} \qquad \text{Eq 4.10}$$

A function in time $h(t)$ can be transformed to a function in the frequency domain $H(j\omega)$ using the Fourier transform:

$$H(j\omega) = \int_{-\infty}^{\infty} e^{-j\omega t} h(t)dt \qquad \text{Eq 4.11}$$

combining Eq 4.11 and Eq 4.10:

$$H(j\omega) = \int_{-\infty}^{\infty} e^{-j\omega t} \sum_{n=-\infty}^{n=\infty} c_n e^{jn\Omega_0 Vt} dt = \sum_{n=-\infty}^{n=\infty} c_n \int_{-\infty}^{\infty} e^{-j\omega t} e^{jn\Omega_0 Vt} dt \qquad \text{Eq 4.12}$$

and using standard Fourier transform pairs $H(j\omega)$ is given by:

$$H(j\omega) = 2\pi \sum_{n=-\infty}^{n=\infty} c_n \delta(\omega - n\Omega_0 V) \qquad \text{Eq 4.13}$$

Comparing Eq 4.13 with Eq 4.9 an angular position frequency of $n\Omega$ will be seen in the frequency domain with frequency $n\Omega V$ whose magnitude c_n is unchanged. The position frequency spectrum multiplied by velocity V will give the time frequency spectrum. This is shown graphically in figure 4.1.

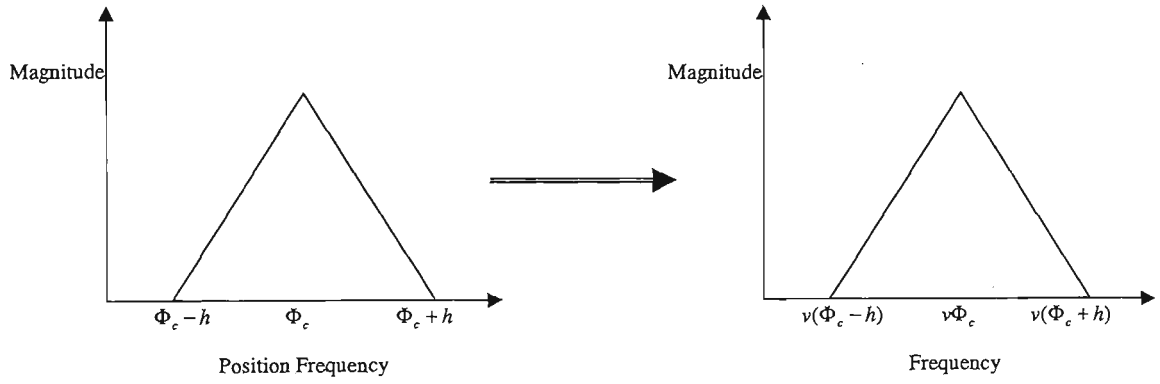

Fig 4.1 Position Frequency to Frequency Transforms

Useful equations relating the time frequency f, velocity v, screw pitch l and position frequency Φ are:

$$\Phi' = \frac{f}{v} \qquad f = v\Phi' \qquad f = \frac{v\Phi}{l} \qquad \Phi = \frac{lf}{v} \qquad \text{Eq 4.14}$$

Having solved this problem for a general function $g(x)$ consider the servo system described by Eq 4.5 when the velocity is a constant V so that $\frac{dx}{dt} = V$ and $\frac{d^2x}{dt} = 0$. Eq 4.5 then becomes:

$$F_{motor} = f_v V + f_c + \frac{a_0}{2} + \sum_{n=1}^{n=\infty} a_n \sin(n\Omega_0 x) + b_n \cos(n\Omega_0 x) \qquad \text{Eq 4.15}$$

Grouping all the constant terms together and letting:

$$\frac{a_0'}{2} = f_v V + f_c + \frac{a_0}{2} \qquad \text{Eq 4.16}$$

Consequently Eq 4.15 reduces to:

$$F_{motor} = \frac{a_0'}{2} + \sum_{n=1}^{n=\infty} a_n \sin(n\Omega_0 x) + b_n \cos(n\Omega_0 x) = \sum_{n=-\infty}^{n=\infty} c_n' e^{jn\Omega_0 x} \qquad \text{Eq 4.17}$$

The expression for the motor force F_{motor} is a function of position and is in the same form as the function g(x) given in Eq 4.7 so similarly the position frequency spectrum for the motor force is:

$$F_{motor} = 2\pi \sum_{n=-\infty}^{n=\infty} c_n \delta(\Omega - n\Omega_0) \qquad \text{Eq 4.18}$$

and its time frequency spectrum is therefore:

$$F_{motor} = 2\pi \sum_{n=-\infty}^{n=\infty} c_n \delta(\omega - n\Omega_0 V) \qquad \text{Eq 4.19}$$

Hence, for the mechanical system moving with constant velocity the PDFV will have the same magnitude in the time domain and the frequency will be the position frequency multiplied by the velocity.

4.3.2 Constant Force Analysis

As another example showing how PDFV are seen in the time domain the servo system's behaviour is analysed for a constant motor force. In this example the system is operating in open loop so the velocity is not controlled or constant. A Simulink model is used to give a numeric solution to the differential equation describing the system. Also as part of the model there is only one PDFV with one position frequency. This was done primarily to make the results of the simulation easier to analyse and interpret. The simulation gives a specific solution for one PDFV component and although not detailed in this section running the simulation with PDFV components of different position frequencies gave solutions consistent with those given in this section.

The differential equation used to describe the system Eq 4.5 in a rearranged form is:

$$\frac{d^2x}{dt^2} = \frac{1}{m}\left\{F_{motor} - f_v \frac{dx}{dt} - f_c + \sum_{n=-\infty}^{n=\infty} c_n e^{jn\Omega_0 x}\right\} \qquad \text{Eq 4.20}$$

The PDFV $F_{pos}(x)$ is made up of only one position frequency such that:

$$F_{pos}(x) = a \sin n\Omega_0 x \qquad \text{Eq 4.21}$$

The PDFV is translated into the time domain using an observer whose output is $F_{posit}(t)$ such that:

$$F_{posit}(t) = F_{motor} - f_c - m\frac{d^2x}{dt^2} - f_v\frac{dx}{dt} \qquad \text{Eq 4.22}$$

Combining Eq 4.20, 4.21 & 4.22 results in the Simulink model shown in figure 4.2.

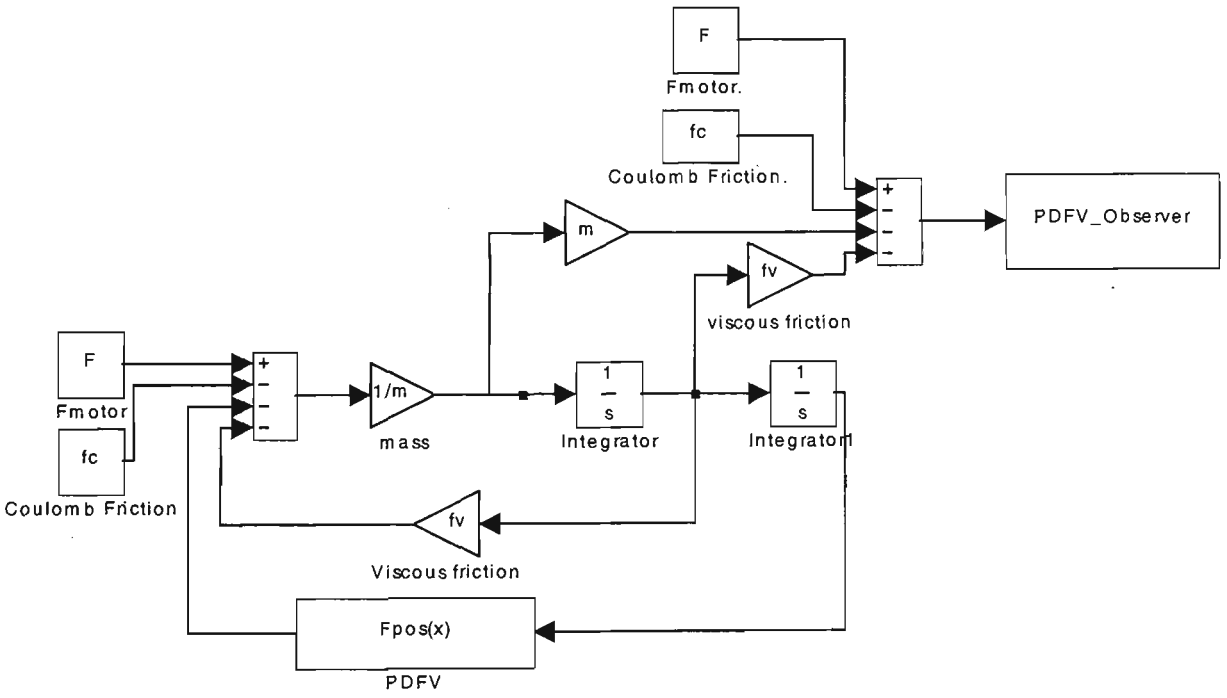

Fig 4.2 Simulink model with friction observer

The parameters used in the model shown in figure 4.2 are those of the X-axis of the grinding machine whose mass, viscous and Coulomb friction values are given in Section 2.3.1. The Force applied by the motor F_{motor} was selected to give a mean steady state velocity of approximately 10mm/s. A PDFV with a position frequency of 1(CPR) was used. The magnitude of the PDFV was selected so that it caused a variation in the velocity of 1mm/s or 10 % of the steady state velocity. The velocity and PDFV observer output are shown in figure 4.3.

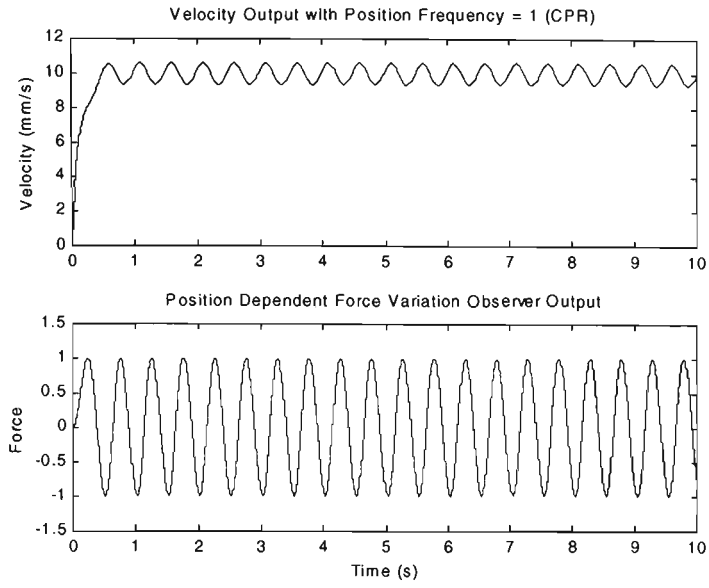

Figure 4.3 Velocity and PDFV Observer Output

The output of the PDFV observer is expressed in normalised force units. A value of 1 represents the same magnitude force value as the magnitude of the PDFV used in the model. The same convention is also used in figure 4.4.

The friction observer output is a function in time. A Fourier transform applied to this signal produces a frequency spectrum. The whole process using a PDFV with the same position frequency and magnitude was repeated for a number of other different velocities i.e. 5,50,100 mm/s. The frequency spectrums produced were placed together and are shown in figure 4.4.

As the mean steady state velocity of the system is changed so does the frequency at which the PDFV of 1CPR appears in the frequency spectrum. For velocities of 5,10,50,100mm/s the PDFV of 1CPR produces a peak in the frequency spectrum centred at frequencies of 1,2,10,20 Hz respectively. This is a similar result to that derived in Section 4.2.1 and the relationship between the PDFV's position frequency and the centre frequency of the observed frequency spike can be also described by Eq 4.14.

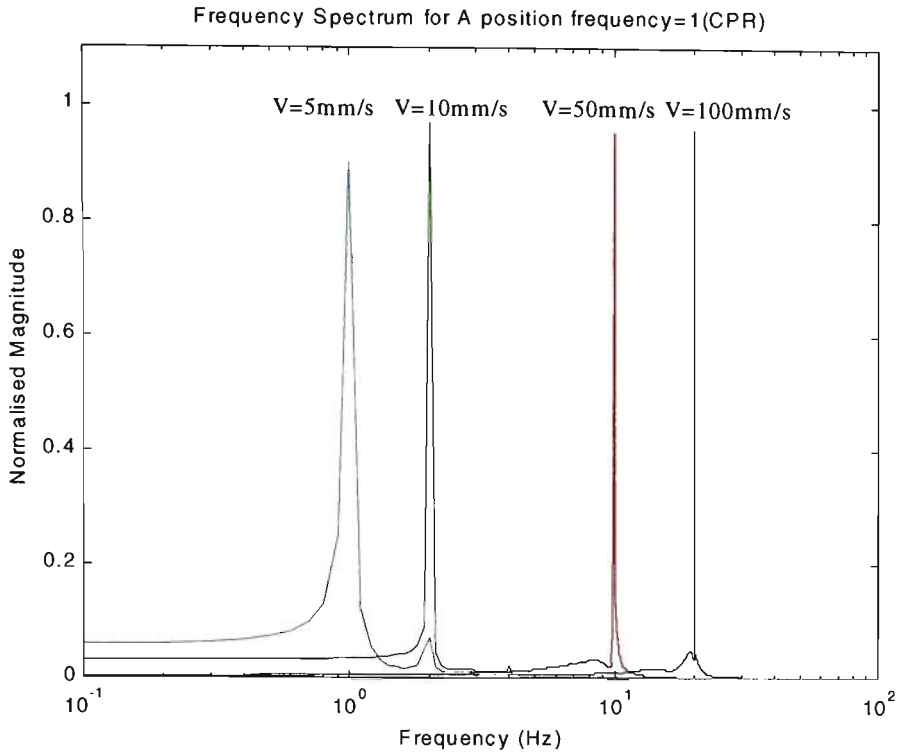

Figure 4.4 Constant Torque Frequency Spectrum

Each PDFV frequency spectral component is spread about the centre frequency and there is an attenuation of the centre frequency of up to 10%. This may be due to the variation in velocity. As the velocity changes the frequency at which the PDFV appears in the frequency spectrum changes. As can be seen in figure 4.3 the velocity oscillates about the mean velocity and consequently a spread in the frequency spectrum is observed when the PDFV's position frequency and magnitude is kept constant across the different velocities. As a consequence the resultant variation in velocity will be a greater fraction of the mean velocity at lower velocities. As can be seen in figure 4.4 the spread of the spectrum and attenuation of the signal is greatest at lower velocities.

The results of this section are consistent with those derived in Section 4.2.1 in that a position frequency multiplied by the system's velocity will give the frequency in the time domain. This is an important result that is used in this chapter to calculate the observability of PDFV. It is used in Chapters 5 and 6 to select the correct sampling rates in both position and time and to select digital filter parameters.

4.3.3 Position Frequencies and Frequencies

In Section 4.3.1 the relationship between position frequencies in the position domain and frequencies in the time domain is derived and described by Eq 4.14. In this section an example illustrating this relationship is given. Consider a PDTV with a position frequency of 1 CPR and which remains constant throughout these examples. Consider also a system with a screw pitch of 1m and moving initially with a velocity of 1m/s. The PDTV is plotted against position and shown in the top left hand plot of figure 4.5. The PDTV has a position period of 1m and a position frequency of 1CPR. In the time domain the PDTV has a period of 1s and a frequency of 1Hz. This is shown in the plots on the right hand side of figure 4.5.

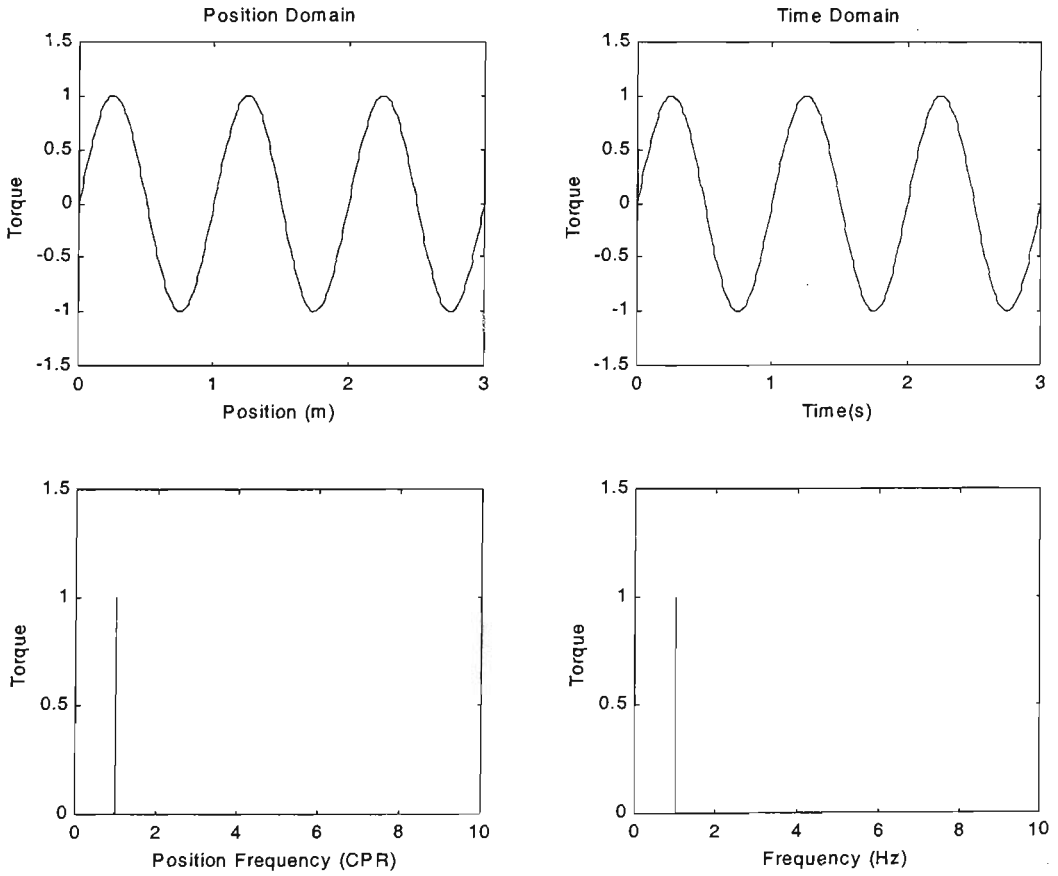

Figure 4.5 Position and Time Domain Signals for V=1m/s

Consider now the system moving with a velocity of 5m/s whose position and time domain signals are shown in figure 4.6. The PDTV component is unchanged and still has a position frequency of 1CPR. However in the time domain the signal now has a

period of 0.2s and a frequency of 5Hz. Normally the PDTV have a constant position frequency which is typically set by some mechanical arrangement of the system. In the time domain however the PDTV will be seen at higher frequencies as the velocity increases.

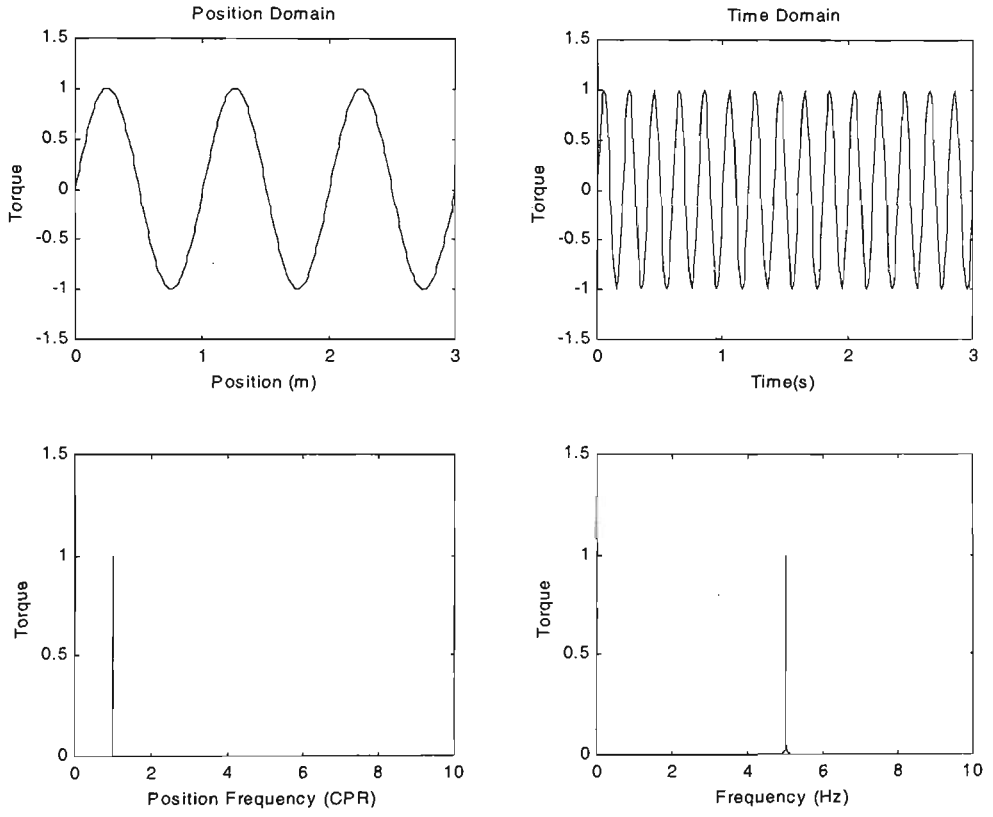

Figure 4.6 Position and Time Domain Signals for V=5m/s

4.4 Position Binning, Bin Size and FFT

By definition PDFV are functions of position. In order to analyse these in computer controlled machinery it is necessary to have a discrete position signal. The process of turning a discrete time signal into a discrete position signal is referred to as "position binning". Once the PDFV are described as a discrete position signal then a FFT can be applied to calculate the position frequency spectrum.

The DSP system controlling the mechatronic system records the position and torque data at set time intervals determined by the DSP's sampling rate. The position and

torque values recorded at the same time are grouped together. If the velocity is not perfectly constant then the torque values will not be recorded at equally spaced positions. To get around this the position axis is divided up into a number of position intervals referred to from now on as "position bins" or simply "bins". The width of these bins is referred to as the bin size.

The bin size is analogous to the sampling period in the time domain. The bin size determines the position frequency sampling rate and the Nyquist position frequency (i.e. half the position sampling rate). The relationship between bin size, position frequency sampling rate Φ_s and Nyquist position frequency Φ_{Nq} both measured in CPR are:

$$\Phi_s = \frac{l}{bin\_size} \qquad \Phi_{Nq} = 0.5\frac{l}{bin\_size} \qquad \text{Eq 4.23}$$

The screw pitch l and the bin size must have the same units, typically millimetres. The Nyquist position frequency should be above the PDFV's highest frequency. The PDFV's position frequency spectrum is calculated by using a FFT. As the highest frequency component is unlikely to be known before the FFT is calculated it is not uncommon to "over sample" the data and use a smaller bin size and record more data points than is absolutely necessary. After the initial measurements and the identification of PDTV frequencies subsequent measurements of the PDTVs normally takes considerably less time.

For the torque to be a function of the discrete position signal there must be at least one torque value falling within each bin. If more than one torque values falls in one bin these values are averaged to give a single torque value for that bin. One method to increase the number of data points recorded and reduce the chance of there being

"empty bins" is to run the mechanism back and forward over the same travel a number times. This approach for "filling the bins" is only applicable to analysing data offline after all the passes have been made. It cannot not be used in real time processing of PDTVs discussed in Chapter 6 because only one pass is available. It is however a useful approach to collect data to be able to calculate the PDTV position frequency spectrum using an FFT. The number of data points per bin is dependent on the bin size, the sampling frequency f_s (time domain) the mechanism's velocity V and the number of passes. If V is constant the number of data points per bin is given by:

$$\text{data points per bin} = \frac{\text{no of passes} \times \text{bin size} \times f_s}{V} \qquad \text{Eq 4.24}$$

Using Eq 4.24 it is possible to determine the parameters to give only one data point per bin (the minimum required). However due to variations in velocity, the spacing of bins, and uncertainties in how different passes overlap there is a fair chance that there may be several data points in some bins and none in others. To allow for a margin of error Eq 4.24 is solved to give a minimum of three data points per bin to give a satisfactory description of the mechanism used here.

In calculating the discrete position FFT the length of travel x_0 over which data is collected determines the fundamental position frequency Φ_0 and for a screw pitch l:

$$\Phi_0 = \frac{l}{x_0} \qquad \text{Eq 4.25}$$

The position frequency spectrum is made up of harmonics that are integer multiples of the fundamental Φ_0. The discrete FFT does not produce a continuous spectrum and sometimes this leads to a position frequency component (which is not an integer multiple of the fundamental) being spread across adjacent position frequencies (which

are integer multiples of the fundamental). This is often referred to as the "picket fence effect". In order to reduce the picket fence effect it is advantageous to choose a travel length x_0 that is an integer multiple of the screw pitch. In this way integer position frequencies i.e. 1CPR, 2CPR will fall on a spectral components that are an integer multiple of the fundamental. Eg choosing a travel length of $x_0 = 100\text{mm}$ and for a screw pitch $l = 5\text{mm}$ using Eq 4.25 the fundamental position frequency Φ_0=0.05CPR. The 20^{th} harmonic will have a position frequency of 1CPR and the 40^{th} harmonic will have a position frequency of 2CPR and so on.

The processing of PDFV as discrete position signals requires consideration of the bin size, position sampling rates, Nyquist sampling rates and fundamental position period. The bin size determines the position sampling frequency. The position sampling rate should be chosen so that the Nyquist position frequency is above the PDFV highest position frequency. The fundamental position period should be chosen so that it is an integral multiple of the screw pitch. These results are fundamental for dealing with position domain signals. As Chapters 5 and 6 rely on servo system data in the position domain to estimate forces these results are also fundamental to this work.

4.5 System's Frequency Response and Observable PDFV

The PDFV position spectrum is calculated from the position and torque data recorded from the mechatronic system. As the PDFV's position frequency increases and the system's velocity increases then so does the frequency at which the PDFV appears in the time domain. The mechatronic system has a frequency response that decreases with frequency. Hence the system's response to the PDFV will decrease as the system's

velocity increases and the position frequency of the PDFV increases. In this section this attenuation is calculated and the limits of observability of PDFV determined.

The PDFV as seen in time are given by the time signal $F_{posit}(t)$ and can be calculated using Eq 4.22. The acceleration and velocity values used in Eq 4.22 to calculate $F_{posit}(t)$ are all obtained from the position values, which are measured via the shaft encoder. There are at least two experimental approaches that could be taken to get data to calculate $F_{posit}(t)$. The first is to apply a constant motor force F_{motor} and observe the change in velocity and acceleration (calculated from the position encoder data). The second approach is to change F_{motor} so the velocity stays constant. This can only be achieved with an ideal velocity control loop and in any practical experiment there will be some change in velocity with whichever control loop is used. Whichever method is used and independent of how accurate the control loop is Eq 4.22 is still used to calculate $F_{posit}(t)$. Rearranging Eq 4.22 slightly the system can be described by the differential equation:

$$F_{motor} - f_c - F_{posit}(t) = m\frac{d^2x}{dt^2} + f_v\frac{dx}{dt} \qquad \text{Eq 4.26}$$

In block diagram form this differential equation can be drawn as shown in figure 4.7

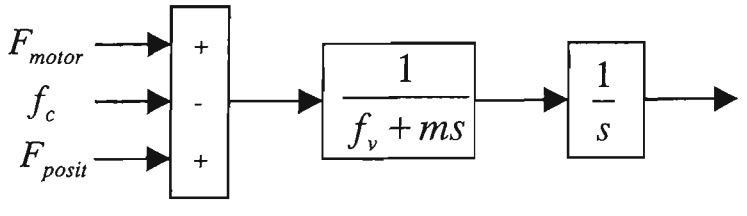

Figure 4.7 Block Diagram for position response

Consider the case where the motor force and the Coulomb friction are constant and the PDFV ignored. The system will have velocity and position in the steady state:

$$v = \frac{F_{motor} - f_c}{f_v} \qquad x = \frac{F_{motor} - f_c}{f_v} t \qquad \text{Eq 4.27}$$

For a linear system the response is this plus the response due to the signal $F_{posit}(t)$. If the signal $F_{posit}(t)$ is a sine function with frequency f and angular frequency $\omega = 2\pi f$, magnitude a_{pos} and phase ϕ such that $F_{poits}(t) = a_{pos}\sin(\omega t + \phi)$ the position response $X(j\omega)$ is given by:

$$X(j\omega) = \frac{a_{pos} e^{j\phi}}{j\omega(j\omega m + f_v)} \qquad \text{Eq 4.28}$$

If the frequency is much greater than the mechanical systems break frequency $\frac{f_v}{m}$=7.3rad/s =1.2Hz (as given in Section 2.3.1) then the magnitude of the position system can be approximated by:

$$|X(j\omega)| = \frac{a_{pos}}{\omega^2 m} = \frac{a_{pos}}{4\pi^2 f^2 m} \qquad \text{Eq 4.29}$$

If the signal $F_{posit}(t)$ is the time signal resulting from a PDFV with position frequency Φ and the velocity is approximately constant then the relationship with the time signals frequency f can be given by Eq 4.14 and substituted in Eq 4.29

$$|X(j\omega)| = \frac{a_{pos} l^2}{4\pi^2 v^2 \Phi^2 m} \qquad \text{Eq 4.30}$$

Clearly as the velocity increases and/or the position frequency of the PDFV increase the position response of the system decreases. Assuming the position response has to be greater than 1 decoder count ($3.05\text{x}10^{-7}$m) the maximum allowable velocity can be calculated for each position dependent frequency. In Section 4.5 the experimentally determined frequency spectrum of PDFV for the x-axis of the grinding machine is given and the magnitude and frequency of the largest PDFV are listed in table 4.2. From these

values and using equation Eq 4.30 the maximum allowable velocity can be calculated and these are also listed in table 4.2.

Table 4.2 Maximum Allowable Velocity for Measuring PDFV

Position Frequency (CPR)	**Magnitude (Volts)**	**Maximum Velocity (mm/s)**
1	0.028	241
2	0.034	133
27	0.014	6.3
54	0.035	5.0

Clearly the lower the velocity the higher the position frequency component that can be observed. In taking measurements to characterise the PDFV spectrum the most reliable result that minimises the chance of position frequencies not being observed is to use the lowest velocity possible. Typically a velocity control loop will allow a lower velocity than an open loop system.

As discussed in Chapter 3 in many mechanical systems the non-linear friction characteristic and associated stick slip behaviour determine the minimum sustainable velocity achievable. The friction models used in the force estimation work have only considered viscous and Coulomb friction and have not included static friction or the non linear Stribeck region. Therefore the mechanism should not operate in this region as the model and the results derived will not be reliable. For a system running under velocity control this is easily determined by looking at the velocity signal. If the velocity goes to zero (i.e. sticks) over the mechanism's travel a higher minimum velocity is needed. The optimum method to characterise the PDFV position frequency spectrum is to use a velocity control loop and run it at the minimum sustainable constant velocity.

4.6 Experimental Results

Measurements were conducted on the x-axis of the grinding machine to collect data to calculate the PDFV position spectrum. The lowest velocity achievable without stick slip

occurring using a PID control loop was 2mm/s. The sampling frequency was 500Hz and a bin size of 50 encoder counts ($15.3x10^{-6}$m) was used. The mechanism was moved back and forth over the same travel 5 times. Using Eq 4.24 this gives 19 data points per bin. A position sampling frequency of 328 CPR and a Nyquist position frequency of 164 CPR was used. The motor force is recorded and with mass, viscous and Coulomb friction known, the PDFV in the time domain can be calculated from Eq 4.22. This discrete time signal is then turned into a discrete position signal. A FFT is applied to the discrete position signal and the result gives the position frequency spectrum of the PDFVs. The spectrum is shown in figure 4.8. The three plots shown in figure 4.8 are of the same spectrum with expanded position frequency axes.

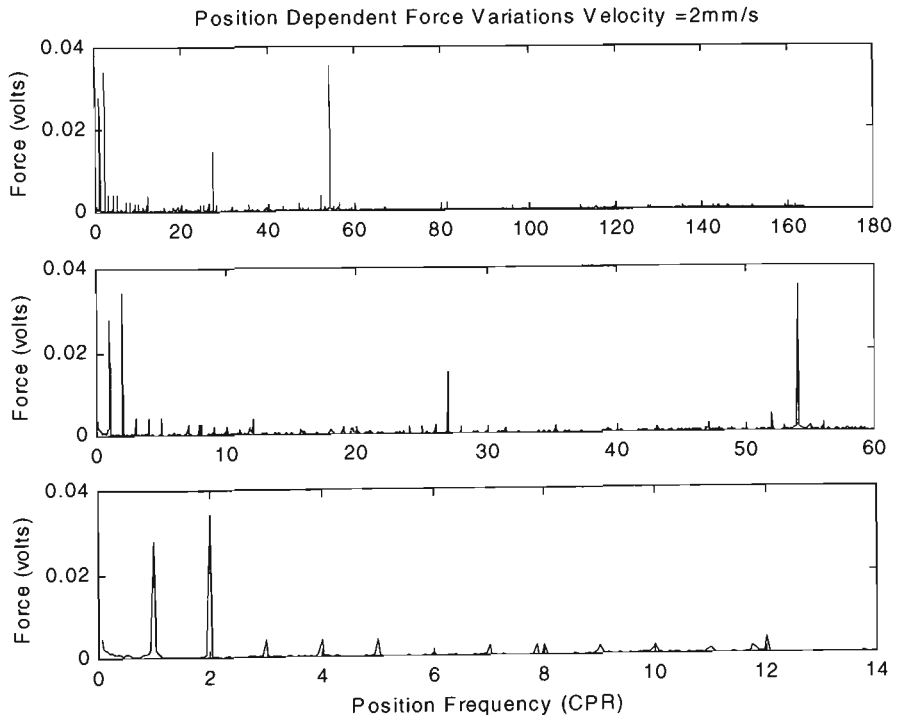

Figure 4.8 PDFV Position Frequency Spectrum (1 Volt =1382N)

The servomotor has 27 stator teeth and the large PDFVs with position frequencies of 27 and 54 CPR are related to this. The servomotor has four rotor poles and this explains the harmonics at 2 CPR. There is also a large PDFV at 1 CPR related to small mechanical inaccuracies such as misalignment of the ball screw and the motor.

A series of other measurements were made for velocities of 2,3,4,5mm/s and these are shown in figure 4.9.

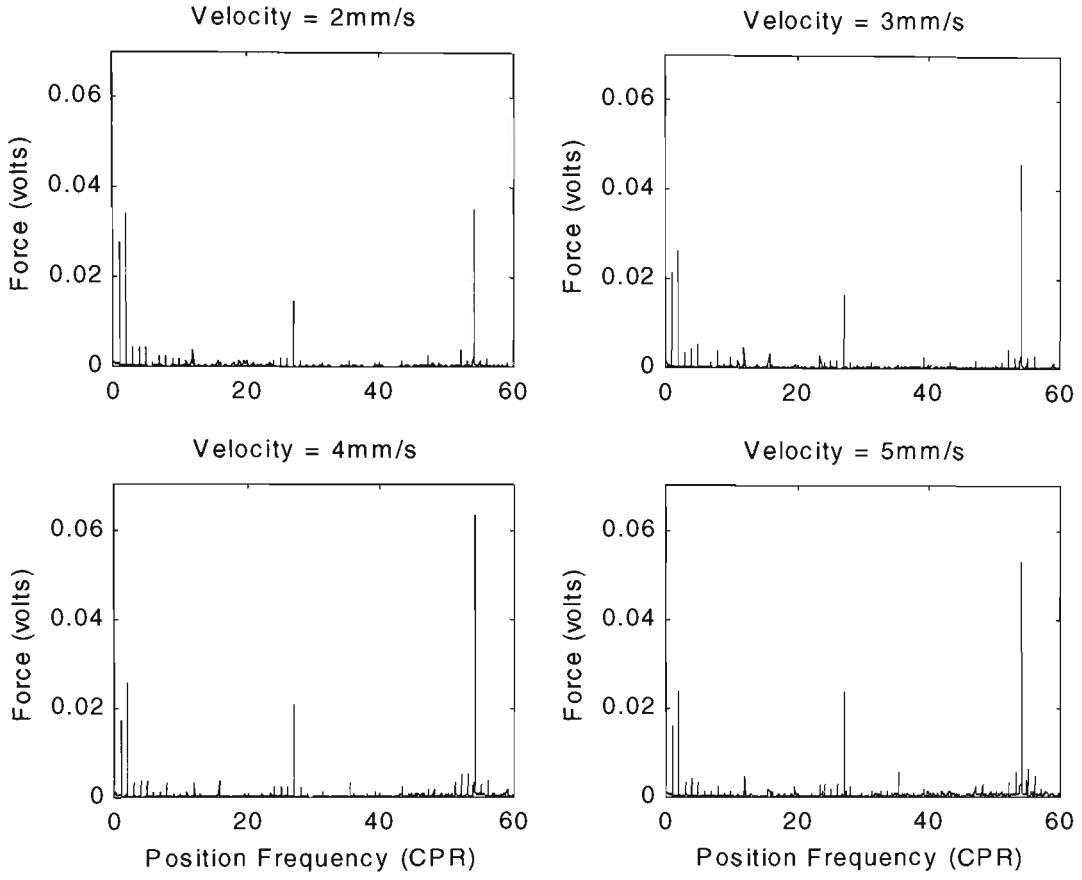

Figure 4.9 PDFV Position Frequency Spectrum at Different Velocities (1 Volt =1382N)

The PDFV spectrum does not shift with different velocities. This suggests that the methodology proposed is accurately finding position rather than time dependent variations. If the original force signal had a variation with a constant time frequency then it would be seen in the position frequency spectrum at different position frequencies as the velocity changes.

As can also be seen from figure 4.9 there is a variation of up to 50% in the magnitude of spectral components at a given frequency. It is shown in Chapter 6 that PDFVs can be used to calculate grinding forces and the variation in magnitude of the PDFVs is not of importance. However the precise position frequencies are important and as can be seen the position frequencies at which the PDFV occur are highly repeatable.

4.7 Conclusions

In this chapter the terms and concepts necessary to process a position domain signals have been given. Position Dependent Force Variations (PDFV), Position Dependent Torque Variations (PDTV), bin size, position bins, position period, position frequency and its units of measure Cycles per Revolution (CPR) have all been introduced.

Position binning which is the process of turning a discrete time signal into a discrete position signal has been defined. A discrete position signal cannot exist unless there is at least one data point in each position bin. The methods for choosing bin size and techniques for estimating the number of data points per bin are given. The bin size sets the position sampling rate and the Nyquist position frequency. The Nyquist position frequency should be chosen so that it is above the highest position frequency in the PDFV spectrum.

At constant velocity the position frequencies of the PDFV will be seen in the time domain with the same magnitude and with a time frequency that is the position frequency multiplied by the system's velocity.

Taking a FFT of a discrete position signal can be used to produce a position frequency spectrum of the PDFV and this in turn can be used to characterise the mechanism. When calculating the FFT it is best to choose a fundamental position period that is an integer multiple of the screw pitch to avoid position frequency components being spread across adjacent position frequencies (i.e. the picket fence effect.). When collecting data to characterise the mechanism the servo system should be operating under velocity

control and moving at the minimum sustainable non-zero velocity. This will give the maximum range of position frequencies in the position frequency spectrum.

The X-axis of the grinding machine was characterised and the PDFV components measured. It was shown that every PDFV component could be attributed to a mechanical cause such as stator slots, rotor poles and mechanical misalignments. The PDFV's position frequencies were highly repeatable and did not change with velocity. This is as expected from the theoretical analyses.

5 FORCE ESTIMATION

5.1 Introduction

A major objective of this thesis is to use servo motor position and current data to estimate external forces applied to a mechatronic system. A motivation for this work was to estimate grinding forces and the majority of the development work was undertaken on the grinding machine. Consequently the majority of the results given in this chapter are for the grinding machine. For completeness and to show the force estimation techniques are not limited to one mechatronic system the force estimation techniques were also applied to the Hirata robot.

As part of the grinding process, forces are applied to the work piece by the grinding wheel. Useful information about the grinding process and work piece condition can be gained by measuring these grinding forces. It is desirable in a production machine to derive force signals from servo motor current and position data rather than additional force sensors. However in the experimental work discussed here, to validate the grinding forces calculated from servo motor data, normal and tangential forces have been measured using force sensors. In addition tangential grinding forces were obtained from spindle motor power measurements.

In Section 5.2 the force estimation procedure is described. The force estimation techniques use an accurate model of the mechanical system including its mass, friction and PDFV. The friction model includes viscous and coulomb friction components. The PDFV components are divided into low and high frequency components. The low frequency PDFV components are included in the system model and the high frequency PDFV components are removed as part of the signal processing. The force estimation

signal is generated by subtracting from the motor torque the acceleration, friction and the low frequency PDFV torque components.

The force estimation signal is first processed in the time domain with a low pass filter. The characteristics of this filter are discussed in Section 5.2. The filtered force estimation signal is then turned into a discrete position signal and processed in the position domain. The interrelationship between time domain and position domain sampling rates, system velocity and PDFV spectrum are also discussed. Also in Section 5.2 the results from a series of experiments with a known force, applied via a spring, are given. The force estimation signal is compared to the known force and the noise on the force estimation signal is quantified.

In Section 5.3 a discussion of noise sources that affect the force estimation signal is given. As part of this discussion a computer simulation of the system was made. The simulation includes the PID controller, the system's mass, coulomb and viscous friction, decoder resolution and PDFV. The same signal processing is applied to the computer simulation's outputs as the force estimation signal in Section 5.2 and the resultant noise is discussed. The magnitude of the noise from decoder quantisation is also calculated.

In Section 5.4 the force estimation techniques are used to measure grinding forces. A series of grinding experiments using different depths of cut and feedrates are given. The force estimation results are compared to the grinding forces measured from spindle motor power calculations and force sensor measurements.

In Section 5.5 force estimation techniques are applied to the Hirata robot. A known spring force is applied to the Hirata robot's end effector. The force estimation experiments were for coordinated motion of the A and B axes of the Hirata Robot. The external force causes torques that the A and B axes servo motor have to overcome. The magnitudes of these torques are dependent on the position of the end effector and the direction and magnitude of the applied force. The A axis inertia is dependent on the angle of the B axis joint. Apart from this the A and B axes are assumed to be independent of each other. The same force estimation procedure as used on the X axis of the grinding machine was used individually on the A and B axes of the Hirata Robot.

5.2 Force Estimation Procedure

The force estimation procedures use servo motor position and current data to calculate a force applied to the system. In the initial experiments the force was applied by stretching a spring. The force increases linearly with the extension of the spring as shown in figure 5.1.

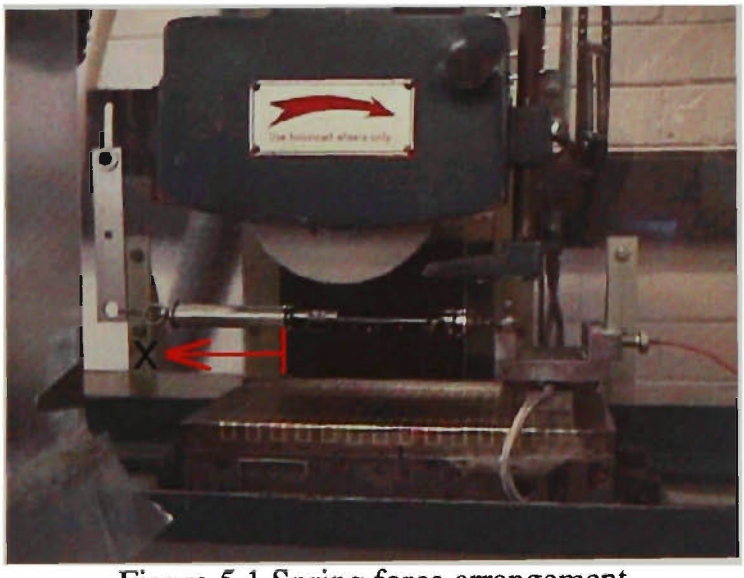

Figure 5.1 Spring force arrangement

The magnitude of the force applied by the spring can be easily controlled and calculated from the displacement in the x direction. The force estimated from the X axis servo motor position and torque data can be compared to the known spring force and the

accuracy of the force estimation procedure can be determined. The same signal processing techniques used with the spring force are then used with the grinding force. The grinding force results are given in Section 5.4.

5.2.1 System Model

The differential equation describing the system with mass m, viscous friction f_v, coulomb friction f_c, PDFV $F_{pos}(x)$ and grinding force F_G is given by:

$$F_{motor} = m\frac{d^2x}{dt^2} + f_v\frac{dx}{dt} + f_c + F_{pos}(x) + F_G \qquad \text{Eq 5.1}$$

Hence the force F_G is given by:

$$F_G = F_{motor} - m\frac{d^2x}{dt^2} - f_v\frac{dx}{dt} - f_c - F_{pos}(x) \qquad \text{Eq 5.2}$$

The PDFV components can be broken up into high and low position frequency components and using Eq 4.4 can be written as:

$$F_{pos} = \sum_{n=-\infty}^{n=\infty} c_n e^{jn\Omega_0 x} = \sum_{n=-n_{LP}}^{n=n_{LP}} c_n e^{jn\Omega_0 x} + \sum_{n=-\infty}^{n=-n_{LP}-1} c_n e^{jn\Omega_0 x} + \sum_{n=n_{LP}+1}^{n=\infty} c_n e^{jn\Omega_0 x} \qquad \text{Eq 5.3}$$

The last two summations on the right hand side of Eq 5.3 describe the high position frequency components and the first summation describes the low position frequency components. The term n_{LP} is given by:

$$n_{LP} = \frac{\Omega_{LP}}{\Omega_0} = \frac{2\pi\Phi_{LP}}{2\pi\Phi_0} = \frac{\Phi_{LP}}{\Phi_0} \qquad \text{Eq 5.4}$$

where Φ_{LP} is the cutoff position frequency between low and high position frequencies. Φ_0 is the fundamental position frequency, Ω_0, Ω_{LP} are the fundamental and cutoff angular position frequencies respectively.

The PDFV position frequency spectrum has been characterised in Section 4.6. Let the position frequencies below 1CPR be referred to as the low position frequency

components and those above be referred to as the high position frequency components. Only the low frequency PDFV with position frequencies below 1 CPR have been included in the system model because there are no significant frequencies less than 1CPR for this mechanism. This means the major position frequency components at 1,2,4,12,27,54 CPR are not explicitly included in the $F_{pos}(x)$ term in Eq 5.2 as they can easily removed by filtering. As discussed in Section 4.6 there are significant variations in the magnitudes of the high position frequency PDFV at different velocities which are not easily modelled. However there are no variations in their position frequencies and so the approach taken in Section 5.2.4 is to apply position frequency filters at the main PDFV frequencies. This approach removes the need for a separate PDFV model at each velocity and it also makes the force estimation more robust to changes in the PDFV. The PDFV magnitudes do change with velocity and change over time as mechanical components wear. They may also change after maintenance, due to realignments of shafts, changes in bearing preloads and so on. However the position frequencies at which PDFV occur are highly repeatable and do not change with velocity or over time. Using this approach the position frequency spectrum only needs to be characterised once and only at one velocity.

Using Eq 5.2 and Eq 5.3 and only including the low frequency position frequency components the expression for the force F_G, is:

$$F_G = F_{motor} - m\frac{d^2x}{dt^2} - f_v\frac{dx}{dt} - f_c - \sum_{n=-n_{LP}}^{n=n_{LP}} c_n e^{jn\Omega_0 x} \qquad \text{Eq 5.5}$$

The parameters included in Eq 5.5 may also change over time. However these values can be recalculated quickly and easily. The mass, viscous and coulomb friction can be

recalculated using the method described in Section 2.3.1. The low frequency PDFV component can also be readily calculated as will be demonstrated below.

A model of the low position frequency PDFV is produced by running the mechanism over its travel at a constant velocity and recording the motor force signal. This is repeated for a number of different velocities. The discrete force signal is turned into a discrete position signal and is then filtered to remove all position frequencies 1CPR and above. A low pass position filter with a low pass cutoff position frequency of 0.8CPR was used. The resultant force signals for a number of different velocities are shown in figure 5.2.

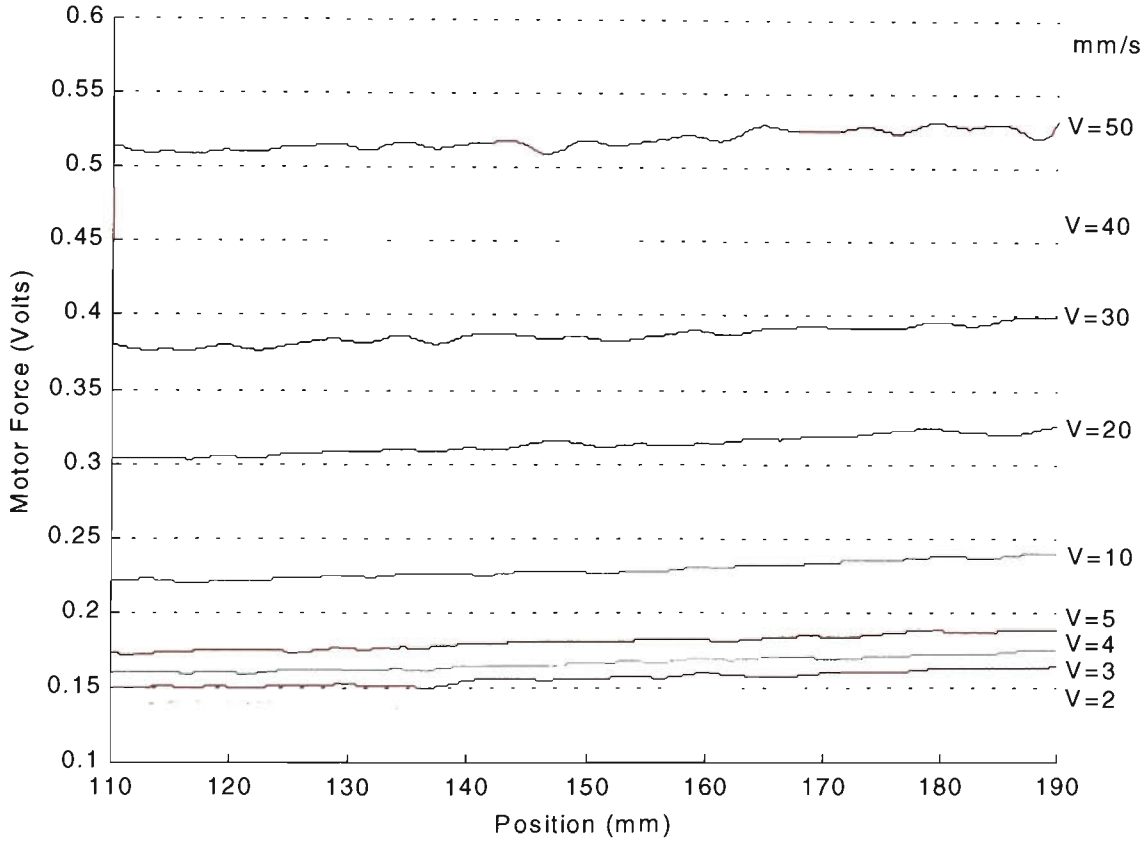

Figure 5.2 Force signal after low pass position frequency filtering (1 Volt =1382N)

For a constant velocity $\frac{dx}{dt} = V$ the acceleration $\frac{d^2x}{dt^2} = 0$ with no external force i.e. $F_G = 0$ and the expression for the motor force is given by:

$$F_{motor} = f_v V + f_c + \sum_{n=-n_{LP}}^{n_{LP}} c_n e^{jn\Omega_0 x} \qquad \text{Eq 5.6}$$

If the low position frequency PDFV were zero then the motor force which is the sum of the Coulomb and viscous friction would be a constant at each velocity. However as can be seen from figure 5.2 the force is not constant and increases as the mechanism moves along its travel. This variation in the applied motor force is accounted for by the low frequency PDFV. There are many possible causes for this variation including shaft bearing and slide alignments etc. For the X axis of the grinding machine (i.e. the results shown in figure 5.2) a first order polynomial was used to describe the low position frequency PDFV:

$$\sum_{n=-n_{LP}}^{n=n_{LP}} c_n e^{jn\Omega_0 x} = f_{x0} + f_{x1} x \qquad \text{Eq 5.7}$$

For other mechanisms with different variations along their travel higher order polynomials or other functions may give a better fit. For each individual mechanism this would have to be determined.

In figure 5.2 the force signals F_{motor} are the sum of the low position frequency PDFV and the viscous and Coulomb friction values:

$$F_{motor} = f_c + f_v v + f_{x0} + f_{x1} x \qquad \text{Eq 5.8}$$

The viscous and Coulomb components are already known and f_{x0} and f_{x1} can be calculated from figure 5.2. The equation used to estimate the force becomes:

$$F_G = F_{motor} - m\frac{d^2x}{dt^2} - f_v \frac{dx}{dt} - f_c - f_{x0} - f_{x1} x \qquad \text{Eq 5.9}$$

This expression is used in the force estimation work described in Section 5.2.4 and 5.4. This expression is only valid for the X axis of the grinding machine; however a similar approach can be adopted to determine the appropriate expression for other mechanisms.

Another mechanism could similarly be run at a number of constant velocities. The force signal is then filtered with a low pass position frequency filter and the results shown in a form similar to figure 5.2. A function of x is then used to describe the low frequency PDFV. This may be a first order polynomial, a higher order polynomial or other function which gives a good fit.

5.2.2 Closed Loop Frequency Response, Low Pass Filter

The spring force and grinding force estimation experiments have all been conducted with the X axis of the grinding machine under velocity control. A PID velocity controller is used and the velocity feedback is obtained by differentiating the shaft encoder position data. The velocities used in the grinding force experiments are much higher than the non linear low velocity region in which the friction controller described in Chapter 4 is used. The impulsive friction controller techniques were not used as part of this work and a standard PID controller was used with transfer function:

$$c(s) = K_p + \frac{K_I}{s} + K_D s \qquad \text{Eq 5.10}$$

The transfer function of the AC servo motor is discussed in Section 2.3.1. Combining the transfer function of the AC servo motor with the PID controller the compensated open loop transfer function G(s) is:

$$G(s) = \left(K_p + \frac{K_I}{s} + K_D s \right) \frac{K_{VII} K_m}{\left(1 + \frac{L_a}{R_a} s \right)(ms + f_v)} \qquad \text{Eq 5.11}$$

The closed loop frequency response of the system is shown in figure 5.3. Also shown in figure 5.3 is a low pass filter's response. The low pass filter is the first stage of the signal processing applied to the force estimation signal. The filter removes a large component of the noise from the force estimation signal. The low pass filter's frequency cutoff can be chosen arbitrarily. A low cutoff frequency removes more noise but also

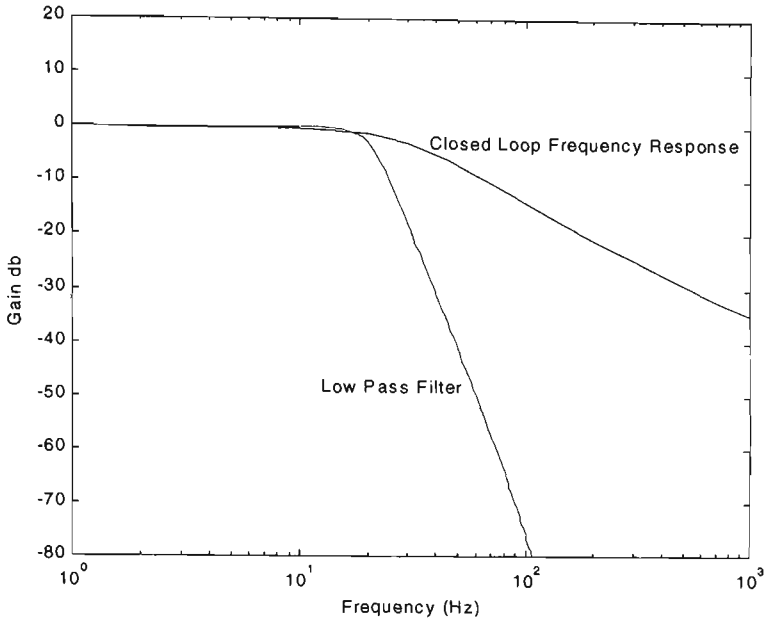

Figure 5.3 Closed Loop Frequency Response.

more of the signal of interest and inversely for a higher cutoff frequency less of the original signal is removed but more noise will be present. The filter used here was a digital 5^{th} order low pass IIR Butterworth filter with a cutoff frequency of 20Hz.

As can be seen from figure 5.3 the cutoff frequency is just below the control loop's break point frequency. The force estimation procedure will therefore not respond above about 20Hz, but if the force estimation signal is ultimately used for real time control (as discussed in Chapter 7) there is little advantage in having the force estimation's response greater than the system's response.

In the grinding experiment (discussed in Section 5.3) the force measuring systems used to validate the force estimated from the servo motor position and torque data also have a limited frequency response. For example the spindle motor power measurement which is used to calculate the tangential grinding force has a frequency response of 20 Hz (as discussed in Appendix B.5).

The low pass filter will remove different PDFV depending on the system's velocity. It is necessary to consider the low pass filter's characteristics in the position frequency domain. Using Eq 4.14 the low pass filter's response in the frequency domain can be transformed into the position frequency domain. In figure 5.4 the position frequency response of the low pass filter is shown for a number of different velocities.

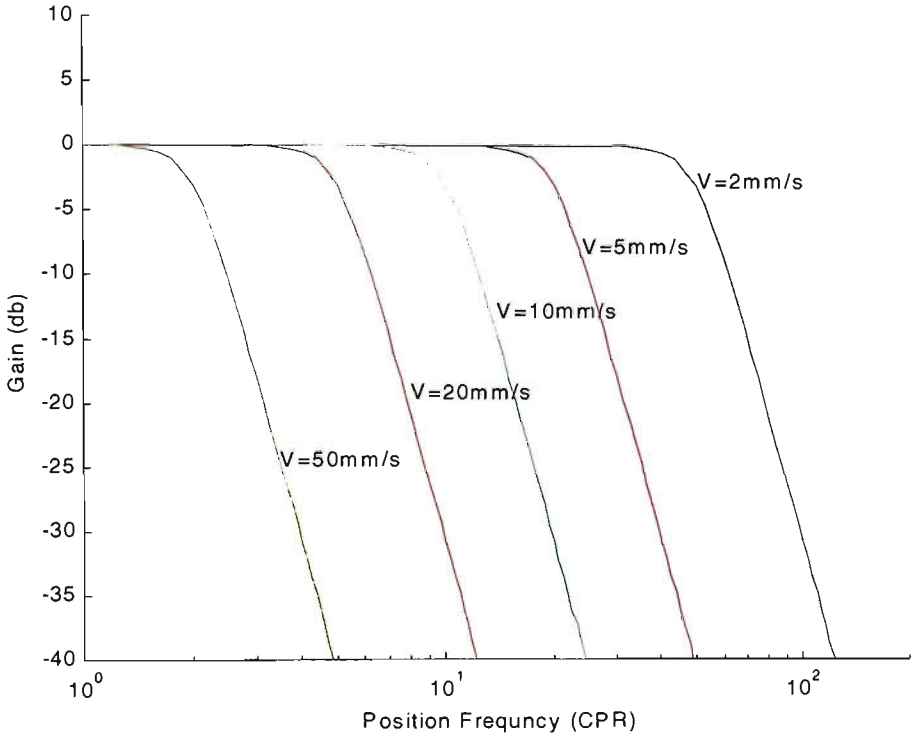

Figure 5.4 Low Pass Filter's Position Frequency Response

As the velocity increases the low pass filter removes more of the position frequency spectrum. This is an alternative way of viewing the low pass filter's characteristics. In reality the filter does not change, but the frequency of the PDFV increases as the velocity increases and more of the PDFV are removed by the low pass filter.

5.2.3 PDFV Position Frequency and Frequency Sampling Rates

Prior to processing the force estimation signal in either the time or position domain consideration needs to be given to the sampling frequency, the sampling position frequency, the PDFV spectrum and the system's velocity.

The first stage is to process the force estimation signal with the low pass filter described in Section 5.2.2. The low pass digital filter has a cutoff frequency f_{LP}=20 Hz. The sampling frequency f_s used for all the results given in this chapter was 500Hz. The Nyquist frequency *Nq* is half the sampling frequency and frequencies above the Nyquist frequency will be folded about the Nyquist frequency(aliased). This happens as part of the sampling process and before the signal is processed with a low pass digital filter. Frequencies between $f_s - f_{LP} \rightarrow f_s$ are folded back into $0 \rightarrow f_{LP}$ frequency range and will not be removed by the low pass filter

The frequency at which the PDFV components appear is dependent on their position frequency and the system's velocity. The system's velocity should be chosen so that the PDFV do not appear in the position frequencies range between $f_s - f_{LP} \rightarrow f_s$ (and aliased to $0 \rightarrow f_{LP}$). Using Eq 4.14 the maximum allowable velocity is given by:

$$v = \frac{l(f_s - f_{LP})}{\Phi_{max}} \qquad \text{Eq 5.12}$$

where l is the screw pitch and Φ_{max} is the maximum position frequency. The PDFV frequency spectrum characteristics are given in Section 4.6 and the highest position frequency PDFV was 54 CPR. This gives a maximum allowable velocity of 44mm/s. This guarantees that no PDFV components are aliased into the $0 \rightarrow f_{LP}$ position frequency range. This does not mean there are no PDFV components in the $0 \rightarrow f_{LP}$ position frequency range since PDFV components with position frequencies between $0 \rightarrow f_{LP}$ will still be there as part of the filtered force estimation signal. The digital filter does however remove any PDFV components that appear between f_{LP} and $f_s - f_{LP}$.

After the force estimation signal is processed with the low pass filter the time domain filtered force estimation signal only has frequency components from $0 \rightarrow f_{LP}$. The filtered force estimation signal is turned into a discrete position signal using the position binning techniques described in Section 4.4. The time domain frequency range $0 \rightarrow f_{LP}$ (using Eq 4.14) will appear in the position domain as the position frequency range $0 \rightarrow \frac{lf_{LP}}{v}$. The position sampling rate should be chosen so that the Nyquist position frequency is above the maximum position frequency component:

$$\Phi_{Nq} > \frac{lf_{Lp}}{v} \qquad \Phi_s > \frac{2lf_{Lp}}{v} \qquad \text{Eq 5.13}$$

A low pass filter cutoff of 20 Hz, a minimum velocity of 2mm/s and a screw pitch l=5mm corresponds to a Nyquist position frequency of 50CPR and a position sampling rate of 100CPR. As the velocity increases it is possible to use a lower position sampling rate. It should also be noted that the maximum PDFV component has a frequency of 54CPR. If the Nyquist frequency is chosen above 54CPR then independent of how slow the velocity none of the PDFV components will be aliased into the spectrum of interest. If the position sampling rate were simply set at 128CPR for all velocities no PDFV component would be aliased.

As part of the binning process there must be at least one data point in each position bin. This is discussed in Section 4.4 and an expression (Eq 4.24) to calculate the number of data points per bin is given. For a set sampling frequency as the velocity increases the position sampling frequency must decrease (the bin size increases) to maintain the same number of data points per bin. Decreasing the position sampling frequency is acceptable as long as Eq 5.13 is satisfied.

5.2.4 Signal Processing

The force estimation signal calculated from Eq 5.9 is typically a noisy signal. As will be discussed in Section 5.3 a majority of this noise is due to encoder quantisation and PDFVs. There are also additional noise sources such as inverter switching noise. The results given in this section are for the force applied via a spring. In the graphs shown the red line is the actual spring force. The green plots are the force estimation signals at various stages of processing.

The force estimation signal for the X axis moving at 5mm/s is shown in figure 5.5. The first stage of the signal processing is to apply the low pass filter (described in Section 5.2.2) to the force estimation signal. In figure 5.5 the bottom plot is the force estimation signal after the data is passed through the low pass filter and henceforth will be referred to as the filtered force estimation signal. The signals shown in figure 5.5 are both discrete time signals (although the signals are plotted against position). The low pass filtering is done in the time domain.

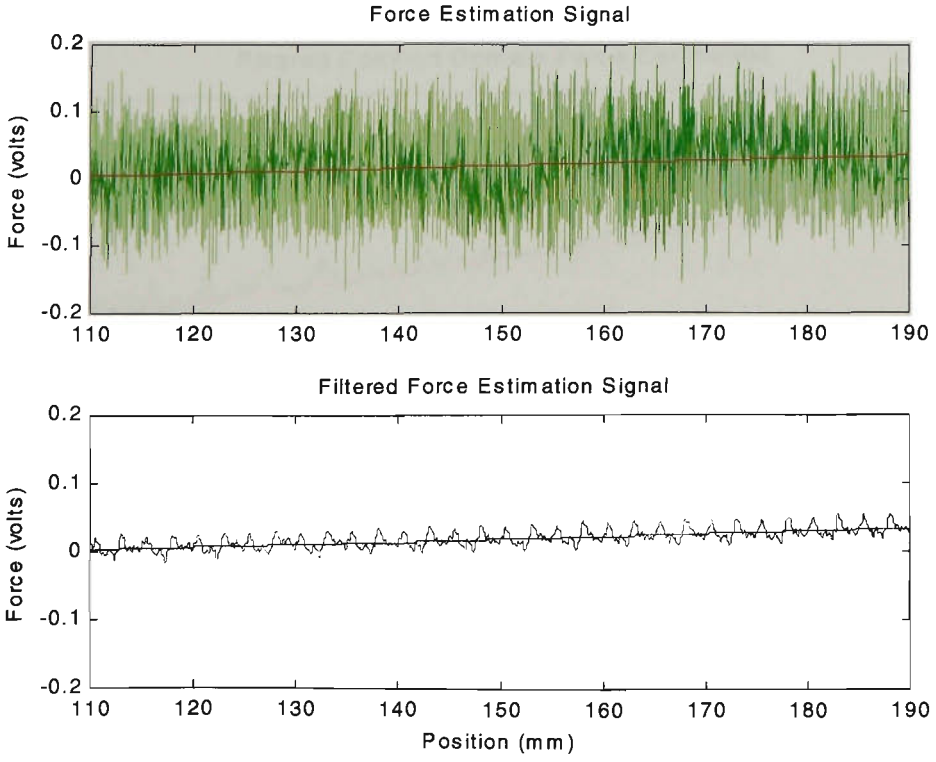

Figure 5.5 Time Domain Force Estimation Signals V=5mm/s (1 Volt =1382N)

The filtered force estimation signal is turned into a discrete position signal using the position binning technique discussed in Section 4.4. This discrete position signal is shown as the top graph of figure 5.6 and will be referred to as the position domain force estimation signal. The position domain force estimation signal is then filtered to remove the PDFV. The filtering is done in the position frequency spectrum. A FFT is applied to the position domain force estimation signal, the position frequencies to be removed are set to zero and the signal is reconstructed using an Inverse Fast Fourier Transform IFFT. The resultant signal will be referred to as the filtered position domain force estimation signal. The bottom graph of figure 5.6 shows the filtered position domain force estimation signal.

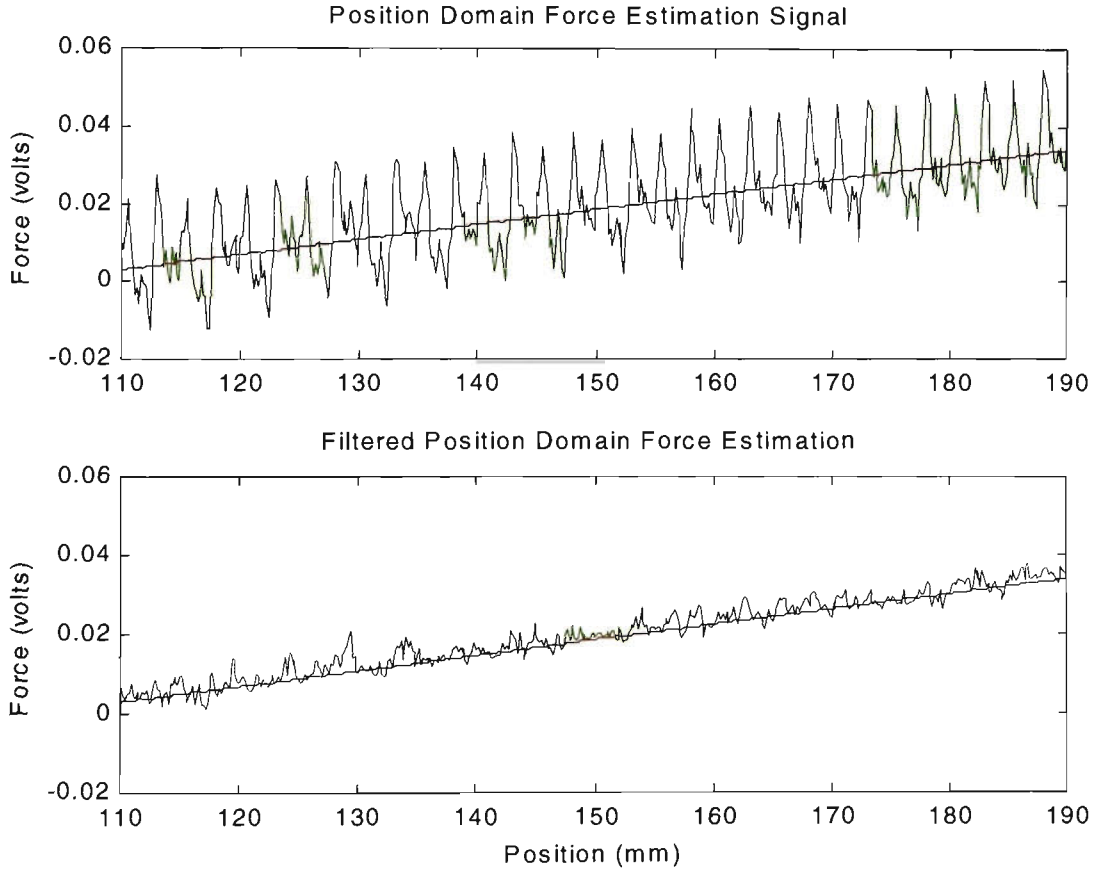

Figure 5.6 Position Domain Force Estimation Signals (1 Volt =1382N).

In Section 4.6 the position frequency spectrum of the X axis has been characterised and the major PDFV have been identified. The main PDFV components occur at position frequencies of 1,2,3,4,5,8,12,27,54 CPR. Depending on the velocity some of these

PDFV will be removed by the time domain low pass filter. Those remaining are removed by filtering in the position domain. The velocity also affects the position sampling rate (and therefore the bin size that) can be used as discussed in Section 5.2.3. A number of force estimation experiments were made at different velocities. Table 5.1 lists the different velocities, the bin sizes and the position sampling rates used.

Table 5.1 Velocity and Position Frequency Parameters

Velocity (mm/s)	Bin size (mm)	Position Sampling Frequency (CPR)	Low pass filter Cut off (CPR)	PDFV filters (CPR)
2	0.039	132	50	1 2 3 4 5 8 12 27
3	0.039	132	33	1 2 3 4 5 8 12 27
4	0.039	132	25	1 2 3 4 5 8 12
5	0.039	64	20	1 2 3 4 5 8 12
10	0.078	32	10	1 2 3 4 5 8
20	0.156	32	5	1 2 3 4 5
30	0.156	32	3.3	1 2 3
40	0.156	32	2.5	1 2

Table 5.1 also lists the cutoff frequency of the low pass filter in the position domain and the PDFV frequencies that still have to be removed after the application of the low pass filter. As can be seen from table 5.1 as the velocity increases the filtering in the position domain of the PDFV becomes less important because of the removal of higher frequencies by the low pass filter in the time domain.

In each of the graphs the spring force calculated from the extension of the spring is shown (in red). The force estimation error is the difference between the force estimation signal and the calculated spring force. This error is characterised using its standard deviation and is listed in table 5.2 for various stages of signal processing.

Table 5.2 Standard Deviation of the Noise on the Force Estimation Signal V=5mm/s

	Force Estimation Signal	Filtered Force Estimation Signal	Position Domain Force Estimation Signal	Filtered Position Domain Force Estimation Signal
Force (volts)	0.0052	0.0095	0.0092	0.0021
Force (N)	72.3	13.1	12.7	2.9
% of the original noise signal	100	18.1	17.5	4.0

All the figures so far in Section 5.2.4 have expressed the force estimation values in volts. These can be converted easily to actual force by using the constants defined in table 2.5. The value of the noise in newtons is given in the second row of table 5.2. The third row of table 5.2 gives the noise signal as a percentage of the noise on the force estimation signal. The noise on the original force estimation signal is defined as 100%. The greatest reduction in the noise is due to low the pass filtering and this reduces the noise by 72 % to 18%. The noise is then reduced by a factor of 4 i.e. 18% to 4% by removing the PDFV position frequencies.

A number of measurements were made at different velocities and the force estimation noise listed as force value (Newtons) is given in table 5.3 The discrete position force signals before and after filtering of PDFV for velocities of 2,20 and 40 mm/s are also shown in figures 5.7, 5.8 and 5.9.

Table 5.3 Standard Deviation of the Noise on the Force Estimation Signal

Velocity	Force Estimate Signal (N)	Filtered Force Estimation Signal (N)	Position Domain Force Estimation Signal (N)	Filtered Position Domain Force Estimation Signal (N)
2	70.1	20.2	19.3	5.3
3	70.4	18.4	17.8	3.8
4	71.0	13.5	13.4	3.7
5	72.3	13.1	13.0	3.2
10	77.1	13.7	12.5	3.4
20	124.1	17.0	16.9	5.8
30	165.9	23.5	23.4	5.5
40	198.4	29.8	29.8	5.3

Over the range of velocities used the noise signal's standard deviation is a maximum of 5.8N. The effect this noise has depends on the magnitude of the original applied force. In the case of the spring the maximum applied force was 50N giving an error of 11% of the maximum value.

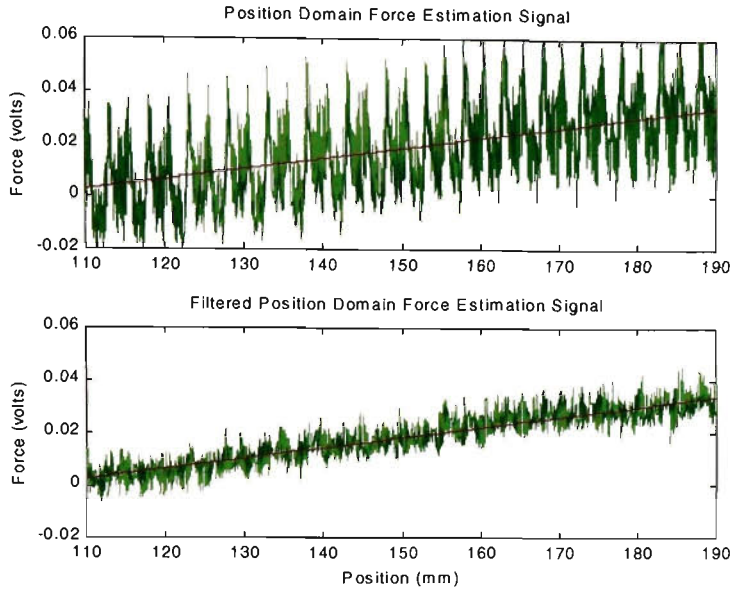

Figure 5.7 Position Domain Force Estimation Signals V=2mm/s (1 Volt =1382N)

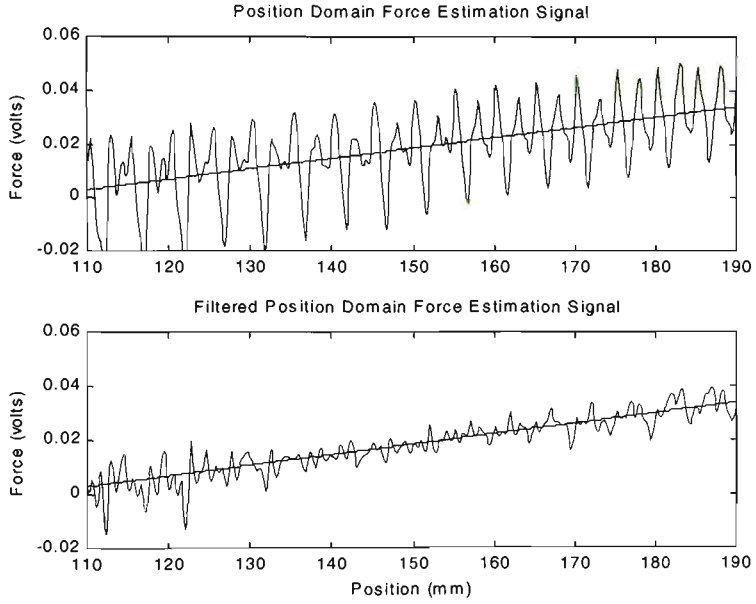

Figure 5.8 Position Domain Force Estimation Signals V=20mm/s (1 Volt =1382N)

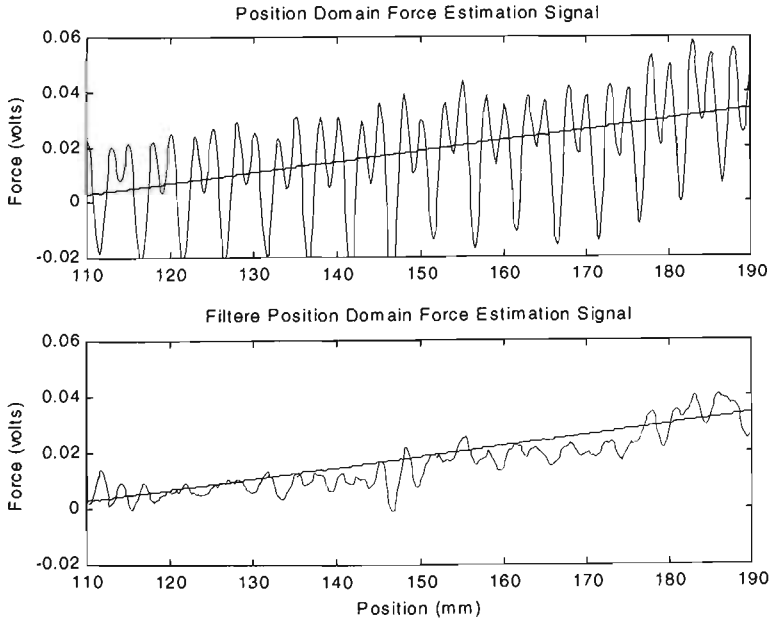

Figure 5.9 Position Domain Force Estimation Signals V=40mm/s (1 Volt =1382N)

5.3 Noise

As part of the investigation of the noise sources that affect the force estimation signal a Simulink model of the system was made. The model includes the PID controller, mass, viscous and Coulomb friction. Decoder quantisation and PDFV are also included. A force the same magnitude as that applied by the spring is included as part of the model. The PDFV model is calculated from the position frequency spectrum given in Section 4.6 for a velocity of 5mm/s.

The Simulink model is shown in figure 5.11. The set point for the velocity controller was set at 5mm/s. The motor torque and position data produced by the Simulink model are processed in an identical fashion to the actual data recorded (as given in Section 5.2.4). The force estimation signal is shown in the top plot of figure 5.10. The time domain force estimation signal is then filtered with a low pass filter. The filtered force estimation signal is shown in the bottom plot of figure 5.10.

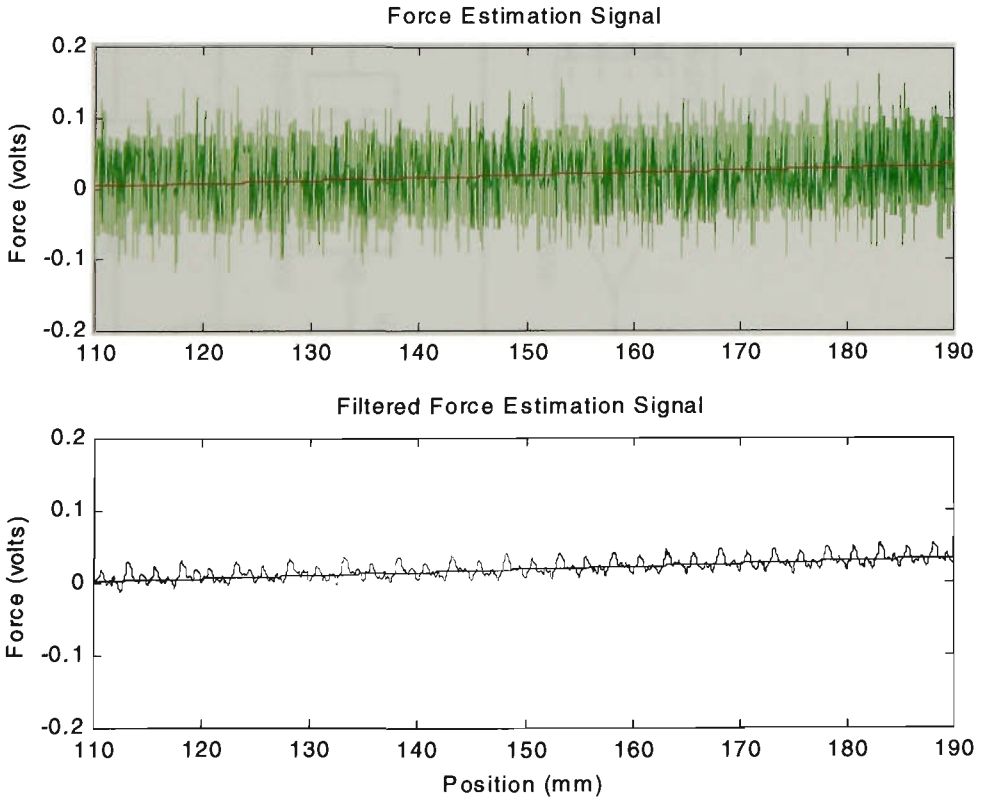

Figure 5.10 Simulink Model Time Domain Force Estimation Signals V=5mm/s (1Volt=1382N)

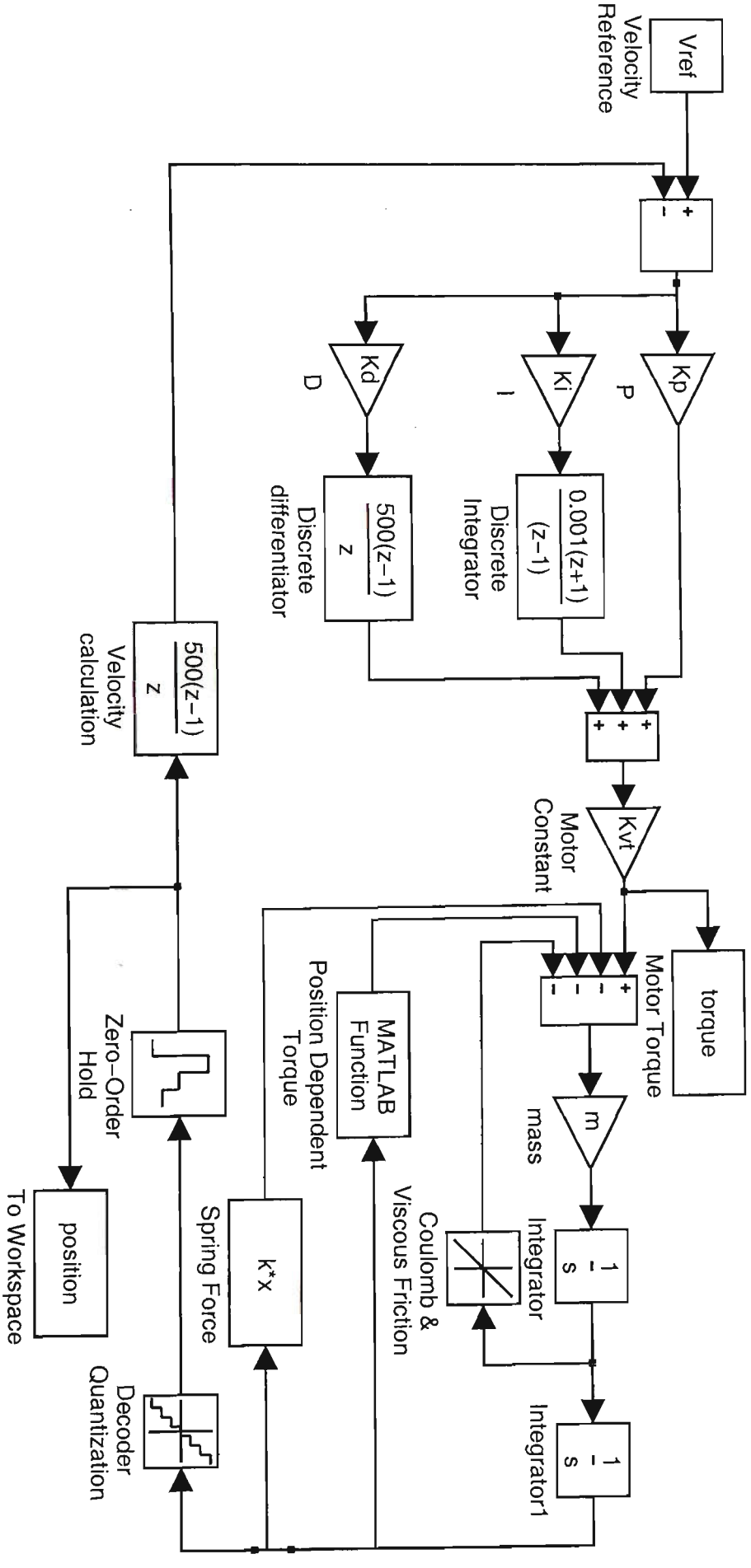

Figure 5.11 Simulink Model

The filtered force estimation signal is turned into a discrete position signal using the position binning technique discussed in Section 4.4. The position domain force estimation signal is shown as the top graph of figure 5.12. The position domain force estimation signal is then filtered to remove the PDFV components and the resultant signal is shown in the bottom plot of figure 5.12. The simulation results shown in figures 5.10 and 5.12 should be compared with those produced from the actual data as displayed in figures 5.5 and 5.6 respectively. The graphs although not identical have similar characteristics.

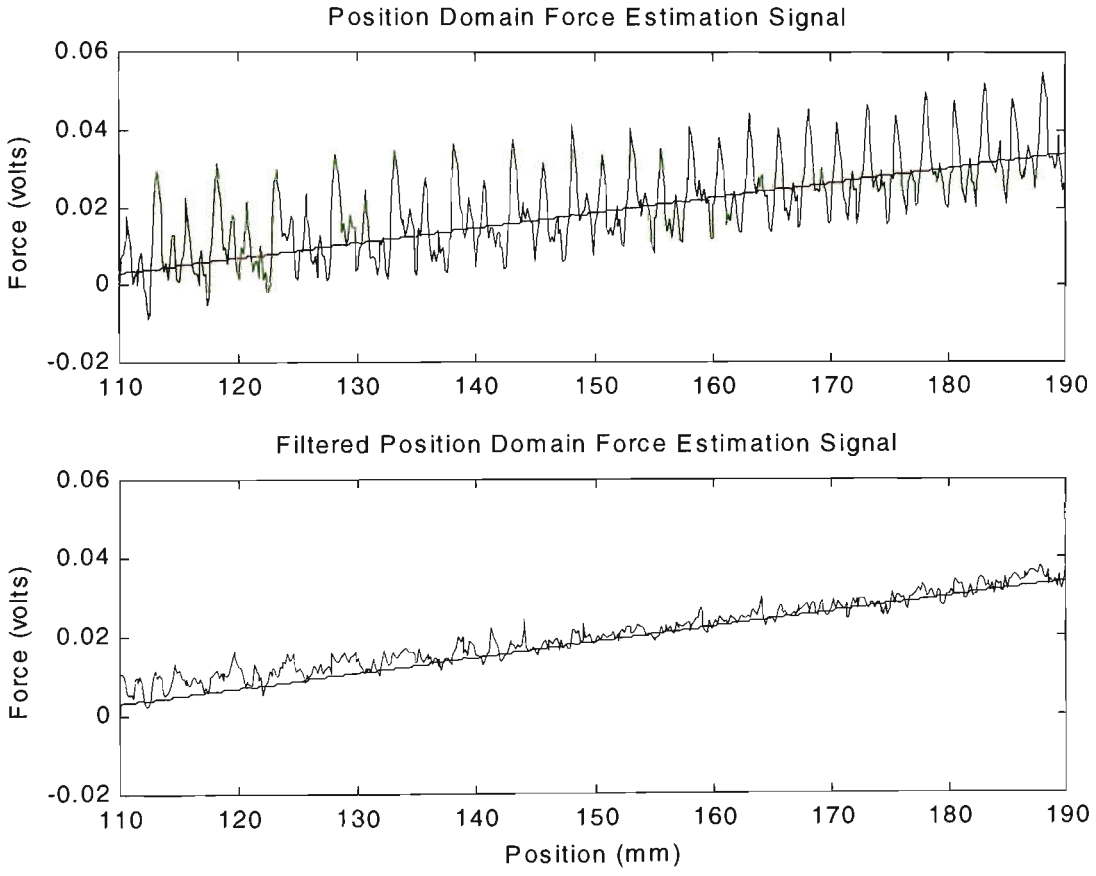

Figure 5.12 Simulink Model Position Domain Force Estimation Signals V=5mm/s (1 Volt =1382N)

Using the same approach as in Section 5.2.4 the noise is characterised using the standard deviation of the error of the force estimation signal. In the Simulink model there are two sources of noise: the PDFV and the decoder quantisation. The noise on the Simulink model and that of the noise from the measured data is given in table 5.4.

Table 5.4 Force Estimation Signal Noise, Comparison of Computer Simulation and Measured V=5mm/s

	Force Estimation Signal	Filtered Force Estimation Signal	Position Domain Force Estimation Signal	Filtered Position Domain Force Estimation Signal
Measured Force (N)	72.3	13.1	12.7	2.9
Modelled Force (N)	58.7	11.9	11.5	3.0

The measured original force estimation signal has a higher noise component than the modelled value. There are many other noise sources other than PDFV and decoder quantisation that have not been modelled. These include noise on the torque command signal to the drive which includes noise due to power electronic switching etc. As can be seen from table 5.4 the low pass filter reduces the noise level difference between the actual and modelled to less than 4% so this suggests that most of the unmodelled noise is at a frequency above the cutoff frequency of the low pass filter. After position binning of the signal and removal of the PDFV position frequencies the noise signal of the model and measured signal are fairly close.

5.3.1 Decoder Quantisation Noise

The position measurement is obtained from the shaft resolver signals which are fed into a decoder chip (as discussed in Appendix B.3). The position measurement accuracy depends on the decoder resolution d. The position measurement error ε, depends on how close the actual position is to a decoder position increment(pulse). The minimum error is when the position is exactly on a decoder position increment and the maximum error is just before the next decoder transition occurs. The error ε will be between:

$$0 \leq \varepsilon < d$$

The error signal ε can be thought of as a form of quantisation noise. As described in [52] quantisation noise is assumed to be a white noise source with mean $\bar{\varepsilon}$ and standard deviation σ given by:

$$\bar{\varepsilon} = 0.5d \qquad \sigma = \frac{d}{2\sqrt{3}} \qquad \text{Eq 5.15}$$

The position signal is differentiated once to give the velocity and differentiated twice to give the acceleration. For sampling frequency f_s and consecutive measured position values $x(k-2), x(k-1), x(k)$ the velocity and acceleration is given by:

$$v(k) = f_s\big(x(k) - x(k-1)\big) \qquad a(k) = f_s^2\big(x(k-2) - 2x(k-1) + x(k)\big) \qquad \text{Eq 5.16}$$

Let $x'(k), v'(k), a'(k)$ be the actual position, velocity and acceleration and $x(k), v(k)$ and $a(k)$ be their measured values respectively. Let $\varepsilon(k)$ be the position error:

$$x(k) = x'(k) + \varepsilon(k) \qquad \text{Eq 5.17}$$

Using Eq 5.16 and Eq 5.17 the velocity and acceleration can be expressed as:

$$v(k) = v'(k) + f_s\big(\varepsilon(k) - \varepsilon(k-1)\big) \qquad \text{Eq 5.18}$$

$$a(k) = a'(k) + f_s{}^2\big(\varepsilon(k) - 2\varepsilon(k-1) + \varepsilon(k-2)\big) \qquad \text{Eq 5.19}$$

The error signals $\varepsilon(k), \varepsilon(k-1), \varepsilon(k-2)$ are uncorrelated noise sources with the same mean and standard deviation given by Eq 5.15. The velocity and acceleration error signals $\varepsilon_v(k)$ and $\varepsilon_a(k)$ are then:

$$\varepsilon_v(k) = f_s(\varepsilon(k) - \varepsilon(k-1)) \qquad \varepsilon_a(k) = f_s^2(\varepsilon(k) - 2\varepsilon(k-1) + \varepsilon(k-2)) \qquad \text{Eq 5.20}$$

The standard deviation of the acceleration error σ_a and velocity error σ_v can be calculated from Eq 5.20 and standard manipulation of independent random variables (uncorrelated white noise sources) as given in Appendix C:

$$\sigma_v = f_s \frac{d}{\sqrt{6}} \qquad \sigma_a = f_s^2 \frac{d}{\sqrt{2}} \qquad \text{Eq 5.21}$$

Let $F'(k)$ be the actual force , $\varepsilon_F(k)$ be the force estimation error and $F(k)$ be the estimated force and is given by:

$$F(k) = F'(k) + \varepsilon_F(k) \qquad \text{Eq 5.22}$$

For a system with mass m and viscous friction f_v and coulomb friction f_c, the force estimation signal $F(k)$ can also be calculated:

$$F(k) = ma(k) + f_v v(k) + f_c \qquad \text{Eq 5.23}$$

An expression for the standard deviation of the force estimation error σ_F is derived in Appendix C and is given by:

$$\sigma_F = df_s \sqrt{\frac{3m^2 f_s^2 + 3mf_s f_v + f_v^2}{6}} \qquad \text{Eq 5.24}$$

In a well designed digital control system the sampling frequency f_s (500Hz) should be higher than the system's response. As discussed in Section 2.3 the mechanical response determines the system response of the grinding machine and has a break frequency given by $\frac{f_v}{2\pi m}$ (=1.1Hz). The sampling frequency should be considerably higher than the system's break frequency i.e. $f_s >> \frac{f_v}{2\pi m}$ which expressed in a slightly different form is $4\pi^2 m^2 f_s^2 >> f_v^2$. Hence $3m^2 f_s^2 >> f_v^2$ and similarly $3m^2 f_s^2 >> 3mf_s f_v$ and Eq 5.24 reduces to:

$$\sigma_F = \frac{mdf_s^2}{\sqrt{2}} \qquad \text{Eq 5.25}$$

The sampling frequency f_s is 500Hz and the decoder chip resolution is given in table B.5, the mass is given in table 2.7. These values give the noise on the force signal as 52.2N. A Simulink model was also run with no PDFV and the results are shown in figure 5.13. The standard deviation of the noise was 53.2N; this is within 2% of the value calculated from Eq 5.25. The force estimation signal from the Simulink model output is then processed with a low pass filter. The filtered force estimation signal is shown in the lower plot of figure 5.13. The low pass filtering reduces the standard deviation of the noise to 1.3N.

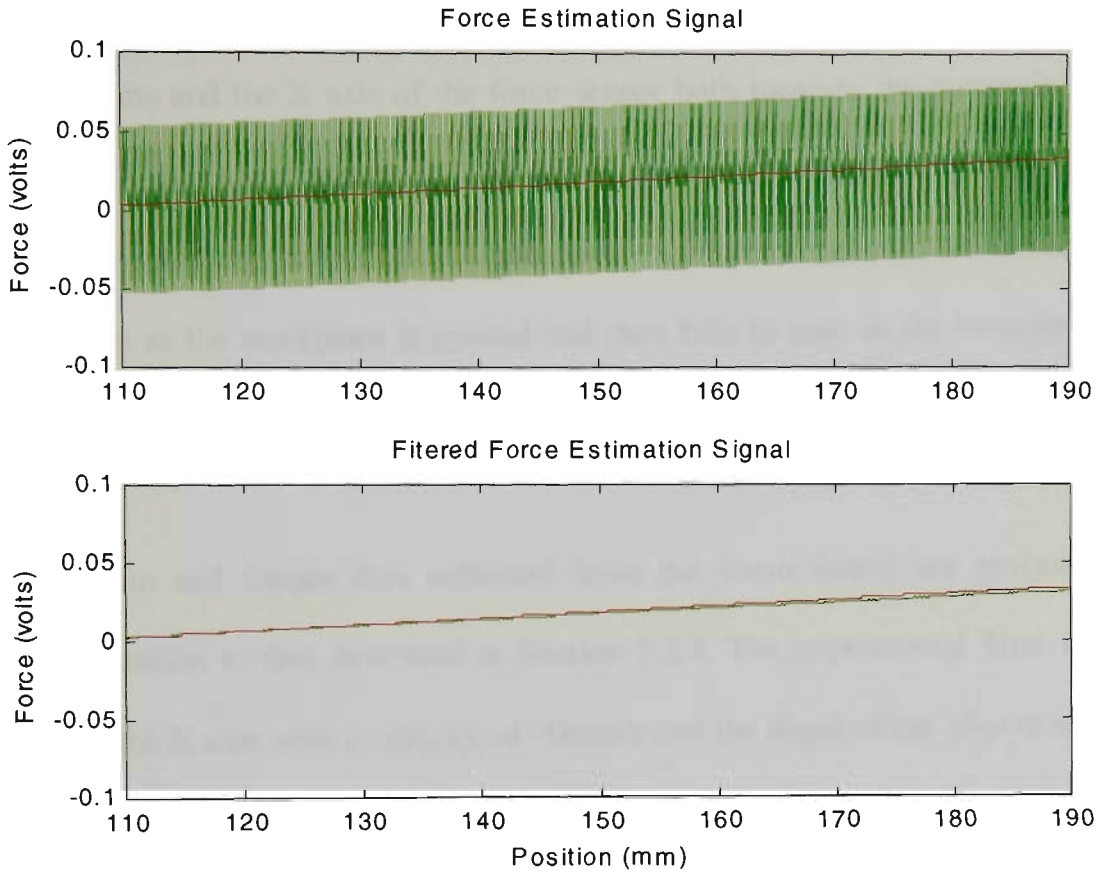

Figure 5.13 Time Domain Force Estimation Signals for Simulink Model V=5mm/s (1 Volt =1382N)

The acceleration signal induces a large noise signal in the force estimation signal. However this is almost all removed by the low pass filter. Hence the remaining noise due to the decoder quantisation (1.3N) is a relatively small part of the noise left on the final processed measured force estimation signal (3.0N). The other noise sources will have a standard deviation of 2.5N. Hence even if the decoder noise is reduced to zero the remaining noise would still be 2.5N.

5.4 Grinding Force Results

In this Section the force estimation process using servo motor torque and position data is used to calculate grinding forces. Several grinding measurements were carried out using different feed velocities and depths of cuts to give a range of grinding forces. As the depth of cut increases and the velocity increases so does the grinding force. All the

grinding was plunge surface grinding. In this arrangement the tangential force is in the x direction and the normal grinding force is in the Z direction. The spindle motor power measurements and the X axis of the force sensor both measure the tangential grinding force. The X axis servo system will be driving against the tangential grinding force. In the experiments the grinding force is zero as the workpiece moves towards the grinding wheel, rises as the workpiece is ground and then falls to zero as the workpiece moves past the grinding wheel.

The position and torque data collected from the servo motor are processed in an identical fashion to that described in Section 5.2.4. The unprocessed force estimation signal for the X axis with a velocity of 20mm/s and the depth of cut 16 μ m is shown in the top plot of figure 5.14. The force estimation signal is then passed through a low pass filter and the resultant signal is shown in the bottom graph of figure 5.14. This shows grinding is occurring between approximately 120 and 170mm.

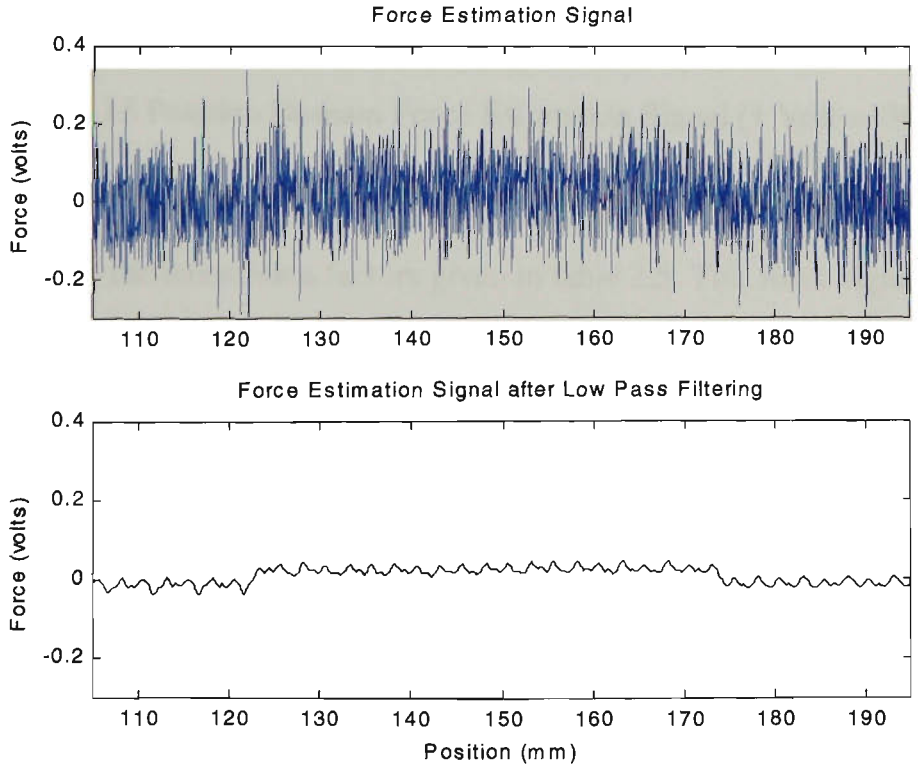

Figure 5.14 Time Domain Force Estimation Signals V=20mm/s Depth of Cut=16 μ m (1 Volt =1382N)

The discrete time signal is then turned into a discrete position signal using the position binning technique. This signal is shown in the top plot of figure 5.15. The position signal is then filtered to remove the PDFV in exactly the same manner as described in Section 5.2.4. The resultant force estimation signal is shown in the bottom graph of figure 5.15

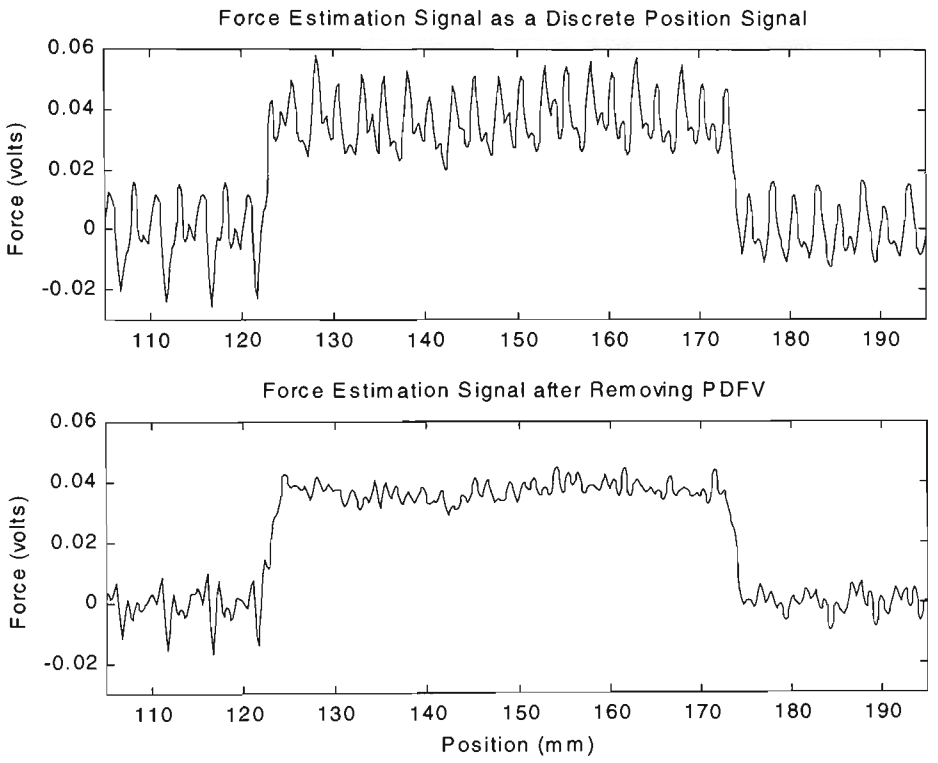

Figure 5.15 Position Domain Force Estimation Signal (1 Volt =1382N)

The force estimation signal shown in the lower plot of figure 5.15 can be converted to a force signal using the conversion factors given in table 2.5. This force signal can then be compared to the tangential grinding force calculated from the spindle motor power and that measured from the X axis of the force sensor. The three different force measurements are shown in figure 5.16.

As discussed in Section 5.2.2 both the force estimation signal and the spindle motor power measurement have a cutoff frequency of 20Hz. The force sensor signal shown in figure 5.16 has been filtered with a low pass filter with a cutoff frequency of 5Hz. There

is a strong agreement between the tangential grinding force measured with the force sensor and that calculated from the spindle motor power. The force estimation signal is similar but is a much noisier signal.

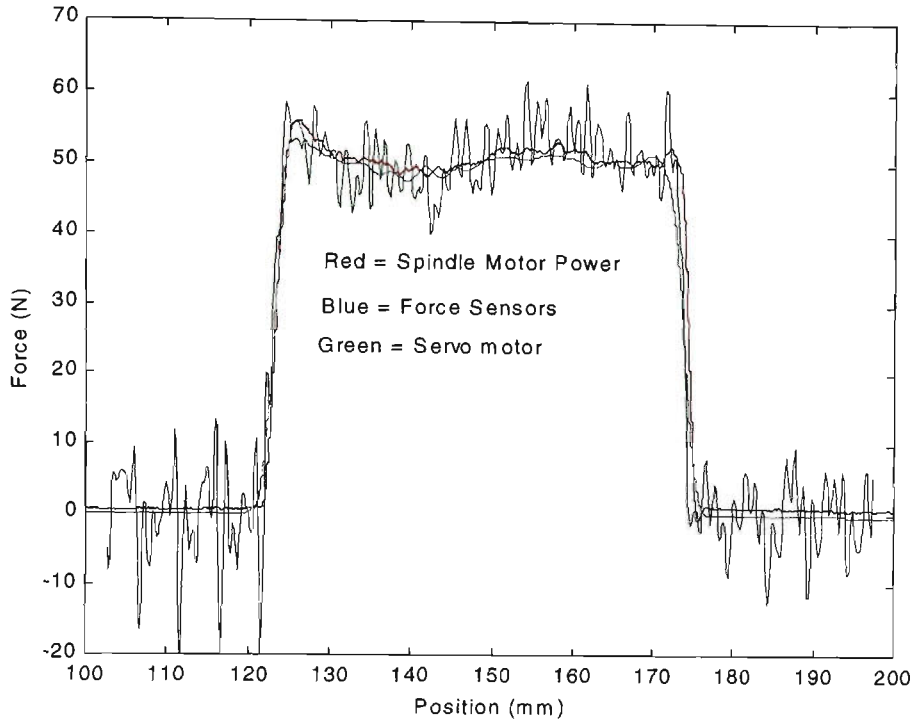

Figure 5.16 Tangential Grinding Forces V=20mm/s Depth of Cut=20μ m

Results from a series of different grinding forces and velocities are shown in figures 5.17, 5.18. The force estimation signals are shown in green; these are compared to the force calculated from the spindle motor power shown in red. Assuming the spindle motor power gives an accurate measure of the tangential grinding force, the force estimation error is then the difference between the two signals. Considering only the region where grinding takes place (130-170mm) the standard deviations of the force estimation errors for the graphs shown in figures 5.17, 5.18 are given in table 5.5.

Table 5.5 Grinding Force Estimation Errors

Feedrate (mm/s)	**Depth of Cut (μm)**	
	20	**30**
2	6.9N	7.9N
5	5.3N	6.9N
10	5.0N	4.7N
20	5.3N	3.8N

The force estimation errors range from 3.8-7.9N with a mean value of 5.7N. These errors or noise levels although slightly higher are similar to those calculated in Section 5.2.4 when a known force was applied via a spring. The noise levels and the grinding

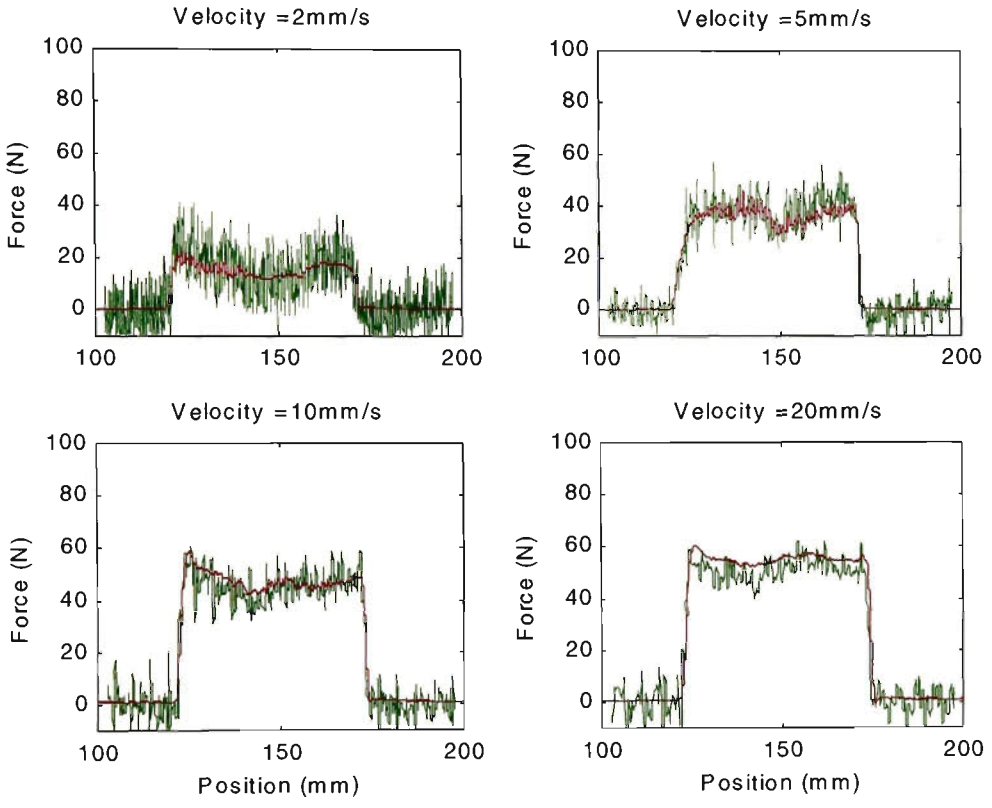

Figure 5.17 Grinding Force Results Depth of Cut =20 μ m

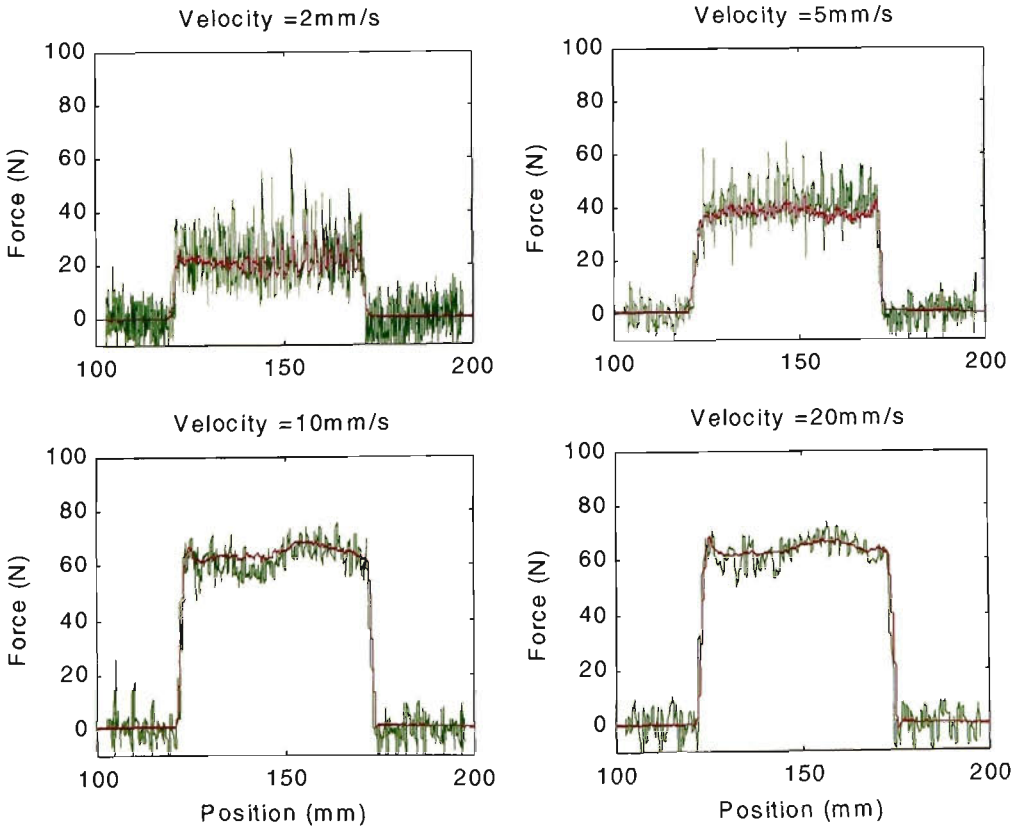

Figure 5.18 Grinding Force Results Depth of Cut =30 μ m

force that can be observed will be unique to each mechanical system. Whether the force estimation techniques are useful will depended on each individual application and the magnitude of the force applied and the resolution desired. In the present application the maximum tangential grinding force is limited by the spindle motor power. The maximum tangential grinding force can be calculated using the equations given in Appendix B.5 and is approximately 80Nm. This would make the force estimation error 7% of the maximum tangential grinding force.

As mentioned in Section 1.2 the grinding force increases with the metal removal rate. As the velocity and the depth of cut increases the grinding force increases. As can be seen in figures 5.17, 5.18 the clarity of the force estimation signal increases with velocity. Part of this is due to the larger grinding force since one method of improving the signal to noise ratio is to increase the signal.

Part of the increased noise at lower velocities may be due to the grinding process itself. The tangential grinding force calculated from the spindle motor power and the force estimation signal both have increased noise at lower velocities suggesting the force being measured is actually noisier. There are a number of variations along the workpieces travel which may cause the grinding force to vary. These include variations in depth of cut due to non uniform workpiece, machine vibration, alignment of slides and ballscrews. These all may effect the amount of metal being removed and hence the grinding force. At lower velocities with longer measurement times more of these variations may be seen in the force signal.

Part of the noise at lower velocities may be due to the PDFV spectrum. As shown in table 5.1 less of the PDFV spectrum is removed by the time domain low pass filter at low velocities. Although the position domain filtering removes the major PDFV components there will still be some minor PDFV components left. These minor PDFV will effectively add noise to the force estimation signal at lower velocities.

5.5 Robot Force Estimation

The force estimation techniques developed for measuring grinding force on the grinding machine can also be used to estimate external forces applied to the Hirata robot. An external force is applied to the end effector of the robot by stretching a spring. One end of the spring is connected to a fixed point and the other end is connected to the robot's end effector. In the experiments discussed in this section coordinated motion of the A and B axes of the Hirata robot is used to track a circular path about the fixed point of the spring. For this arrangement the magnitude of force will be constant and the direction of the force will always be in the normal direction to the circular path being tracked. The magnitude of the spring force can be changed by tracking circular paths of different radii. A schematic representation of the Hirata robot's path and the spring arrangement is shown in figure 5.19

The link lengths of the A and B axes are denoted as r_a and r_b and are also shown in figure 5.19. Let the magnitude of the force applied by the spring be F_{spring}. Let θ_F be the angle the direction of the spring force makes with the X axis. The spring force can be resolved into its x and y components F_x and F_y respectively such that:

$$F_x = F_{spring}\cos\theta_F \qquad F_y = F_{spring}\sin\theta_F \qquad \text{Eq 5.26}$$

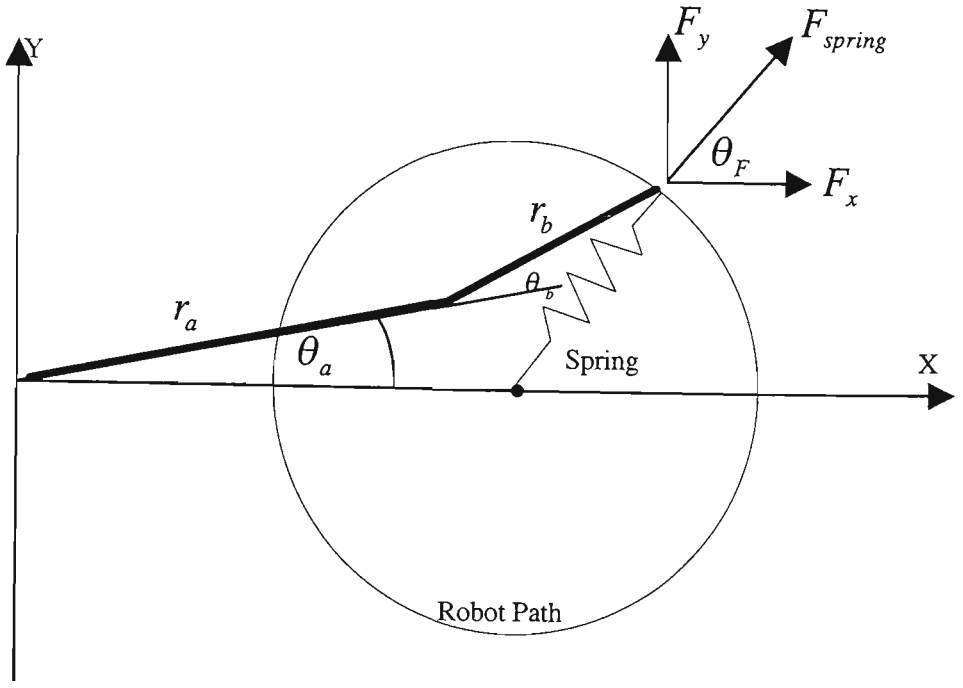

Figure 5.19 Robot Path and Spring Forces

Let (x,y) be the Cartesian coordinates of the end effector's position. The (x,y) coordinates are related to the A and B joint angles θ_a and θ_b respectively by the standard kinematic equation for a SCARA robot and as given in Section 3.3:

$$x = r_a \cos\theta_a + r_b \cos(\theta_a + \theta_b) \quad y = r_a \sin\theta_a + r_b \sin(\theta_a + \theta_b) \qquad \text{Eq 5.27}$$

The force F_{spring} will produce Torques at the A and B joints denoted T_a and T_b respectively. Letting a torque that causes rotation in the clockwise direction be positive the relationship between the spring force components and the joint torques is given by:

$$\begin{bmatrix} T_a \\ T_b \end{bmatrix} = \begin{bmatrix} -y & x \\ -r_b \sin(\theta_a + \theta_b) & r_b \cos(\theta_a + \theta_b) \end{bmatrix} \begin{bmatrix} F_x \\ F_y \end{bmatrix} \qquad \text{Eq 5.28}$$

5.5.1 System Model

The system model for the Hirata robot is very similar to the model used to describe the grinding machine given in Section 5.2.1. The linear system variables of force, mass and velocity have been replaced by rotary system variables torque T, angular velocity ω, angular position θ and inertia J. The differential equation used to describe the system of the A and B axes of the Robot is:

$$T_{motor} = J\frac{d^2\theta}{dt^2} + f_v\frac{d\theta}{dt} + f_c + T_{pos}(\theta) + T_{spring} \qquad \text{Eq 5.29}$$

Where T_{motor} is the torque applied by the motor, f_v is the viscous friction, f_c is the coulomb friction, $T_{pos}(\theta)$ is the position dependent torque component and T_{spring} is the torque component due to the spring. This can be calculated using the spring force from Eq 5.28.

The inertias of the A and B axes of the Hirata are given in Section 2.2.3. The A axis inertia given is only valid when the B axis at its maximum extension i.e. when the B axis angle $\theta_b = 0$. As the B axis angle changes the inertia seen by the A Axis motor changes. To describe the A axis inertia J_A Evans [53] used an expression of the form:

$$J_A = a_0 + a_1 \cos\theta_b \qquad \text{Eq 5.30}$$

The A Axis inertia was calculated for a number of different B axis angles and these points are shown in figure 5.20.

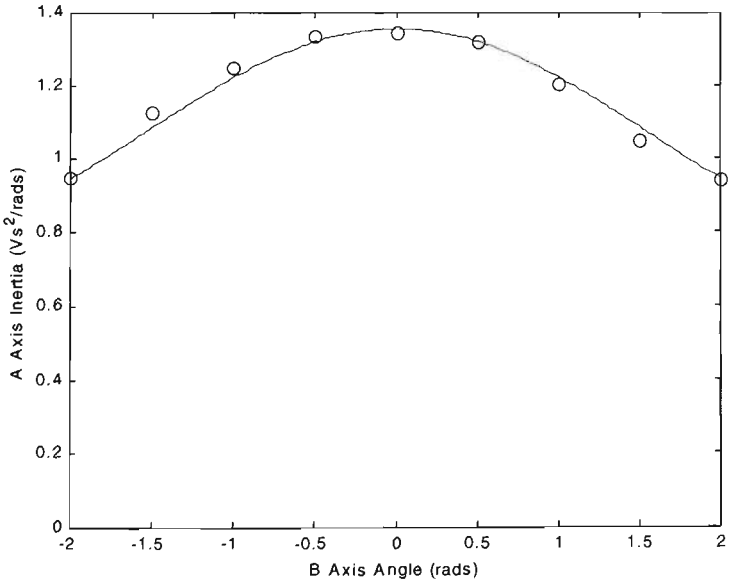

Figure 5.20 A Axis Inertia ($1Vs^2/rads = 1kgm^2$)

A curve was drawn between these points using Eq 5.30. The parameters a_0 and a_1 were chosen to give the best curve fit and are used in the system model to calculate the A axis

inertia. Because of the very low speeds used here the centripetal forces, Coriolis forces and coupling inertias have been neglected.

Using the same approach as described in Section 5.2.1 the low frequency PDTV are explicitly included in the friction model and the high frequency PDFV components are removed as part of the filtering process. The Low frequency PDTV components are determined by running the mechanism over its travel at a constant velocity and recording the motor torque signal. This is repeated for a number of different velocities. The discrete time torque signals are turned into discrete position signals and then filtered to remove all position frequencies above 1CPR. The resultant A axis torque signals for a number of different velocities are shown in the top graph of figure 5.21.

For the A Axis of the Hirata robot a third order polynomial was used to describe the low frequency PDFV components. The model is shown as the dark blue line in the bottom plot of figure 5.21. The light blue lines are the measured data as shown in the top plot of figure 5.21 with the viscous and Coulomb friction components removed.

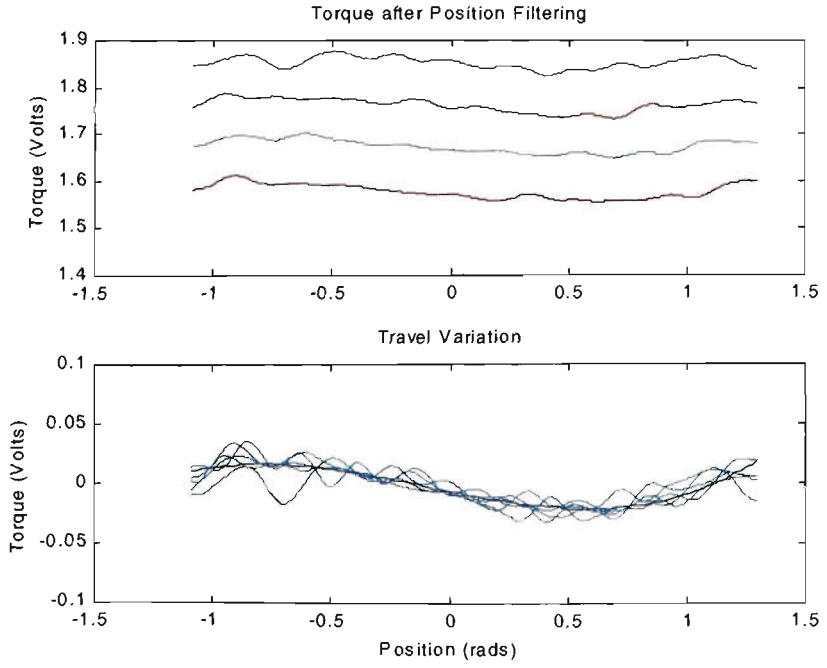

Figure 5.21 A Axis Low Frequency PDTV components (1 Volt =4.4Nm)

5.5.2 Signal Processing

The force estimation techniques developed and used in Section 5.2 have only been used on mechanisms travelling in one direction. The position domain signal processing used as part of the force estimation procedure assumes that the position and torque data are generated with velocity is one direction. The position domain techniques do not work for velocity reversals as this is effectively going back in time in the time domain. In order to avoid this the torque and position data for each axis is divided into sections with the same velocity direction. This is shown for the motor torque and velocity data from the A and B axes in figure 5.22. Different colours are used to indicate the section the data is divided up into. Each of these separate sections for the A and B axes of the robot is processed individually.

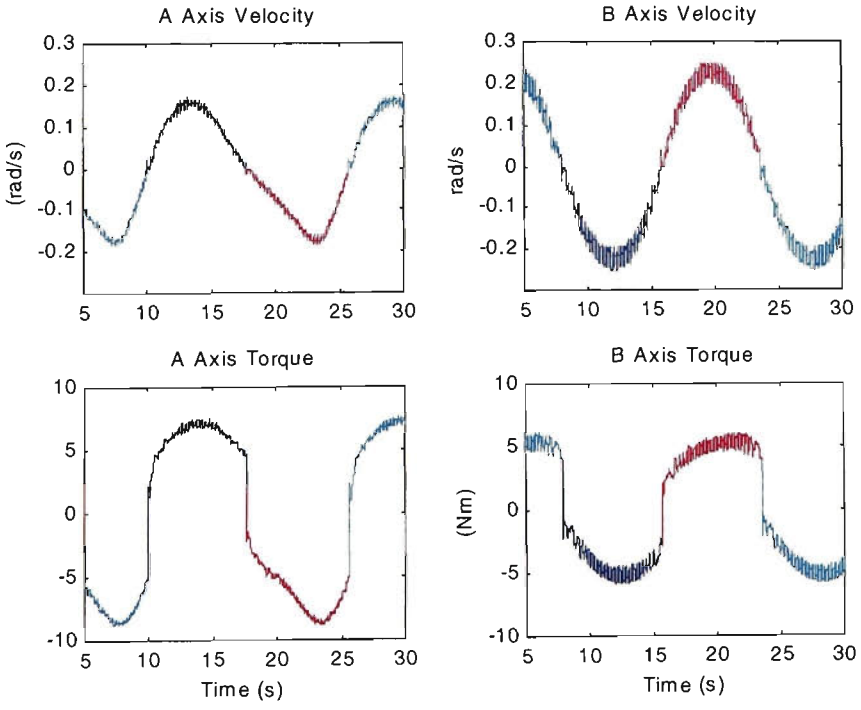

Figure 5.22 Velocity and Motor Torque for the A and B axes of the Hirata Robot

As discussed in Section 5.5 a spring was used to generate the external force and a circular path was used to keep a constant spring force. The results given in this section are for the robot tracking a circular path with a 130mm radius and an angular velocity of 0.4rad/s. For the spring being used a radius of 130mm corresponds to a spring force of

3.5 N. Using Eq 5.26, 5.28 the expected torques at the A and B axis can be calculated. These torque values are shown in figure 5.23.

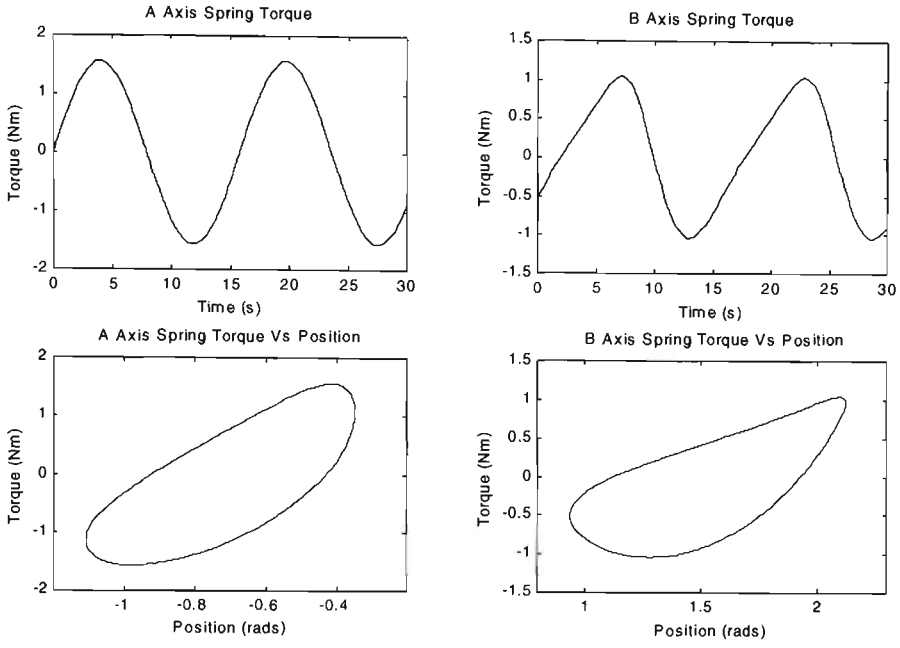

Figure 5.23 A and B Axes Spring Torques

The top two graphs show the spring torque values plotted against time and the bottom two graphs shown the torque values plotted against position. The graphs plotting torque against position are used as a baseline to compare the output of each stage of the signal processing. The output of the torque estimation processing should ideally be the spring torque components.

The torque estimation signal is calculated using Eq 5.29 and is shown for the A and B axis data in the top two plots of figure 5.24. The green plots show the torque estimation signal calculated from the recorded position and torque data. The red line is the calculated spring force and is taken from figure 5.23. The first stage of the signal processing is to filter the torque estimation signal with a low pass filter in the time domain. The filtered torque estimation signals are show in the bottom plots of figure 5.24

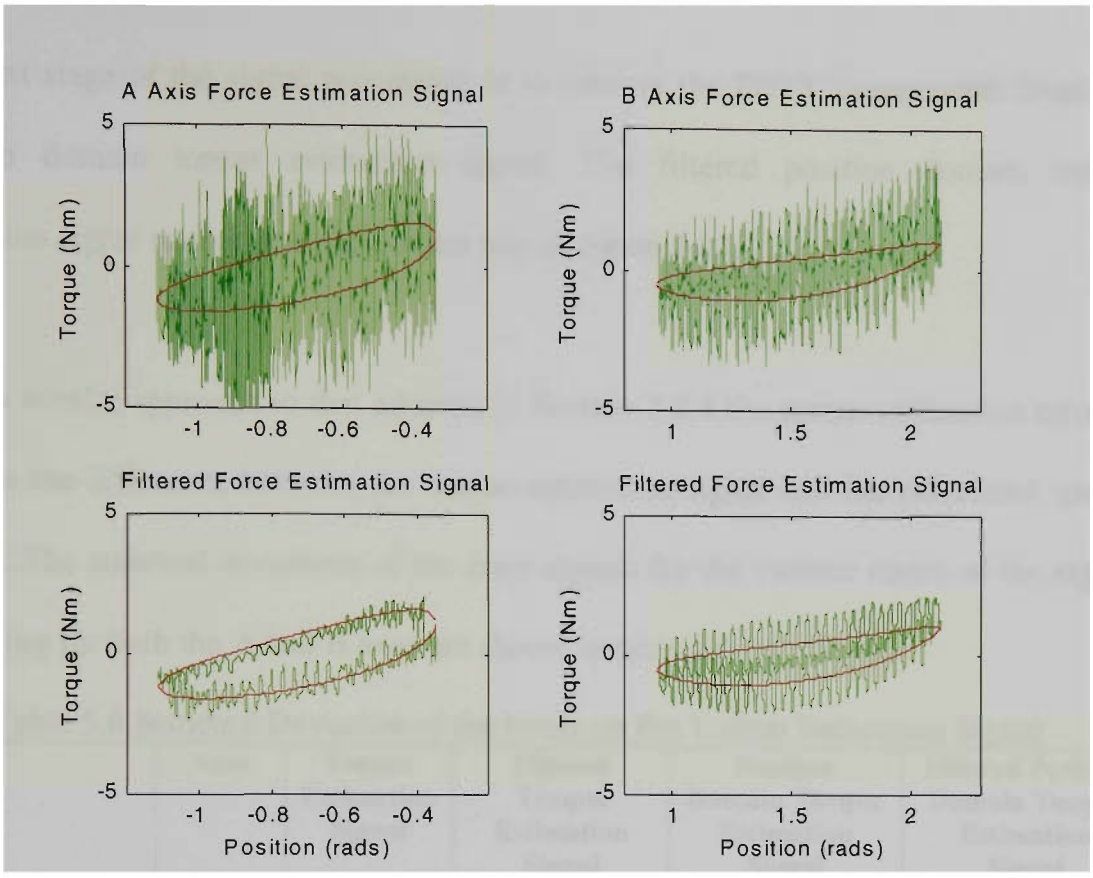

Figure 5.24 Time Domain Torque Estimation Signals

The filtered torque estimation signal is turned into a discrete position signal using the position binning techniques discussed in Section 4.4. The position domain torque estimation signals for the A and B axes are shown in the top plots of figure 5.25.

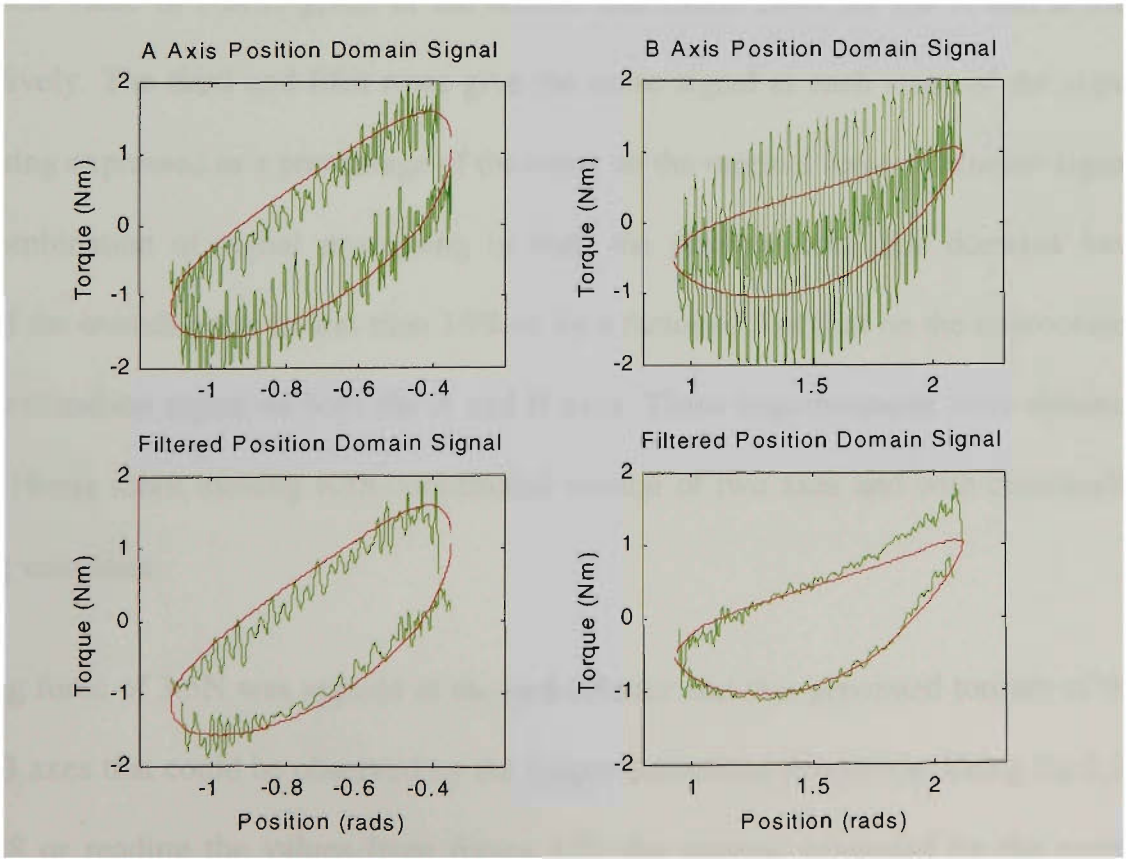

Figure 5.25 Position Domain Torque Estimation Signals.

The next stage of the signal processing is to remove the PDTV components from the position domain torque estimation signal. The filtered position domain torque estimation signal is shown in the bottom plot of figure 5.25.

Using a similar approach to that adopted in Section 5.2.4 the torque estimation error is taken as the difference between the torque estimation signal and the calculated spring torques. The standard deviations of the error signals for the various stages of the signal processing for both the A and B axes are shown in table 5.6

Table 5.6 Standard Deviation of the Noise on the Torque Estimation Signal

	Axes	Torque Estimation Signal	Filtered Torque Estimation Signal	Position Domain Torque Estimation Signal	Filtered Position Domain Torque Estimation Signal
Torque (Nm)	A	1.38	0.34	0.33	0.22
% of original noise signal	A	100	25	24	16
Torque (Nm)	B	0.932	0.64	0.64	0.16
% of original noise signal	B	100	68	68	17

The noise value in Nm is given in the second and fourth rows for the A and B axes respectively. The third and fifth rows give the noise signal at each stage of the signal processing expressed as a percentage of the noise on the original force estimation signal. The combination of signal processing in both the position and time domains have reduced the overall noise to less than 18% or by a factor of 5 of that on the unprocessed torque estimation signal on both the A and B axes. These improvements were obtained for the Hirata robot moving with coordinated motion of two axes and with continually varying velocities.

A spring force of 3.5N was applied at the end effector and this generated torques at the A and B axes that could be observed by the torque estimation procedure. Using Eq 5.26 and 5.28 or reading the values from figure 5.23 the torques generated by the spring

force are 1.5Nm and 1.0Nm for the A and B axes respectively. These values are listed with other relevant torque values in table 5.7.

Table 5.7 Hirata Robot Torque Values

	A Axis (Nm)	B Axis (Nm)
External Spring Force of 3.5Nm	1.5	1.0
Coulomb Friction	6.6	4.8
Torque Limit - Motor Rating	60	29

The main torque component the A and B axes motors have to overcome is the frictional torque and at low velocities this value approaches the Coulomb friction. The Coulomb friction values for the A and B axes of the Hirata robot are calculated in Section 2.2.3 and are given again in table 5.7. Hence the torque estimation techniques are capable of observing torques which are 25% of the Coulomb friction. Using the values given in table B.4 and the conversion factors given in table 2.2 it is possible to work out the maximum continuous torque that can be delivered by each axis and these values are also listed in table 5.7. It can be seen that the torque estimation techniques are capable of observing torques which are less than 4% of the rated torque values.

5.6 Conclusions

In this chapter a technique using servo motor position and torque data to estimate an external force applied to a mechantronic system is developed. The signal processing techniques used in both the time and position domains are described and the interrelationship between position sampling rates and frequency sampling rates are detailed. The characteristics of the low pass filter used as part of the time domain signal processing is given and its characteristics in the position domain are also derived.

A series of experiments were carried out on the grinding machine in which a known force was applied to the system. This known force was compared to the results obtain from the force estimation procedure and the effectiveness of each stage of the signal

processing was quantified. The time domain low pass filter reduced the noise by 72%. The filtering of PDFV components in the position domain reduced the noise by a further factor of four from 18% to 4 %.

A computer simulation of the X axis of the grinding machine was made. The model included the system mass, friction, PDFV decoder quantisation and an external force. The force estimation signals produced from the computer simulation were very similar to those produced from the actual position and torque data. Decoder quantisation was identified as a major source of noise. This is caused mainly by the force component due to the acceleration which requires the double derivative of the position data. It was shown that the majority of this noise source was removed by the time domain low pass filter.

Several grinding experiments were undertaken and it was shown that grinding forces could be measured in practice using the force estimation techniques. The results were compared with grinding forces measured with force sensors and calculated from spindle motor power measurements. The force estimation techniques on the X axis of the grinding machine had an overall noise level of 5.8N. The force estimation techniques would easily be able to measure and detect grinding force of an order of magnitude greater than this i.e. 60 N. In the grinding machine the maximum tangential grinding force that could be generated was 80N so the force estimation techniques were not applicable at the upper end of the grinding machines operating range. The maximum grinding force is limited by the spindle motor power and on the grinding machine the spindle motor rating is 1.1kW. It should be noted that there are many grinding applications using much greater spindle motor powers and so the force estimation

techniques are expected to be applicable over a wider operating range in these larger machines.

Force estimation techniques were also successfully applied to robot systems using coordinated motion in two axes and varying velocities. The force or torque estimation techniques were modified to deal with velocity reversals by dividing the data into regions with the same velocity direction. The torque estimation techniques when applied to the robotic system reduced the noise by a factor of 5. The torque estimation techniques were capable of observing torques of 1.5Nm and 1.0 Nm on the A and B axes respectively. These torque values are less than 4 % of the rated torque that could be produced by the robot's servo motors.

A method for estimating applied external forces was presented and verified on two different mechatronic systems and experimental results were presented for both systems. The signal processing techniques to remove the noise from the force estimation signals were described in detail and their effectiveness has been illustrated with experimental data. The techniques were robust enough to be applied to two different mechanical systems and by implication could be used in many other mechanical systems with friction.

The signal techniques processing developed in chapter are used as a basis for the real time and force control experiments of the following chapter. Although the signal processing techniques are implemented offline they have many applications in there own right (as well as the basis for the work in Chapter 6). E.g measuring the grinding

forces applied to a part as it is manufactured and from this information deciding to manufacture the next identical part with a higher or lower feedrate.

6 REAL TIME FORCE ESTIMATION AND CONTROL

6.1 Introduction

One of the main motivations for the force estimation schemes developed in the previous section was the measurement of grinding forces. There are additional benefits in having real time grinding force measurements. Such measurements provide a monitoring tool if the force signal is observed as a part is being machined and more significantly the force could be used as a feedback signal in a real time force control scheme. The benefits in using constant force grinding are discussed in Section 1.3. If the real time force signal is derived from motor torque and position data then the benefits of constant force grinding can be achieved without the need for any additional sensors. Sensorless operation removes many of the disadvantages of force sensors. These disadvantages include the cost of the sensor, the reduction of the system's stiffness induced by the sensor and the special mounting arrangements required by the sensor.

The real time force estimation procedure is very similar to the force estimation procedure described in Chapter 5. The same signal processing steps are followed for the calculation of the force estimation signal from measured position and torque data using the systems parameters i.e. low pass filtering in the time domain and then processing in the position domain to remove the PDFV. All the signal processing steps are implemented in real time on the DSP. Although the processing steps are the same the implementation of position binning and filtering of the PDFV vary significantly from the offline processing described in Chapter 5.

In Section 6.2 the real time force estimation procedure is described. Real time position binning techniques used to convert real time signals to "real position" signals are

described. The real time position filter used to remove PDFV components is developed. The filter's design is discussed and its characteristics are described.

In Section 6.3 a real time force control scheme is developed. The real time force estimation signal is used as the force feedback in the control loop to control the tangential grinding force. The tangential grinding force is proportional to the metal removal rate. In the experiments a fixed depth of cut is used and the metal removal rate and the tangential grinding force are changed by varying the feedrate. The force control scheme is demonstrated for a number of different force references.

6.2 Real Time Force Estimation

A real time force estimation signal is calculated from the differential equation describing the mechanical system Eq 5.2. The mass, low frequency PDFV, viscous and coulomb friction are needed to calculate the force estimation signal. These values are calculated in the same manner as described in Section 5.2.1 and have to be known before running the real time force estimation software. The friction parameters are downloaded to the DSP as part of the startup procedure and these values with the position and torque value measured in real time are used to calculate the force estimation signal. The real time force estimation signal is then filtered with a low pass filter in real time and the filtered force estimation signal is then processed in the position domain.

In order to process the force estimation signal in the position domain the concept of "real position processing" needs to be considered. The information is processed at the position the data is recorded. The data collected and processed signal are "real position"

signals. This is analogous to real time processing at which information is processed at the time it occurs and the data and the processed signal are real time signals.

The discrete real time signals are turned into discrete position signals using real time position binning techniques. The position sampling rate and hence the bin size is selected using the same method as described in Section 5.2.3. In offline signal processing it is simple to adjust the position sampling frequency after the data has been collected and to choose the most appropriate for each measurement. In the real time system the position sampling rate is set for each measurement and changing the position sampling rate between measurements also means modification of PDFV filter coefficients (discussed in Section 6.2.1). As a change in the position sampling rate is difficult in practice a position sampling rate is set and used over a specified range of velocities.

The real time position binning process involves dividing the mechanism's travel into a series of position bins. At each sampling period the position is recorded and the filtered force estimation signal calculated. The filtered force estimation signal is then placed into one of the position bins determined from the current position. At the next sampling period the process is repeated and if the position value has not increased sufficiently to move to the next position bin the filtered force estimation signal is placed in the same position bin. If the position value has moved to the next bin the filtered force estimation signal is placed in that position bin and the filtered force estimation signals that fell into the previous bin are averaged to give one value for that bin. If a bin is passed over altogether then the value for this bin is taken as the average of the present filtered force estimation signal value and its value for the preceding bin. The real position domain

force estimation signal is then used as an input to the PDFV filter (described in Section 6.2.1).

The real position domain force estimation signal is not necessarily updated every sampling period since it is only updated if the position has moved to the next position bin. Consequently the PDFV filter output is not calculated every sampling period. The software developed only allows travel in one direction and the results given in this section are for travel in one direction.

6.2.1 PDFV Filter

The PDFV filter is used to remove the PDFV components from the real position force estimation signal. The real position force signal should ideally be the actual grinding force and the PDFV components that the filter will remove. In figure 6.1 an oversimplified idealised real position force estimation signal is shown. The signal is made up of only one of the PDFV components and the grinding force. As the grinding wheel hits the work piece there is sudden increase in force. The PDFV are of constant position frequency and their magnitude does not vary over the mechanism's travel. In figure 6.1 a stepped force response of 50N with a PDFV of position frequency 1CPR and magnitude of 20N is shown. These values are typical of what was observed in Chapter 5. Ideally the PDFV filter removes all the PDFV leaving the grinding force component untouched and the filter has no delay. The output of this ideal filter is shown in the bottom graph of figure 6.1.

Consider a discrete positional signal with value $u(k)$ at the kth sampling interval and value $u(k-1)$ at the previous position sampling interval. Consider a window of N points starting at point $u(k)$ which includes all the previous points to $u(k-N+1)$ i.e.

$$u(k),u(k-1),u(k-2).....u(k-N+1),u(k-N),u(k-N-1)$$

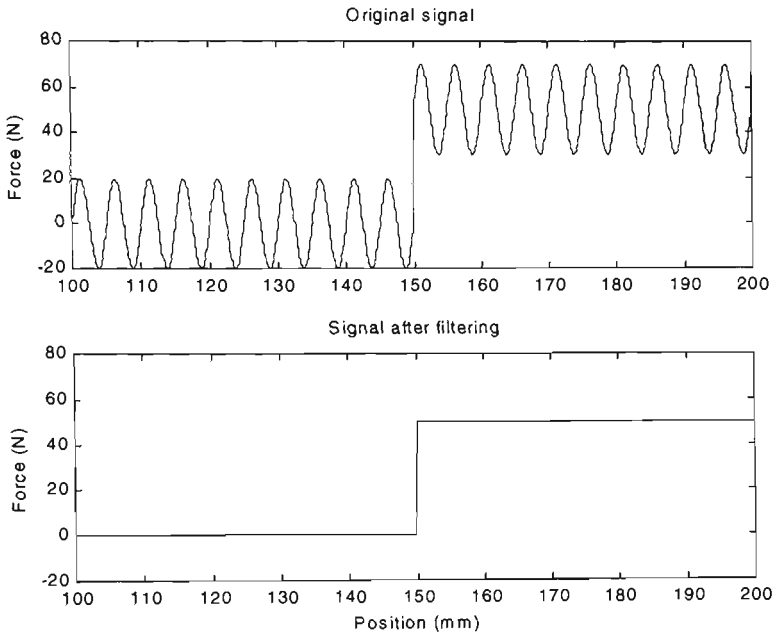

Figure 6.1 Idealized Real Position Force Estimation Signal and Filtered Signal

If the discrete Fourier transform is calculated over this window the position frequency spectrum made up of position frequencies $U(m)$ is given by:

$$U(m)=\sum_{n=0}^{N-1}u(k-n)W^{mn} \quad \text{for} \quad m=0,1,.....,N-1 \text{ where } W^{mn}=e^{-j2\pi mn/N} \qquad \text{Eq 6.1}$$

The signal $U(m)$ is filtered in the position frequency domain with a filter with frequency response $H(m)$. The filtered signal $Y(m)$ is given by:

$$Y(m)=H(m)U(m) \qquad \text{Eq 6.2}$$

The filter $H(m)$ is required to remove the PDFV frequency components. This is achieved if the magnitude of $H(m)$ is set to zero at the PDFV position frequencies. The phase of the original signal is to be left unaltered so the phase of $H(m)$ is zero for all m. If the PDFV occur at position frequencies $\Phi_1,\Phi_2,\ldots$ and the position sampling frequency is Φ_s the parameters of $H(m)$ are given by:

$$H(m)=0 \quad \text{for} \quad m=\frac{N\Phi_1}{\Phi_s},\frac{N\Phi_2}{\Phi_s},.....,\frac{N(\Phi_s-\Phi_2)}{\Phi_s},\frac{N(\Phi_s-\Phi_1)}{\Phi_s}$$

$$H(m)=1 \quad \text{for all other } m \qquad \text{Eq 6.3}$$

The filtered response in the position domain $y(n)$ is then the inverse discrete Fourier ansform of $Y(m)$ and this is given by:

$$y(n) = \frac{1}{N}\sum_{m=0}^{N-1} Y(m)W^{-mn} \qquad \text{for } n = 0,\ldots\ldots N-1 \qquad \text{Eq 6.4}$$

The first point of the window is when $n = 0$ and the last point is when $n = N-1$. The original window was for the points between $u(k)$ and $u(k-N+1)$ and keeping the same order for the filtered signal then $y(0) = y(k)\ldots.. y(k-N+1) = y(N-1)$. The signal processing sequence is shown in figure 6.2.

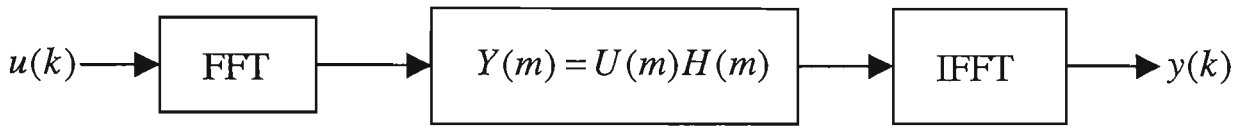

Figure 6.2 PDFV Filtering Process

Since after the inverse discrete Fourier transform is calculated only the point $y(k)$ is kept, only the point $y(k)$ has to be calculated and Eq 6.4 reduces to:

$$y(k) = \frac{1}{N}\sum_{m=0}^{N-1} Y(m) \qquad \text{Eq 6.5}$$

At the next discrete position sample $u(k+1)$ the window is moved along one point so the points from $u(k+1), u(k)\ldots\ldots u(k-N+2)$ are included in the window which the FFT is calculated over and in a similar manner $y(k+1)$ is calculated and so on for subsequent discrete position samples.

The filtered value $y(k)$ is available at the same time as $u(k)$ is recorded (neglecting computation time) so the filtering process has no delay. This makes the PDFV filter particularly useful in control applications where a time delay is undesirable. For the signal $u(k)$ the FFT calculates the position frequencies over the previous N points. The phase and magnitude of the PDFV frequency components removed from the signal

$u(k)$ are determined from the previous N samples. The filter output $y(k)$ is the original signal $u(k)$ with the PDFV frequency components removed.

The filter position frequency response $H(m)$ is defined as a set of discrete position frequencies. The position frequency response outside these discrete position frequencies is not defined. The actual frequency response of the filter can be determined by applying a range of position frequencies with a higher frequency resolution than the filters. The filter implemented used a 512 point window with a position sampling frequency of 64 CPR. The position frequency resolution of the filter is 64/512 =0.125CPR. The filter removes the position frequencies [1 2 3 4 5 8 12 27] CPR as is removed in the offline processing as discussed in Section 6.1.4. The filter's actual position frequency response is shown in the top graph of figure 6.3.

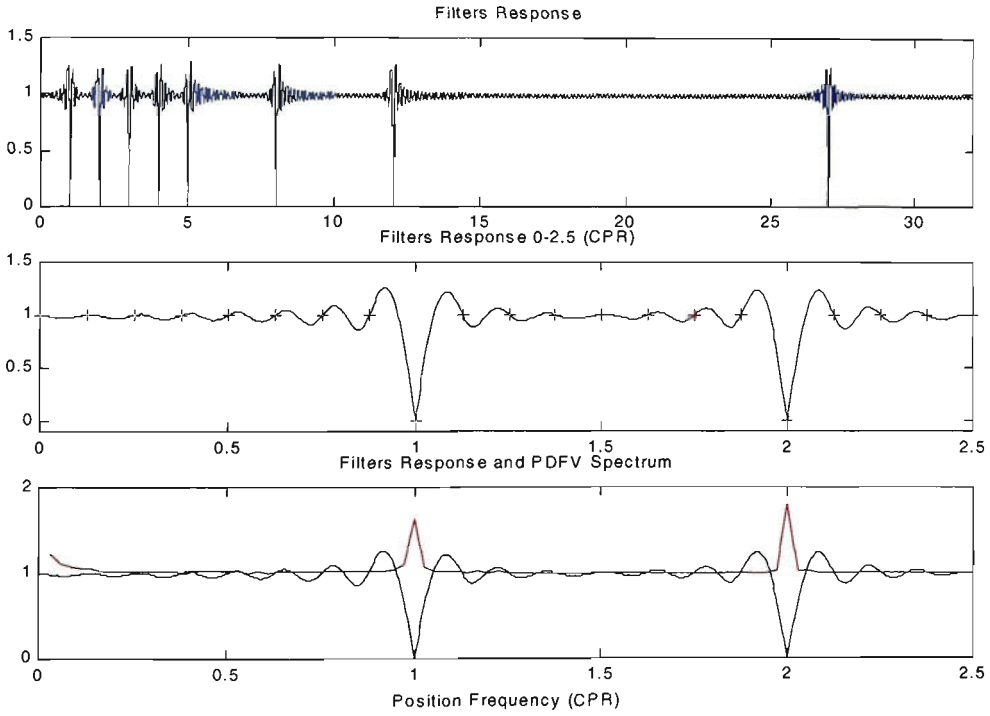

Figure 6.3 Filter's frequency Response.

The middle plot of figure 6.3 shows the position frequency response between 0-2.5 CPR. Also shown in this graph are the points defined by the filter $H(m)$ marked with red crosses. As can be seen the actual filters response does pass through all the points

specified by $H(m)$. However between these points there are quite large oscillations. This oscillation at the frequency notches is referred to as the Gibbs phenomenon [54,55] and is discussed in detail in these texts. In short the oscillation are due to the FFT being calculated over a limited window. Any sharp changes in periodic signal will cause these oscillations because of the limited frequency range of the FFT.

The oscillation on either side of the frequency notch is 18% higher than the desired response. For the PDFV being filtered this is not a large disadvantage. In the bottom graph of figure 6.3 the PDFV to be filtered are shown with the filter's characteristics. The PDFV spectrum shown is derived from the position frequency spectrum shown in figure 4.6. The PDFV values have been scaled so they can be plotted on the same graph as the filter's characteristics. As can be seen the PDFV spectrum falls within the filter's frequency notches.

One property of a discrete Fourier transform is that a convolution in the discrete position domain is equivalent to a multiplication in the position frequency spectrum:

$$\sum_{n=0}^{N-1} u(k-n)h(n) \Leftrightarrow H(m)U(m) \qquad \text{Eq 6.6}$$

Therefore there exists a filter $h(n)$ that will give the same response filtering in the position domain using a convolution as the filtering method described in the preceding part of this Section. The filter parameters $h(n)$ are simply the inverse discrete Fourier transform of *H(m)*.

The filter used is applied to the idealised signal shown in figure 6.1 and the output is shown in figure 6.4. The top graph shows the result of implementing the filter in the

position frequency domain and the bottom graph is with the filter implemented in the position domain. The results are as expected. The PDFV filter is implemented as a convolution in the position domain because this is computationally more efficient. The filter has 512 coefficients (or a window with 512 points) and using a position sampling rate of 64CPR this corresponds to a window length of 40mm. As can be seen from figure 6.4 it takes 40mm for the filter to remove the PDFV. This means the mechanism needs a section of travel of at least 40mm before it hits the workpiece. The force estimation signal in this run up period is not particularly useful due to the large PDFV component still present.

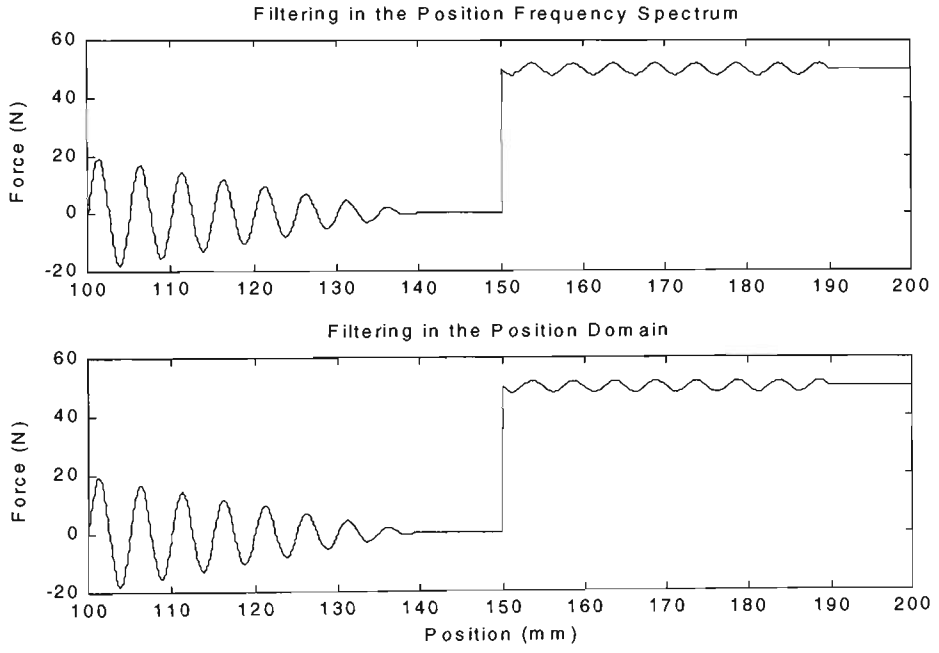

Figure 6.4 PDFV filter

As can also been seen from the right hand side of figure 6.4 there is a ripple with a position frequency of 1CPR on the top of the step response. The ripple lasts for one filter length (40mm) until the step has passed through the window. The ripple is caused by the PDFV filter, which removes not only the PDFV components but also the components of the idealised signal of the same frequencies. This slightly degrades the signal trying to be measured. However it is still a significant improvement over the signal with the PDFV component present. When the idealised signal is a constant within

the window it is not affected by the filter because it has a zero frequency component which is not affected by the PDFV filter.

6.2.2 Grinding Force Measurements

A series of real time grinding force measurements were made. The results given in this Section use a position sampling rate of 64 CPR and the velocity range used is 2-20mm/s. In the offline measurements discussed in Chapter 5 a low pass filter with a frequency cutoff of 20Hz was used. In the real time system a low pass filter with a frequency cutoff of 10Hz was used. Although this reduces the frequency response it does allow a wider range of velocities to be used.

As discussed in Section 5.1.3 the position sampling rate should be chosen to be twice that of the low pass filter's position frequency cutoff. The low pass filter's position frequency cut off is listed for a number of velocities between 2-20mm/s in table 6.1. The low pass filter's cutoff determines the minimum velocity that can be used. For example if a low pass filter with a cutoff frequency of 20Hz was used, when the velocity is 2mm/s the position frequency cutoff would be 50CPR. This is more than the Nyquist position sampling frequency of 32 CPR and as discussed in Section 5.2.3 would not be acceptable. A low pass filter with a cutoff frequency of 10 Hz when the velocity is 2mm/s gives a position frequency cutoff of 25 CPR (as listed in table 6.1) which is acceptable.

Table 6.1 Real time Position Frequency Parameters.

Velocity (mm/s)	**Bin Size (counts)**	**Position Sampling Rate (CPR)**	**Low Pass Filter Cut off (CPR)**	**Samples per Bin**	**PDFV Filter (CPR)**
2	256	64	25	19.5	1,2,3,4,5,8,12
5	256	64	10	7.8	1,2,3,4,5,8
10	256	64	5	3.9	1,2,3,4
20	256	64	2.5	2.0	1,2

The maximum allowable velocity is determined by the number of samples per bin. The number of samples per bin can be estimated using Eq 4.24 and as the velocity increases the number of counts per bin reduces. As discussed in Section 4.4 the number of counts per bin should ideally be at least 3, although theoretically there only needs to be one. In the following this requirement was reduced to 2 counts per bin to maximise the speed range. It was found that this method used with the real time binning process which estimates a force value if a bin has been missed, was adequate to ensure there was at least one data point in each bin in practice.

A series of grinding measurements was made with depths of cut varying between 20 μ m and 40 μ m and a range of velocities between 2 and 20mm/s. The real time force measurements are shown in figures 6.5, 6.7, 6.9 and the offline measurements calculated from data recorded at the same time are shown in figures 6.6, 6.8, 6.10. The force estimation signal is shown in green and the tangential force calculated from the spindle motor power is shown in red.

The real time force estimation signals have very similar characteristics to the offline force estimation signals. Both have the same response to the step input in the grinding force (i.e. when the workpiece first hits the grinding wheel) and rise to the same magnitude. A method to compare the relative accuracies of real time and offline force estimation as a measure of grinding forces is to compare the force estimation values to the grinding force calculated from the spindle motor power. Considering only the grinding region (130-180mm) the standard deviation of the force estimation error for the signals shown in figures 6.5, 6.6, 6.7, 6.8, 6.9, 6.10 are given in table 6.2. The error values are listed against depth of cut and feedrate and each error value corresponds to

one of the graphs in the figures mentioned. E.g. a depth of cut of 21 μm and feedrate of 5mm/s corresponds to the top graphs in figure 6.5 and 6.6 for offline and real time measurements respectively.

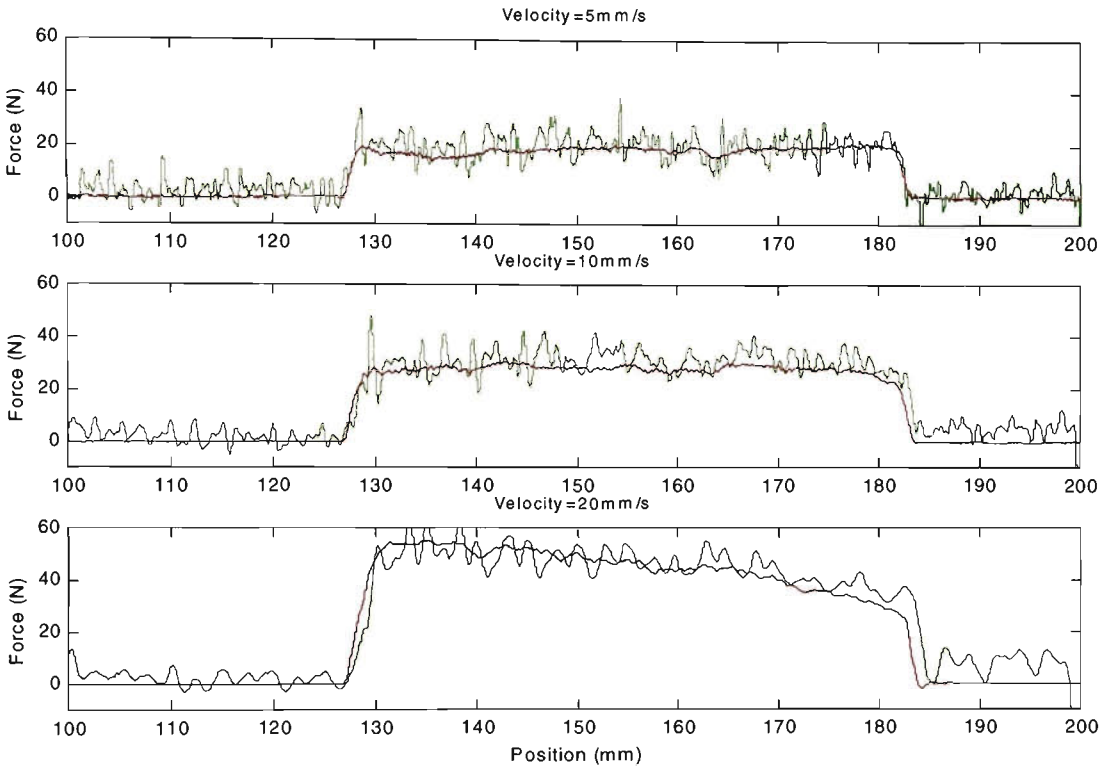

Figure 6.5 Real Time Grinding Force Results Depth of cut =21 μ m

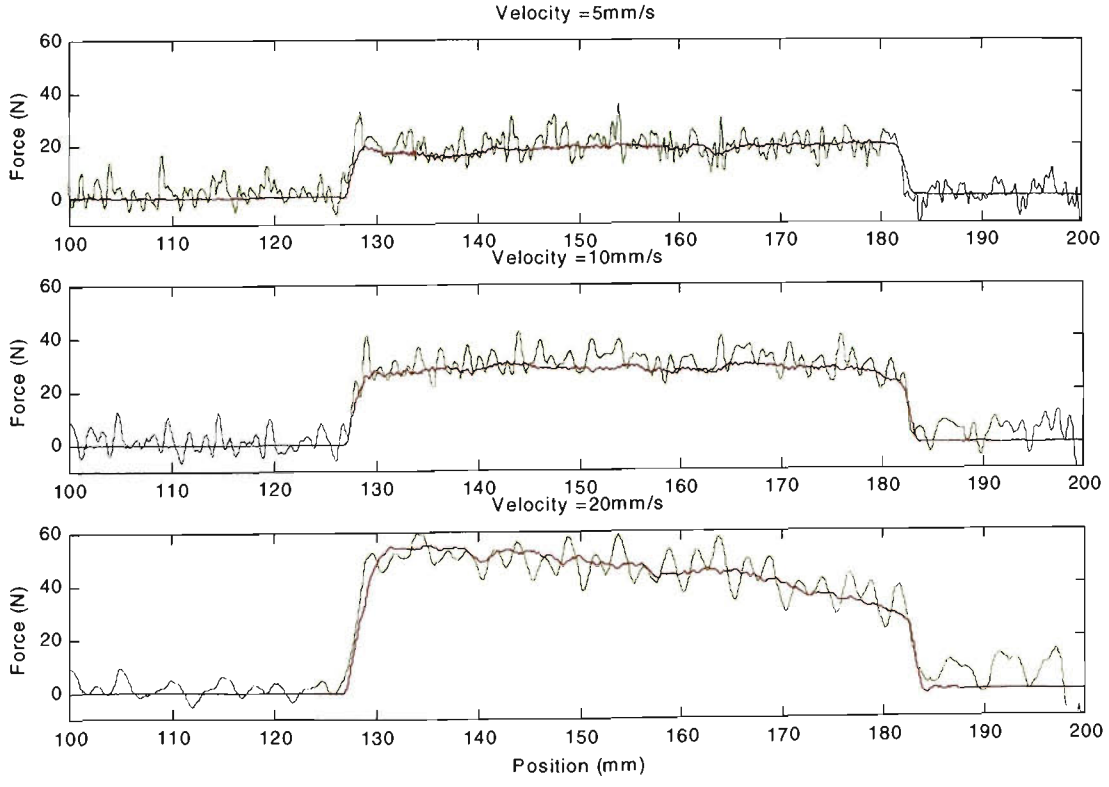

Figure 6.6 Offline Grinding Force Results Depth of cut =21 μ m

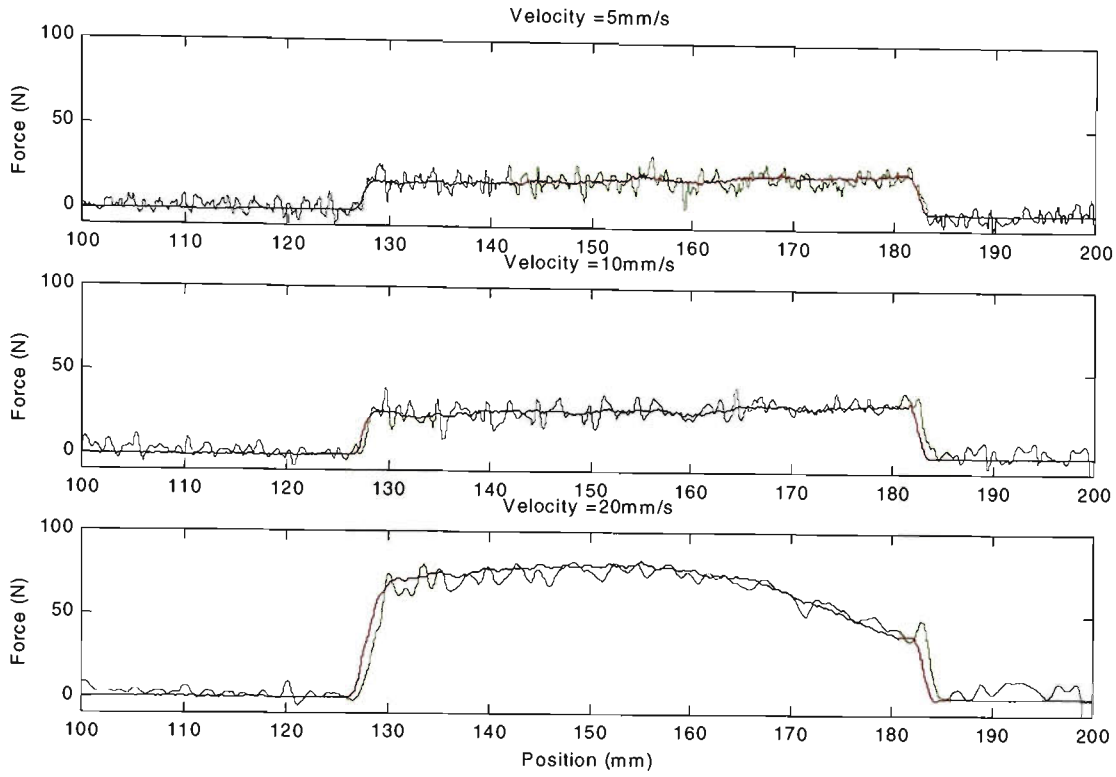

Figure 6.7 Real Time Grinding Force Results Depth of cut =31 μ m

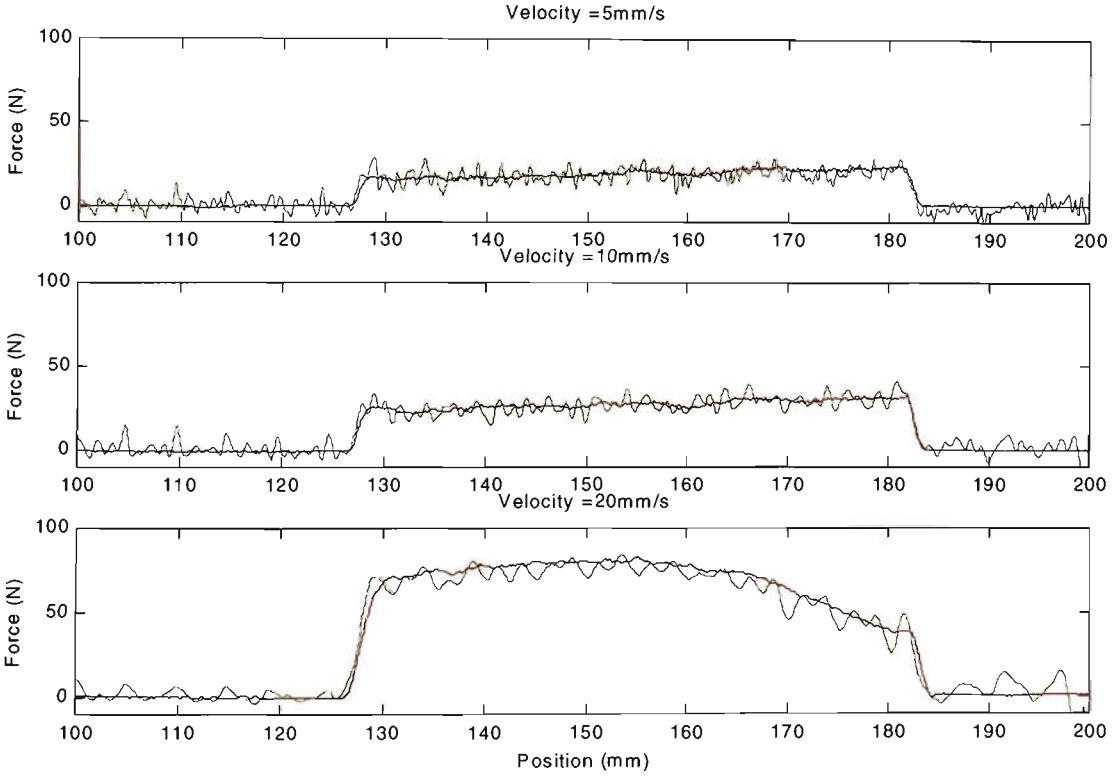

Figure 6.8 Offline Grinding Force Results Depth of cut =31 μ m

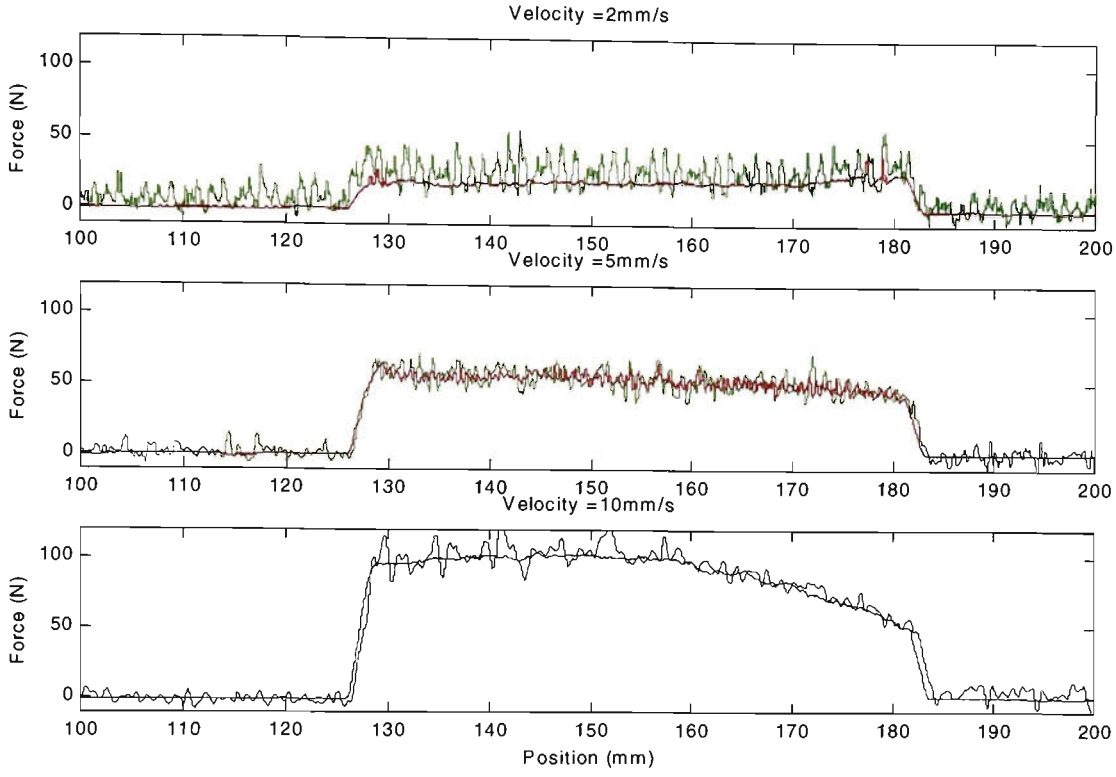

Figure 6.9 Real Time Grinding Force Results Depth of cut =38 μ m

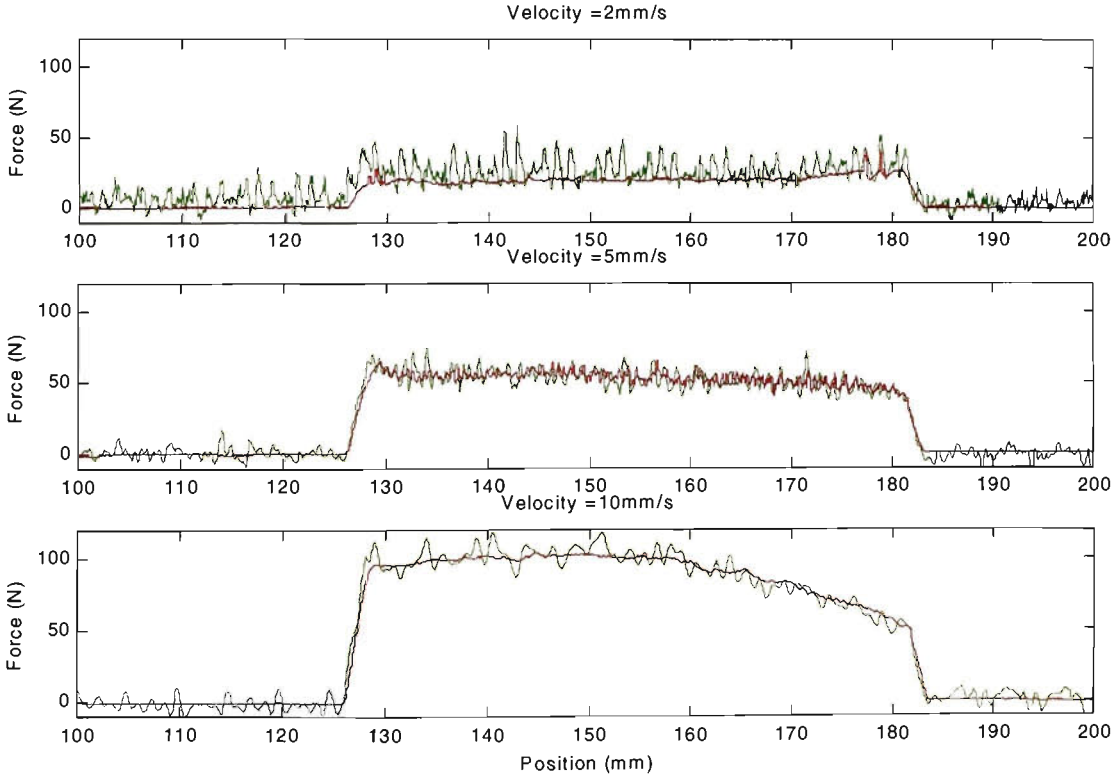

Figure 6.10 Offline Grinding Force Results Depth of cut =38 μ m

Table 6.2 Force Estimation Errors

Depth of Cut (μm)	Real Time Error (N)			Offline Error (N)		
	Feedrate (mm/s)			Feedrate (mm/s)		
	5	10	20	5	10	20
21	4.8	5.3	4.7	4.3	4.7	5.3
31	4.4	4.4	4.6	4.1	4.1	5.6
	Feedrate (mm/s)			Feedrate (mm/s)		
	2	5	10	2	5	10
38	11.8	7.1	6.7	10.2	5.4	5.8

The real time errors range from 4.4-11.8N with a mean value of 6.0N. The offline errors range from 4.1-10.2N with a mean of 5.5N. It can be seen that the error or noise on the real time signal is only slightly higher than that for the offline measurements. As previously mentioned in Section 5.4 the maximum tangential grinding force is 80Nm.The mean real time force estimation error is 7.5% of the maximum tangential grinding force.

The real time and offline measurements both have similar characteristics. For a constant depth of cut and feedrate the grinding force should be constant. As can be seen from figures 6.5, 6.6, 6.7, 6.8, 6.9, 6.10 the force varies along the length of the workpiece. There are many possible reasons for variation in grinding forces. Variation in the applied forces due variation of depth of cut due to non uniform workpiece, machine vibrations alignment of slides deflection of part. Also changes in the grinding process, these include flow of coolant onto the workpiece and workpiece temperature. These all effect the grinding process and grinding forces as a measure of this process change.

6.3 Force Control

A control scheme that controls the tangential grinding force is discussed in this section. The real time force estimation signal derived from servo motor position and torque data is used as the force control loop's feedback signal. The tangential grinding force is related to the metal removal rate and one means of modifying the metal removal rate is

to change the feedrate. The basic control strategy is to keep a constant depth of cut and control the tangential force by changing the feedrate (X axis velocity). The force control loop is outside the velocity control loop. The force control loop uses a PI controller whose output is a velocity reference for the inner velocity control loop. This is shown in figure 6.12 and discussed more fully in Section 6.3.2

6.3.1 Metal Removal Rate and Tangential Grinding Force.

As mentioned in Section 1.2 the specific grinding energy u is a very useful measure of the grinding process and relates the grinding power P with the metal removal rate Q_w. As also discussed in Section 1.2 other authors have described the grinding process in terms of specific energies. The specific energy is not constant and changes with each grinding process. The specific energy changes with the material being machined, the type of grinding wheel being used, the sharpness of the grinding wheel and is affected by work piece burning. From the control scheme perspective most of these do not change or change very slowly. The same material and grinding wheel are used for all the results given in this section. The grinding wheel sharpness also changes relatively slowly and if the grinding forces are limited so that work piece burn does not occur then parameter u can be assumed to be constant for the grinding experiments in this section.

In Section 1.2 an expression for the tangential grinding force F_G is given as:

$$F_G = \frac{uvab}{v_s} \qquad \text{Eq 6.7}$$

where a is the depth of cut, b the wheel width v is the feed velocity and v_s is grinding wheel peripheral velocity. The metal removal rate is given by:

$$Q_w = vab \qquad \text{Eq 6.8}$$

The grinding wheel is driven by an induction motor which operates essentially as a constant speed motor and hence v_s is constant. Combining Eq 6.7, 6.8 the tangential grinding force can be given by:

$$F_G = K_G Q_w = K_G vab \qquad \text{where} \qquad K_G = \frac{u}{v_s} \qquad \text{Eq 6.9}$$

Using the results of Section 6.2.3 the mean tangential force is plotted against the metal removal rate and this is shown in figure 6.11. The value of K_G can be determined from the slope of the line.

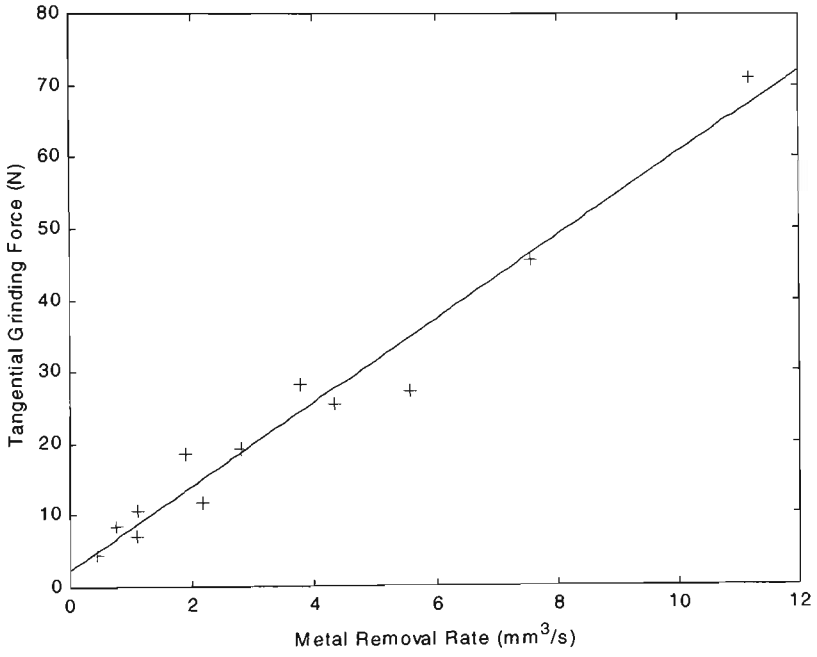

Figure 6.11Tangential Grinding Force Versus Metal Removal Rate

6.3.2 Control Loop Response

The force control loop is implemented outside the velocity control loop. The velocity controller is a standard PID controller. The low speed friction control techniques developed in Chapter 4 were not used in this section of work as the velocities used were all above than the low speed non linear friction region. The complete block diagram of the system is shown in figure 6.12. In the block diagram the force feedback signal is shown being passed through a low pass filter. The force feedback signal is the force estimation signal derived from the servo motor torque and position data.

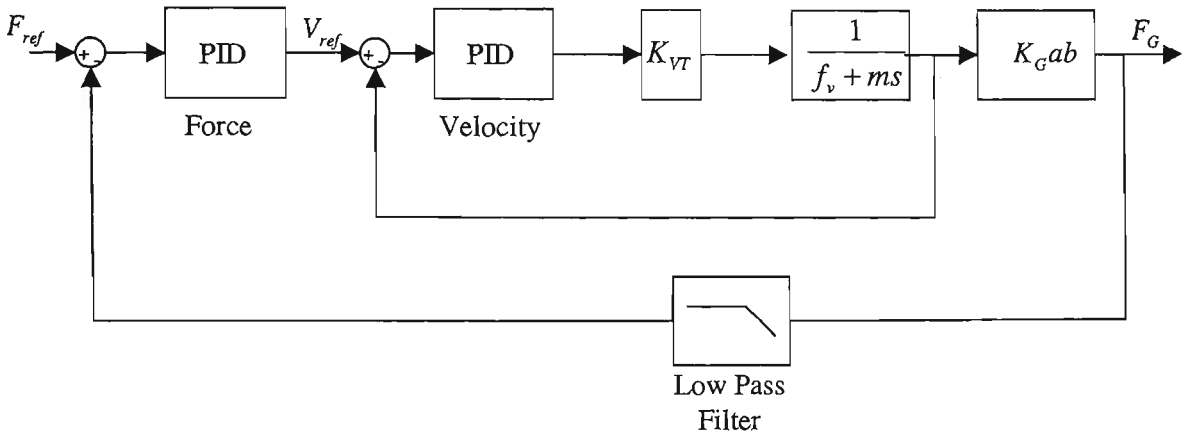

Figure 6.12 Force Control Complete Block Diagram

As discussed in Section 6.2 the first part of the force estimation process is to filter the signal with a low pass filter. The filter's characteristics are used to describe the frequency response of the force estimation process in the control loop. In Section 5.2.2 the closed loop response of the inner velocity loop was calculated and is shown as a single block in the simplified force control block diagram figure 6.13.

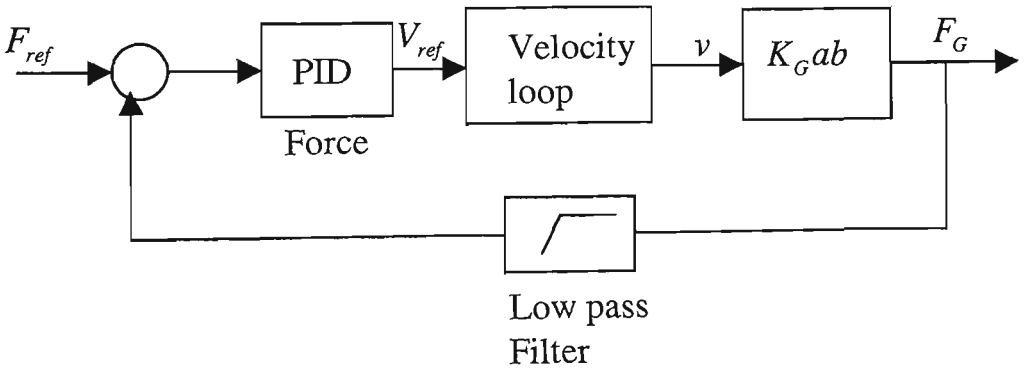

Figure 6.13 Simplified Force Control Block Diagram

The relationship between the grinding force and the velocity is described by Eq 6.9. As discussed in Section 6.3.1 the K_G term should remain constant and the wheel width b will not change; however the depth of cut a will change from experiment to experiment. A range of depths of cut between 10 and 50 μm were used. Changing the depth of cut will change the overall gain of the control loop. The open loop frequency response of the simplified force control scheme (shown in figure 6.13) is plotted in figure 6.14.

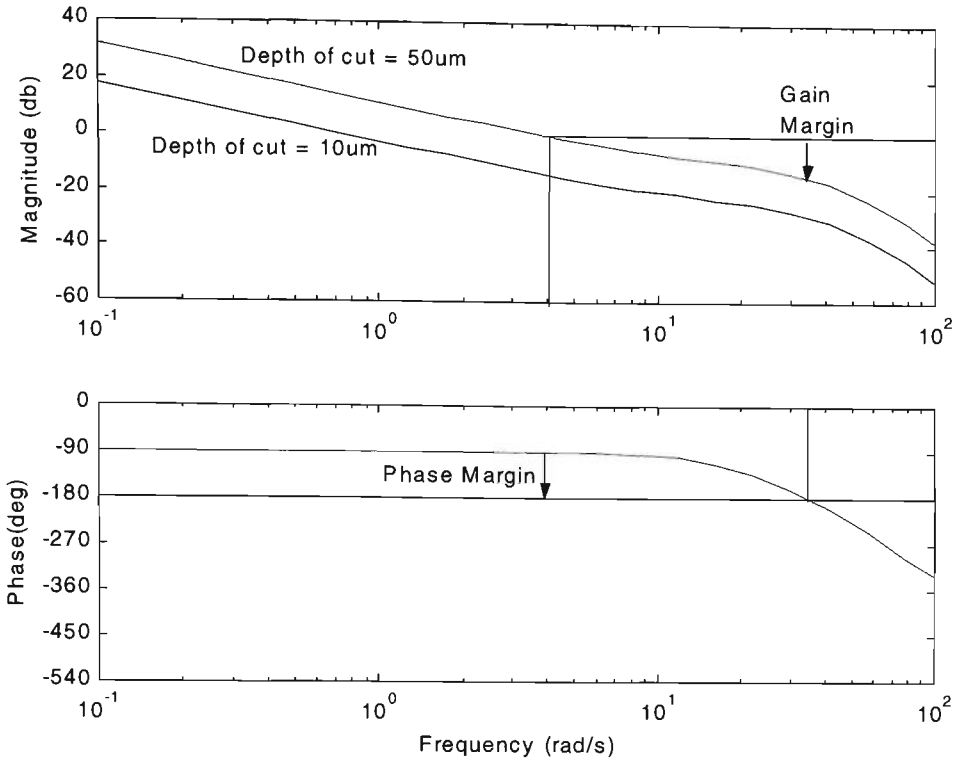

Figure 6.14 Bode plot of Force Control loop.

The magnitude response shows two graphs one for $10\,\mu m$ and one for 50 μm. The phase response is the same for both. As can be seen from these Bode plots the system is stable for the range of depth of cuts being used. In the worst case when the depth of cut is 50 μm the phase margin is 90 degrees and the gain margin is 15db.

6.3.3 Force Control Implementation and Results

One of the limitations of the force control loop described in Section 6.3.2 is that if the grinding force is zero then the velocity will keep increasing until the grinding force is the same as the force reference value. This is not a problem when the system is actually grinding but if the system is not grinding (e.g. is moving to the start of the work piece) the grinding force will always be zero no matter how high the velocity. This is overcome by having a force threshold. The system runs under velocity control until a certain measured force value is exceeded and the force control scheme takes over. In reality the system runs under velocity control until it hits the start of the workpiece

where there is a sudden increase in the grinding force, the force threshold is exceeded and the force control takes over.

The control loop also has a limited velocity range of 2-20mm/s set by the force estimation process as discussed in Section 6.2.3. In the force control experiments a range of depths of cut has used between 20-50 μm and force references between 40-80N were used. A typical force control result is shown in figure 6.15.

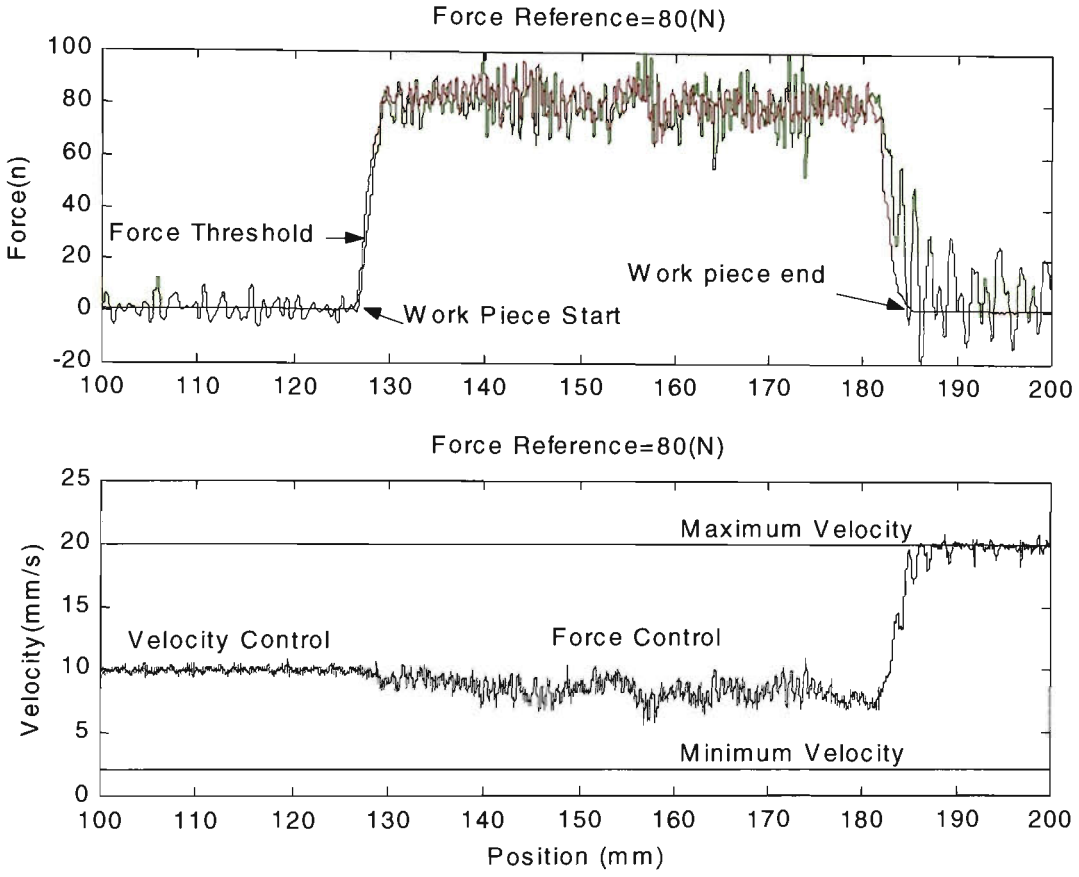

Figure 6.15 Constant Force Grinding Depth of Cut =40 μm

The system initially runs under velocity control where the velocity set point has been arbitrarily set at 10mm/s. The force control loop takes over once the force value exceeds the force threshold (30N) which is just after the start of the workpiece. Under force control the velocity is adjusted to try and maintain a constant force. After the end of the workpiece the system is still under force control and as the grinding force is zero the velocity increases to the maximum allowable i.e. 20mm/s.

If the grinding force reference is large and the depth of cut is small the maximum velocity will be reached; alternatively if the force reference is low and the depth of cut is large the minimum velocity limit can be reached. This is shown in figure 6.16 where the force reference is 40N and the depth of cut is $50\,\mu m$. As can be seen the velocity is always near 2mm/s.

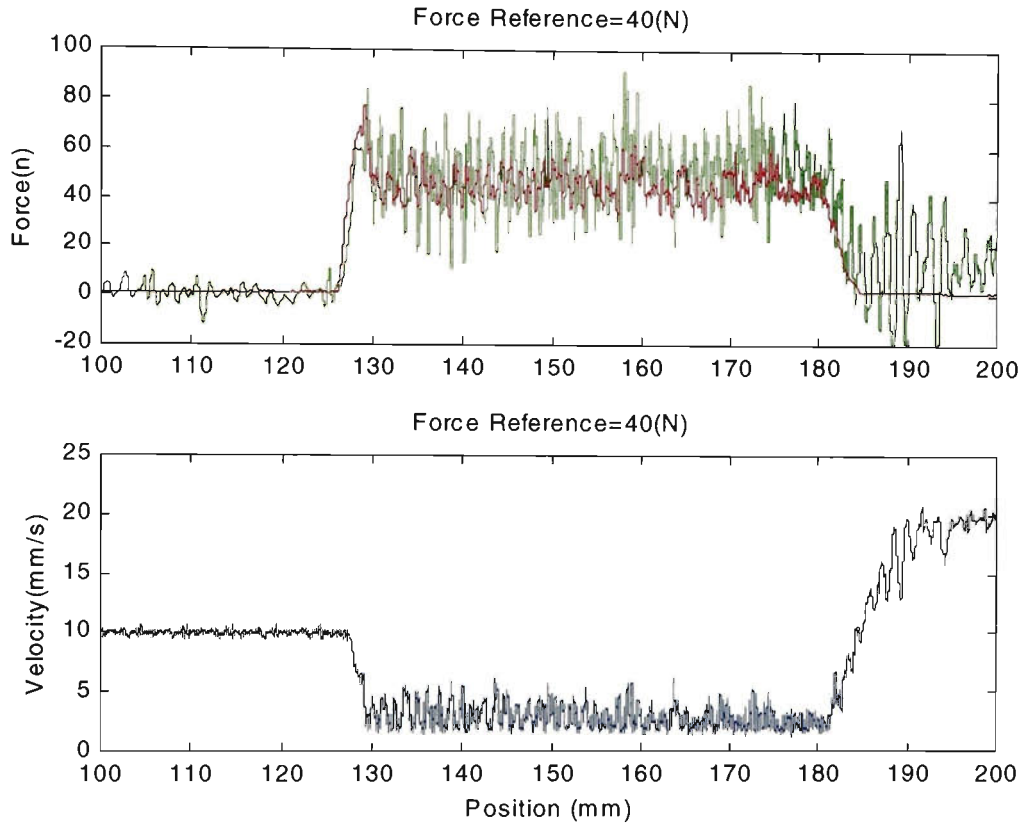

Figure 6.16 Minimum Velocity Limit Depth of cut =$50\,\mu m$

The force control results for $20\,\mu m$ and $40\,\mu m$ depth of cuts and force reference values of 40,60,80 N are shown in figures 6.17, 6.18. These figures also show how the velocity varies as it tries to maintain a constant force. The mean of each force estimation signal between 135-180mm for each of the graphs shown in figures 6.17, 6.18 is given in table 6.3. In this region the system is operating under force control and grinding is taking place. Also listed are the force reference values.

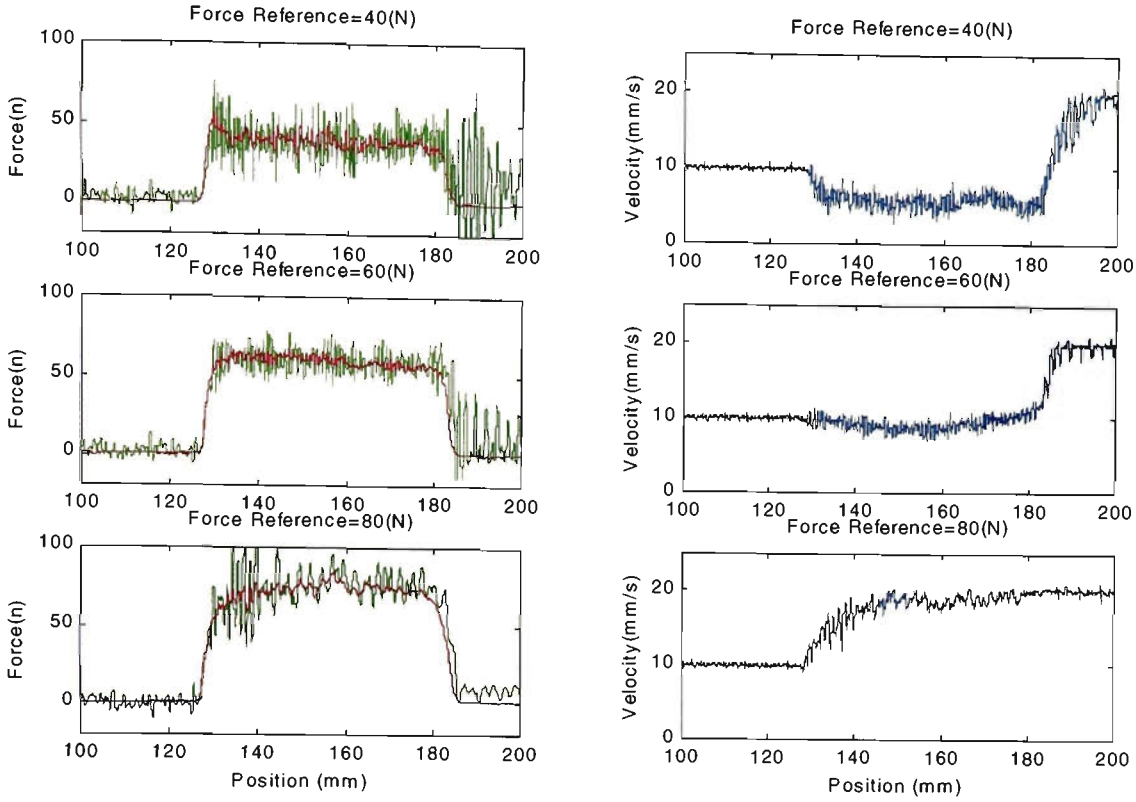

Figure 6.17 Force Control results Depth of cut =20 μm

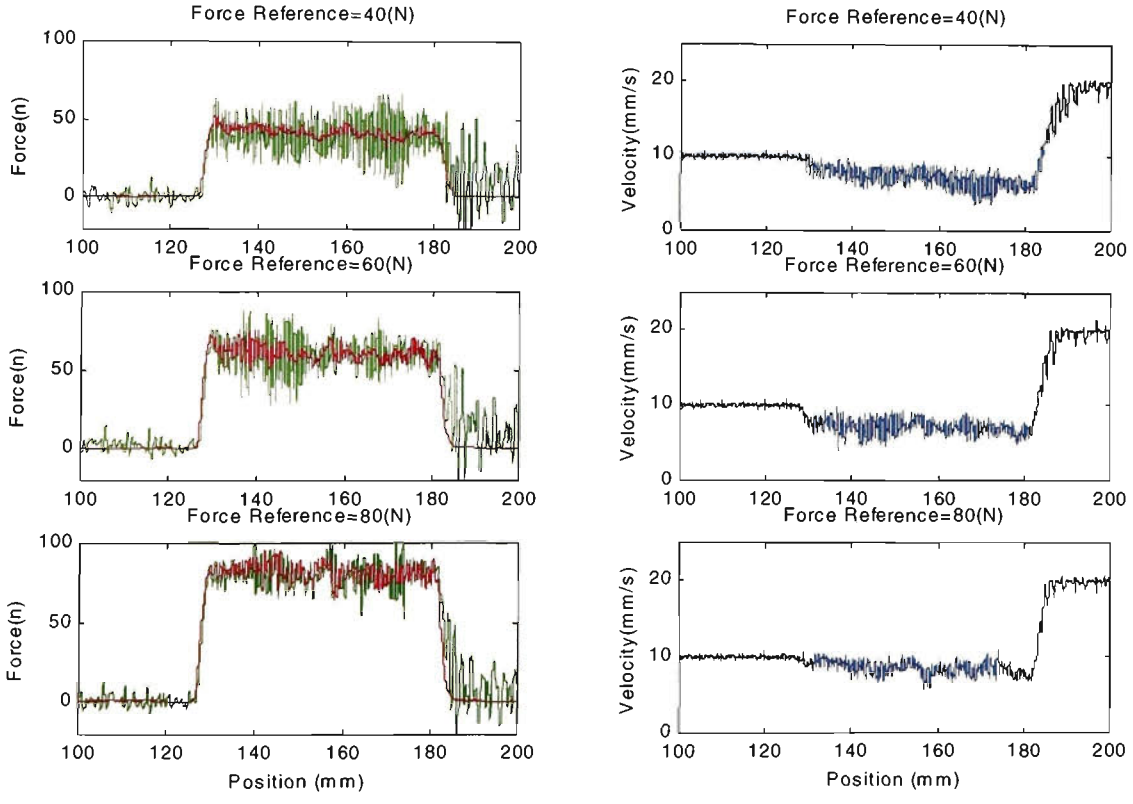

Figure 6.18 Force Control results Depth of cut =40 μm

Table 6.3 Force Control Results

Depth of Cut (μm)	Force Reference (N)	Mean Force Estimation Signal (N)	Standard Deviation (N)
20	40	40.1	9.9
	60	59.7	7.0
	80	76.5	11.1
40	40	40.4	11.8
	60	60.3	10.8
	80	80.4	7.9

It can be seen that there is close agreement between the force reference and the mean of the force estimation signal. The standard deviation of each of the force estimation signals is also given and ranges between 7.0–11.8 N. For a grinding force below 40N the standard deviation of the error signal would be more than 25% of the reference signal and the control scheme would not be recommended for control forces in this region. As discussed previously in Section 5.4 the maximum tangential grinding the grinding machine can generate is 80N and hence the force control scheme would only be applicable at the upper end of the grinding machine's machining region.

6.4 Conclusions

The real time force estimation procedure was described in this chapter. Concepts of real time position processing and real position signals were introduced. Real time position binning techniques that convert real time signals to real position signals were developed.

A real time position PDFV filter was designed. This filter removed the PDFV components in real position (and time) and had zero delay. This filter was particularly suited to filtering of PDFV components in which each component has a narrow and well defined position frequency peak.

The real time force estimation techniques were used to measure grinding forces. A series of grinding experiments using a number of different feedrates and depths of cut were conducted. The real time force estimation results were recorded and so were the position and torque data needed for the offline force estimation techniques. The results of the real time force estimation were compared to the offline force estimation results. The real time force estimation procedure produced very similar results to the offline force estimation techniques. In the series of experiments the real time force estimation procedure had a mean noise of 6N which was 0.5N or 8% more noisy than the offline force estimation procedure.

A sensorless grinding force control scheme was also implemented. The real time force estimation signal was used as the force feedback signal. The control system controlled the tangential grinding force by changing the metal removal rate. This was achieved by keeping a constant depth of cut and changing the feedrate. The control scheme was tested with a number of different force references and depths of cut. It was shown that the force estimation method can be implemented in practice and in real time as part of an online force control system. It was shown that the grinding force could be controlled within 12N (15% of the maximum grinding force) by changing feedrates in a feedback control scheme based on servo motor current and position data.

7 CONCLUSIONS AND FUTURE WORK

7.1 Conclusions

This thesis has studied two mechatronic system whose mechanical arrangements have large friction components. An understanding of friction and of position dependent forces has been used to implement force estimation and control schemes and to improve low speed position tracking in both these mechatronic systems.

In Chapter 1 a literature review of the objectives and an outline of the thesis were given. In Chapter 2 the mechatronic systems used in this thesis: the Hirata robot and the grinding machine are described. The mechanical and electrical systems' responses are given and the mechanical system parameters of mass, Coulomb and viscous friction are calculated.

In Chapter 3 a friction controller that improved the low speed tracking of mechanisms with friction was developed. Friction has a highly non linear characteristic at low velocities and using a conventional PID controller the system can exhibit "Stick Slip" behaviour when moving at low velocities. New friction controllers developed from that of Li et al [2] were implemented on the two mechatronic systems used in this thesis. In both systems the friction controller's improved the position tracking performance. These friction controllers are easy to tune and need a minimum knowledge of the system's friction parameters since the pulse height of the friction controller is greater than the largest difference between the Coulomb and static friction.

The friction controller was improved by adding velocity reversal compensation as discussed in Section 3.3. The velocity reversal compensation reset the integral part of the PID controller to the Coulomb friction value at velocity reversals.

In another improved version of the friction controller as described in Section 3.4, a static friction lookup table was used to select pulse heights. This version of the controller generally reduced the pulse heights applied to the mechanism and reduces the stress on the mechanical components.

In still another version of the friction controller a fuzzy logic controller detailed in Section 3.5 was used to adjust the pulse height. The velocity is observed to see if the mechanism is sticking and this information is used to adjust the pulse height. In this scheme the pulse height is adjusted without user intervention and no knowledge of the system friction parameters is needed.

All the friction compensation schemes were supported by experimental results showing the improvement obtained.

In Chapter 4 the techniques required to process position domain signals essential to the force estimation work in Chapters 5 and 6 were developed. Position dependent force\torque variations (PDFV\PDTV) were described. Concepts of discrete position, position frequency and position bins were introduced. The techniques to transform a discrete time signal into a discrete position signal or position binning were detailed. A proof defining the relationship between a position frequency in the position domain and a frequency in the time domain was given. It was shown that for a constant velocity the

position frequency of the PDFV will be seen with the same magnitude and with a time frequency that is the position frequency multiplied by the system's velocity.

An idea developed in Chapter 4 and used throughout Chapters 5 and 6 is that many of the signal processing techniques used in the time domain can also be applied to discrete position domain signals. Fast Fourier Transforms (FFT) and digital filters have been used to process position domain signals in this thesis. A FFT is taken of the discrete position force signal recorded to produce a position frequency spectrum used to characterise the PDFV. To give the maximum position frequency range the mechanism should be run under velocity control at the minimum sustainable non zero velocity. Quantitative relationships between bin size, sample rate, velocities and frequencies of PDFV were discussed. It was shown that the PDFV's position frequencies were well defined and did not change with velocity or over time.

In Chapters 5 and 6 the estimation of external forces using servo motor information and without the use of force sensors was described. The force estimation techniques were dependent on an accurate system model that includes mass, coulomb and viscous friction and PDFV components. The PDFV components were divided into low and high position frequency components. The low frequency components were included in the system model and the high frequency PDFV components removed as part of the signal processing. The force estimation signals were processed in both the time and position domains. The first stage of the signal processing was low pass filtering in the time domain. To process PDFV consideration needs to be given to the sampling rate, the position sampling rate, the PDFV spectrum and the system's velocity and these are all discussed in Section 5.2.3. The maximum position frequency for the PDFV and the

sampling rate set the maximum system velocity. The position sampling rate selection is based on two considerations, the first is the maximum position frequency of the PDFV spectrum and the second is the combination of the (time domain) low pass filter's cutoff and the minimum velocity.

In Section 5.3 the noise on the force estimation was attributed to two main sources: the PDFV components and decoder quantisation noise. The signal processing of the force estimation signal reduces both these noise sources. The time domain low pass filter removes almost all of the decoder quantisation noise and part of the high frequency PDFV. After processing in the time domain the force estimation signal is turned into a discrete position signal and processed in the position domain. The position domain filtering removes the remainder of the high position frequency PDFV components

A grinding machine was used to conduct a number of grinding experiments using different feedrates and depth of cuts to give a range of grinding forces. It was shown that the force estimation techniques were capable of measuring the grinding forces in these experiments. When a known force was applied to the grinding machine the overall noise level on the force estimation signal after processing in the time and position domain were quantified and the force estimation techniques used on the grinding machine shown to be capable of measuring grinding forces. The force estimation techniques were also capable of measuring forces applied to a robotic system. The force estimation techniques were used in coordinated motion of two axes of the robot and with the continually varying velocity. These force estimation techniques were capable of measuring forces as low as 4% of rated values.

The minimum force able to be detected by the force estimation procedure is unique to each mechanical arrangement. As the gearing ratio increases and friction increases the minimum force capable of being measured increases.

In Chapter 6 the force estimation techniques were implemented in real time. This required the development of a method for finding PDFV in real time. The PDFV position domain filter was implemented as a convolution. The filter designed was capable of removing the PDFV and had zero delay. It was shown that the real time force estimation signal after processing in the time and position domain was only slightly more noisy (8%) than the offline measurements. In Section 6.3 a sensorless grinding force control scheme was implemented in which the force feedback signal was the real time force estimation signal. A force control scheme which controlled the grinding force by modifying the feedrate was developed and results showing its effectiveness were presented.

7.2 Future Work

There are a number of areas of future work related to this thesis. These include; a better understanding and a more accurate model of PDFV; the use of different signal processing techniques to analyse and filter PDFV; the further development of the force estimation techniques to deal with low velocities and velocity reversals; extending the force estimation and control techniques to different applications; Correlating workpiece finish with grinding forces estimation results; consideration of different pulse shapes to be used by the friction controller.

In the modelling of PDFV the position frequencies were found to stay constant over time and over a range of velocities. However their magnitudes varied. The reason for

this variation was not addressed. A further study of PDFV to explain/model this variation may be very useful. It could have application as a machine monitoring tool where variations in a particular PDFV give an indication of deterioration in a particular part of the mechanical system. It could also be used in the force estimation procedure. At present the PDFV components are removed by filtering. If an accurate model of the PDFV were known they could simply be subtracted from the motor torque signal. This PDFV model could also be used in a compensation scheme as part of a velocity control loop.

Different signal processing techniques could be used to analyse and filter PDFV components. In this thesis FFT and digital filters were used to process discrete position domain signals. There are numerous other signal processing techniques used on discrete time signals that could be applied to discrete position domain signals. These include wavelets, filter banks, and cross correlation and covariance analyses that could be applied to discrete position signals.

The friction models used as part of the force estimation process are not applicable to the non linear low velocity region. The friction model does not include static friction or Stribeck friction. A model that includes a non linear Stribeck friction parameter is very hard to generate. A possible solution is the combination of the friction controller and the force estimation techniques developed in this thesis since the friction controller can operate in this non linear region. There would have to be some way of accounting for the torque pulses applied as the PWMH part of the friction controller in the force estimation procedure. In addition the force estimation procedure developed does not cope with velocity reversal when the mechanism moves back over the region it has just

travelled. In this thesis this was dealt with by breaking the signal up into two separate signals; one for when the mechanism was moving with a positive velocity and the other when the mechanism was moving with a negative velocity. A single method to process the position domain signals that copes with velocity reversal would be useful

The force estimation and control techniques could also be applied to other machining processes, include milling, drilling and turning. The force estimation techniques were applied successfully to a robotic system. There are numerous force control problems that could be solved without the use of a force sensor. These include various assembly, and grasping tasks. In many of these tasks the robot would be moving at low velocities so the force estimation techniques at low velocities suggested in the last paragraph may be particularly useful.

A further area of research is relating grinding forces measurements and force control schemes using force estimation techniques to workpiece quality. There is a large body of work relating grinding mechanism, workpiece quality and grinding forces (measured using force sensors) and this could be used as the basis for this work. In particular the accuracy of the force estimation measurements and the fidelity of the control scheme required to control workpiece finish.

Further work on the friction controller could include consideration of how different pulse shapes may improve performance. The pulse shape is also constrained by the practical limits of the system used to implement the friction controller, including the electronic drive's ability to apply sharp pulse fronts and the effect of encoder resolution

on the low velocity performance. In particular the noise injected by the encoder quantisation and its effect on the control loop's performance would be important.

REFERENCES

[1] Woodbury.R.S, *Studies in the History of Machine Tools,* Massachusetts, MIT Press, 1972.

[2] Li.Z, Cook. C.D, "A PID controller for machines with friction", Proceedings of the Pacific Conference on Manufacturing, Brisbane, Australia, 18-20, August, 1998 pp. 401-406.

[3] Malkin.S, *Grinding Technology,* Chicester Ellis Horwood, 1989.

[4] Tonshoff H.K, Peters J, Inasaki I, Paul T, "Modelling and simulation of grinding processes", *Annals of CIRP,* vol 41 no2 pp. 677-688, 1992

[5] Whitney.D.E, Edsall.A.C, Todtenkopf.A.B, Kurfess.T.R, Tate.A.R, "Development and control of an automated robotic weld bead grinding system," *Journal of Dynamic Systems, Measurements, and Control,* vol 112 pp. 166-176, June, 1990.

[6] Srivastava.A.K, Elbestawi.M.A, "Control strategy for multipass robotic grinding," *International Journal of Robotics and Automation,* vol 10,No3, pp.114-119, 1995.

[7] Srivastava.A.K, Rogers.D.B, Elbestawi.M.A, "Optimal planning of an adaptively controlled disk grinding process," *International Journal of Machine Tool Manufacture,* pp. 809-825, 1993.

[8] Gorinevsky.D.M, Formatsky.A.M, Schneider.A.Y, *Force Control of Robotics Systems,* New York, CRC Press, 1997.

[9] Bhattacharyya.B, Fowell.B, Wallbank.J, "Control of workpiece surface quality in grinding," *ASME High Speed Machining Symposium,* p425-444, 1984.

[10] Hahn.R.S, "Controlled-Force Grinding - A New Technique for precision internal grinding," *Journal of Engineering for Industry,* August 1964.

[11] Hahn.R.S, Graham.G, "An application of force-adaptive grinding," *Society of Manufacturing Engineers Technical Paper,* MR84-530 1-11, 1984.

[12] Jenkins.H.E, Kurfess.T.R, Dorf.R.C, "Design of a robust controller for a grinding system," *IEEE Transactions on Control System Technology,* vol 4 No1, 1996.

[13] Jenkins H.E, Thomas R.K, "Adaptive pole cancellation in grinding force control," *IEEE Transactions on Control Systems Technology,* vol 7 , No 3 p363-370, May 1999.

[14] Brinksmeier.E, Popp.C, "A self tuning control system for grinding process," *Annals of CIRP,* vol 40 No1, 1991.

[15] Chang S.H, Balasubramhanya, Chandrasekar S, Farris T.N, Hashimoto F, Shaw M.C, "Forces and specific energy in superfinishing of hardened steel", *Annals of CIRP*, vol 46 no1, pp. 257-260,1997.

[16] Tonshoff H, Zinngrebe M, Kemmerling M, "Optimization of internal grinding by microprocessor based force control", *Annals of CIRP,* vol 35 no1 pp. 293-296 1986.

[17] Hatamura Y, Nagao T, Mitsuishi, "Development of a Force Controlled Automatic Grinding System for actual NC Machining Centre", *Annals of CIRP*, vol 38 No 1, 1989.

[18] Wada.H; Kosuge.K, Fukuda.T, Watanabe.K, "Design of force controller based on frequency characteristics," *IEEE International Conference on Robotics and Automation,* vol 1 pp 610-615, May 8, 1994.

[19] Rocco P, Ferretti.G, Magnani.G, "Implicit force control for industrial robots in contact with stiff surfaces", *Automatica,* vol 33 No 11 pp. 2041-2047, 1997.

[20] Ohishi.K, "Sensorless force control using H acceleration controller," *Asia-Pacific Workshop on Advances in Motion Control,* pp13-16, June 15, 1993

[21] Wang.Y.T, Jan.Y,J, "Grinding force models in the finishing processes," *IEEE/ASME International Conference on Advanced Intelligent Mechatronics,* pp. 882-827, July 8, 2001.

[22] Elosegui.P, Daniel.R.W, Sharkey.P.M, "Joint servoing for robust manipulators force control," *IEEE International Conference on Robotics and Automation,* vol 1 pp. 246-251, May 13,1990.

[23] Taghirad.H.D, Belanger.P.R, "Intelligent torque sensing and robust control of harmonic drive under free motion," *IEEE International Conference on Robotics and Automation,* pp. 1749-1754, April 1997

[24] Taghirad,H.D, Helmy.A, Belanger.P.R, "Intelligent built in torque sensor for harmonic drive systems," *IEEE Conference Instrument and Measurement Technology,* pp.969-974, May 1997.

[25] Luh.J.Y.S, Fisher.W.D, Paul.R.P.C, "Joint torque control by a direct feedback for industrial robots," *IEEE Transactions on Automatic Control,* vol AC-28, No2, February, 1983.

[26] Armstrong-Helouvry.B, Dupont.P, Canudas de Wit.C, "A survey of models, analysis tools and compensation methods for the control of machines with friction", *Automatica,* vol 30 No 7 pp. 1083-1138,1994.

[27] Astrom K.J, "Control of systems with friction", *The 4th International Conference on Motion and Vibration,* pp. 25-32, August 1998.

[28] Popovic.M, Goldenberg.A, "Modelling of friction using spectral analysis", *IEEE Transactions on Robotics and Automation,* Vol 14,No1 pp.114-122, February 1998.

[29] Armstrong.B, *Control of Machines with Friction,* Boston, MA Kluwer, 1991.

[30] Webb.S, Li.Z, Cook.C, "Identification of drive train torque disturbances for an X-Y table test bed," *Proceedings of the 5th International Conference on Control, Automation, Robotics and Vision,* Singapore, 1998, vol 1 pp. 439-443.

[31] Olsson.H, *Control Systems with Friction,* PhD Thesis, Lund, Lund Institute of Technology, 1996.

[32] Armstrong B, Amin B, "PID Control in the presence of static friction: A comparison of algebraic and describing function analysis", *Automatica,* vol 32 No5 pp. 679-692, 1996.

[33] Rabinowicz.E, *Friction and Wear of Materials,* New York, John Wiley &Sons, 1965.

[34] Canudas de Wit C.A, *Adaptive Control for Partially known Systems Theory and Application,* New York, Elsevier, 1988.

[35] Canudas de Wit.C, Noel.P, Aubin.A, Brogliato.B, "Adaptive friction compensation in robot manipulators: low velocities," *International Journal of Robotics Research,* vol 10 No3 pp. 189-199, June 1991.

[36] Walrath.C, "Adaptive bearing friction compensation based on recent knowledge of dynamic friction", *Automatica,* vol 20 No6 pp. 717-727, 1984.

[37] Canudas de Wit.C, Olsson.H, Astrom.J, Lischinsky.P, "A New Model for control of systems with friction," *IEEE Transactions on Automatic Control,* vol 40, No3, March 1995.

[38] Mossaheb S, "Application of a method of averaging to the study of dithers in non linear systems," *International Journal of Control,* vol 38, No3, pp. 557-576, 1983.

[39] Yang.S, Tomizuka.M, "Adaptive pulse width control for precise position under the influence of stiction and coulomb friction," *Journal of Dynamic Systems, Measurements and control,* vol 110 pp. 221-227, September 1988.

[40] Popovic M.R, Gorinevsky D.M, A.A.Goldenberg, "High precision positioning of a mechanism with nonlinear friction using a fuzzy logic pulse controller," *IEEE Transaction on Control Systems Technology,* vol 8 no1 pp. 151-158, 2000.

[41] Popovic.M.R, Goldenberg.A.A, Gorinevsky.D.M, "A study of response to short torque pulses and fuzzy control of positioning for devices with stick slip friction," *IEEE 4th conference on Control Applications,* pp. 302-307, September 1995.

[42] Popovic M.R, Gorinevsky.D.M, Goldenberg A.A, "Fuzzy logic controller for accurate positioning of direct drive mechanisms using force pulses," *IEEE International Conference on Robotics and Automation,* pp.1166-1171, 1995.

[43] Baldor, *DCServo Drives TSD Series Tech Manual,* Baldor Motion Products Group.

[44] Astrom K.J, Wittenmark B, *Computer Controlled Systems,* Englewood Cliffs, N.J., Prentice-Hall, 1984.

[45] Leonhard W, *Control of Electrical Drives,* Berlin, Springer-Verlag, 1985.

[46] Platt D, *Variable Speed Drives* , lecture notes University of Wollongong.

[47] Jacquot R.G, "*Modern Digital Control Systems*", New York, Marcel Dekker, 1994.

[48] Franklin G.F, Powell D.J, Emami-Naeini, *Feedback Control of Dynamic Systems*, Reading Massachusetts, Addison-Wesley, 1986.

[49] Schilling R.J, *Fundamentals of Robotics: Analysis and Control*, New Jersey, Prentice-Hall, 1990.

[50] Matlab *Fuzzy Logic Toolbox User Guide,* MathsWork Inc 1995.

[51] Shigley E.J, *Mechanical Engineering Design,* New York, McGraw-Hill, 1986.

[52] Stanley W.D, Dougherty G.R, Dougherty R, *Digital Signal Processing.* New Jersey , Prentice-Hall, 1984.

[53] Evans B.J, *Comparative Evaluation of Real Time Robot Control Systems* PhD Thesis, Wollongong, University of Wollongong, 1998

[54] Manolakis D.G, Proakis J.G, *Digital Signal Processing : Principles, Algorithms, and Applications,* New York, Maxwell Macmillan, 1992.

[55] Parks T.W, Burrus C.S, *Digital Filter Design,* New York, Wiley, 1987.

[56] Loughborough Sound Images plc, *User Documentation PC/32 Real Time Applications Platform,* Loughborough Sound Images PLC, Leicesterchire 1995.

[57] Simpson J.W.L, *Digital I/O board for use with Blue wave system PC/32 board,* Internal report University of Wollongong 1999.

[58] Texas Instruments, *TMS320 Floating Point DSP optimising C Compiler,* Texas Instruments, Houston, 1991.

[59] Hirata Ltd, *ARM-BASE Manuals,* Hirata Industrial Machines Co Ltd, 1985

[60] Yaskawa Electric Ltd, *DC Servomotor controller Servopack,* Japan, Yaskawa Electric Ltd, 1988

[61] Baldor, *Baldor Servo Product & Position Systems,* Australian Baldor Pty Ltd, Sydney 1998.

[62] Baldor, *Motor Drives and MINT Motion Control Products,* Baldor Motors and Drives, 1999.

[63] Hwang P.Y.C, Brown R.G *Introduction to Random Signals and Applied Kalman Filtering.* New York, John Wiley and Sons, 1992 .

[63] Tonshoff H.K, Karpuschewski B, Mandrysch, Grinding process achievements and their consequences on machine tools and challenges and opportunities, *Annals of CIRP,* vol 47 No2, 1998

[64] Shaw M.C, *Principles of Abrasive Processing,* Oxford, Clarendon Press, 1996.

[65] Shiyuki sakave, Yoshihiro Yanagihara, Youichi Nonaka, Kenji Yokoshima, "Development of an impeller grinding robot system and gyro-moment compensated compliance control," *IEEE International Conference on Robotics and Automation,* vol 2, pp. 2084-2089, 1995.

[66] Minami.M, Asakura.T, Dong.L.X, Huang.Y.M, "Position control and explicit force control of constrained motions of a manipulator for accurate grinding tasks," *Advanced Robotics,* vol 11, No3 pp. 285-300, 1997.

APPENDIX A LIST OF SYMBOLS

a =depth of cut
b =wheel width
e =error signal or controller input
d =decoder increment
d_s = grinding wheel diameter
f =frequency
f_c =coulomb friction
f_{LP} =low pass cutoff frequency
f_v =viscous friction
f_{stic} =static friction
f_s =sampling frequency
F =force
F_G =grinding force
F_m =motor force
F_N =normal grinding force
F_{motor} =motor force
F_{pos} =position dependent force variation
F_{spring} = force generated by a spring
F_T =tangential grinding force
$\tilde{i}$ =phasor current
i_a, i_b, i_c =three phase currents
i_d =direct axis current
i_q =quadrature current
I =current
$\hat{I}$ =peak current
I_a =armature current
I_{ref} =reference current
I_{rms} =RMS current
J = inertia
K_d =servo drive current loop gain
K_D =PID controller derivative constant
K_G =grinding constant
K_I =PID controller integral constant
K_m =motor constant, ratio of armature current to motor torque
K_P =PID controller proportional constant
K_{PWM} =pulse width controller gain
K_{VI} = ratio of servo drive input voltage to output current
K_{VT} = ratio of servo drive input voltage to servo motor torque
l =screw pitch

L =inductance
L_a =armature inductance
m =mass
n =gear ratio
P =power
P_G =grinding power
P_{inst} =instantaneous power
P_{rot} =rotational losses
P_{elec_loss} =electrical losses
Q =metal removal rate
r_a, r_b =link lengths of axes A and B respectively
R =resistance
R_a =armature resistance
R_r =rotor resistance
R_s =stator resistance
s =slip
T_a =A axis torque
T_b =B axis torque
T_d = disturbance torque
T_m =motor torque
T_{motor} =motor torque
T_p =pulse height
T_{spring} =torque produced by spring force
u =specific grinding energy
u =controller output
u_{PID} =PID controllers output
u_{PWM} =output of PWMH part of controller
u_{pk} =controller peak output
v =velocity
v_s =grinding wheel peripheral speed
v_w =workpiece velocity
V =voltage
$\hat{V}$ =peak voltage
V_a =armature voltage
V_d =drive saturation voltage
V_{DSP} = servo drive input voltage
V_{RMS} =RMS voltage
X = position period
X_l =leakage reactance
X_m =magnetising reactance
β =angle between rotor and stator mmfs

Δ =pulse width
ε =position error
Φ =position frequency
Φ_0 =fundamental position frequency
Φ_{nq} =nyquist position frequency
Φ_s =position frequency sampling rate
μ =ratio of tangential to normal grinding force
θ =angle
θ_a =angle of A axis
θ_b =angle of B axis
θ_F =angle of the applied force
σ = standard deviation
σ_a =standard deviation of acceleration error
σ_v =standard deviation of velocity error
τ =time constant
τ =period
τ_s =sampling period
ω = angular frequency/velocity
ω_m = mechanical angular velocity
ω_{ref} =reference angular velocity
ω_s =supply angular frequency
Ω =angular position frequency
Ω_0 =fundamental angular position frequency

APPENDIX B EXPERIMENTAL EQUIPMENT DATA

A description of the experimental equipment used in this thesis is given in Chapter 2. This appendix gives additional information relating to the experimental equipment. The DSP system is described and the servo system data and constants for both the Hirata robot and the grinding machine are given. The force sensor and spindle motor power measurement circuit are also described

B.1 Digital Signal Processor and Associated Software

The Digital Signal Processor (DSP) system used in both the Hirata robot and grinding machine was supplied by Blue Wave systems (formerly Loughborough Sound Images). A detailed description of the Blue Wave system PC/32 board, associate daughter modules and software is given in [56]. The PC/32 board is built around the Texas Instrument(TI) TMS320C32 floating point DSP. The Blue Wave system in addition to the TI processor has 32Kbytes x 32bits of zero wait state memory, 1Kbytes x 32 bit two wait state dual port RAM (DPRAM), a 32 bit memory mapped parallel expansion interface (DSPLINK2) and two daughter module sites. The PC/32 board fits into one ISA slot of a standard PC.

On the Hirata robot and the grinding machine both the PC/32 board's daughter module sites are populated with AMD16SA Burr Brown daughter modules. Each daughter module has two analogue inputs and two analog outputs making a total of 4 analog inputs and outputs per PC/32 board. Each analogue input channel is capable of sampling data at 200kHz. The output signal can be reconstructed at 500kHz. The voltage range of both the analog input and outputs is $\pm$ 3 Volts.

The Hirata robot's DSP system was fitted with a 32 channel digital input/output board PC/32DIO supplied by Blue Wave systems. The board is connected to the PC/32 board through the DSPLINK2 parallel interface. The PC/DIO32 digital I/O is TTL compatible and is configured for 16 bits of input and 16 bits of output. This board is installed in an ISA slot of the personnel computer and is linked to the PC/32 board by a 50 way ribbon cable. The grinding machine also uses the PC/32DIO board and also an additional digital I/O board. This board was designed at University of Wollongong and is similar to the PC/DIO32 board. It uses the DSPLINK2 interface and gives 16 bits of TTL compatible input and 16 bits of TTL compatible output. A more detailed description of this board is given in [57].

The DSP programs are all written in C and are compiled using the TI TMS320 floating point DSP optimising C compiler. The compiler is discussed in detail in [58]. The TI C compiler takes an ASCII file, compiles the C code and produces a file with a .out extension. This file is an executable program that can be run on the TMS320C3x family of DSP's. There are also facilities to compile assembly language programs if faster execution is required. Executable files can be run from the MPCView program or from the dataxfer.exe program.

The MPCView program supplied by Blue Wave Systems is a C source debugger. The software allows executable DSP code to be run from this program. It also allows the user to single step through code, set breakpoints, check variables and register values. The software runs under windows 98 and there is not an NT version of this software.

The DPRAM is a Section of memory on the DSP board which can be accessed from both the DSP and the PC. This allows for a fast interchange of data between the DSP and the PC. The Blue Wave system also includes PC/32 DOS interface libraries. They are a series of C functions that can be included in a C program. Once compiled the programs can be run from the Windows98 DOS prompt. The compiled program can include C function calls that reset the DSP, down load and run DSP code, allow data to be transferred to and from the Dual port RAM. A program has been written for use with the grinding machine and the Hirata robot and is called dataxfer.exe. This program downloads a DSP program, gets data stored in file input.txt and transfers it to the DSP and saves data received from the DSP in file data.txt. Matlab is used to analyse the data

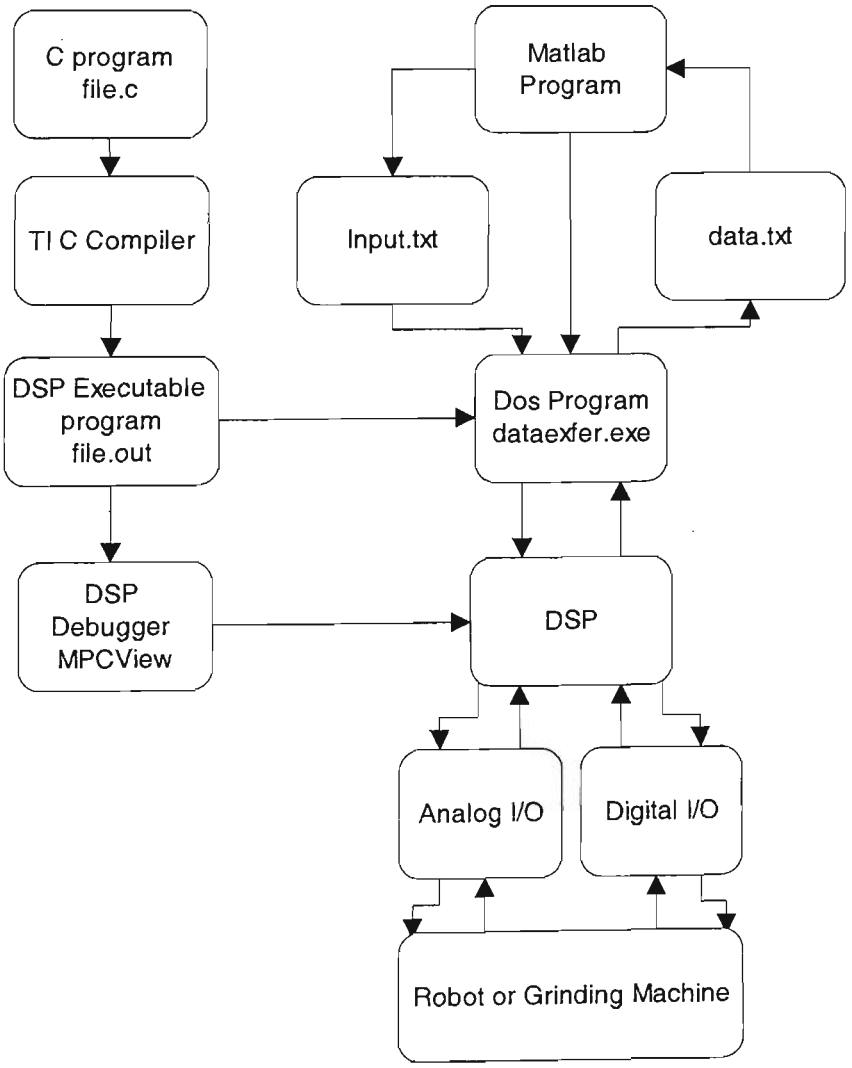

Figure B.1 DSP software flow chart.

received from the experimental systems. The Matlab program has a DOS command that allows a DOS program to run from the Matlab environment. Normally the dataexfer.exe program is run from Matlab and once the DSP program has finished controlling a process (eg a machining operation) the data recorded is then processed and displayed in Matlab. This can all be done within in one Matlab m-file.A flow chart describing the software process is shown in figure B.1

B.2 Hirata Robot

The physical layout of the Hirata robot is shown in figure B.2

B.2.1 Position Data and Calibration

The position information is obtained from rotary shaft encoders. The shaft encoders provide a two channel output signal. Each channel gives a pulsed output; the number of pulses per motor shaft revolution for each axis is shown in table B.1. The two channels are displaced by 90 degrees and are fed into a quadrature decoder/counter interface chip (HCT2016). This increases the effective resolution or counts by four and this value is shown in table B.1. Also included in table B.1 are the conversion factors for changing between decoder counts and other more conventional angular/linear position units. The angular measurements can either be referred to the rotation of the motor shaft or the rotation of the robots arm. The two reference frames are related by the gear ratio (given in Section 2.2).

Table B.1 Encoder Resolution

	A axis	B axis	Z axis	W axis
Encoder pulse/rev	1000	1000	500	500
Decoder chip resolution (counts/rev)	4000	4000	2000	2000
Decoder counts to Radians (motor)	1.57e-3	1.57e-3	3.14e-3	3.14e-3
Decoder counts to Radians (robot)	1.57e-5	1.964e-5	-	2.54e-4
Decoder counts to Degrees (robot)	9.0e-4	1.12e-3	-	1.45e-2
Decoder counts to mm (robot)	-	-	2.5e-3	-

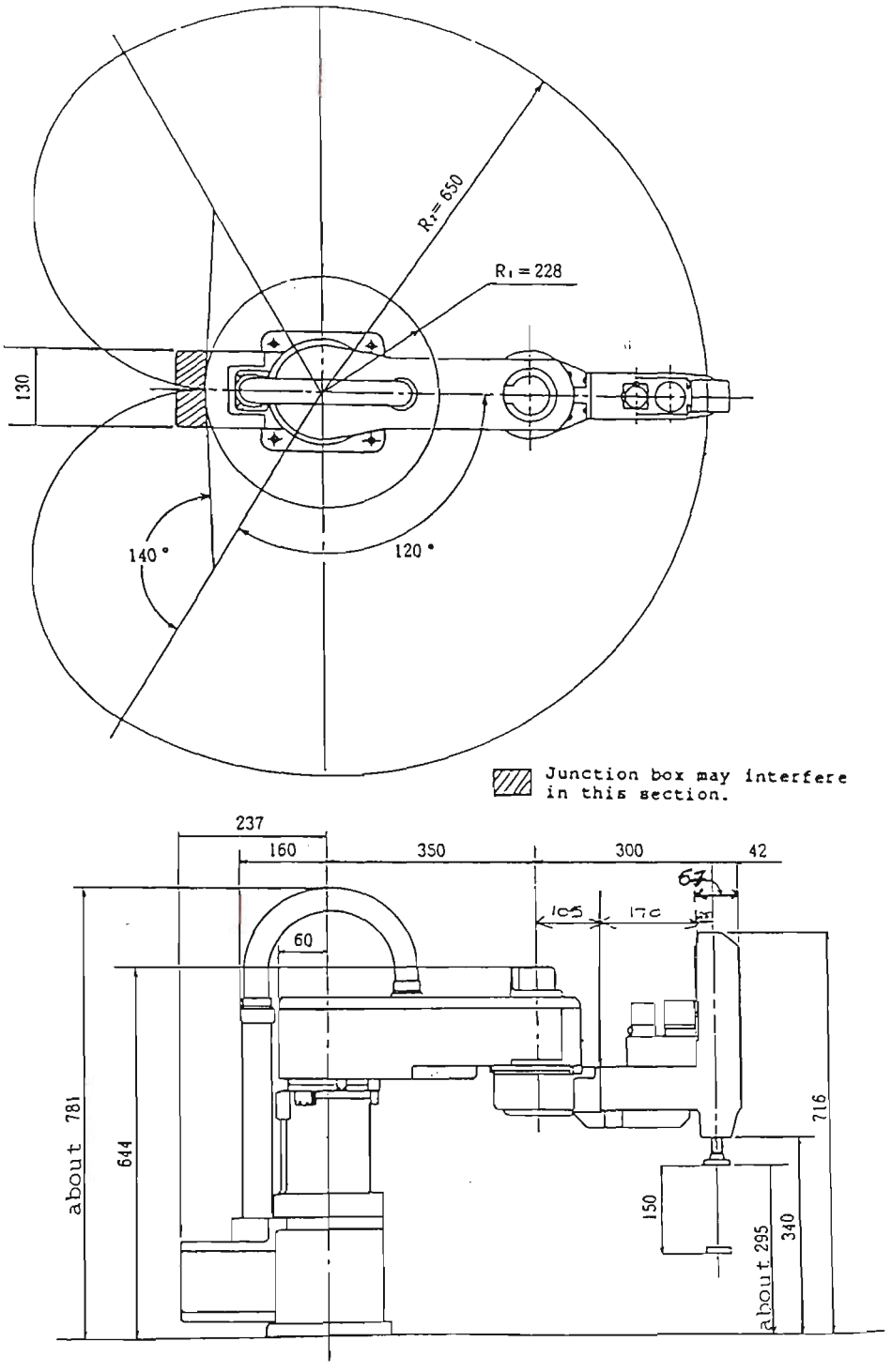

Figure B.2 Hirata Robot Physical Layout [59]

At the end of each axis travel there are magnetic proximity switches, which are used to home the robot and to limit the travel of the robot. The range of movement of each axis of the robot is shown in figure B.2 these ranges are also listed as the first row of table B.2. The range of movement can be modified by moving the proximity switches as has been done in the case of the A axis. The Actual movement is calculated using the encoder position information and listed in the second row of table B.2.

Table B.2 Range of Movement

	A axis	**B axis**	**Z axis**	**W axis**
Range of Movement	120deg	140deg	75mm	270deg
Actual Movement	83deg	141deg	77mm	271deg

The proximity switches are also used to home the robot. The home routine moves each axis in a clockwise (CW) direction until it hits the CW limit. The robot then moves in an anticlockwise direction until it hits the counter clockwise limit (CCW). The robot then positions itself midway between the two limits. The accuracy to which the robot can home itself is dependent on the accuracy of the proximity switches. The homing routine was repeated 20 times and each time there was a slightly different range of movement recorded. The results are summarised in table B.3

Table B.3 Homing Accuracy

	A Axis	**B Axis**
Mean	184769.8	250317.7
Standard deviation	5.77	22.8
Range	-9.8 to 7.2	-40.7 to 29.3

The values in table B.3 are expressed in decoder counts. i.e. for the A axis 184770 counts using the conversion factor listed in table B.1 corresponds to 166degs=±83deg, the value given in table B.2 for the range of movement. The homing routine only has to be run each time the robot is restarted. The values given in table B.3 are a measure of the robot to find the same origin on each subsequent restarting of the robot. Once the robot has been "homed" any subsequent sequence of movements of the robot's arm can be determined to within 1 decoder count.

It should be noted that the homing accuracy and subsequent position resolution only refer to the ability to measure where the robot is. Whether it can actually move there will depend on the position control loop. It should also be noted the measurements are of the motor shaft and not the robot's end effector.

B.2.2 Motors and Drives

The motors on all axes of the Hirata robot are permanent magnet DC servo Motors. The A and B axis motors are driven by Baldor TSD series DC servo-drives and the Z and W axes are driven by Yaskawa DC servo-drives. The motor and drive ratings are given in table B.4. The Baldor drive values are taken from [43] and the Yasakawa drive and motor values are taken from [60].

Table B.4 Motor and Drive Ratings

Motor	**Units**	**A Axis**	**B Axis**	**Z Axis**	**W Axis**
Rated Power	Watts	190	120	95	100
Rated speed	RPM	3000	3000	3000	3750
Rated Current	Amps	6.2	5.4	4.5	4.1
Rated Torque	N.m	0.60	0.36	0.30	0.0028
Motor Constant (K_m)	N.m/Amps	0.098	0.067	0.067	0.00068
Drives					
Output voltage	Volts	100	100	30	42
Cont Current	Amps	5	5	5.6	6.4
Peak current	Amps	10	10	12	20
V_{DSP} to current (K_{VI})	Amps/Volts	0.45	0.46	3.2	9.6
Actual outputs					
DSP Max output	Volts	3	3	3	3
Max Current	Amps	1.35	1.38	9.6	20
Max Torque	Nm	0.13	0.09	0.64	0.13
V_{DSP} to Torque (K_{VT})	Nm/Volts	0.044	0.038	0.21	0.0065

The motors all use the armature circuit for control and all the servo drives are in current control mode with fast time constants (see Section 2.2.2) so that the drives may be thought of as a voltage controlled current source. The output current i_{ref} for all practical transients will be proportional to an input control voltage. The ratio of the control voltage to the output current is designated as K_{VI} and is listed in table B.4. This control

voltage is the output voltage of the DSP V_{DSP} and as discussed in Section B.1 its maximum value is 3V. The remaining constants relating voltage to current and torque K_m and K_{VT} are given in table B.7.

B.3 Grinding Machine

The grinding machine is described in Section 2.3. Its has three linear axes X,Y and Z. The X axis linear screw arrangement has a pitch of 5mm. The Z axis screw has a pitch of 5mm and is connected to a bevel gear arrangement with a gear ratio of 2.5, giving an effective overall pitch of 5mm/2.5=2mm. The Y axis screw has a pitch of 4mm.

B.3.1 Position Data and Calibration

The position information is obtained from resolvers on the motor's shafts. The resolvers give a 3 channel output. There are 2 channels displaced 90 degrees and each giving 4096 pulses per revolution. The third channel gives a marker pulse once per revolution. The quadrature channels are fed into a decoder/counter chip (HCT2016) which increases the resolution by 4. These values are shown in table B.5.

Table B.5 Grinding Machine Resolver Resolution

	X axis	**Y axis**	**Z axis**
Encoder pulse/rev	4096	4096	500
Decoder chip resolution (counts/rev)	16384	16384	16384
Decoder counts to Radians (motor)	6.1e-5	6.1e-5	6.1e-5
Screw pitch (mm)	5	4	2
Decoder counts to μm	0.3	0.24	0.12
Range of Movement(mm)	300	160	120

The fifth row of table B.5 shows the decoder counts to micrometer conversion factor for each axis. This value is derived by dividing each axis screw pitch by the decoder counts per revolution. For the X axis it is 5mm/16384=0.3 μm. Mechanical limit switches are used to limit the travel of each axis. The travel or range of movement for each axis is given in table B.5. The limit switches are also used to "home" each axis of the grinding machine. The homing routine moves each axis in a counter clockwise (CCW) direction

until it hits the CCW limit. The axis is then moved in a clockwise (CW) direction until the first marker pulse(channel 3 of the resolver) is recorded. The position is then reset to zero. The accuracy of the homing routine is not dependent on the limit switch accuracy and is only dependent on the resolution of the resolver. The accuracy of the homing operation is 0.3 μ m, 0.24 μ m. and 0.12 μ m on the X,Y and Z axes respectively. These measurements are for the motor shaft not the workpiece.

B.3.2 Motors and Drives

The motors and drives on all three axes are identical. The motors are permanent magnet synchronous motors. This type of motor is often referred to as Brushless AC servo motors. These motors are controlled by Baldor DSBC 100 series AC servo controllers used in current control mode. The motor and drives ratings and other relevant parameters are listed in table B.6 and are taken from Baldor manuals [61,62].

Table B.6 Motor and Drive Ratings

Motor	**Units**	**Value**
Rated speed	RPM	4000
Rated Current	Amps	5.7
Rated Torque	N.m	4.52
Torque Constant (K_m)	N.m/Amps	0.83
Winding Constant	V/krpm	75
Resistance	ohms	2.2
Inductance	mH	9.3
Drives		
Cont Current	Amps	5
Peak current	Amps	10
V_{DSP} to current (K_{VI})	Amps/Volts	1.33
Actual outputs		
DSP Max output	Volts	3
Max Current	Amps	3.0
Max Torque	Nm	1.1
V_{DSP} to Torque (K_{VT})	Nm/Volts	1.1

B.4 Force Sensors

To measure grinding forces a force sensor was used. The force sensor is a three-axis piezo-electric sensor supplied by Kistler . A multi axis piezo electric sensor consists of a

B.4 Force Sensors

To measure grinding forces a force sensor was used. The force sensor is a three-axis piezo-electric sensor supplied by Kistler . A multi axis piezo electric sensor consists of a stack of quartz disks whose orientation determines the force to be measured. Shear or transverse forces are transmitted to the sensor surface by friction. Therefore to measure forces in the X and Y directions the sensor must be preloaded in the Z direction. The sensor's mounting arrangement is shown in figure B.13. The sensor is clamped between the two mounting plates with a preload of 25KN. The workpiece is then bolted to the top mounting plate.

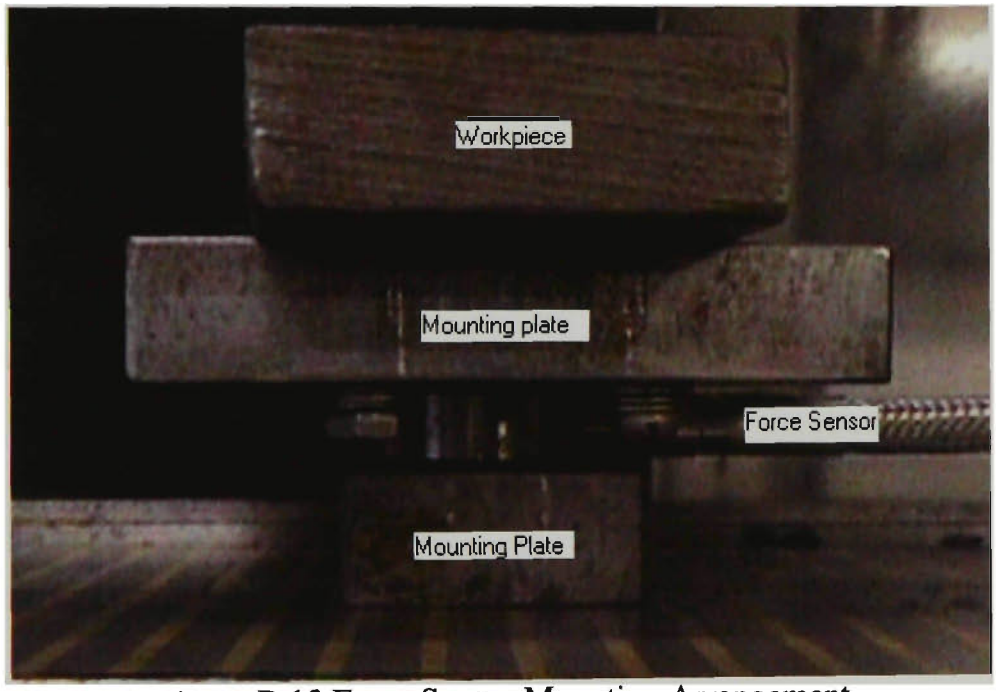

Figure B.13 Force Sensor Mounting Arrangement

The force sensor system comprises the sensor itself and a charge amplifier unit. Piezoelectric sensors produce a charge when they experience a change in load. The sensitivity listed in table B.7 is a measure of charge in pico coulombs produced for an applied force of N newtons. The charge amplifier reads the charge produced by the sensor. The maximum charge the amplifier can measure is 10000 pC and the maximum force reading given in table B.7 is simply the measuring range (10000pC) divided by the sensitivity. The charge amplifier has a range of gains from 1 to100.

Amplifier	**Measuring Range (pC)**	±10000	±10000
	Maximum Force Reading(N)	±3.1k	±2.6k
	Minium Force Reading (N)	0.062	0.052
	Maximum force reading with gain =10	310	260
	Minimum Force Reading with Gain=10	0.62	0.52
	Drift (pC/s)	0.03	0.03
	Drift per minute with 100N Force (%)	0.56	0.47

The relationship between the gain and the measurable force range is;

$$Force\_range = \frac{10000}{sensitivity \times gain} \qquad \text{Eq B.1}$$

The maximum force reading is for a gain of 1. The gain decreases the maximum measurable force but increases the sensitivity of the sensor. The minimum force reading is achieved when using a gain of 100. The output of the charge amplifier is ±10Volts. The background noise on the force measuring circuit was found to be ±20mV. This corresponds to a force value of 0.052 N on the Z axis. In all the grinding experiments described in this thesis an amplifier gain of 10 was used.

The charge from the piezo electric sensors is stored in a capacitor whose voltage is then proportional to the applied force. The ability of the measuring circuit to store this charge affects the sensor's measuring accuracy. The rate at which the charge decays is referred to as the drift as listed in table B.7. Consider the Z axis with an applied load of 100N and an amplifier gain of 10:

$$\frac{drift \times 60 \times 100}{sensitivity \times applied\_force} = \frac{0.03 \times 60 \times 100}{3.8 \times 100} = 0.47\%$$

If a constant load of 100N is applied to the Z axis then after 2 minutes there will be an error of 1%. This sensor is suitable for the grinding experiments used in this thesis because the machining process (hence the applied force) never lasted for more than 2 minutes. However the sensor would not be useful in measuring static force over long periods of time.

B.5 Spindle Motor

The grinding wheel is directly coupled to the shaft of a three phase squirrel cage induction motor. This motor is referred to as the spindle motor and has name plate ratings;

Rated Power = 1.1Kw
Rated Voltage=380Volts
Rated Current=2.5Amps
Rated Speed = 2840 RPM

A locked rotor test using a reduced terminal voltage and a no load test were conducted on the spindle motor. The parameters of the equivalent circuit in figure B.3 were calculated from these tests. The rotational losses were calculated from the no load test and found to be P_{rot}=94watts.

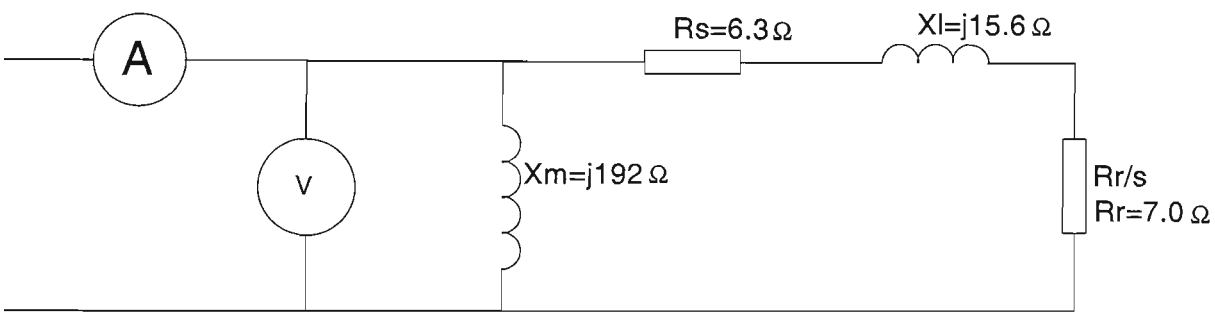

Figure B.3 Induction Motor equivalent circuit

A power measuring circuit was wired to one phase of the induction motor and was used to measure the spindle motor's power. The power is calculated from voltage and current measurements. The voltage V is measured via a voltage transformer and the current I is measured from a current transducer. For a 50 Hz supply the measured V and I can be described by:

$$V = \hat{V}\sin 100\pi t \qquad \text{and} \qquad I = \hat{I}\sin(100\pi t + \theta) \qquad \text{Eq B.2}$$

The instantaneous power P_{inst} is given by multiplying the voltage and current:

$$P_{inst} = 3VI = 3\hat{V}\hat{I}\sin 100\pi t \sin(100\pi t + \theta) = \frac{3\hat{V}\hat{I}}{2}\{\cos\theta - \cos(200\pi t + \theta)\} \qquad \text{Eq B.3}$$

The real power P is then the average of the instantaneous power:

$$P = \frac{1}{T}\int_0^T 3VIdt = \frac{3VI}{2}\cos\theta = 3V_{RMS}I_{RMS}\cos\theta \qquad \text{Eq B.4}$$

The transformed voltage and current transducer output are connected to analog inputs of the DSP (see Section B.1). The voltage and current waveforms are sampled at 1kHz. The real power is calculated from the sampled data by multiplying the voltage and current and then taking the average over 20 consecutive samples (20ms when sampling at 1KHz) which corresponds to one cycle at 50Hz supply . The power at the nth sample time *P(n)* is given by:

$$P_{av}(n) = \frac{3}{20}\sum_{m=n-10}^{m=n+10} V(m)I(m) \qquad \text{Eq B.5}$$

The rms voltage and current are also calculated using a moving average over 20 consecutive points. Using RMS values of voltage, current and the real power, the power factor θ can be calculated.

The power measuring circuit response needs to be considered as the circuit may have to measure sudden increases in power as happens for example, when the grinding wheel first hits the work piece. If the voltage is assumed to be constant an increase in power will be seen as an increase in the measured current. Let the current I be given by a 50Hz signal with amplitude varying with frequency f so that:

$$I = \hat{I}\sin(2\pi ft)\sin(100\pi t) \qquad \text{Eq B.6}$$

The expression for the power then becomes:

$$P = \hat{V}\hat{I}\sin(2\pi ft)\sin(100\pi t)\sin(100\pi t) \qquad \text{Eq B.7}$$

A range of frequencies f from 1 to 50 Hz were used and the power measuring circuit's response is shown in figure B.4.

A range of frequencies f from 1 to 50 Hz were used and the power measuring circuit's response is shown in figure B.4.

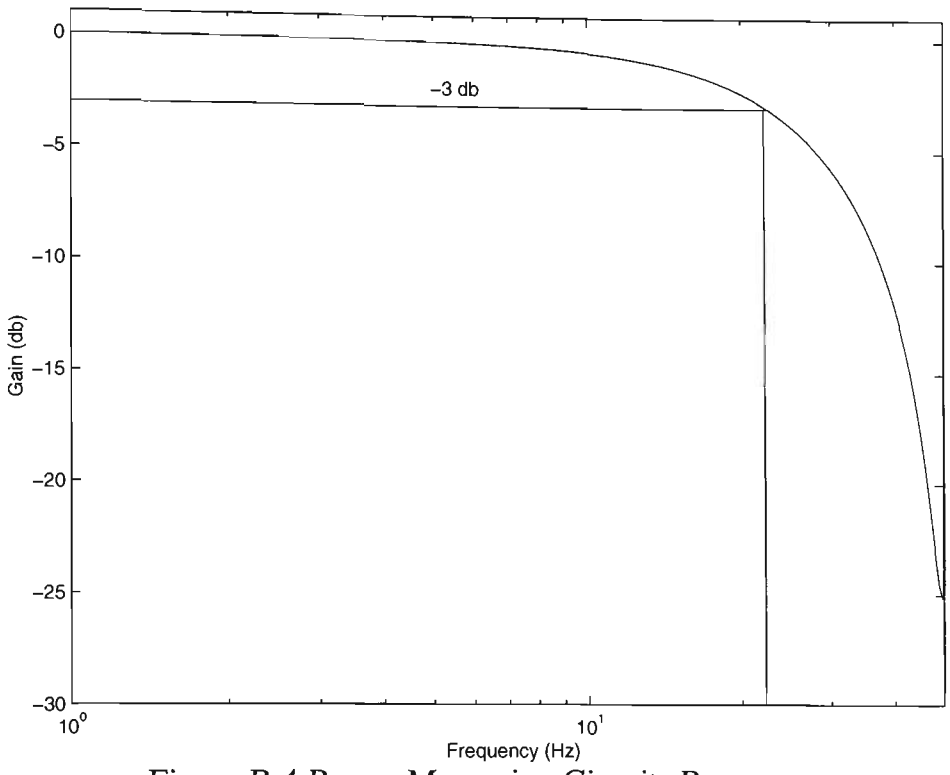

Figure B.4 Power Measuring Circuits Response

As can be seen in figure B.4 the circuit cutoff frequency is about 20Hz.

The measured real Power P is assumed to be the sum of the power used in the grinding process P_G, the rotational losses P_{rot}, the electrical losses P_{elec_loss} and the power used in accelerating the induction motor's rotor and the grinding wheel attached to it P_J:

$$P = P_G + P_{rot} + P_{elec\_loss} + P_J \qquad \text{Eq B.8}$$

For speeds near synchronous speed i.e. for low values of slip s $R_r/s >> R_S$ and $R_r/s >> X_L$ so from the equivalent circuit in figure B.3 the slip can be given as:

$$s = \frac{I_{RMS} R_r \cos\theta}{V_{RMS}} \qquad \text{Eq B.9}$$

Expressing this in terms of the power P the slip can be expressed as:

$$s = \frac{PR_r}{3V_{RMS}^2} \qquad \text{Eq B.10}$$

calculated rated speed is slightly higher the name plate rating listed at the beginning of this section and this is most likely caused by the simplifying assumptions used to calculate the slip. As the change in speed between no load and full load is relatively small the system is assumed to be operating at constant velocity and the power used in accelerating the system can be neglected i.e $P_J = 0$. The electrical losses can be given by:

$$P_{elec\_loss} = I_{RMS}^2 (R_r + R_S)\cos^2\theta \qquad \text{Eq B.11}$$

The grinding power including the expression for electrical losses becomes:

$$P_G = P - P_{rot} - I_{RMS}^2 (R_s + R_r)\cos^2\theta \qquad \text{Eq B.12}$$

The angular velocity of the spindle motor ω_m is related to the slip s and supply frequency ω_s such that:

$$\omega_m = \omega_s (1 - s) \qquad \text{Eq B.13}$$

The peripheral speed of the grinding wheel v_s with diameter d_s is given by:

$$v_s = \omega_m \frac{d_s}{2} \qquad \text{Eq B.14}$$

The grinding power is also related to the tangential grinding force F_T and wheel speed such that:

$$P_G = F_T v_s \qquad \text{Eq B.15}$$

Combining Eq B.15, Eq B.14, Eq B.13, Eq B.12 and Eq B.9 an expression for the tangential grinding force using known or measurable variables is:

$$F_T = \frac{2V_{RMS}}{d_s \omega_s} \frac{P - P_{rot} + I_{RMS}^2 (R_s + R_r)\cos^2\theta}{V_{RMS} - I_{RMS} R_r \cos\theta} \qquad \text{Eq B.16}$$

APPENDIX C RANDOM VARIABLE MANIPULATION

The expressions given in Eq C.1 for manipulating random variables are taken from Brown and Hwang [63]. Let X,Y and Z be three independent random variables with means $\bar{x}, \bar{y}, \bar{z}$ and standard deviations $\sigma_x, \sigma_y, \sigma_z$. Z is produced by the manipulation X and Y and relationship between the means and standard deviations using standard random variable manipulation for three arithmetic operations are:

$$\begin{aligned} Z &= X + Y & \bar{z} &= \bar{x} + \bar{y} & \sigma_z &= \sqrt{\sigma_x^2 + \sigma_y^2} \\ Z &= X - Y & \bar{z} &= \bar{x} - \bar{y} & \sigma_z &= \sqrt{\sigma_x^2 + \sigma_y^2} \\ Z &= aX & \bar{z} &= a\bar{x} & \sigma_z &= a\sigma_x \end{aligned} \qquad \text{Eq C.1}$$

Eq C.1 is used in Section 5.3.1 and in the following discussion to calculate an expression for the standard deviation of the force estimation error signal. The force estimation signal is given by Eq 5.23 and is given again here:

$$F(k) = ma(k) + f_v v(k) + f_c \qquad \text{Eq C.2}$$

The expressions for velocity and acceleration also given in Section 5.3.1 and also reproduced here:

$$\begin{aligned} v(k) &= v'(k) + f_s\big(\varepsilon(k) - \varepsilon(k-1)\big) \\ a(k) &= a'(k) + f_s{}^2\big(\varepsilon(k) - 2\varepsilon(k-1) + \varepsilon(k-2)\big) \end{aligned} \qquad \text{Eq C.3}$$

Substituting Eq C.3 in Eq C.2 the expression for the force estimation signal becomes:

$$\begin{aligned} F(k) = {} & ma'(k) + f_v v'(k) + f_c \\ & + \varepsilon(k)\big(mf_s^2 + f_v f_s\big) - \varepsilon(k-1)\big(2mf_s^2 + f_v f_s\big) + \varepsilon(k-2)\big(mf_s^2\big) \end{aligned} \qquad \text{Eq C.3}$$

The actual force $F'(k)$ is given by:

$$F'(k) = ma'(k) + f_v v'(k) + f_c \qquad \text{Eq C.4}$$

The force estimation error ε_F is given by:

$$\varepsilon_F = \varepsilon(k)\big(mf_s^2 + f_v f_s\big) - \varepsilon(k-1)\big(2mf_s^2 + f_v f_s\big) + \varepsilon(k-2)\big(mf_s^2\big) \qquad \text{Eq C.5}$$

As discussed in Section 5.3.1 the error signals $\varepsilon(k), \varepsilon(k-1), \varepsilon(k-2)$ are uncorrelated white noise sources and let there standard deviations be $\sigma_k, \sigma_{k-1}, \sigma_{k-2}$ respectively and where:

$$\sigma_k = \sigma_{k-1} = \sigma_{k-2} = \sigma = \frac{d}{2\sqrt{3}} \qquad \text{Eq C.6}$$

Using the results given in Eq C.1 with Eq C.5 and C.6 the standard deviation of the force estimation signal σ_F is given by:

$$\sigma_F = \sqrt{\sigma^2\left(mf_s^2 + f_v f_s\right)^2 + \sigma^2\left(2mf_s^2 + f_v f_s\right)^2 + \sigma^2 m^2 f_s^4} \qquad \text{Eq C.7}$$

This reduces to:

$$\sigma_F = f_s^2 \sigma \sqrt{6m^2 f_s^2 + 6mf_s^2 f_v + 2f_v^2} \qquad \text{Eq C.8}$$

and substituting in the value for σ given in Eq C.6 the expression reduces to that used in Section 5.3.1

$$\sigma_F = df_s \sqrt{\frac{3m^2 f_s^2 + 3mf_v f_s + f_v^2}{6}} \qquad \text{Eq C.9}$$